2-D and 3-D high frame-rate Pulse Wave Imaging for the characterization of focal vascular disease

Iason Zacharias Apostolakis

Submitted in partial fulfillment of the
requirements for the degree of
Doctor of Philosophy
In the Graduate School of Arts and Sciences

COLUMBIA UNIVERSITY

2018

ABSTRACT

2-D and 3-D high frame-rate Pulse Wave Imaging for the characterization of focal vascular disease

Iason Zacharias Apostolakis

Cardiovascular diseases are major causes of morbidity and mortality in Western-style populations. Atherosclerosis and Abdominal Aortic Aneurysms (AAAs) are two prevalent vascular diseases that may progress without symptoms and contribute to acute cardiovascular events such as stroke and AAA rupture, which are consistently among the leading causes of death worldwide. The imaging methods used in the diagnosis of these diseases, have been reported to present several limitations. Given that both are associated with mechanical changes in the arterial wall, imaging of the arterial mechanical properties may improve early disease detection and patient care.

Pulse wave velocity (PWV) refers to the velocity at which arterial waves generated by ventricular ejection travel along the arterial tree. PWV is a surrogate marker of arterial stiffness linked to cardiovascular mortality. The foot-to-foot method that is typically used to calculate PWV suffers from errors of distance measurements and time-delay measurements. Additionally, a single PWV estimate is provided over a relatively long distance, thus inherently lacking the capability to provide regional arterial stiffness measurements. Pulse Wave Imaging

(PWI) is a noninvasive, ultrasound-based technique for imaging the propagation of pulse waves along the wall of major arteries and providing a regional PWV value for the imaged artery.

The aim of this work was to enable PWI to provide more localized PWV and stiffness measurements within the imaged arterial segment and to further extend it into a 2-D and 3-D technique for the detection and monitoring of focal vascular disease at high temporal and spatial resolution. The improved modality was integrated with blood flow imaging modalities aiming to render PWI a comprehensive methodology for the study of arterial biomechanics *in vivo*.

Spatial information was increased with the introduction of piecewise PWI. This novel technique was used to measure PWV within small sub-regions of the imaged vessel in murine aneurysmal (n = 8) and atherosclerotic aortas (n = 11) *in vivo*. It provided PWV and stiffness maps while capturing the progressive arterial stiffening caused by atherosclerosis. PWI was further augmented with a sophisticated adaptive algorithm, enabling it to optimally partition the imaged artery into relatively homogeneous segments, automatically isolating arterial stiffness inhomogeneities. Adaptive PWI was validated in silicone phantoms consisting of segments of varying stiffness and then tested in murine aortas *in vivo*.

Subsequently, the conventional tradeoff between spatial and temporal resolution was addressed with a plane wave compounding implementation of PWI, allowing the acquisition of full field of view frames at over 2000 Hz. A GPU-accelerated PWI post-processing framework was developed for the processing of the big bulk of generated data. The parameters of coherent compounding were optimized *in vivo*. The optimized sequences were then used in the clinic to assess the mechanical properties of atherosclerotic carotids (n=10) and carotids of

patients after endarterectomy (n=7), a procedure to remove the plaque and restore blood flow to the brain. In the case of atherosclerotic patients undergoing carotid endarterectomy, the results were compared against the histology of the excised plaques. Investigation of the mechanical properties of plaques was also conducted for the first time with a high-frequency transducer (18.5 MHz).

Additionally, 4-D PWI was introduced, utilizing high frame rate 3-D plane wave acquisitions with a 2-D matrix array transducer (16x16 elements, 2.5 MHz). A novel methodology for PWV estimation along the direction of pulse wave propagation was implemented and validated in silicone phantoms. 4-D PWI provided comprehensive views of the pulse wave propagation in a plaque phantom and the results were compared against conventional PWI. Finally, its feasibility was tested in the carotid arteries of healthy human subjects (n=6). PWVs derived in 3-D were within the physiological range and showed good agreement with the results of conventional PWI.

Finally, PWI was integrated with flow imaging modalities (Color and Vector Doppler). Thus, full field-of-view, high frame-rate, simultaneous and co-localized imaging of the arterial wall dynamics and color flow as well as 2-D vector flow was implemented. The feasibility of both techniques was tested in healthy subjects (n=6) *in vivo*. The relationship between the timings of the flow and wall velocities was investigated at multiple locations of the imaged artery. Vector flow velocities were found to be aligned with the vessel's centerline during peak systole in the common carotid artery and interesting flow patterns were revealed in the case of the carotid bifurcation

Consequently, with the aforementioned improvements and the inclusion of 3-D imaging, PWI is expected to provide comprehensive information on the mechanical properties of pathological arteries, providing clinicians with a powerful tool for the early detection of vascular abnormalities undetectable on the B-mode, while also enabling the monitoring of fully developed vascular pathology and of the recovery of post-operated vessels.

Contents

List of Figures

List of Tables

Acknowledgements

What a ride it has been! As I type these last paragraphs on a Wednesday evening, a typically productive time for me, I am looking incredulously at the screen. I still can't believe that this dissertation, the product of five and a half years of hard work, is finally complete. A significant number of people contributed towards this accomplishment, and in this section I would like to acknowledge them.

Firstly, I would like to thank my advisor, Dr. Elisa Konofagou for believing in me and giving me the opportunity to do my PhD at Columbia University while supporting me at every step of the way. Her trust in me since day one is something that I am very grateful for, especially given that I originally enrolled at Columbia as an MS-only student. Dr. Konofagou was instrumental in my transition into a PhD student, a role through which I gained immense amounts of knowledge and experience in medical ultrasound and biomedical engineering.

I would also like to thank my committee, Dr. Gerard Ateshian, Dr. Jay Humphrey, Dr. Andrew Laine and Dr. Sander Connolly for their scientific guidance and their constructive comments regarding my work. Special thanks to Dr. Humphrey for agreeing to be a member of my committee despite the location constraints.

Furthermore, I would like to thank our pre-clinical and clinical study collaborators: Dr. Fusako Sera, Dr. Shunichi Homma, Ashley Daniel, Evangeline Reyes-Pastorella, Dr. Eliza Miller and Dr. Randolph Marshall. Special thanks to Dr. Eric Stohr for introducing me to new areas of research and for helpful discussions.

Many thanks also go to my UEIL colleagues who guided me through my early years, collaborated with me throughout my PhD and with whom I shared interesting conversations and great laughs. Special thanks go to Marilena Karakatsani, Ronny Li, Mania Samiotaki, Gary Hou, Julien Grondin, Pierre Nauleau, Paul Kemper, Grigorios Karageorgos, Matthew McGarry, Clement Papadacci, Nancy Kwon, Ethan Bunting, Mark Burgess, Adriaan Campo, Tara Kugelman, Alexandre Costet, Matthew Downs, Vincent Sayseng, Lea Melki, Sacha Nandlall, Thomas Payen, Camilo Acosta, Oluyemi Olumolade, Stefanos Papadopoulos, Morgan Smith, Prathyush Narayanan, Jean Provost, Antonios Pouliopoulos, Robin Ji, Stephen Lee, Christian Aurup, Rachel Weber, Koen Hobelman and Marc Heidmann.

Additionally, I would like to thank from the bottom of my heart my friends here in New York that made my transition into the big city smoother and way more fun, imbuing me with their positivity. Special shout-outs to Pia Fouilloux and Antonio Troncoso, Giorgos Argyros, Alexandros Sylaidis, Giannis Mantzouratos, Theofilos Petsios and Stella Lianou, Maria Stella Vradi, Nathan Weber, Areti Karkania, Alex Antoniadis and Ajay Perumal. You guys made New York feel like home.

Finally, I would like to thank my family. Without the constant support of my parents Niko and Sofia and the always positive spirit of my sister Elli, I can’t imagine any way in which I would have achieved everything I have achieved today. No words can describe how much I appreciate all they have done for me throughout the years, aiding me in every way possible. Even during my most hopeless days, they helped me find solutions to my problems, believe in myself and be the best that I can be. After 5 years apart the aim has been achieved, this one’s for you!

I would like to dedicate this dissertation to my ever-supportive family.

Niko, Sofia and Elli I love you.

Chapter 1. Background and Motivation

1.1. Properties of the arterial wall

The circulatory system is comprised of two primary types of vessels – veins and arteries. The function of the arterial system is to conduct oxygenated blood from the heart to the peripheral organs at high pressure and in continuous stream [1]. The pressure in the arterial tree is kept at a relatively high value since the it is divided into many arterioles and hereby forms a large peripheral resistance [2]. According to specific anatomic and physiologic features arteries are divided into three categories [3]:

1) Large elastic arteries
2) Medium-sized muscular arteries
3) Small arteries or arterioles

Given that the flow from the heart is very pulsatile, blood pressure and flow velocity fluctuate throughout the cardiac cycle, thus acquiring values that are significantly different than their mean values. However, flow in the arterioles should be steady in order to minimize the hydraulic power supply requirements of the heart and the drag forces imposed to the delicate endothelium of smaller arteries [4], [5]. When healthy, the large elastic arteries (aorta, carotid, iliac, femoral and brachial) contribute to the reduction of the flow pulsatility and conversion into continuous blood flow by passive expansion and elastic recoil. This is known as the Windkessel effect [2], [5], [6]. More specifically, the compliance of large arteries acts as the

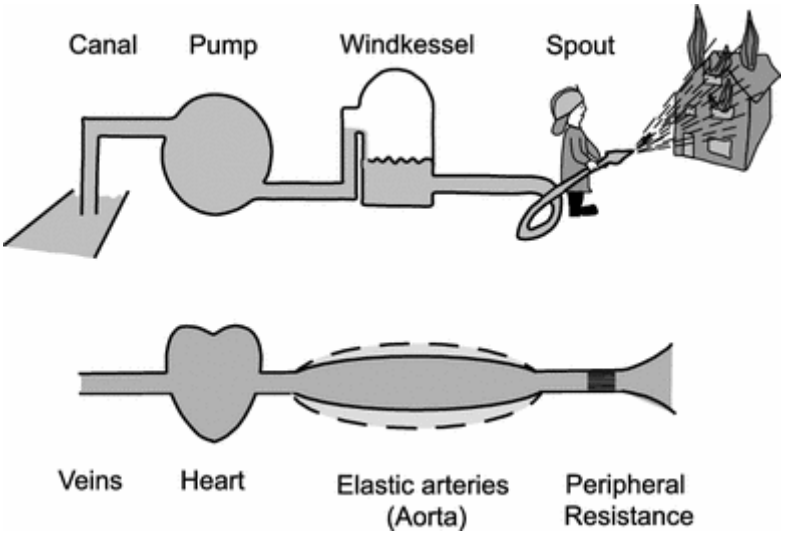

Figure 1.1: Graphical depiction of the Windkessel effect. Comparison of the large artery elasticity to the Windkessel present in fire engines. Source: [7]

Windkessel as graphically shown in Figure 1.1 and is estimated as the ratio of a volume change ΔV and the resulting pressure change ΔP [7]:

$$C = \frac{\Delta V}{\Delta P} \quad (1)$$

Furthermore, arterial compliance, as determined by the large arteries, prevents the arterial pressure from falling abruptly due to the closure of the heart valve. The medium-sized muscular arteries draw blood from the large elastic arteries and distribute it to vital organs and arterioles, which in turn are responsible for maintaining the mean blood pressure and delivering continuous flow of blood to organs. These smaller vessels predominantly contribute to the peripheral resistance which can be estimated as the ratio of mean pressure over the mean flow in the system [8].

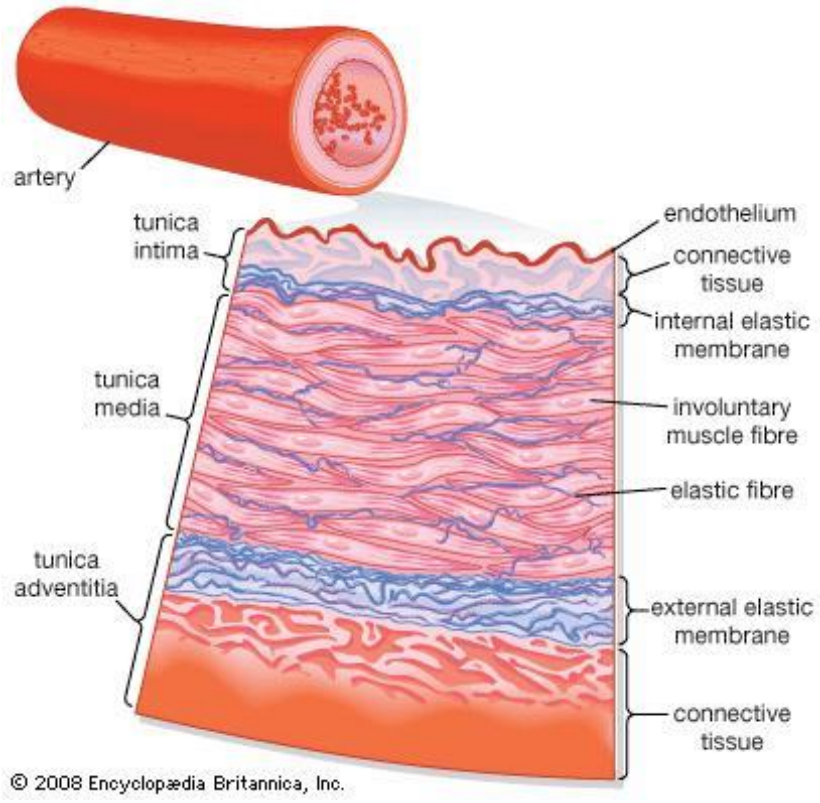

Figure 1.2: Anatomical description of the arterial wall. The three main layers (intima, media and adventitia) as well as the internal and external laminae are indicated. Furthermore, the most prominent constituents of each layer are marked. Source: *Encyclopedia Britannica, Inc., 2008.*

The arterial wall of elastic arteries possesses three layers or tunics called the intima, media and adventitia (Figure 1.2). The media layer is bounded by the internal and external elastic laminae. These structures consist of meshes of elastin, which are lined on the intimal side by a coarse fibrous network [6]. The tunica intima is the innermost layer of the arterial wall. It consists of a single layer of endothelial cells and a thin layer of elastin and collagen fibers that allows attachment to the internal elastic lamina. The tunica media has a fibrous structure and consists mostly of smooth muscle cells, elastic laminae and bundles of collagen and elastin fibers [6]. As also seen in Figure 1.2 it is the largest layer of the arterial wall and thus determines both the

vessel's mechanical properties and physiological responses [9]. It should be noted that even though the media is histologically heterogeneous, the interlocked structure of elastin, smooth muscle cells and collagen it causes is it to act mechanically as a homogeneous material [6]. Finally, the tunica adventitia along with the tunica media mainly contribute to the arterial wall's histological heterogeneity and is mostly made of collagen and some elastic fibers that are connected with the surrounding soft tissue [10].

It has been reported that the most important elastic materials that define the mechanical behavior of the arteries are elastin and collagen. Smooth muscle cells, being another major constituent of the arterial wall, contribute to wall tension. However, they are not considered to be an elastic material and in general contribute minimally to the mechanical behavior of large elastic arteries [6], [11]. Elastin is highly distensible and provides reversible extensibility at low pressure levels during the cardiac cycle. Meanwhile, collagen fibers are 100-1000 times stiffer, start elongating as pressure levels rise and provide a safety net to prevent the vessel from bursting at high transmural pressures [6], [11]. The relative ratio of these two materials is, consequently, a major determinant of the vascular elasticity [6].

1.2. Vascular disease

Cardiovascular disease and produces immense health and economic burdens both in the United States and globally [12]. Vascular disease refers to any condition that affects the circulatory system and according to the latest update of the American Heart Association (AHA)

approximately 44% of the US adult population is projected to have some form of CVD by 2030 [13]. For the purposes of this work focus will be shifted to vascular diseases affecting large elastic arteries. Two of the most prevalent arterial diseases are atherosclerosis and abdominal aortic aneurysms (AAA).

1.2.1. Atherosclerosis

Stroke is one of the most prevalent CVDs and when considered separately from other cardiovascular diseases, it's the 5th leading cause of death in the US, 2nd leading single cause of death in Europe and leading cause of death in China [13]–[16]. Symptomatic large-artery and especially carotid atherosclerosis has been repeatedly linked to an increased risk of stroke [17]–[19]. Additionally, especially in hypertensive patients, atherosclerosis affects the extremities (i.e. peripheral artery disease), the kidneys (i.e. chronic renal disease) and is associated with all major adverse cardiovascular events leading to higher mortality rates [20]–

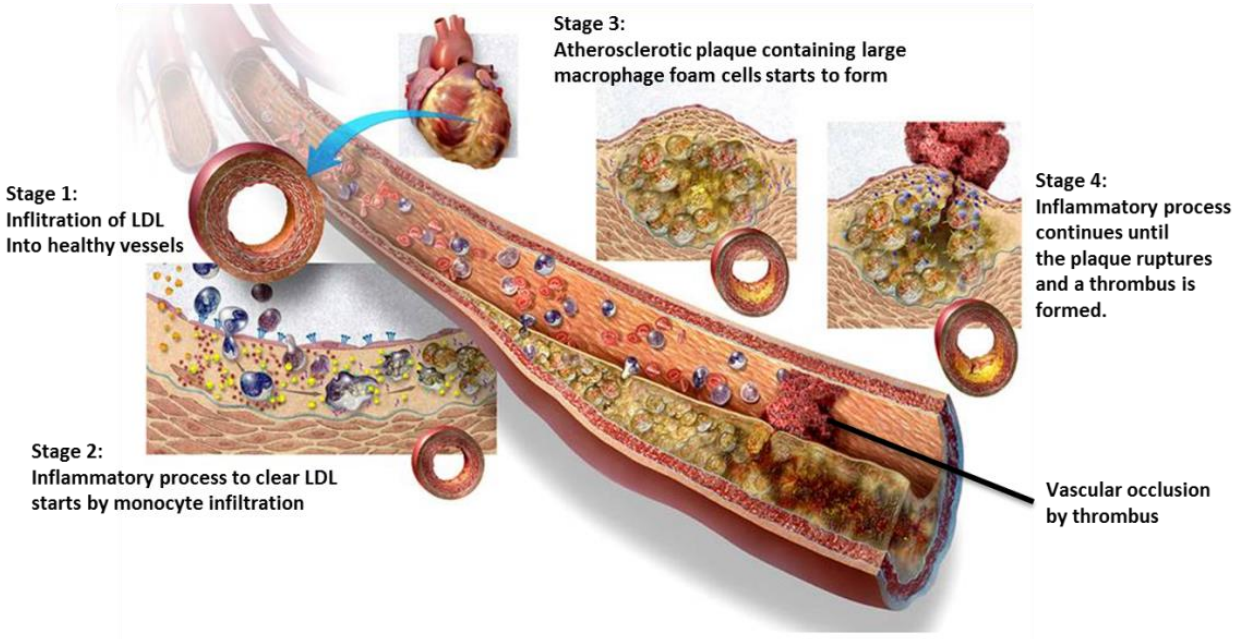

Figure 1.3: Schematic illustrating the progression of atherosclerosis. Source: [282]

[22]. It primarily affects large- and medium-sized vessels and is characterized by a focal accumulation of lipids, complex carbohydrates, blood cells, fibrous tissues and calcified deposits [6], [23].

A widely accepted model describing the early stages of atherosclerosis is the response-to-retention model [24]–[28]. According to this model, during the initial stages of atherosclerosis pre-existing conditions such as hypertension or hyperlipidemia precipitate changes in the permeability of the intima layer's endothelial cell and alterations in the sub-endothelial extracellular matrix. These changes result to the entry and retention of low density lipoprotein (LDL) particles within the intima layer of the arterial wall [25], [29]. High concentration of LDL in the bloodstream has been reported to facilitate the retention of these cholesterol-rich lipoproteins in the sub-endothelial matrix [25]. This lipoprotein retention attracts macrophages from the bloodstream into the intima that eventually become engulfed in lipoprotein particles and attain a foamy appearance [30], [24]. These lipoprotein-laden macrophages are referred to as foam cells and are indicators of the initial atherosclerotic lesion.

As the atherosclerotic plaque increases both in size and complexity, smooth muscle cells migrate from the media layer to the intima and then resynthesize components of the extracellular matrix, forming a fibrous cap that walls off the lipoprotein and macrophage deposits in the intima layer [25]. Additionally, as several foam cells die (macrophage apoptosis), they release lipids forming a lipid-rich pool under the fibrous cap, known as the lipid or necrotic core of the plaque [25], [30], [31]. Frequently, as the atherosclerotic plaque develops over time

and ultimately turns into a chronic inflammatory condition of the arterial wall, it becomes calcified [32]. This process of calcification of the atherosclerotic lesion, originally thought to be a passive mechanism, has been relatively recently posited to be an active process that resembles bone formation triggered by chronic inflammation of the arterial wall by the atherosclerotic lesion [33]–[35]. A schematic of atherosclerotic disease progression can be seen in Figure 1.3.

The two mechanisms through which atherosclerotic plaques produce clinical symptoms are by completely occluding the lumen of the affected artery thus inducing ischemia to the affected tissues and by facilitating the creation of thrombi that may become detached and ultimately embolize arteries at distal sites [30]. For example, stroke events are frequently caused by thrombi generated from the disruption of carotid plaques that become lodged upstream in the smaller vessels of the brain (Figure 1.4 a) [36]. Such thrombogenic events occur after the rupture of the fibrous cap of the plaque. A ruptured fibrous cap ceases to shield the lipid core from the blood stream, thus promoting thrombosis. Frequently, plaques that are prone to rupture (vulnerable plaques) do not coincide with plaques that are highly occlusive. Vulnerable plaques, as also confirmed by pathological studies [37], are plaques with a large lipid core, a thin fibrous cap (cap thickness<65 μm) and abundant macrophages [38]. The thin fibrous cap increases the risk of plaque rupture, while the large necrotic core and the macrophages are the catalysts for thrombosis [30].

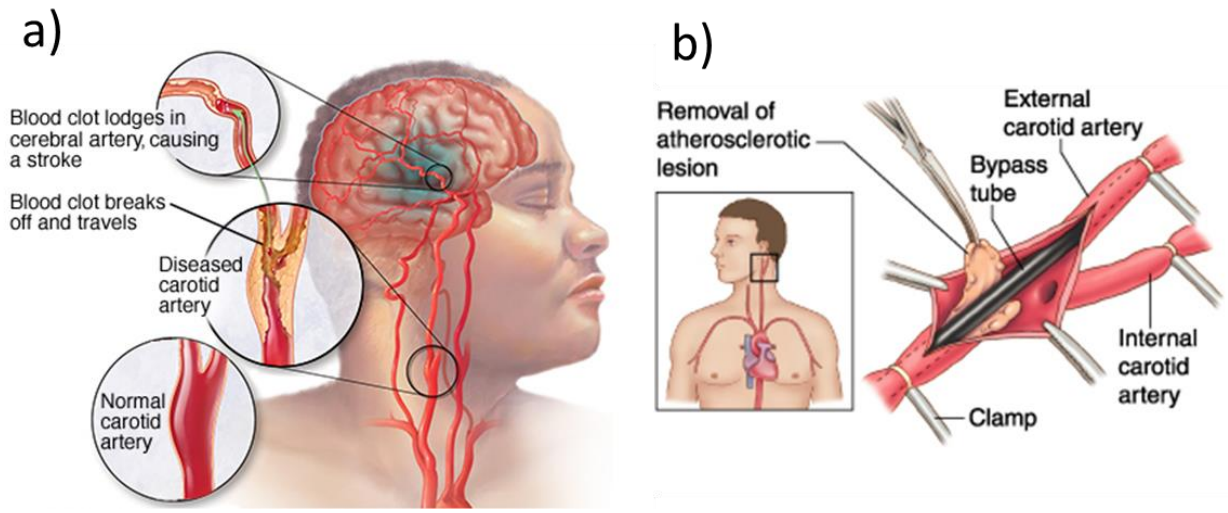

Figure 1.4: a) Schematic of a normal and a stenotic carotid artery and graphical depiction of an ischemic stroke due to a blood clot lodged upstream in a smaller vessel in the brain, b) illustration of the endarterectomy procedure. Sources: a) Mayo Clinic b) Reed Group/MDGuidelines

It should be noted that hemodynamics have been shown to play a crucial role in atherogenesis as well as plaque rupture. Atherosclerosis has been shown to develop in areas of the arterial tree where the arterial wall is subjected to low or oscillatory shear stress or secondary flows [39], [40]. For example, the carotid bulb opposite of the flow divider is a common site of plaque development [41]. Additionally, high tensile stress in the arterial wall has been reported to promote diffuse atherosclerosis [6]. On the contrary, high arterial wall shear stress is indicated as a major plaque destabilization factor causing plaque rupture especially on its upstream side [42], [6], [43]. More specifically, a previous biomechanics study investigating the anisotropic properties of atherosclerotic plaques has indicated that increase of circumferential stress on the fibrous cap leads to the greatest risk of rupture [44].

Current clinical tests used to detect atherosclerotic plaques in the carotid artery include duplex Doppler ultrasonography, magnetic resonance angiography, computed tomographic angiography and catheter angiography [45]. It should be noted that all of these techniques focus on deriving the degree of stenosis of the affected artery. Subsequently, in the cases of stenotic arteries with more than 60-70% of the carotid diameter occluded due to atherosclerosis, carotid endarterectomy (CEA) (Figure 1.4b) operation is suggested with increased benefits in the case of symptomatic patients [46], [47]. However, although the degree of stenosis has been shown to be a relevant marker of the risk of stroke [48], [49] non-stenotic and less stenotic plaques can also rupture [30],[50]. More specifically, in the case of carotid plaques just as in the case of coronary plaques, it has been reported that soft, lipid-laden and often less occlusive plaques are the most likely to rupture [6]. Additionally, another study has found reduced correlation between characteristics of vulnerable plaque (necrotic core size and cap thickness) to the degree of stenosis [51]. Finally, the consistency of measurements conducted with the aforementioned techniques may be affected by arterial remodeling, which functions as a compensatory factor for the lumen narrowing due to atherosclerosis [52], [53].

Both noninvasive techniques in major clinical studies and *ex vivo* mechanical testing experiments have pointed out that atherosclerosis appears to produce an overall increase in arterial stiffness [6], [54], [44]. However, plaque components linked to a higher plaque rupture risk (i.e. a large lipid core) have been reported to be softer [55], [56], [57], [58]. Conversely, stiffening of the necrotic core of the plaque, either due to lipid-lowering therapy that converts

liquid cholesterol deposits in the lipid core into crystalline cholesterol monohydrate, or due to severe calcification (>45% of the total plaque) has been associated with carotid plaque stability [59], [60], [61]. Additionally, it has previously been suggested that further insight into the complex mechanical properties of the plaque components will allow the precise estimation of the peak stress concentration on the plaque's fibrous cap, a known predictor of rupture [61], [58], [62], [40]. The aforementioned data establish that atherosclerosis alters the mechanical properties of the arterial wall and also suggest that characterization of the mechanical properties of the atherosclerotic plaques and the surrounding wall tissue may provide complementary information crucial to patient care [63].

1.2.2. Abdominal aortic aneurysm

The abdominal aortic aneurysm (AAA) is a common form of aneurysm. It is typically defined as a permanent and irreversible dilation of the abdominal section of the aorta by at least 50% over its normal diameter. AAAs are significant causes of morbidity, especially in older populations as

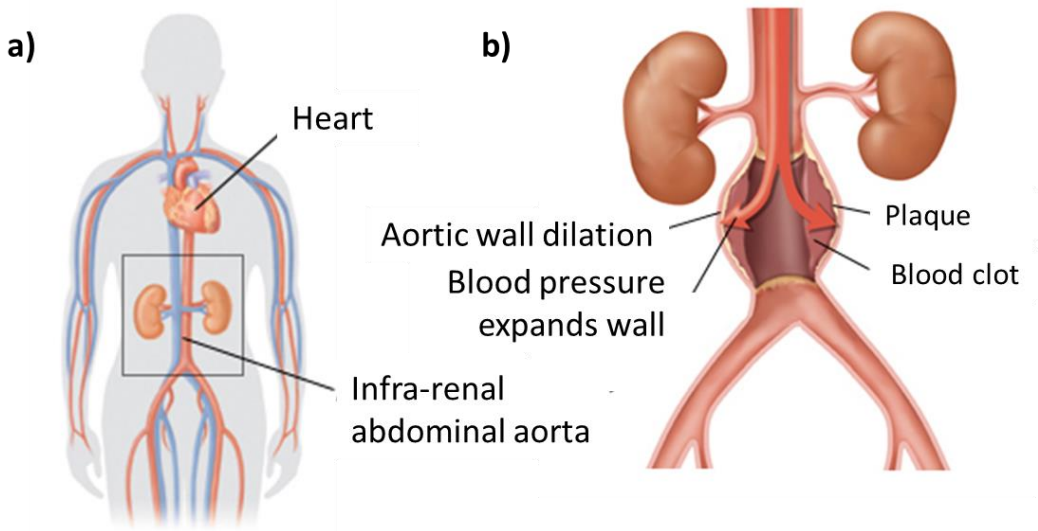

Figure 1.5: a) Location of AAA development. b) Illustration of AAA morphometry. Modified from source: *www.health.harvard.edu*

their prevalence is 12.5% in elderly males and 5.2% in elderly females [64]. AAAs cause more than 10,000 deaths in the United States annually [24]. It affects more men than women and the overall mortality following rupture of an aortic aneurysm exceeds 75%, including emergency surgical intervention [65]. In humans, most AAAs occur in the infrarenal abdominal aorta as shown in Figure 1.5 a), a site that is known to consist of a lower number of elastic lamellae for a vessel of its size [66], [67]. Major causes of the dilatation of the arterial wall are either congenital (i.e. Marfan syndrome) or acquired (i.e. excessive stress on the wall due to long-standing hypertension, elastin fatigue due to old age) [6]. Typically, the initiation of the dilatation of the vessel is due to the degradation of elastin in the arterial wall and subsequent shift of the load of pulsatile flow to collagen causing structural damage in the artery [68], [69]. Atherosclerosis may also play a role in aneurysm development by encroaching on the media layer of the aorta, weakening of structural elements and promoting diffuse inflammation to all arterial wall layers (Figure 1.5 b)) [6]. This hypothesis is also supported by hemodynamic studies indicating that the infrarenal abdominal aorta is subjected to oscillatory wall stresses, a promoter of atherosclerosis [67]. As the aortic wall dilates, the adventitia thickens, increasing its collagen content and thus, attempting to compensate for the altered arterial wall genetics and mechanics [67], [70].

Aneurysm dissection is a partial disruption of the aortic wall that further weakens the wall and predisposes to complete rupture [6]. It usually initiates with a tear of the intima followed by degeneration of the already weakened media. On a microscopic level, at sites of aneurysm dissection, rarefaction of interconnection between the elastic lamellae in the media, has been reported, possibly leading to the local weakness of the arterial wall [71]. Another factor that

may render the wall prone to rupture, especially in the aging aorta, is medionecrosis, namely the loss of smooth muscle cells of the arterial wall as they're replaced by collagen fibers, a result of the wall adapting to altered stress conditions [72].

From a biomechanics standpoint, aneurysm dissection occurs when the wall stresses exceed the diseased wall strength [73]. Given the spatially varying properties of the aneurysm it has been reported that the anterior region of the aneurysm is the most susceptible to rupture, especially to stress along the longitudinal direction [74]. In agreement with the significance of wall stress on AAA rupture, it has been previously reported that dissections frequently occur during instances of acute hypertension (i.e. severe exertion or emotion) [75]. Typically, AAAs are known to contain intraluminal thrombi due to blood clotting in the false lumen [6]. These clots have been found to shield the wall from increased stress, thus promoting fibrous repair [6], [73], [76].

Currently, the typical diagnostic techniques for detecting AAAs are abdominal ultrasound and computed tomography (CT) [73], [77] and the highest risk of rupture is identified when the transverse diameter of the aneurysm reaches or exceeds 5-5.5 cm, or if the maximal diameter of the lesion increases more than 0.5-1 cm within a year [78], [79]. In order to prevent adverse events in the case of higher risk patients, preventative aortic repair surgery is performed [80]. More specifically, endovascular aneurysm repair (EVAR) and open repair are the two current aneurysm repair options. Recent longitudinal studies following a large number of patients have shown that while survival is significantly higher with EVAR during the first 8 years post-surgery,

open repair shows higher survival after that period [81], [82]. A major cause of long term morbidity and mortality in the case of EVAR are stent leaks into the aneurysmal sac (endoleaks), an open problem that various imaging modalities have attempted to solve with CT being the current gold standard, an expensive and ionizing modality [83].

However, while the diameter of the aneurysm as a risk assessment criterion is reasonable, small AAAs rupture too and it does not have a physically sound theoretical basis [73], [84]. Consequently, the rupture risk prediction using the current diagnostic techniques available in the clinic is flawed. AAAs are known to affect the mechanical properties of tissues [69], [70] and in order to accurately predict aneurysm dissection, a more sophisticated criterion that is based on knowledge of both wall strength and wall stress is needed [73], [84]. Additionally, progression and enlargement of the AAA has been linked to changes in wall stiffness with aneurysms having a diameter > 6 cm showing a significant decrease of distensibility [6], [85]. Furthermore, a currently open problem in AAA prediction is to investigate how AAA risk factors such as atherosclerosis, hypertension, cigarette smoking, or diabetes influence the stiffness of the affected vessels [69]. Consequently, gaining insight into the arterial mechanical properties would effectively complement the AAA size criterion and also elucidate the mechanisms of early AAA formation and vulnerability.

1.3. Arterial pulse wave

1.3.1. Pulse wave velocity

At the start of every cardiac cycle, blood is pumped into the circulatory system generating pressure waves that propagate throughout the arterial tree inducing causing arterial vessels to distend as seen in Figure 1.6. Propagation of pressure waves within an elastic vessel along the longitudinal direction x is governed by the wave equation:

$$\frac{\partial^2 p}{\partial x^2} - \frac{1}{PWV^2}\frac{\partial^2 p}{\partial t^2} = 0 \quad (2)$$

where p is the pressure within the elastic vessel and PWV is the velocity of the pressure wave

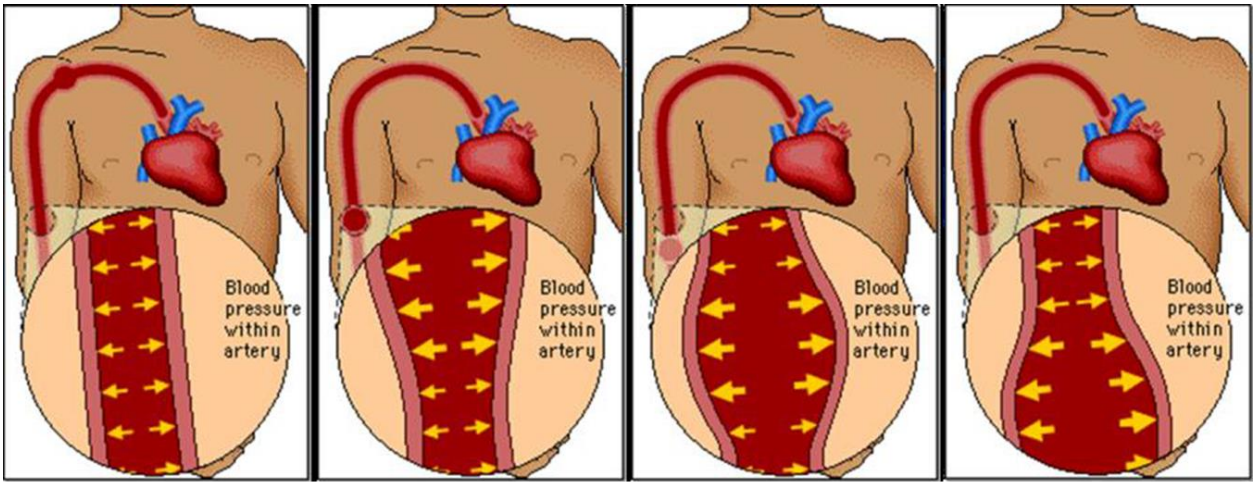

Figure 1.6: Simplified animation depicting the pulse wave-induced arterial wall expansion. a) Each left ventricular contraction expels a volume of blood into the arterial tree. (b-d) The resulting pressure wave propagates along the large elastic arteries causing distension of the arterial wall. Source: *Goldie's Room Online, R.X. Li (2016), Ultrasonic Pulse Wave Imaging for in vivo assessment ofvascular wall dynamics and characterization of arterial pathologies, Doctoral dissertation, Columbia University, New York, NY, USA.*

propagation [1]. In theory, however, blood flow velocity is linearly related to *p* and small changes of the artery's radius are linearly related to changes of *p* and thus related by the same wave equation [1], [86]. Consequently, it can be seen that the pulse wave manifests itself as a pressure, flow velocity and wall distension wave [6]. The velocities at which these waves travel have been both theoretically and experimentally found to be the same and have been used interchangeably denote the pulse wave velocity (PWV) [1], [6], [87]. PWV is widely accepted as one of the most robust parameters directly related to arterial stiffness [6], [88]. PWV increases as the arterial wall becomes stiffer and has been proposed as a marker of cardiovascular risk [6], [89], [90] and has been included in the European society of hypertension guidelines for the management of hypertension [91]. Additionally, PWV has been found to increase with both pressure and age, thus indicating arterial stiffening in hypertensive and ageing populations (Figure 1.7) [92].

Assuming the arteries behave similarly to elastic, thin-walled tubes filed with an ideal incompressible and inviscid liquid, the modified Moens-Korteweg equation relates the wave velocity to the Young's modulus of the artery in the circumferential direction, a direct index of arterial stiffness, as follows:

$$\boldsymbol{E = \frac{2R\rho(1 - v^2)PWV^2}{h}} \qquad \textbf{(3)}$$

where E is the Young's modulus of the elastic tube wall, h is the wall thickness, ρ is the blood density, R is the inner radius of the tube and v is the Poisson's ratio (the latter appears in the

equation to compensate for the finite thickness of the wall). Furthermore, by eliminating the thin wall assumption as well as the vessel circumferential homogeneity assumption, the PWV is also linked to arterial compliance (C) via the Bramwell-Hill equation:

$$C = \frac{A}{\rho \cdot PWV^2} \quad \textbf{(4)}$$

where ρ is the blood density, C=dA/dP indicates the cross-sectional compliance, namely a change in the vessel's cross-sectional area (dA) over a given change in blood pressure (dP) with A being the arterial cross-section luminal area and P the arterial blood pressure within the vessel [93].

As the pulse wave travels along the arterial tree, arterial junctions, arterial tapering, sites of arterial stiffness discontinuities such as focal arterial diseases cause wave reflections [6]. in healthy young subjects reflected waves from the periphery return to the heart causing an increase in pressure during diastole having a beneficial effect on coronary perfusion [94]. However in the case of ageing, stiffer arteries where the PWV of the pulse wave is higher, these reflected waves return to the heart earlier during late systole and boost pressure, increasing left ventricular load and decreasing ventricular ejection ultimately raising the risk for congestive heart failure and coronary artery disease [95], [96], [97]. Arterial reflections in stiff arteries have been shown to alter the morphology of the pressure and distension waveforms as the reflected wave merges with the forward wave with only the early wavefront of the propagating pulse

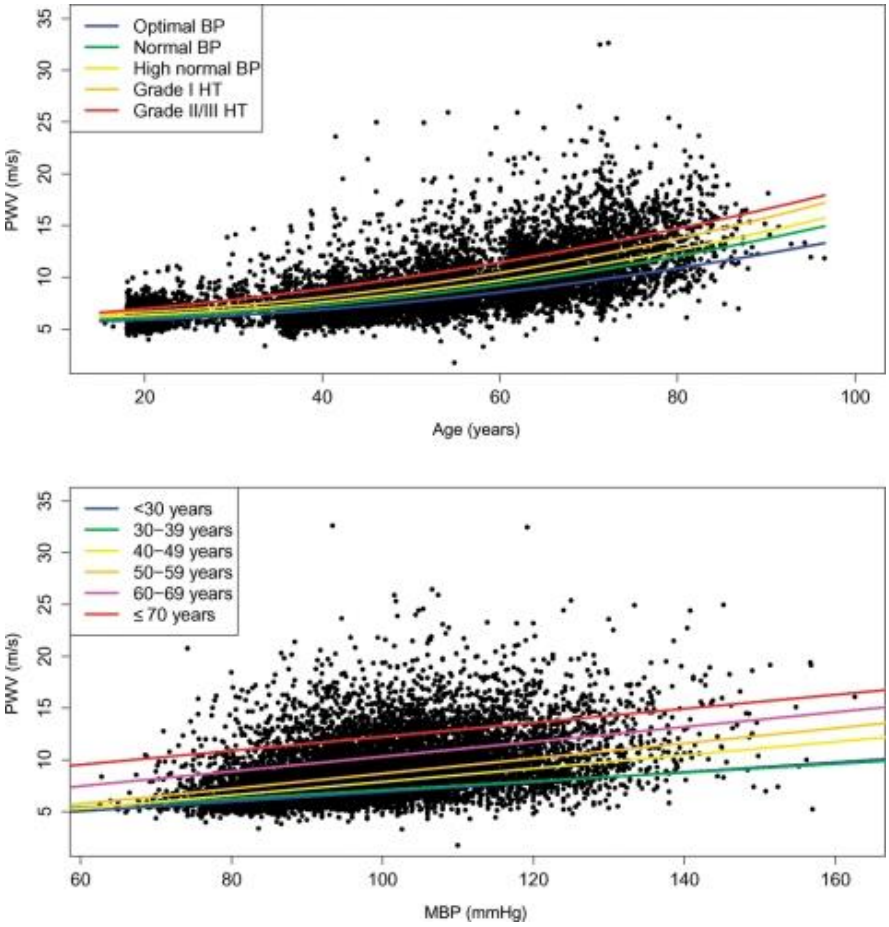

Figure 1.7: (Top) PWV vs. age in 11,092 subjects. Regression lines denote the results of regression on age for different blood pressure (BP) categories. (Bottom) PWV vs. mean blood pressure (MBP) in the same population (11,092 subjects). Regression lines denote the results of linear regression on mean blood pressure for different age categories. HT, hypertension; BP, blood pressure. Source: [92]

wave retaining its "identity" and thus being the prime candidate for tracking the pulse wave as will be discussed in the next section [6], [96].

1.3.2. Current measurement techniques

Currently, in most large-scale longitudinal studies that use PWV as an index of arterial stiffness, PWV measurements are obtained noninvasively using applanation tonometry or Doppler flow velocimetry [89], [98], [99], [100], [6]. PWV is usually determined over the carotid-femoral

region by dividing the total length of the propagation pathway over the time of travel of the pressure wave between the two sites.

Three of the most prevalent systems used in the majority of arterial stiffness clinical studies include SphygmoCor (AtCor Medical, New South Wales, Australia), Complior (Artech Information Systems, Morristown, New Jersey, USA) and Pulse Pen (DiaTecne s.r.l., Milan, Italy). These systems differ in their sensor technology and the algorithm used for calculating the pulse propagation time [101], [6]. The SphygmoCor and Pulse Pen devices use arterial tonometers for recording pressure waveforms. Propagation time is measured using the foot-to-foot method, which consists of measuring the time between the foot of the carotid waveform and the foot of the femoral waveform using sequential ECG-gated recordings (Figure 1.8) In the Complior system, carotid and femoral waveforms are recorded simultaneously using mechanotransducers, and timing is referenced to the point of maximum systolic upstroke. Both of these techniques require distance measurements of the pulse wave propagation pathway. These distance measurements are taken with a measurement tape from the sternal notch to the carotid and femoral arteries at the sensor locations [102]. Although this seems to be a crude way of estimating the total length of the pulse propagation pathway, a more recent study comparing the accuracy of PWV measurements using various techniques of measuring the carotid-femoral distance against invasive catheter measurements showed agreement and reproducibility of the PWV measurements as long as the distances were estimated using flexible tape, accounting for the tortuosity of the pathway, and not a straight caliper [103].

Carotid-femoral PWV has been repeatedly shown to be a reliable predictor of all-cause cardiovascular mortality (both cardiac and cerebral events) in large scale studies such as the Framingham and the Rotterdam study [98], [104], [105], [106] , atherosclerotic vascular burden [54] and target organ damage in the arterial circulation, especially among hypertensive patients [103], [107]. However, the aforementioned methods to estimate the carotid-femoral PWV present limitations due to errors in both distance and time-delay measurements [108], [109]. Further compromising the accuracy of these measurements is the fact that the waves the pulse in the carotid and the femoral is travelling towards opposite directions and also that the waveform shapes are significantly different, thus complicating the correct identification of the same feature (i.e., the foot of the wave) in both waveforms. As mentioned previously the factor that predominantly compromises the correct identification of the wave features is wave reflection [110], [111]. Multiple reflection points exist along the arterial tree, and their location remains elusive [112]. Consequently, local identification of these points is an open problem the solution of which would greatly benefit PWV estimation.

Another major drawback of the carotid-femoral estimation methods is that the measured PWV provides a global estimate of the PWV across the entire circulation, ignoring variations in arterial stiffness along the arterial tree and inherently lacking the capability to provide regional arterial stiffness measurements [6]. The severity of this limitation can be further stressed given that vascular diseases such as atherosclerosis and AAAs are focal vascular diseases affecting localized regions and precipitating spatial inhomogeneities of the mechanical properties along the arterial tree.

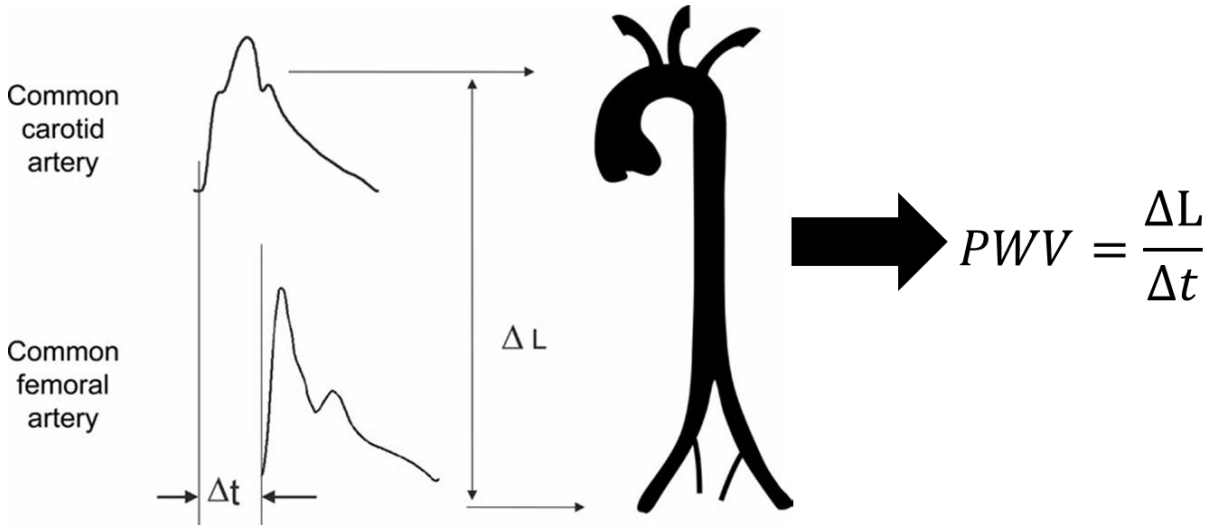

Figure 1.8: Implementation of the foot-to-foot method for PWV measurement using applanation tonometry entails measuring the travel time and distance of the pressure waveform between two remote sites, commonly the carotid and femoral arteries. The difference in the morphology of the two waveforms can be observed. Source: [88]

Several medical imaging-based methods have been previously developed for noninvasive measurements of regional PWV, mainly using magnetic resonance imaging [113], [114], [115], [116] and ultrasound methods, including Doppler velocimetry, and echo tracking [117], [118], [119], [120], [121]. However, while the aforementioned techniques present some advantages (i.e. MRI providing accurate estimation of arterial distance travelled), they lack either the temporal resolution, spatial resolution, or both to capture the propagation of the pulse wave along of a few millimeters of the arterial wall. To this end, ultrasound imaging could provide a cost-effective, non-ionizing solution, offering both superior frame rate and a high scan line density.

In Chapter II there will be a brief description of the basic principles of ultrasound and its use in imaging arterial disease, followed by an introduction to Pulse Wave Imaging (PWI), a technique developed by our group to image the pulse wave propagation. Furthermore, at the end of that chapter there will be a description of all of the following chapters, providing the structure of the present thesis.

Chapter 2. **Ultrasound Imaging of Arterial Disease**

2.1. Principles of ultrasound imaging

Diagnostic ultrasound involves the use of high frequency (2-20 MHz) sound waves to visualize structures within the body. In pulse-echo ultrasound, the ultrasound transducer includes piezoelectric crystals that convert electrical pulses to ultrasound pulses and subsequently transmits them into the body (also referred to as ultrasound beams).

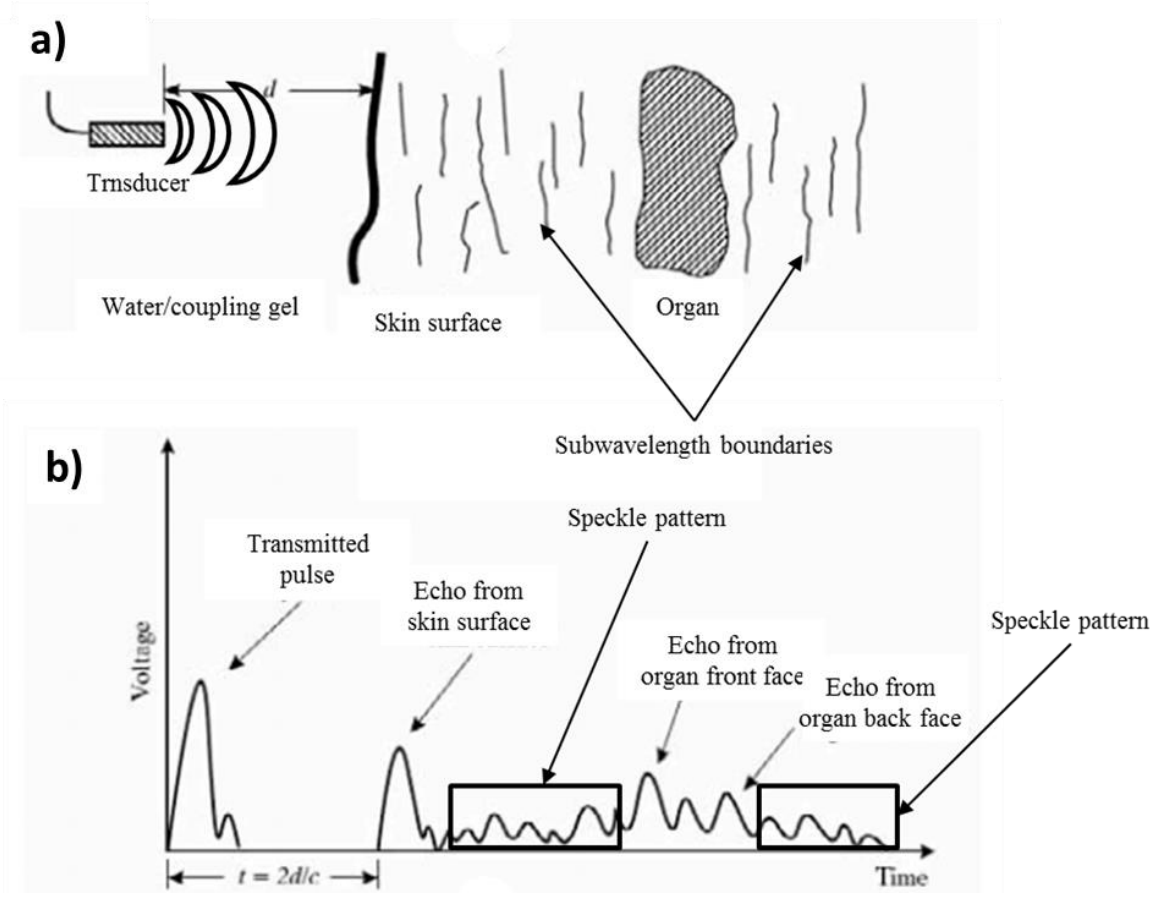

Figure 2.1: a) An ultrasonic transducer transmitting ultrasound waves towards an organ within the body. b) The resulting amplitude of the transmitted and reflected waves as picked up by the piezoelectric element of the transducer.

At each boundary between neighboring regions of different acoustic impedance a certain amount of the ultrasound pulse of the ultrasound pulse gets reflected and a remainder continues as a transmitted wave. The reflected echoes are recorded by the piezoelectric elements of the ultrasound transducer and by using an approximation of the speed of sound in tissue (1540 m/s) the position of the boundary position and shape can be determined (Figure 2.1) [122]. There are two types of reflection occurring in ultrasound pulse echo imaging [123]:

- Specular reflection, that occurs in the case of reflection from large (i.e. with dimensions a few times larger than the wavelength of the ultrasonic pulse), regularly shaped objects with smooth surfaces. It should be noted that specular reflection is highly angle-dependent and produces

- Scattering, a type of reflection in which the wave gets dispersed in all directions and occurs in the case of relatively small (i.e. sub-wavelength), weakly reflective, irregularly shaped objects. Scattering produces less angle-dependent weaker reflections that also interact with each other. This interaction causes constructive and destructive interference of the waves. The granular appearance of the resultant image is termed “speckle”. Blood cells are prime examples of ultrasound scatterers.

It should be noted that most tissues exhibit a combination of the two reflection patterns.

The conventional paradigm of ultrasonic image formation involves an array transducer (a transducer with an arrangement of piezoelectric elements either in linear or curvilinear format), adjacent groups of elements are electronically excited sequentially. Appropriate delays are applied to the excitation of each element of the element group in order to generate a focused ultrasound beam which is subsequently moved to neighboring groups of elements along the surface of the array transducer in order to create an image [123]. The time delays between the excitation of each element group can be further used to direct the ultrasound beam and create a focus. The ultrasound system then receives the reflected echoes from the scanned body's interfaces and scatterers in the form of radiofrequency (RF) data, which represent the received acoustic pressure waves.

Subsequently, the envelope of the received RF-data for each ultrasound beam is detected and the estimated amplitude values are mapped nonlinearly according to a logarithmic function which adjusts the dynamic range. These amplitude values at each determined depth for all the beams are then stacked laterally and a 2-D brightness (B-mode) image is formed by representing the amplitude values with a brightness level at each corresponding point of the image. Each line in the B-mode image corresponds to one ultrasound beam emitted by a group of elements (Figure 2.2). It can be seen however that in the case of conventional B-mode imaging a tradeoff is introduced between the number of lines employed to create an image (beam density) and the rate at which images are acquired (frame rate). This particular tradeoff between spatial and temporal information is crucial for using ultrasound to track high-propagation-velocity transient waves in the body and will be further discussed in this thesis.

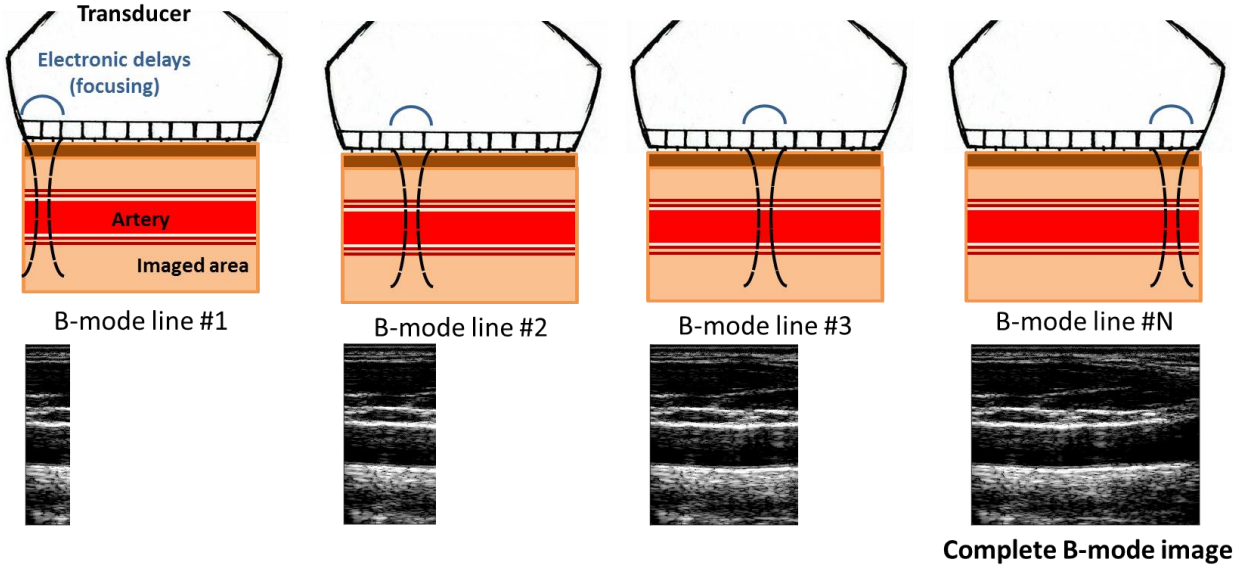

Figure 2.2: Conventional focused ultrasound scanning of a common carotid artery. Focused beams are sequentially fired by neighboring groups of elements. Each ultrasound beam corresponds to a single line in the resulting B-mode image.

The duration (or conversely the bandwidth) of the transducer's pulse and center frequency of the transducer determine axial resolution (i.e. along the ultrasound beam), while lateral resolution is determined by the width of the beam at the depth of imaging. In both cases a higher central frequency leads to higher overall spatial resolution, thus allowing the inspection of smaller structures within the body. However, this is at the cost of penetration depth due to tissue attenuation [123].

B-mode imaging has been extensively used in vascular ultrasound to investigate tissue structure of arteries in the upper and lower limbs, extracranial arteries and in the abdomen. More specifically, in the case of carotid atherosclerosis, B-mode imaging has been used to examine the morphology of atherosclerotic lesions [124], [125]. More recently, 3-D conventional B-mode

imaging was introduced with 2-D arrray transducers, expanding the paradigm of conventional ultrasound scanning in three dimensions, and used to assess plaque volume as an indicator of the risk of rupture [126]. Additionally, abdominal ultrasound detects AAA with almost 100% sensitivity and B-mode imaging has been used to determine the AAA's diameter with reasonable reproducibility (approximately 0.6 cm) [127]. However, limitations have been reported regarding the effectiveness of solely B-mode imaging for the assessment of stenosis [128]. Towards that end, Doppler ultrasound methodologies measuring blood flow velocities were developed and subsequently used extensively in conjunction with B-mode imaging to diagnose and evaluate carotid atherosclerosis.

Pulsed Wave (PW) Doppler and Color Doppler are two popular techniques used in vascular ultrasonography for the visualization and quantification of blood flow velocities. Doppler techniques use the frequency shift caused by moving blood to derive the flow velocity based on the Doppler shift equation:

$$f_d = \frac{2f_t|v|cos\theta}{c} \quad \textbf{(5)}$$

where f_d is the Doppler shift frequency, θ is the angle between the ultrasound beam and flow vector, $|v|cos\theta$ is the component of the velocity of the target along the axial dimension of the transducer, f_t is the transmitted ultrasound frequency and c is the velocity of ultrasound in the tissue [129]. As seen from the equation, only the velocity component along the ultrasound

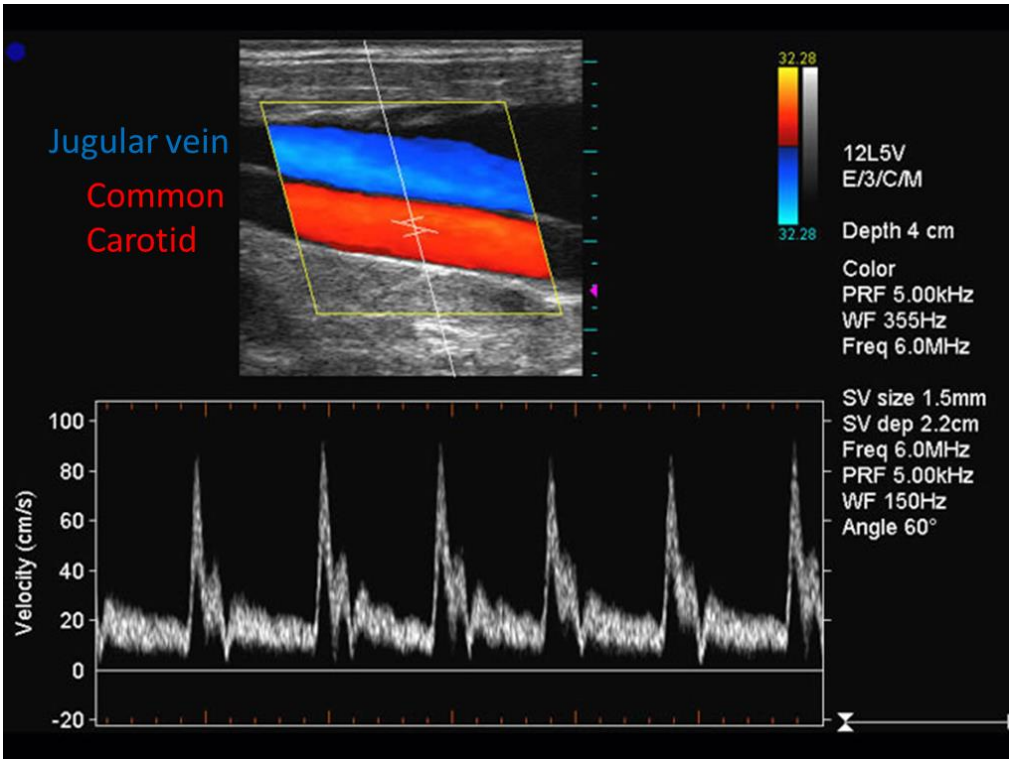

Figure 2.3: Screenshot from a triplex ultrasound modality. Color Doppler is shown for both the common carotid and the jugular vein. Spectral Doppler is shown for a range gate within the common carotid artery. In color Doppler red indicates flow towards the transducer while blue indicates flow away from it. Source: *Well. D Medical Electronics Company Ltd.*

beam can be estimated, thus making angle-dependence a limitation of all conventional Doppler tissue/blood velocity estimation techniques, however they can be combined with B-mode imaging systems and thus provide visual feedback on the angle of observation of the blood flow velocities [123].

In the case of PW/spectral Doppler the transducer transmits short pulses and receives echoes only from a defined «range gate» that corresponds to a sample volume at a specific depth in the tissue. This enables the system to start recording the returning echoes at a given time after the transmission of the acoustic pulse as determined by the sample volume's depth [130]. Although this method is generally described as a Doppler technique, PW Doppler does not

make use of the Doppler shift on each transmitted pulse. This is due to the short length of the received echo and because other mechanisms such as frequency-dependent attenuation and frequency-dependent scattering significantly change the spectrum of the pulse and make it impossible to estimate the change due simply to the Doppler effect [131]. Instead, PW Doppler is based on transmitting multiple pulses (an ensemble of pulses) and then estimating the change in the round-trip time (phase shift) of the transmitted pulses from the transducer to the moving scatterers within the sample volume. Subsequently, a spectrogram is shown with time in the horizontal axis and the distribution of Doppler frequencies within the sample volume (scaled to velocities) in the vertical axis. Combining B-mode imaging with PW/spectral Doppler is referred to as «duplex» imaging [123].

In Color Doppler imaging, PW Doppler is performed at multiple sample volumes corresponding to range gates that cover an area of the image. The mean velocity within each sample volume is then color-coded and superimposed onto the B-Mode image. Several methods have been introduced to efficiently estimate color Doppler velocities, with the most prominent and widely used being the 1-D and 2-D autocorrelation methods [132], [133]. Both of the aforementioned Doppler modalities can be combined with real-time B-mode imaging into a single «triplex» modality (Figure 2.3).

Duplex and triplex Doppler scans are currently used as the gold standard method to assess carotid atherosclerosis using ultrasound in the clinic [45]. More specifically, the utility of color Doppler has been repeatedly demonstrated by correlating blood flow velocities with the degree

of stenosis in patients [134]–[136]. Established criteria for the screening of carotid stenosis using ultrasound such as those set by the Society of Radiologists in Ultrasound [137] and the Sonographic NASCET Index [138] heavily rely on the blood flow velocities estimated with the Doppler techniques. However, as mentioned in Chapter I, vascular diseases affect the local mechanical properties of the arterial wall. Thus, it has been argued that mechanical characterization of the diseased arterial wall would provide important complementary information for disease early diagnosis and monitoring [63]. This has led to the development of ultrasound-based elasticity methods.

2.2. Ultrasound-based elasticity methods

Elasticity imaging is a relatively new medical imaging modality that reveals the elastic properties of soft tissue by measuring the tissue deformation in response to a mechanical force [139]. Its goal is to noninvasively assess and quantitatively map the Young's modulus of tissue within the body, providing additional information that is currently not available by traditional imaging exam s in the clinic.

The earliest elasticity imaging technique utilizing ultrasound is elastography, first defined by Ophir and coworkers in 1991 [140]. It involves applying tissue compression using an ultrasound transducer and imaging of it at different levels of deformation. Cross-correlation of the received ultrasound radiofrequency (RF) signals yields the axial displacement map (i.e. along the ultrasound beam) of the investigated tissue. Subsequently, the tissue strains were obtained through spatial differentiation of the estimated displacement maps. Elastographic methods

have been applied to estimate the strains of both healthy and diseased arteries as they deform under pulsating physiological conditions [121], [122]. De Korte et al. first developed intravascular elastography (IVUS elastography) using intravascular ultrasound catheters and applied it in phantoms, excised femoral and coronary arteries with more higher strain spots corresponding to unstable lesions [63], [141], [142]. However, due to its invasive nature, IVUS elastography didn't evolve into a standard clinical tool. In order to address this disadvantage, noninvasive vascular elastography (NIVE) was developed by Kanai et al. and was tested *in vitro* using excised femoral arteries and comparing with histological staining of the atherosclerotic specimens [143]. NIVE was further developed and improved for arterial cross-sections with the Lagrangian speckle model estimator based on optical flow [144], angular compounding of strains [145] and more recently using high frame rate ultrasound and spatial compounding (which will be further discussed in Chapter IV) coupled with plane strain and tissue incompressibility assumptions [146]. However a limitation of conventional elastographic techniques is that in order to estimate direct stiffness values, the acquisition of blood pressure is required. Pressure can be obtained either invasively with a catheter or by using a brachial cuff and thus potentially inducing errors due to the difference between peripheral and central blood pressure [6]. Additionally, one of the key considerations for robust strain estimation is the size of the strain estimation kernel, which must be small enough to operate within the structure of interest, but large enough to ensure an adequate strain SNR [147]. Thus, strain elastography within a thin structure such as the normal carotid artery wall often yields noisy results. More recently arterial elastography found an additional use as a diagnostic tool for the characterization of endoleaks and thrombus organization in AAAs [83].

More recent methods in ultrasound elasticity imaging of arterial vessels involve an acoustic excitation “push” to induce localized displacements in the tissue of interest. These methods include acoustic radiation force imaging (ARFI) [56] and shear wave elastography (SWE) [123], [124]. ARFI was first developed by Nightingale et al. [148] and involves measuring the peak displacements in the tissue induced by the acoustic radiation force as well the recovery time from peak displacement in some studies [149]. ARFI has been applied both *in vitro* and *in vivo* [149], [150], [151] and high peak ARFI displacements have been shown to correlate well with inflamed, lipid-rich plaques and lower peak ARFI displacements with calcified plaques [150]. However, ARFI suffers from increased attenuation and ARFI displacements are affected by noise due to the physiological motion, especially given the relatively small magnitude of the induced displacements. Additionally, another limitation is that only relative stiffness maps are produced.

SWE is a technique first introduced by Tanter et al. [152] able to map estimates of the arterial Young’s modulus by tracking the propagation of the induced shear waves in the tissue using high frame rate ultrasound acquisitions. The first vascular application of this technique was introduced in [153], validated in normal and plaque phantoms [154], [155] and applied in patients *in vivo* [156]. In the latter, good reproducibility of the method was found between cardiac cycles and the estimated Young’s modulus was found to decrease with increasing degree of stenosis. However, the limitations mentioned in the case of ARFI (attenuation, noise due to physiological motion) also apply in the case of SWE. Furthermore, SWE is based on the assumption of free space, which however is not the case in the arterial wall, where propagation is more complex due to dispersion phenomena as well as multiple reflections resulting in

multiple propagation paths for the shear waves [63]. Finally, according to a more recent study shear wave propagation has been found to vary at different pressure levels for different views and boundary conditions of the vessel, thus indicating that a better understanding of the shear wave propagation is needed [157].

While the aforementioned techniques have several limitations, with further development they could provide important complementary information for the early diagnosis and risk management in focal vascular disease. In this thesis ultrasound will be used to investigate arterial elasticity via local PWV measurements. Towards that end our group has developed Pulse Wave Imaging.

2.3. Pulse wave imaging

An initial method to estimate the local PWV was presented in [120]. In that method two RF-lines were acquired simultaneously at two nearby locations of the artery with known distance between them. Subsequently, the distension waveforms were estimated from the acquired RF-data for each location and the local PWV was estimated using the temporal and longitudinal gradients of the distension waveforms. This method was extended with 16 RF-lines and visual feedback (B-mode) of the site of measurement in [158]. Our group, further developed this method into Pulse Wave Imaging (PWI) a noninvasive ultrasound method that allows the imaging and visualization of the spatio-temporal propagation of the arterial pulse wave [159].

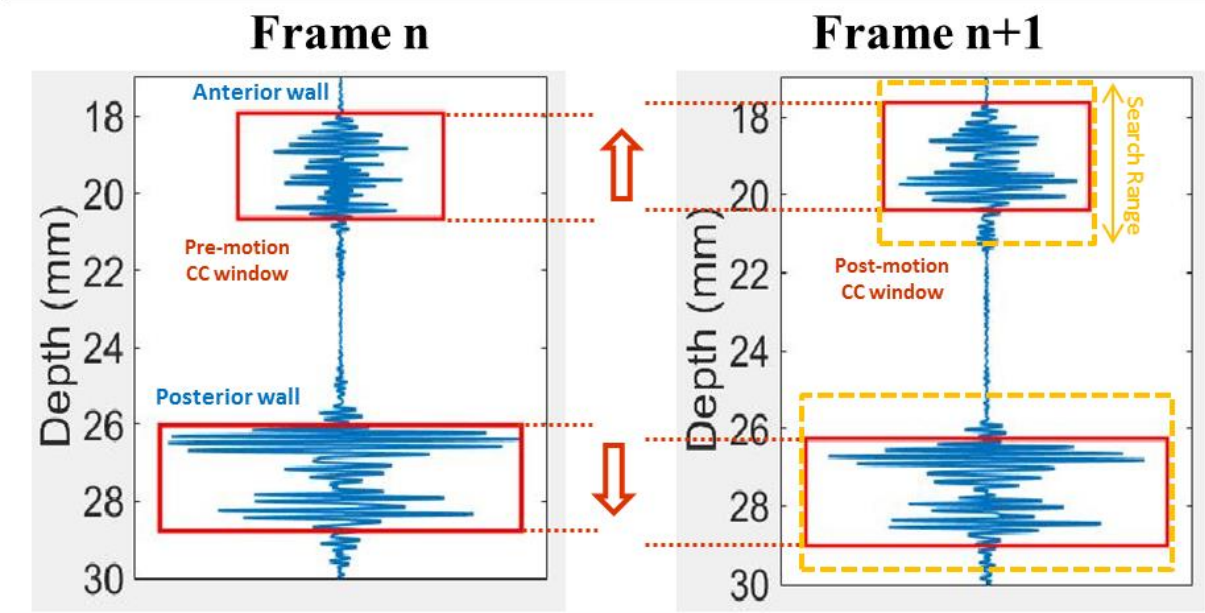

Figure 2.4: Illustration of the cross-correlation motion estimation method for a single RF line of a longitudinal scan of a common carotid artery. The large reflections correspond to the anterior (top) and posterior (bottom) walls. The pre-motion cross-correlation (CC) window is shifted within the search range and the cross-correlation of the RF-signals within the pre- and post-motion windows is estimated. The location of the maximum of the cross-correlation function indicates the axial displacement of the RF-signal within the post-motion window with respect to the pre-motion window. The displacements of the two illustrated windows are denoted with red arrows.

PWI is based on tracking the arterial wall motion using 1-D cross-correlation of the acquired RF-data. With cross-correlation tissue displacement is detected by correlating subsequent RF-signals. Cross-correlation is performed between the RF-signals within a pre-motion window and a post-motion window for each position of the post-motion window within an axial (i.e. along the RF-line) search range. The maximum of the derived cross-correlation function is a measure of the corresponding tissue axial displacements. An illustration of this method is shown in Figure 2.4 where the axial displacements are estimated between two subsequent frames for a single RF-line.

The normalized cross-correlation (R_{NCC}) function used to correlate the pre- and post-motion signals is the following:

$$R_{NCC}(u,\tau) = \frac{\sum_{n=u}^{u+W-1} f(n)g(n+\tau)}{\sqrt{\sum_{n=u}^{u+W-1} f(n)^2 \sum_{n=u}^{u+W-1} g(n+\tau)^2}}, \quad \tau 1 \leq \tau \leq \tau 2$$

(6)

Where f and g are the pre- and post-motion RF-signals respectively, u is the origin of the reference window, W is the size of the reference window, and τ is the shift between the reference and comparison windows within the range of τ1 and τ2. Thus, with R_{NCC} the cross-correlation between the two windows (numerator) is normalized by the square root of the product of their energies (denominator) and is expressed as a function of the shift τ. The shift corresponding to the peak of the R_{NCC} function represents the most likely new position of the wall in the post-motion RF-signal. This shift is subsequently converted to a displacement value using the speed of sound and the system's sampling frequency. However, in order to increase the accuracy of the cross-correlation method and also enable the cross-correlation method to estimate sub-sample displacements, a cosine interpolation is performed around the peak of the R_{NCC} function, producing a finer estimate of the axial displacement [160], [161]. Finally, the efficiency and execution speed of this algorithm was further enhanced by the sum-table method introduced by our group [162].

A diagram showing the basic pulse wave methodology as implemented before the initiation of this thesis on a human common carotid artery can be seen in Figure 2.5. Firstly, RF-frames are acquired scanning along the longitudinal axis of the artery at a high frame rate and then a 1-D cross-correlation algorithm as previously described is applied to acquire the axial wall displacements. These displacements are then normalized by the frame rate in order to obtain uniform values for different frame rates:

$$v_{PWI} = d_{PWI} \cdot fr$$

Where v_{PWI} denotes the resulting axial wall velocity, d_{PWI} denotes the axial wall displacement and fr is the frame rate of the acquisition. Subsequently, the anterior arterial wall is manually segmented and the corresponding v_{PWI} at each lateral position (i.e. along the longitudinal axis of the artery, a single v_{PWI} waveform for each line of the image) of the wall are plotted against time, creating a spatio-temporal map of the pulse wave propagation. Subsequently, the 50% upstroke of each v_{PWI} waveform at each lateral position is detected. This waveform feature is used as the tracking feature of the pulse wave and is defined as the average of the foot and the peak of the waveform. Linear regression is performed on the spatio-temporal variation of the 50% upstroke points along the imaged segment to obtain the slope as the PWV and the coefficient of determination r^2 as an index of propagation uniformity. Thus PWI visualizes the pulse wave propagation using the spatio-temporal map and also quantifies the PWV for the whole imaged arterial segment (regional PWV).

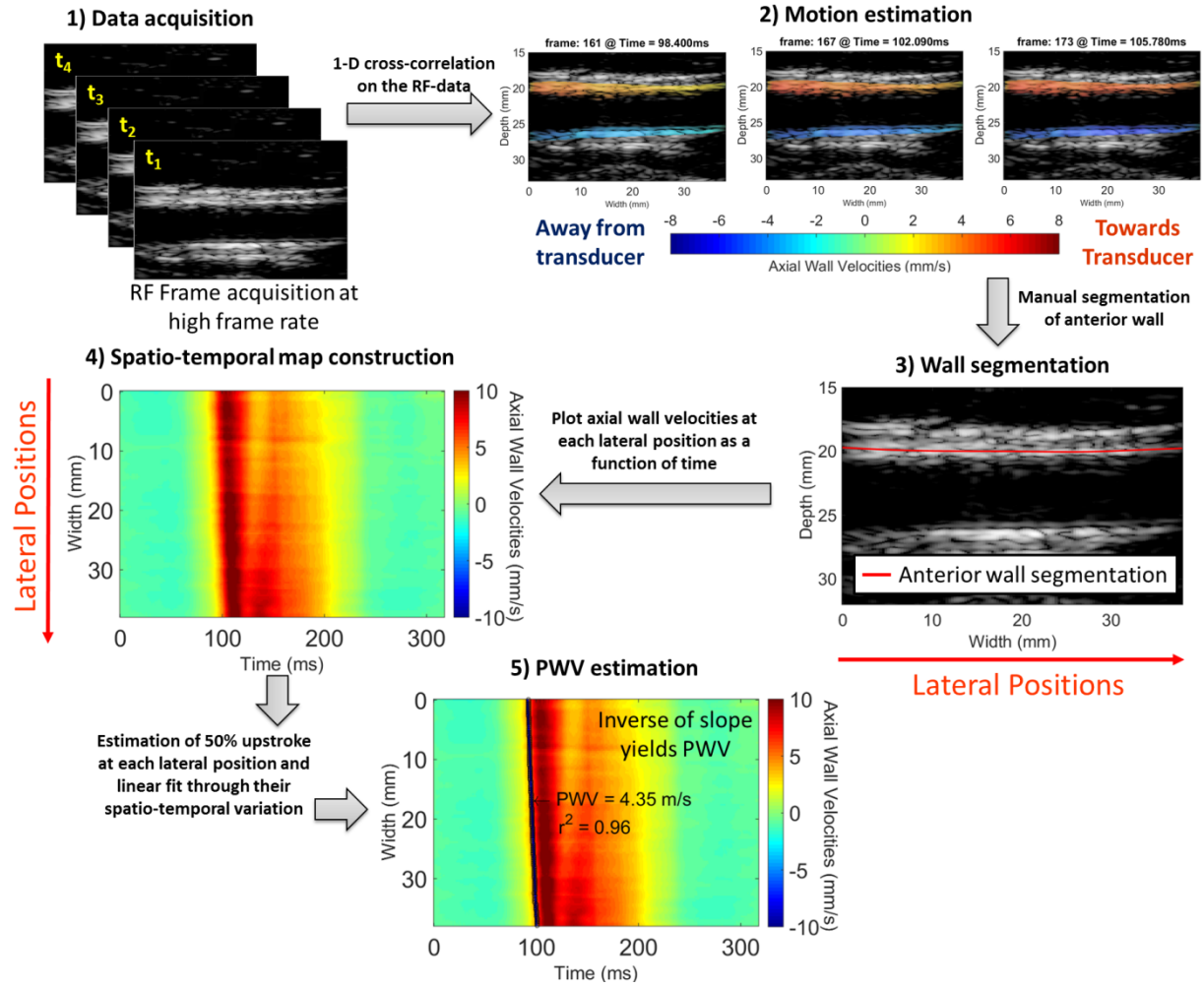

Figure 2.5: Illustration of the conventional PWI method

Previous PWI studies involved inducing AAAs to mouse aortas via infusion of either $CaCl_2$ or Angiotensin-II [159], [163], [164]. The most significant findings from these studies were regarding the uniformity of the pulse wave propagation. More specifically, decreased uniformity of the pulse wave propagation was found as indicated by the significantly decreased r^2 in the diseased aortas. The wave propagation pattern became even more distorted in the case of fissures and ruptures of aneurysms. This was also corroborated by Nandlall & Konofagou in [165], where using a localized PWV method, as it will be introduced in this thesis

in Chapter III, they found a greater variation in local PWVs in unstable aneurysms (i.e. leading to rupture) compared to stable ones. Furthermore, decreased axial v_{PWI} were found in the diseased portion of the arterial wall [163] and in [166] decreased regional PWVs were observed within the aneurysmal sac, a finding that was linked to the stress shielding properties of intraluminal thrombus within the aneurysmal sac. In the aforementioned studies a stroboscopic ECG-gating technique was used where the frames were retrospectively synthesized from moving single-element acquisitions synchronized with the ECG R-peak. Thus, PWI was performed on high-frame rate RF-sequences at 8000 Hz.

Subsequently, PWI was validated in polyacrylamide phantoms and applied to human normal , aneurysmal and hypertensive aortas [167], [168]. In the case of the *in vivo* scans good intra-subject reproducibility of the regional PWV values was found (~10%). Furthermore, PWVs in aneurysmal aortas were found to be significantly higher than in the normal ones and propagation uniformity (r^2) was found to be significantly lower in the diseased aortas. Additionally, a feasibility study in human carotid arteries confirmed good intra-subject reproducibility of the regional PWV and also good agreement with prior literature values. Furthermore, it was able to identify features of the wave, such as the reflection originating from the carotid bifurcation and the dicrotic notch, a propagating wave caused by the closure of the aortic valve at the end of systole.

The aforementioned studies in humans *in vivo* utilized conventional ultrasound scanning. This induced a beam density – frame rate tradeoff. Given that PWI requires frame rates in the range

of kHz [169] to capture the propagation of the pulse wave along multiple positions of the imaged artery, this resulted to significant loss in spatial information (beam density). Thus, low beam density RF-data were acquired with 16 beams impacting the spatial resolution of the spatio-temporal maps. Additionally, in all of the aforementioned studies only one value of PWV was derived for the whole imaged artery. Given that both atherosclerosis and aneurysms are focal diseases occupying specific segments of the imaged arteries more localized PWV measurements are needed.

Some recent developments in PWI enabled by the work presented in this thesis include the introduction of the Pulse Wave Inverse Problem (PWIP). PWIP is a technique that provides estimates of local arterial compliance from measurements of the vessel wall displacements. This was achieved by parameterizing the 1-D equations governing pulse wave propagation by spatially varying mechanical properties and subsequently solving the inverse problem. This technique was validated both *in silico* and in silicone phantoms and its feasibility was more recently shown in healthy subjects [170], [171]. One of the main advantages of PWIP compared to conventional PWI is that pulse wave reflections are takin into account, thus producing more robust local PWV and compliance estimates.

The work in this thesis aimed to address several of the limitations of conventional PWI as well as expand its functionalities. More specifically:

- In Chapter III, piecewise PWI will be introduced; a method to provide localized PWV measurements and ultimately a stiffness map of the imaged artery. Piecewise PWI was further augmented with dynamic programming leading to adaptive PWI, a technique to automatically segment the imaged artery into the most homogeneous regions and detect stiffness inhomogeneity and thus possible reflection points. Both techniques will be tested on normal, atherosclerotic and aneurysmal mouse aortas.

- In Chapter IV, in order to address the conventional PWI tradeoff between spatial and temporal information and thus prime PWI for use in the clinic, a PWI implementation with high frame rate plane wave ultrasound and coherent compounding will be introduced and its parameters will be optimized for scanning the carotid artery in a population of healthy subjects. Additionally, a GPU-enhanced frame work for faster processing of the big bulk of data acquired with this technique will be described. Furthermore, validation of this technique will be shown in silicone phantoms using both static and dynamic testing.

- In Chapter V, the high-frame rate implementation of PWI with the added capabilities of PWV and arterial compliance mapping will be shown feasible in atherosclerotic patients *in vivo* and its results will be compared against plaque histological specimens. Additionally, it was used to assess post-endarterectomy atherosclerotic patients and compare with other stenotic patients.

- In Chapter VI, 4-D PWI will be introduced, a significant expansion upon PWI, especially with respect to the amount of spatial information provided. PWI was implemented using 3-D high-frame rate ultrasound, validated in silicone phantoms and tested in healthy subjects by comparing its results against conventional PWI.

- Finally, in Chapter VII, PWI coupled with flow imaging will be introduced. Given the status of color Doppler as the gold standard in carotid stenosis assessment, PWI and Color Doppler were integrated into a single modality allowing the inspection of both the distension and the flow pulse wave. Furthermore, PWI was integrated with vector Doppler, a technique that provides directional information on the flow. The resulting methodology was tested *in vivo* providing comprehensive inspection of the arterial biomechanics.

Chapter 3. Piecewise Pulse Wave Imaging (pPWI) and Adaptive Pulse Wave Imaging (aPWI) for the Characterization of Focal Vascular Disease and Automatic Stiffness Inhomogeneity Detection in Murine Aortas and Carotids In Vivo

This section of the dissertation focuses on introducing piecewise Pulse Wave Imaging (pPWI) that extends and enhances PWI in order to track the sub-regional PWVs over the length of a few millimeters of the arterial wall. Thus, it increases the spatial resolution of PWI by generating PWV and PWI Modulus (E_{PWI}) maps through the Moens-Korteweg equation. The feasibility of this new method was demonstrated in normal, aneurysmal and atherosclerotic murine aortas, as well as in normal and atherosclerotic murine carotids in vivo in a study by our group published in IEEE Transactions in Medical Imaging in 2016 [172]. The proposed technique was further augmented by the introduction of adaptive pPWI, a method that utilizes a dynamic programming algorithm to optimally map arterial wall stiffness by separating the imaged artery into the most homogeneous segments and also detecting points of stiffness inhomogeneity and thus reflection points, a substantial problem in arterial mechanics. This novel technique was tested in normal and diseased murine aortas in vivo.

3.1. Piecewise pulse wave imaging

3.1.1. Materials and methods

3.1.1.1. Animal study design

For the purpose of the atherosclerosis study, six-month old ApoE knockout mice (ApoE-/-, n = 7) were obtained from the Jackson Laboratories (Bar Harbor, ME, USA) and were fed an atherogenic Western type diet (20% protein, 50% carbohydrate, 21% fat, 0.21% cholesterol; Research Diets, New Brunswick, NJ, USA) ApoE-/- mice are known to spontaneously develop atherosclerosis throughout the arterial tree, a process that is accelerated by maintaining them on a diet rich in cholesterol [173]. One of the acquired mice died after 17 weeks of high-fat diet from myocardial infarction during anesthesia, while another two had to be euthanized due to poor health and deep skin ulcerations after 25 weeks on high-fat diet. The remaining mice were euthanized after approximately 35 weeks of high-fat diet. The abdominal aortas of each mouse were scanned once every three weeks in order to monitor the progress of the disease. After 5 weeks of high-fat diet the same routine was applied to the carotid arteries of the same mouse cohort.

In the case of the aneurysm development study, six male ApoE/TIMP-1 knockout mice (n = 6) were infused with angiotensin II (A9525, Sigma-Aldrich, St. Louis, MO, USA) for 30 days via subcutaneously implanted osmotic pumps (Alzet Model 2004, Durect, Cupertino, CA, USA). The mice were given a dose of 2.2 mg/kg/day (milligrams of angiotensin II per kilogram of body mass per day) and were monitored 2–3 times every week over the course of 30 days. The timelines of both animal studies used in the present work are shown in Figure 3.1.

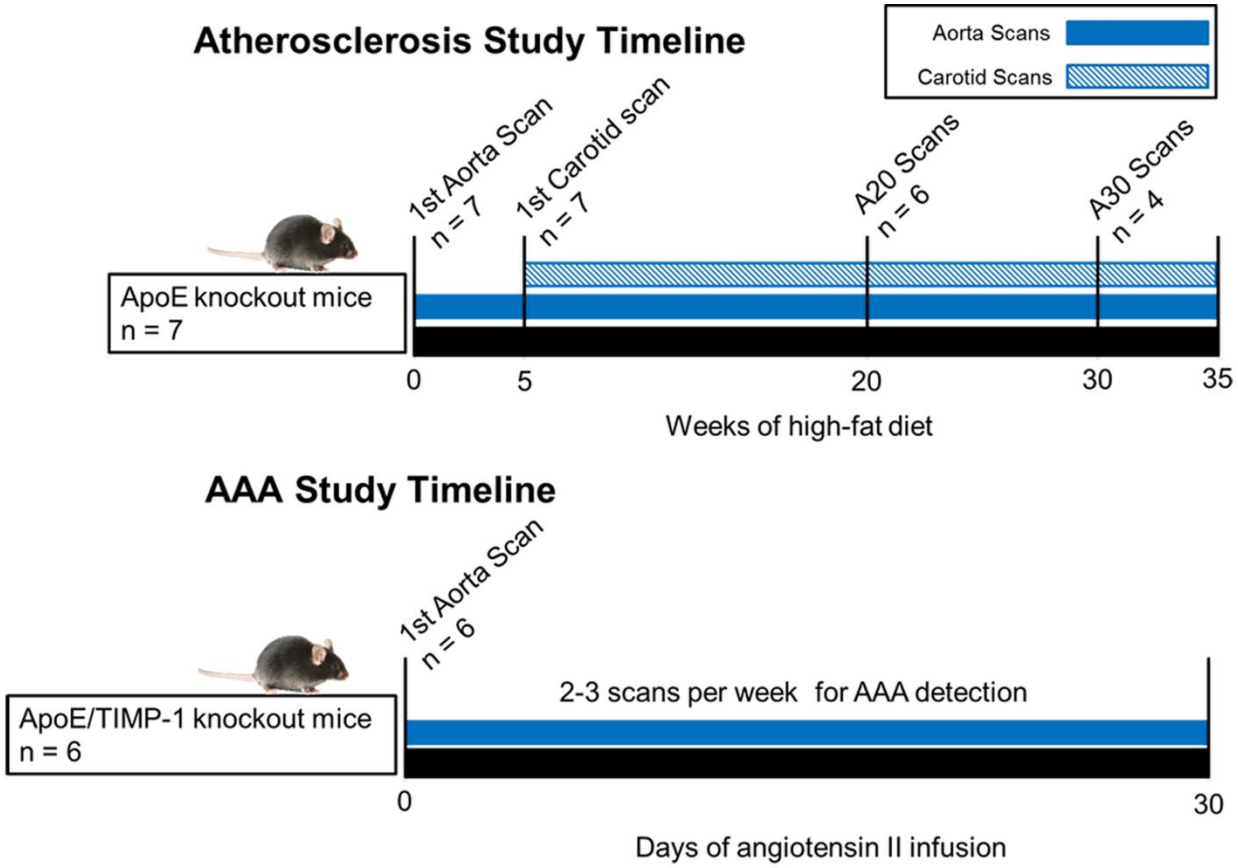

Figure 3.1: Timeline of the mouse experiments designed in [172] (A20: mice on 20 weeks of high-fat diet, A30: mice on 30 weeks of high-fat diet).

3.1.1.2. pPWI Methodology

A diagram of the pPWI methodology on a normal murine aorta is given in Figure 3.2. Ultrasound RF frames were acquired with a previously developed high frame-rate data acquisition system [174]. A high-frequency 30-MHz ultrasound probe (RMV-707B, VisualSonics, Toronto, ON, Canada), specialized for small animal imaging, was placed on the mouse abdomen to obtain a long-axis view of the abdominal aorta in the suprarenal region with a field of view of 12 × 12 mm^2. The single-element transducer operated on a line-by-line-basis using ECG gating. The

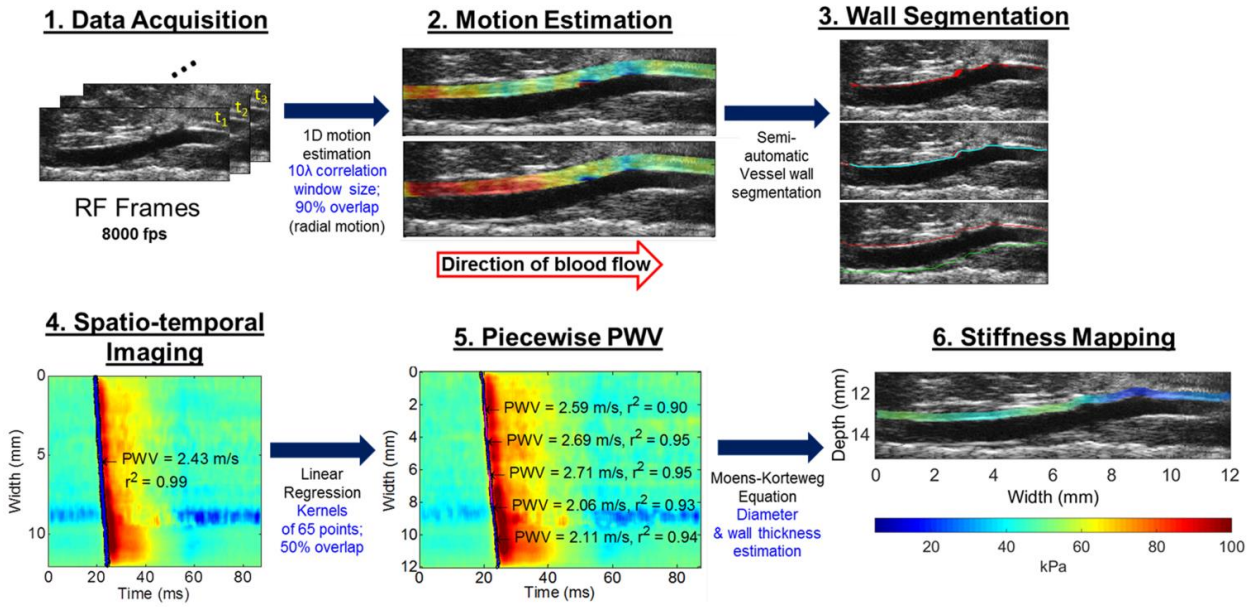

Figure 3.2: Illustration of the post-processing methodology used in the current study for a normal mouse aorta

transducer transmitted and received at a pulse-repetition frequency (PRF) of 8 kHz. Each acquisition lasted approximately 7 minutes. After data acquisition, the received RF lines were synchronized based on the R-wave peak (a reliable peak of the ECG during the cardiac cycle) of the simultaneously recorded ECG signals to reconstruct the RF image sequence for a complete cardiac cycle at an effective frame rate of 8 kHz. In the case of the mouse carotid arteries a 40-MHz ultrasound probe (RMV-704, VisualSonics, Toronto, ON, Canada) was placed on the mouse neck to obtain a long-axis view of the right common carotid artery and its respective bifurcation. The field of view was equal to 10 × 12 mm^2.

The axial wall velocities of the aortic and carotid wall were estimated off-line from the same RF data acquired, using a time efficient, 1-D normalized cross-correlation technique described in [162]. The wall velocity estimates were smoothed by a Savitzky-Golay filter followed by a 3x3

median filter to remove any peak hopping errors. The rigid motion induced by respiration was also removed by subtracting the velocity of the surrounding tissue from the velocity of the wall. Subsequently, in order to trace the extent of the arterial wall, a semi-automated segmentation algorithm was developed. First, each image was subjected to smoothing Gaussian and homomorphic filtering in order to reduce the noise in the image and also impose uniform illumination conditions. Next, each image was thresholded given a user-defined threshold, after which a region around either the anterior or the posterior wall was selected. The wall was segmented using a Sobel-based edge detection method. Finally, a smoothing spline through the resulting segmentation provided a smooth line that accurately delineates the arterial wall.

The PWI axial wall velocities of the arterial wall segment at a specific beam position were plotted as a function of the time elapsed after the R-wave. Thus, the PWI axial wall velocity variation over distance and time of the pulse-wave propagation was depicted in a 2-D image, indicating the spatiotemporal variation of the pulse-wave propagation. The distance was calculated by estimating the length of the aortic wall, as delineated by the segmentation algorithm, since the width of the image does not always coincide with the length of the imaged arterial wall. On the 2-D spatio-temporal images, the 50% upstroke point of the PWI axial wall velocity versus time was selected as the tracking feature in order to estimate the PWV [175]. The 50% upstroke was defined as the time-point, at which the axial wall velocity was closest in value to the average between the foot and the peak of the axial wall velocities at each beam location.

As In the case of conventional PWI, linear regression of the relationship between the 50% upstroke arrival time and the distance along the anterior wall yielded the slope as the regional PWV value for the whole imaged segment and the corresponding coefficient of determination r^2 as an approximate measure of the pulse wave propagation uniformity.

However, in order to acquire more localized PWV measurements and the corresponding stiffness maps, the 50% upstroke points were divided in 50% overlapping kernels of 65 points (4 mm) in the case of the aortic wall and 40 points (2.4 mm) in the case of the carotid wall. Linear regressions were performed for each sub-region, thereby providing a localized PWV value along with the corresponding coefficient of determination, indicative of the quality of the linear fit [168]. The size of the kernels was chosen accordingly, to balance the tradeoff between the resolution of the resulting stiffness maps (smaller kernels) and quality of the linear regression (larger kernels). Most importantly, the resulting resolution of the stiffness maps needed to be comparable to the size of the focal wall disease.

For the purpose of deriving stiffness estimates for each sub-region, the Moens-Korteweg equation was utilized. The diameter of each sub-region of the vessel was estimated using the segmentation curves along the anterior and posterior walls. Subsequently, the arterial thickness of the aortic wall was measured for each sub-region using a standard B-mode method of taking the average of three measurements of the anterior wall within each segment. Finally, in both aortas and carotid arteries the density of the arterial wall was assumed to be equal to 1060 kg/m and Poisson's ratio was set to 0.5 [6]. Consequently, using the aforementioned

parameters along with the calculated PWV, a stiffness estimate—PWI modulus (E_{PWI}) was obtained for each sub-region using the previously mentioned Moens-Korteweg equation.

3.1.2. Results and discussion

Figure 3.3 shows sequences of PWI images at intervals of 1.25 ms in the cases of I) a normal aorta, II) an atherosclerotic aorta and III) an aneurysmal aorta. Only the axial wall velocities on the anterior wall of the aorta were shown. This is in part due to better visualization reasons and in part due to the fact that the posterior wall exhibits little motion *in vivo* because of its close proximity to the spine. Uniform wave propagation along with similar peak PWI axial velocities across the tissue could be observed in the case of the normal aorta. The propagation pattern became more irregular and nonuniform in the aneurysmal and atherosclerotic cases of mouse aortas indicating underlying changes in the mechanical properties of the arterial wall. Furthermore, it was observed that the magnitude of the peak PWI wall velocities was significantly lower than that of the normal case. This indicated that the vessels were less compliant and consequently, hinted at a potential increase in the stiffness of the vasculature of atherosclerotic ApoE-/- mice. This finding was corroborated with the generation of PWV and E_{PWI} maps.

More specifically, as seen in Figure 3.4 significant increases in both the average of piecewise PWV and E_{PWI} were found after both 20 and 30 weeks of high-fat diet. These observations were in agreement with several other studies, which have shown that both PWV and vessel stiffness increase with atherosclerosis and also that the elastic response of the vessel decreases [176], [177], [178]. Additional longitudinal studies in monkeys [179], [180] and humans [54],

[181] have all similarly shown increased PWV measurements in atherosclerotic arteries. Farrar et al. in [179] attributes this increase in the PWV mainly to increases in the total material in the

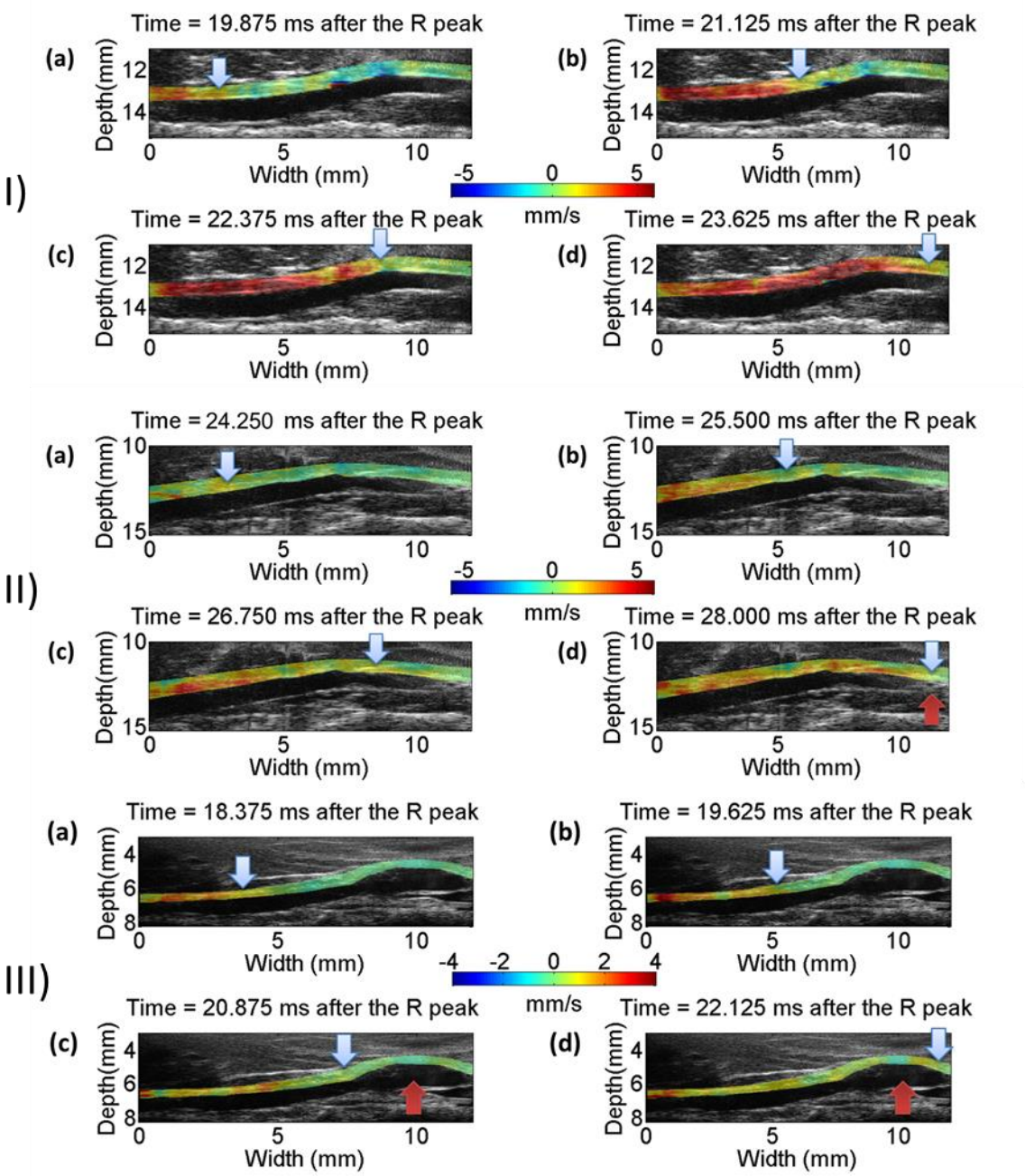

Figure 3.3: Sequence of PWI images every 1.25 ms (i.e., 10 frames) in the cases of I) a normal, II) an aorta of a mouse under high-fat diet for 30 weeks and III) an aorta of a mouse receiving angiotensin II. Solid blue arrows indicate the propagation of the pulse wave while the red arrows indicate the stenotic region in I) and the aneurysmal region in II). Red color indicates motion towards the transducer (top) and blue color indicates motion away from the transducer (bottom)

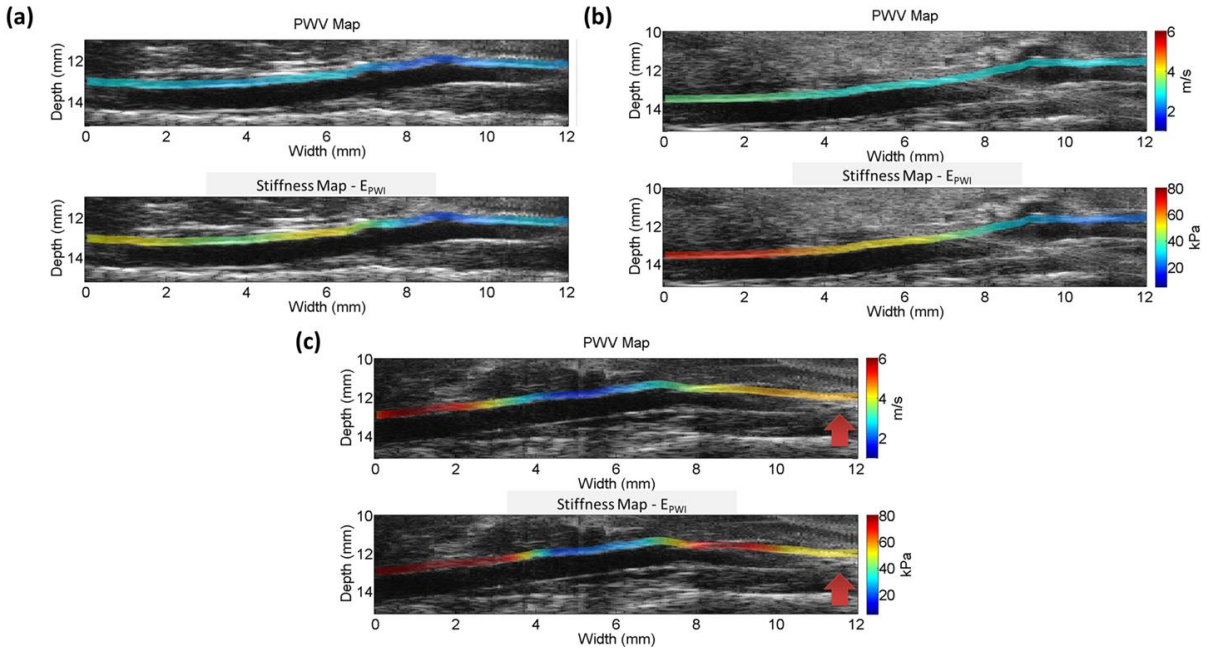

Figure 3.4: PWV and stiffness maps for the case of a mouse aorta (a) before the start of the high-fat diet, (b) after 20 weeks of high-fat diet and (c) after 30 weeks of high-fat diet. In the latter case stenosis had developed on the distal end of the aorta as indicated by the solid red arrow. Both the sub-regional PWVs and E_{PWI} were color-coded and overlaid onto the B-mode images.

wall (i.e., increases in arterial elastin and collagen content) caused by atherosclerosis.

In the case of the aneurysmal aorta as seen in Figure 3.3 the aneurysmal sac exhibited low PWI axial wall velocities, which had been previously reported in other PWI studies [163], [166]. A possible explanation for the significant decrease in aneurysmal wall motion could due to the reduced intra-aneurysmal pressure. The etiology behind this drop decrease may be more complex than the aneurysm's larger diameter alone. For example, it has been shown that the thrombus reduces the effect of the pressure load on the AAA wall [85], [182] also leading to decreased aneurysm expansion [76].

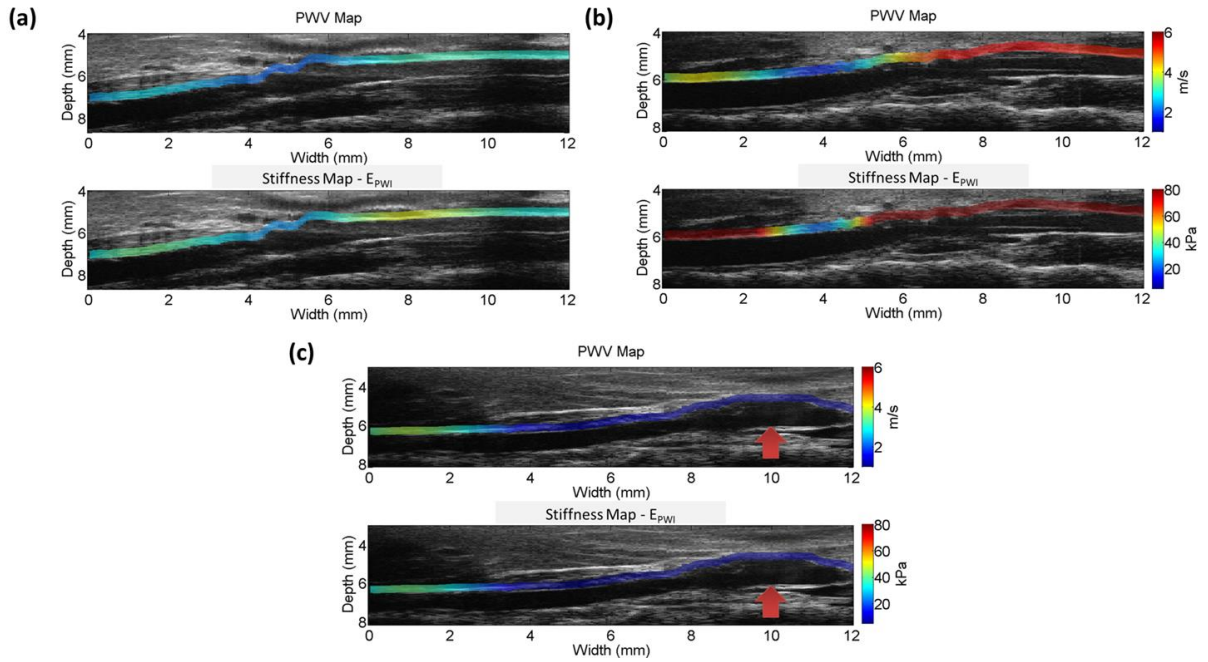

Figure 3.5: PWV and stiffness maps for a mouse aorta (a) before the implantation of the angiotensin II pumps, (b) 6 days after pump implantation and (c) 16 days after pump implantation. In the latter case an aneurysm has developed on the distal end of the aorta as indicated by the solid red arrow. Both the sub-regional PWV and E_{PWI} have been color-coded and overlaid onto the B-mode images

Figure 3.5 shows the PWV and stiffness maps generated in the aneurysm development study. The maps of a) a baseline PWI acquisition of a murine aorta, b) a PWI acquisition six days after the angiotensin II implantation and c) a PWI acquisition sixteen days after the angiotensin II implantation are shown. This figure implied an interesting pattern in aneurysm formation. More specifically, sub-regional PWV and E_{PWI} values increased sharply after a week of angiotensin II administration, thus indicating an increase in the vessel's stiffness. However, at that stage there are no signs of aneurysm formation. According to existing literature [183], within 1–10 days after implantation of the osmotic pump that infuses mice with a dose of angiotensin II, elastin fragmentation is promoted. Hence, one explanation for these observations is that the degradation of elastin transfers the mechanical load to the collagen

fibers present in large arterial vessels, thus increasing the overall stiffness of the vessel [11]. These findings have also been verified in an *ex vivo* setting [184], where angiotensin II-infused murine arteries were subjected to mechanical testing. In the same study higher PWV was measured *in vivo* in the angiotensin infused murine aortas via Doppler velocimetry. However, after formation of the aneurysm, it was observed that both the sub-regional PWVs and E_{PWI} had regressed to lower magnitudes. The aforementioned findings were corroborated by the statistical analysis shown in Figure 3.6. Furthermore, according to Figure 3.6 it was observed that the mean piecewise r^2 quality indicator was significantly lower ($p \leq 0.05$) in the diseased aortas compared to the healthy ones. This drop in r^2 was an indicator of nonuniform propagation of the pulse wave and consequently of underlying tissue inhomogeneity. Especially in the aneurysmal cases significant decrease of r^2 was found within the aneurysmal sac, which can be attributed to variations in both geometry and composition. Additionally, aortic wall inhomogeneities led to the extensive presence of aortic wall reflections, further impacting the r^2 coefficient values. Consequently, in each sub-region where the piecewise PWVs are estimated, the associated r^2 was shown to be a measure of inhomogeneity of the arterial wall thus showing the ability to identify regions with extensive presence of reflections. This reflection detection potential of pPWI was further developed and automated thus leading to the introduction of adaptive PWI which will be introduced in the second half of this chapter.

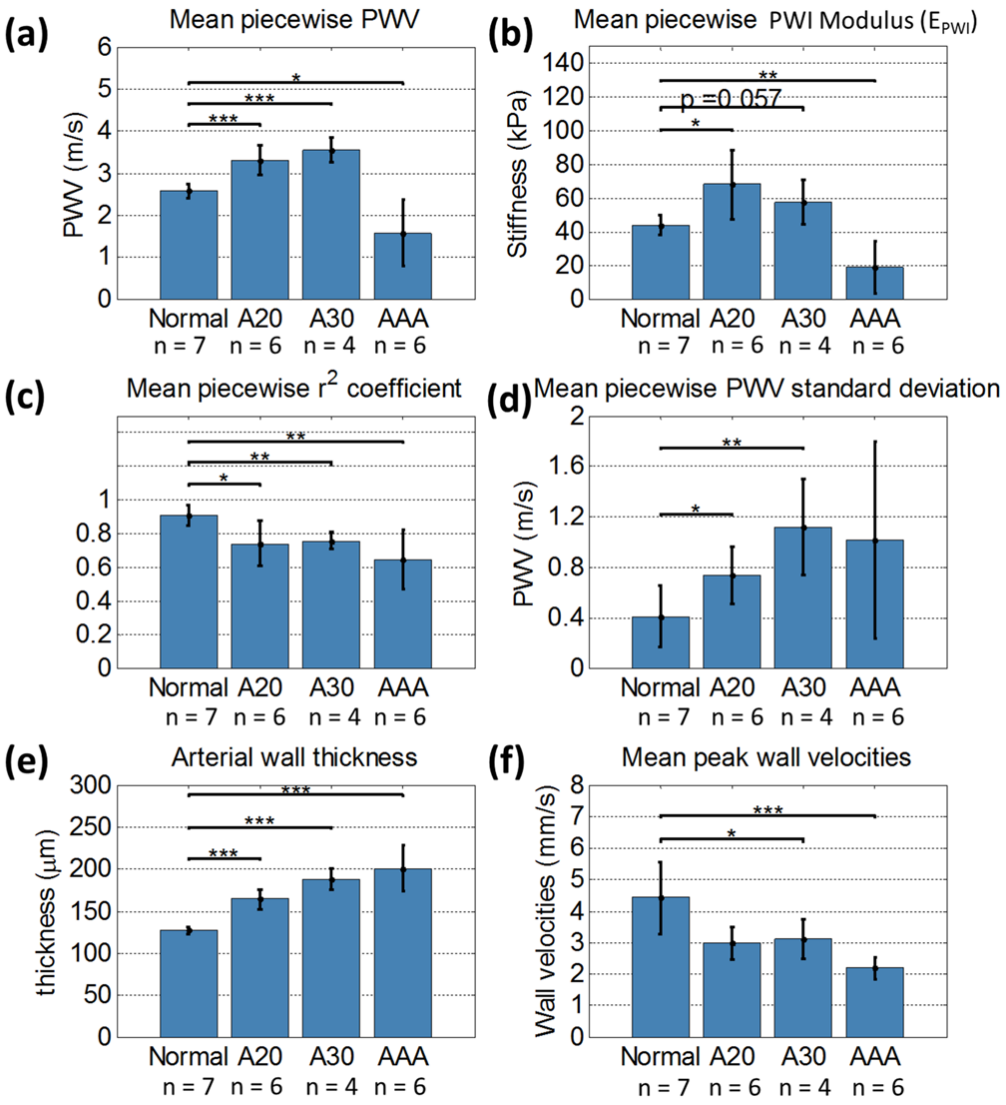

Figure 3.6: Statistical results on seven normal (n = 7, Normal) aortas along with six aortas after 20 weeks of high-fat (n = 6, A20), four aortas (n = 4, A30) after 30 weeks of high-fat diet and six aneurysmal aortas (n = 6, AAA). (a) Mean sub-regional PWVs over the aortic wall averaged over the corresponding mouse population. (b) Mean sub-regional E_{PWI} values over the aortic wall averaged over the corresponding mouse population in each case. (c) Mean sub-regional r^2 coefficient over the aortic wall averaged over the corresponding mouse population in each case. (d) Standard deviation of the sub-regional PWVs over the whole imaged aortic wall averaged over the corresponding mouse population in each case. (e) Mean arterial wall thickness averaged over the corresponding mouse population in each case. (f) Mean peak PWI wall velocities over the whole imaged aortic wall averaged over the corresponding mouse population in each case. Error bars denote standard deviation and significances are marked on the plot.

The PWV values shown in Figure 3.6 were in good agreement with the values reported in literature for normal ([159], [163], [176], [177], [185]), aneurysmal [163] and atherosclerotic ([177], [176]) mouse aortas. Furthermore, the derived PWI modulus values were also compared against stiffness values from other studies employing mechanical testing. The E_{PWI} of the mouse abdominal aortas were estimated at 43.82±5.86 kPa in normal aortas, while in 20- and 30-week high-diet-fed aortas the mean were 68.09± 20.66 kPa and 57.72±13.12 kPa respectively. Notably, Tracqui et al. [55] used Atomic Force Microscopy (AFM) to obtain the stiffness of the elastic lamina and individual components of plaque structure. The mean Young's modulus for the elastic lamina space of the aortic wall was estimated to be kPa while individual components of plaques (lipid rich areas, fibrotic areas) exhibited a wider range of stiffness values that included both lower (5.5 kPa) and higher (59.4 kPa) stiffness values. Additionally, in another study by Santelices et al. [186], the reported moduli in 8-week old wild-type mice were on the order of 80 kPa. In similar studies, the stiffness of the proximal to the heart murine abdominal aorta has been measured to be in the range of 50 kPa [187]. While there was some variability in the arterial stiffness measurements by each methodology, the estimated E_{PWI} were within the range of the reported measurements.

Similar figures were produced in the case of murine carotids on an atherogenic high-fat diet. An interesting finding in the case of the carotids was that especially in the case of the healthy murine carotids a backward-propagating reflected wave could be seen (Figure 3.7), which appeared in the spatio-temporal plots as a characteristic V-shape patter that has also been

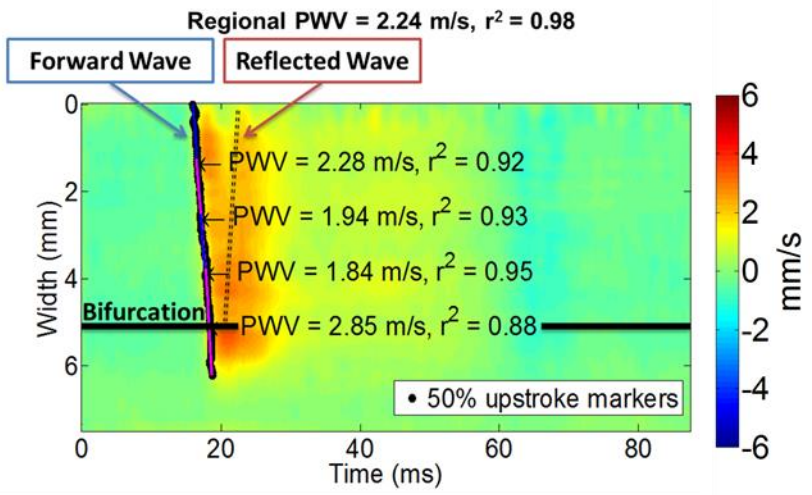

Figure 3.7: Spatio-temporal imaging of pulse-wave propagation in a normal murine carotid artery along with the piecewise linear regression of the 50% upstroke markers overlaid on the spatio-temporal plot. The piecewise PWV and r^2 coefficient values are shown next to each segment, while the regional PWV and r^2 coefficient value for the whole imaged aortic region is shown on top. A characteristic V-shape is delineated using dashed lines to indicate forward propagation of the forward pulse (left dashed line of the V) as well as the backward propagation of a reflected wave (right dashed line of the V).

observed in human carotids [188]. Additionally, PWV and stiffness maps were also generated in the case of the mouse carotids as seen in Figure 3.8.

An small increase in stiffness was observed right after the bifurcation, which was mainly due to the narrowing of the common carotid into its two branches. In the case of the atherosclerotic carotid artery, there was an increase in the PWV at this site and it coincides with the development of a fibrous plaque at the anterior wall. Albeit not significant, an increase in the mean of sub-regional PWVs was observed between the mice after 5 and either 20 or 30 weeks of high-fat diet. Moreover, r^2 derived for carotid arteries were found to decrease significantly after 20 weeks of high-fat diet, which indicates that could be used as potential biomarker of atherosclerosis in the carotid artery. A significant increase was also found between the thicknesses of the carotid arteries after 5 and 30 weeks of high-fat diet. Plaque thickness of the

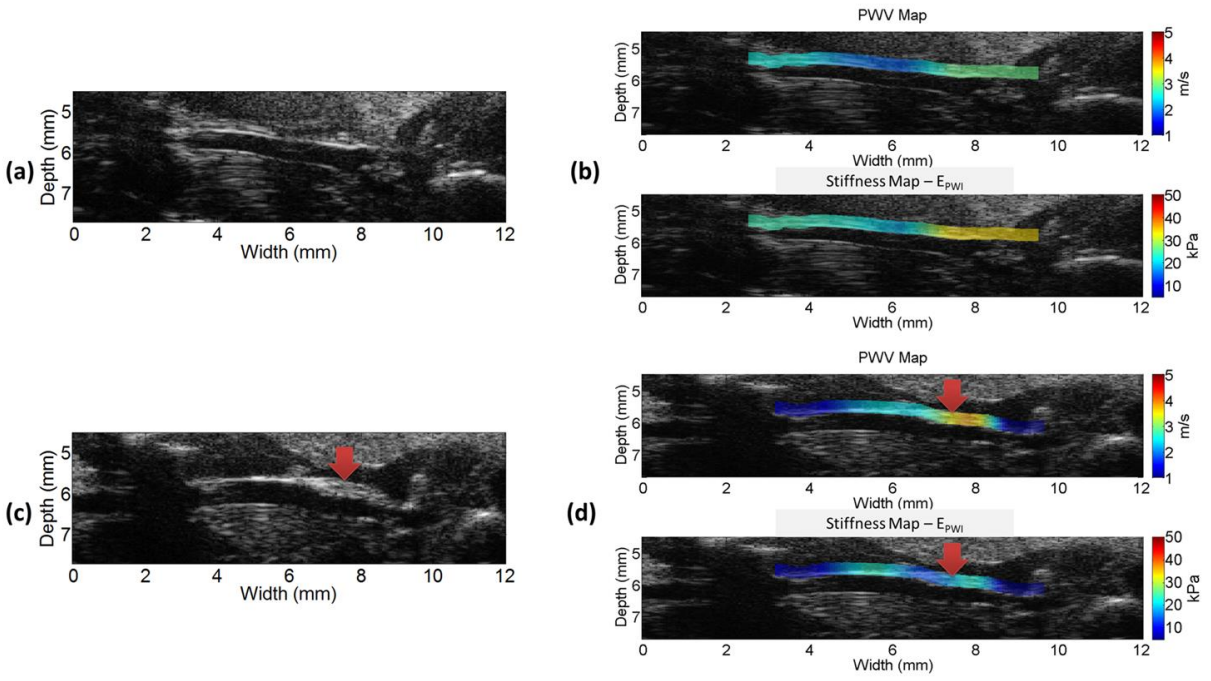

Figure 3.8: B-mode images along with PWV and stiffness maps for the case of a normal mouse carotid artery (a), (b) and an atherosclerotic carotid artery (c), (d). In the atherosclerotic carotid, stenosis has developed on the distal end of the artery as indicated by the solid red arrow (c), (d). Both the piecewise PWV and E_PWI values have been color-coded and overlaid onto the B-mode images (b), (d).

atherosclerotic mice after 30 weeks of high-fat diet was found to be close to those of other ultrasound biomicroscopy studies [189], [190]. However, it needs to be noted that ultrasound biomicroscopy slightly overestimates wall thickness compared to histological measurements.

Finally, an unexpected finding observed in the atherosclerotic mouse data was that a slight decrease was observed in the piecewise PWVs and of the carotid arteries and the piecewise E_{PWI} of the aortas of the mice after 20 and 30 weeks of high-fat diet. One factor that may have contributed to the aforementioned drops in stiffness could be the small number of animals in the population of the 30-week-high-fat-fed mice. However, similar decreases in the PWV and

arterial Young's modulus have been observed in an extensive study by Farrar et al. in which the aortic PWV of a large population of monkeys were fed an atherogenic diet over an extensive period of time [180]. Farrar et al. hypothesized that arteries respond to the hypercholesterolemia caused by the high-fat diet by remodeling and more specifically by proliferating smooth muscle cells and loosening connective tissue. This in combination with the increased lipid accumulation would result to a more compliant vessel overall [180].

3.1.3. Limitations and conclusions

One limitation of the proposed technique that needed to be addressed in order to translate this technique to human subjects is that an ECG gating technique was used, a technique that is very time-consuming and also may contribute to erroneous measurements in the case of arrhythmic patients or in the cases where the coupling of the ECG leads to the patient may be poor.

Furthermore, an additional factor that could have potentially affected the PWV measurements performed in this study could have been the reflection due to tissue inhomogeneities. However, it should be noted that sub-regional PWVs were estimated by tracking essentially the wavefront velocity of the pulse wave which has been shown to be a good measure of the characteristic velocity of all of the pulse wave's components and has also been shown to be less affected by reflections [6].

Another limitation, inherent to the application of the Moens-Korteweg equation to major arterial vessels in vivo, is the fact that the surrounding tissue elasticity is not taken into account.

Nevertheless, it has to be noted that this particular limitation applies to all major longitudinal clinical studies employing tonometry or arterial wall tracking at two distal sites to infer PWV and report on arterial wall stiffness. Because of the aforementioned limitations in Moens-Korteweg equation, the derived metric is dependent on but not necessarily equal to the true stiffness of the arterial wall. Thus, the name, PWI modulus, was used to indicate its nature as a relative (rather than an absolute) measure of stiffness. Its significance was demonstrated in the current study as a new parameter that takes into account and combines three major parameters that have been separately shown to change in the presence of focal vascular disease (PWV, arterial wall thickness, and vessel diameter) to successfully differentiate between normal and pathological arterial tissue.

The main impact of this study lies in introducing the novel technique of pPWI that provided detailed maps of the PWV along the vascular wall. Stiffness maps of normal and pathological aortas as well as carotids were generated and utilized to assess initial feasibility of the new methodology in the detection of the early onset of atherosclerotic and aneurysmal disease in mice in vivo, thus encouraging further testing of pPWI in the case of human patients.

3.2. Adaptive pulse wave imaging

The aim of this study was to introduce adaptive PWI, a technique that combines information from the pulse wave propagation and the arterial wall motion to optimally divide the imaged artery into segments where the pulse wave propagation appears to be the most homogeneous,

thus making the PWV estimation more robust. This method aims to aid in improving PWV estimation, identifying arterial stiffness variation interfaces (reflection points) and providing metrics for arterial spatial homogeneity.

Previous attempts to noninvasively capture the spatial variation of the arterial wall's mechanical properties were presented in [121] and [191] where the spatial variation in arterial distension was investigated. Additionally, texture analysis of strain rate images of plaque tissue has indicated that increased local variations in strain rate in plaques may help identify vulnerable plaques [192]. Moreover, earlier work on arterial elastography by Kanai et al. [143] showed increased spatial heterogeneity of the elasticity around plaques, where large stress is concentrated. Finally, previous work by our group has shown that PWI was able to detect increased nonlinearity in the pulse wave propagation in AAAs [163], [168] with unstable aneurysms appearing to be the most inhomogeneous [165].

Additionally, adaptive PWI showcases how a relatively simple algorithm pertaining to graph modeling and machine learning can be meaningfully integrated into an existing medical imaging (PWI) technique and ultimately help clinicians identify and monitor arterial abnormalities. This study involved validation of the proposed technique by testing its ability to automatically detect the soft and stiff segments of silicone phantoms. The resulting PWV values were also compared with PWV values derived from static testing of the phantoms. Furthermore, the feasibility of this technique was tested in vivo to monitor the progression of atherosclerosis in mice and automatically detect interfaces of stiffness change in aneurysmal mouse aortas.

3.2.1. Materials and methods

3.2.1.1. Silicone phantom design

A phantom with a soft and a stiff segment along the longitudinal axis was constructed according to [193] and [170]. Subsequently, the phantom was embedded in a soft silicone mixture made from 40% A431 gel and 60% Xiameter PMX- 200 100CS silicone fluid (Dow Corning, Midland, MI, USA) to mimic the influence of arterial surrounding tissue. Static testing was performed similarly to [170] to derive the compliance of each segment and subsequently the Bramwell-Hill equation was used to calculate the corresponding PWVs (PWV_{soft}^{static} ; PWV_{stiff}^{static}). Additionally, in order to facilitate the detection of the soft/stiff interface using ultrasound a small hole was made on the top surface of the surrounding material above the phantom 9mm away from the soft/stiff interface. Rubber tubes were attached to the ends of the phantom, fixed above the level of the phantom and were filled with water, applying a small pre-stretch to the phantom. Pulses were generated by releasing a squeeze on one of the rubber tubes.

3.2.1.2. Mouse study design

The mouse study protocols were the same as in the pPWI study. More specifically, for the purpose of the atherosclerosis study, eleven six-month old were fed an atherogenic high-fat-type diet (20% protein, 50% carbohydrate, 21% fat, 0:21% cholesterol; Research Diets, New Brunswick, NJ, USA) [55]. One of the acquired mice died after 17 weeks of high-fat diet from myocardial infarction during anesthesia, while another two of them were euthanized due to poor health and deep skin ulcerations after 25 weeks on high-fat diet. The rest of the mouse

cohort (n = 9) were euthanized after approximately 35 weeks. The abdominal aortas of each mouse were scanned at 0, 10, 20 and 30 weeks after the beginning of the high-fat diet in order to monitor atherosclerotic lesion development.

In the case of the aneurysmal mouse development study, nine male ApoE/TIMP-1 knockout mice (n = 9) were infused with angiotensin II (A9525, Sigma-Aldrich, St. Louis, MO, USA) for 30 days via subcutaneously implanted osmotic pumps (Alzet Model 2004, Durect, Cupertino, CA, USA). The mice were given a dose of 2.2 mg/kg/day (milligrams of angiotensin II per kilogram of body mass per day). These mice were monitored until the formation of a AAA, at which point high frame rate RF-data were acquired at the aneurysmal location of the abdominal aorta.

3.2.1.3. Data acquisition and post-processing

In the case of the silicone phantoms an optimized high frame rate coherent compounding acquisition sequence was used to acquire RF-data. This sequence was designed and optimized in [193], a study included in this thesis and will be further described in Chapter IV. This sequence involved the transmission of 5 plane waves at 1667Hz. The transmission angles were equispaced with a maximum value of 2^{o}. Positive and negative transmission angles were alternated in order to eliminate lateral shift of the focus [194]. The sequence was implemented on a Verasonics Vantage 256 system (Verasonics, Kirkland, USA) with a linear array transducer with 128 elements, a central frequency of 5 MHz, 60% bandwidth and 294 µm of element spacing (L7-4, ATL Ultrasound, Bothell, WA, USA).

In the case of the mouse study, the same ECG-gated imaging technique employed in the pPWI study was used to acquire RF-data of the mouse abdominal aorta. This involved using the Vevo 770 high-resolution microscanning system (FUJIFILM VisualSonics, Toronto, ON, Canada) connected to a 30MHz single element transducer (RMV-707B, VisualSonics, Toronto, ON, Canada). Consequently, a synthetic sequence of RF-frames with a field of view of 12 × 12 mm^2 at 8000Hz was obtained.

The channel data acquired from the phantom scans were beamformed using a GPU accelerated variation of the delay-and-sum algorithm introduced in [193]. The PWI post-processing methodology used for both the beamformed RF-frames and the synthetic ECG-gated RF-frame sequence was the same. The axial wall displacements were estimated off-line using a GPU-accelerated version of the sum-table 1-D normalized cross-correlation algorithm introduced in [162] and also parallelized in [193]. Both the GPU-accelerated beamforming and 1-D cross-correlation method will be further described in Chapter IV. Axial displacements were subsequently normalized (multiplied) by the frame rate in order to produce axial wall velocities (v_{PWI}). Spatio-temporal maps depicting the v_{PWI} variation over time at each lateral position were then generated for each of the anterior and posterior wall segmentations. Finally, to eliminate any rigid motion and thus make PWV estimation more robust, the two spatio-temporal maps were subtracted and a distension spatio-temporal map was generated. A schematic of the post-processing methodology is shown in Figure 3.9.

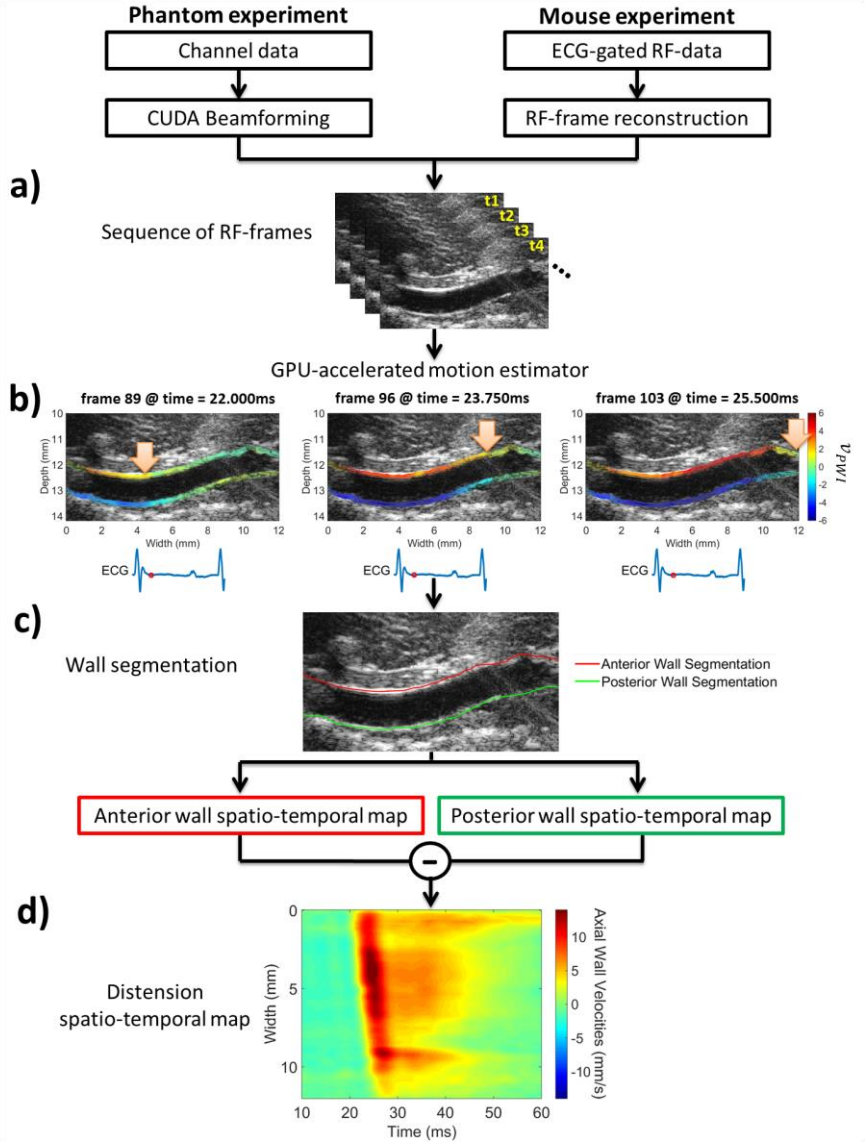

Figure 3.9: PWI post-processing methodology. a) Generated sequence of RF-frames. b) Sequence of B-modes with color-coded and overlaid $v_{PWI.}$ Red indicates motion towards the transducer (upward) and blue indicates motion away from the transducer (downward). c) B-mode with the anterior and posterior walls segmentations (red: anterior wall, green: posterior wall). The orange arrows indicate the approximate location of the pulse wave wavefont at each frame as it propagates from left to right. Time indicates time after the R-peak of the ECG signal. d) Distension spatio-temporal map generated from the subtraction of the anterior and posterior wall spatio-temporal maps. In the figures above, a normal mouse aorta was used as an post-processing example.

3.2.1.4. Adaptive PWI methodology

In this section the methodology employed to divide the imaged artery into segments where the pulse wave propagation is most homogeneous will be described. Homogeneous pulse wave propagation was defined by two criteria:

- Linearity of pulse wave propagation within the segment.
- Homogeneity of peak distension v_{PWI} within the segment.

In order to investigate the pulse wave propagation linearity, in the case of the in vivo study the 50% upstroke points of the v_{PWI} versus time were selected as the tracking feature of the pulse wave. However, in the case of the silicone phantom, releasing a squeeze on one of the rubber tubes generated a negative pulse wave and thus a distension wave with negative v_{PWI} was observed. The squeeze release method generated low v_{PWI} in the stiff segment of the phantom. Consequently, the 50% marker waveform was impacted from increased noise resulting from the susceptibility of low v_{PWI} values to electronic noise [147]. Thus, the more prominent and relatively higher magnitude v_{PWI}feature of the peak negative vPWI was chosen. For the second criterion, the peak distension $v_{PWI}$was estimated at each lateral position from the spatio-temporal map. Thus, an optimization algorithm was required, receiving as inputs the time points of the 50% upstroke markers (MKi) and the peak distension v_{PWI} (PVi) at each lateral position (i =1…M where M is the number of lateral positions/reconstructed beam locations) and producing the number, size and position of the segments generated by the optimal partition of the vessel yielding the most homogeneous arterial regions.

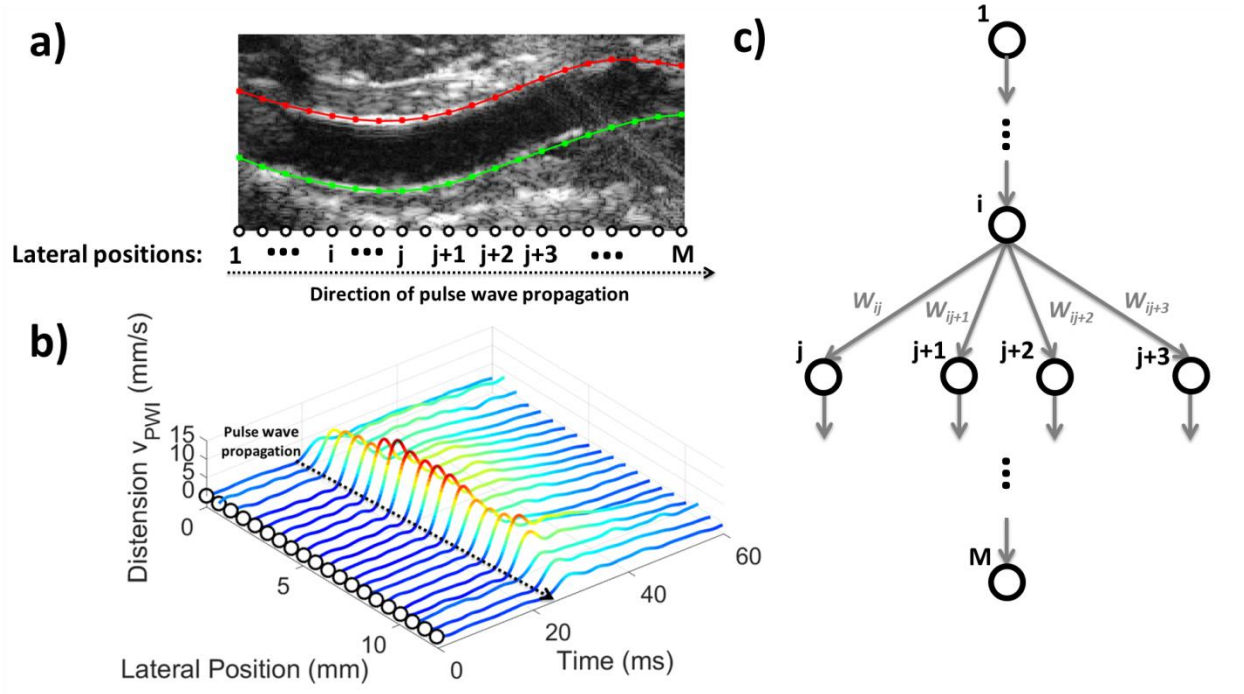

Figure 3.10: Graph modeling of the PWI problem space. a) Segmentation of the anterior and posterior arterial wall of a mouse aorta corresponding to each lateral position. b) Distension v_{PWI} waveforms corresponding to each lateral position of the aorta as indicated in a). c) Graph model of the PWI problem space with each node corresponding to each lateral positions connected with appropriately weighted graph edges.

To solve this optimization the problem space was modeled as a graph as shown in Figure 3.10. Each lateral position of the imaged vessel (Figure 3.10 (a)) and equivalently of the spatio-temporal map (Figure 3.10 (b)) was represented as a node in the graph. Each node was then connected with graph edges (lines in the graph) to nodes corresponding to subsequent lateral positions (Figure 3.10 (c)). A numerical value was then linked to each graph edge (graph edge weight). The weight values were designed appropriately to represent the degree of homogeneity of the segment beginning and ending at the lateral positions corresponding to the connected nodes. Consequently, for two nodes corresponding to the lateral positions *i* and *j*

with $i, j \in [1, M]$ and $i < j$, the weight of the graph edge connecting them w_{ij} is computed as the sum of three metrics as follows:

$$w_{ij} = \widehat{SSE_{MKij}} + \widehat{CV_{PVij}} + \sqrt[\widehat{Lij}]{\widehat{Lij}} \quad (7)$$

A graphical depiction of each metric is shown in Figure 3.11 and a description of each metric follows:

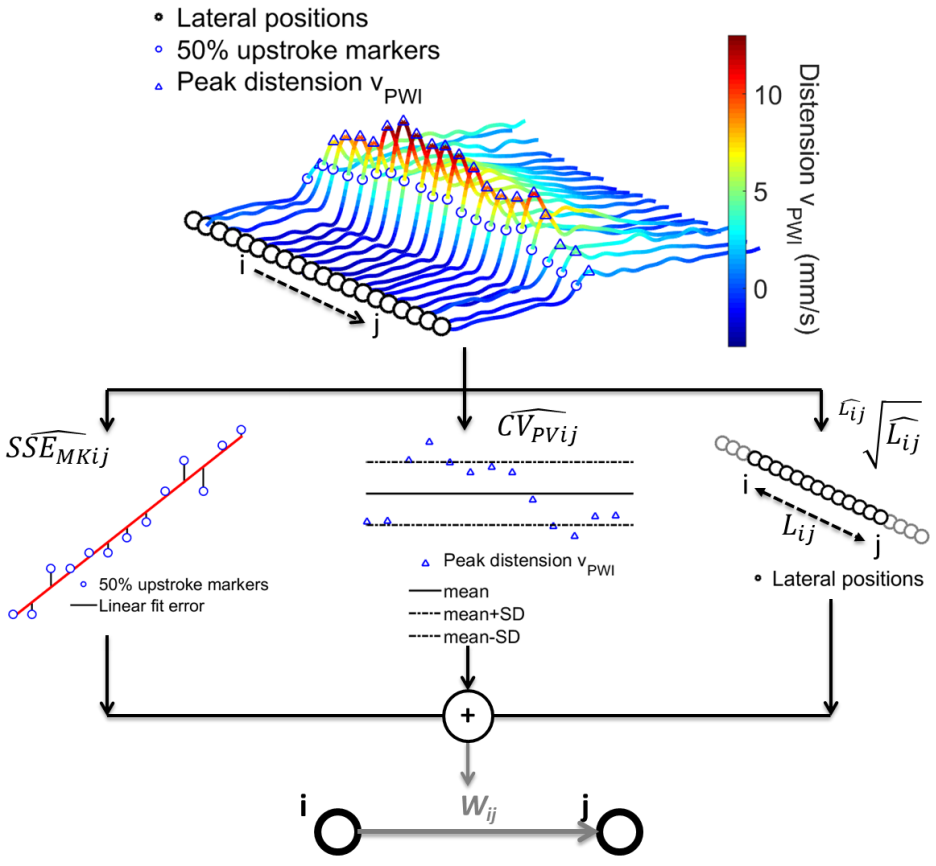

Figure 3.11: Graphical depiction of the metrics used for the edge weight estimation

1) $\widehat{SSE_{MKij}}$ is the normalized sum of squared errors of the linear fit for all the 50% upstroke markers included between the lateral positions i and j. The sum of squared errors is thus estimated as:

$$\widehat{SSE_{MKij}} = \sum_{k=i}^{j} (t_{MKk} - t_{LFk})^2$$

where t_{MKk} is the time point of the 50% upstroke marker corresponding to the k-th lateral position, t_{LFk} is the time point of the k-th lateral position 50% upstroke marker as predicted by the linear regression of all of the 50% upstroke markers between i and j.

This metric assesses the linearity of the pulse wave propagation, as higher nonlinearity in the pulse wave propagation within the segment contained between the lateral positions i and j will produce higher errors in the linear regression and consequently higher SSE_{MKij} values.

2) $\widehat{CV_{PVij}}$ is the normalized coefficient of variation of the PV_K for all the lateral positions k between i and j. CV_{PVij} is thus estimated as:

$$CV_{PVij} = \frac{\sigma_{PVij}}{\overline{PV_{ij}}}$$

where σ_{PVij} is the standard deviation of the PV_k for all lateral positions k between i and j and PV_{ij} indicates the mean of the PV_k for all lateral positions between i and j. This metric reflects

the homogeneity of maximum distension along the arterial segment contained between the lateral positions i and j.

3) Finally, $\sqrt[\widehat{Lij}]{\widehat{Lij}}$ is another metric added to the weight function that involves the length of the ij segment. More specifically, its purpose is to add a penalty in the case of too small segments (segment length ≤ 10% of the imaged artery length) or too large segments (segment length ≈ the imaged artery length). This is achieved by utilizing the function $\sqrt[x]{x}$, a function that increases sharply from $x = 0$ up to $x = e$ and then smoothly diminishes. Appropriate scaling of each segment ij's length allowed moving the maximum to approximately half of the total length of the imaged artery. Subsequently, this metric was normalized so that the maximum of the function corresponds to minimum cost (0) and its minimum corresponds to maximum cost (1).

Normalization in the cases of $\widehat{SSE_{MKij}}$ and $\widehat{CV_{PVij}}$ involved scaling their values in [0,1]. Towards that end, we experimented with different normalization configurations (upper and lower bound of metric) in order to find the one that would prove to be the most consistent in all of the experiments in the current study (phantom, healthy, atherosclerotic and aneurysmal mouse aortas). It should be noted that by allowing different margins of errors this normalization can make the algorithm become either stricter or more lenient thus providing the user with customization capability. The same normalization configuration was employed throughout this study.

Given the modeling described in the previous section, the optimal solution yielding the segmentation of the imaged vessel into segments that are on average the most homogeneous can be represented by the collection of edges (or equivalently the path) connecting node 1 to node M with the lowest average of the w_{ij}. If we think of the sum of the w_{ij} of the graph edges included in that path as the path's total distance, then the initial problem can be converted into a modified shortest path-type problem.

A simple implementation of a well-known dynamic programming algorithm is, thus, sufficient to solve this problem. More specifically, we implemented a modified version of the established shortest-paths Bellman-Ford algorithm [195]. This algorithm repeats an "edge relaxation" step in which distances to each node are updated with a newly discovered shortest path. In the present modified implementation, each time an edge relaxation is performed, additionally to the path distance to each node ($\sum_{i,j\in path} w_{ij}$), the number of segments of each path is kept in memory and is used to normalize the distance and thus prevent the algorithm from developing a bias towards paths with a few segments. Consequently, the following edge relaxation is repeated for each graph edge, $M-1$ times where M is the number of nodes in the graph (equal to the number of lateral positions):

$$D_{1j}^{new} = \min(D_{1j}^{old}, \frac{N_{1i}^{path}}{N_{1i}^{path}+1} D_{1i}^{old} + \frac{1}{N_{1i}^{path}+1} w_{ij})$$

Where D_{1j}^{new} is the new distance from start position to node$j$, D_{1j}^{old} and D_{1i}^{old} are the stored distances to nodes i and j respectively, N_{1i}^{path} is the number of segments included in the path from the start position to node i and w_{ij} is the weight of the edge connecting nodes i and j.

In the end, the number and position of the nodes that are included in the path with the lowest average w_{ij} provides us with the number and position of the lateral positions between which the arterial segments are most homogeneous. Equivalently, these nodes correspond to the lateral positions where the arterial segments on each side exhibit different stiffness and thus constitute stiffness variation interfaces.

3.2.2. Results and discussion

Figure 3.12 shows the spatio-temporal plots and the PWV maps generated for the silicone phantom with the soft and stiff segments. Furthermore TABLE 3.1 concentrates all of the results for four measurements (n=4) for each direction of the pulse wave using adaptive PWI (PWV_{soft}^{PWI}, PWV_{stiff}^{PWI}) and compares with the results from static testing (PWV_{soft}^{static},PWV_{stiff}^{static}).

	Stiff to Soft (n = 4)	Soft to Stiff (n = 4)
PWV_{stiff}^{PWI} (m/s)	$3.96 + \_0.28$	3.59 ± 0.06
PWV_{stiff}^{static} (m/s)	3.52	
PWV_{soft}^{PWI} (m/s)	2.34 ± 0.09	2.93 ± 0.08

$PWV_{soft}^{static}\ (m/s)$	2.41	
Interface error (mm)	4.40 ± 0.7	3.20 ± 0.3

TABLE 3.1: Phantom experiment Results

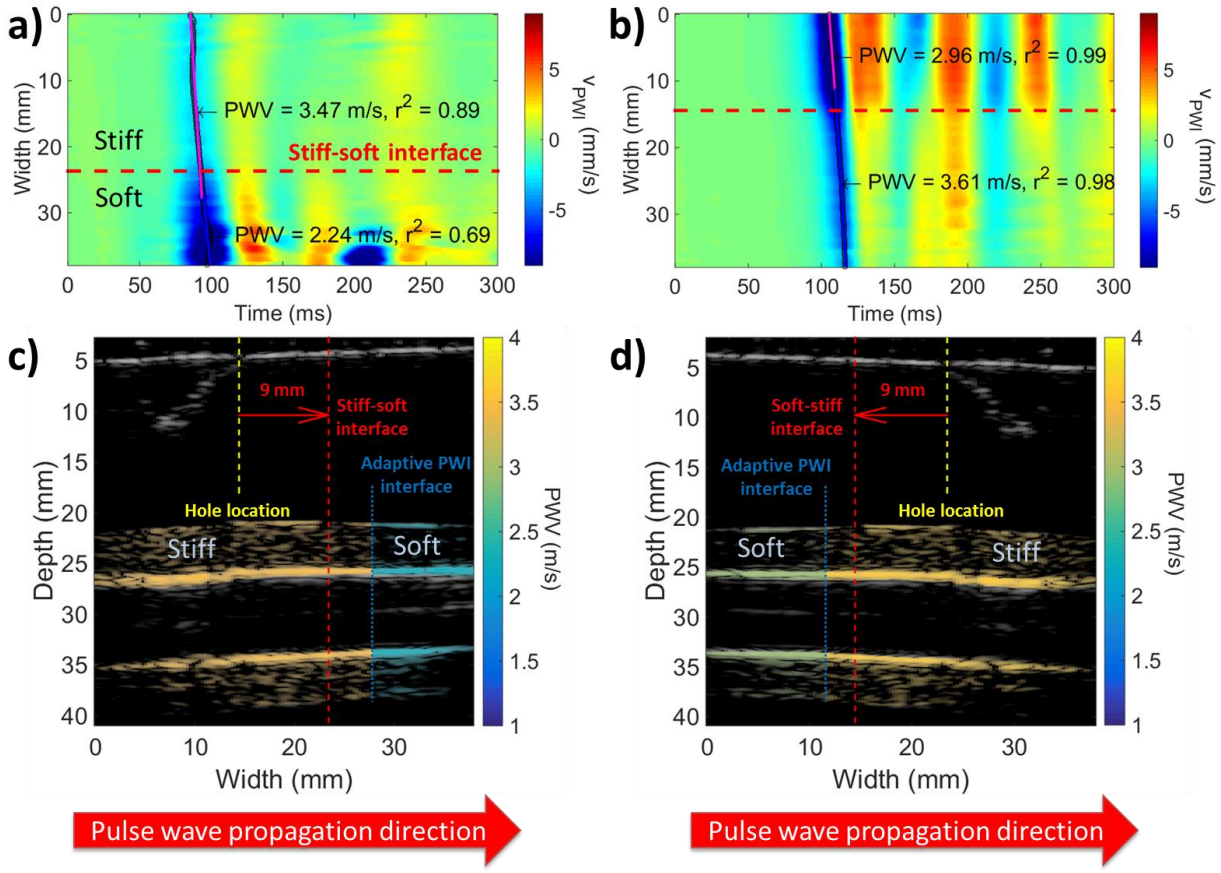

Figure 3.12: a), b) Spatio-temporal plots with the linear regressions generated by adaptive PWI for each propagation direction (stiff towards soft and soft towards stiff, respectively. The interface location detected by the marking of the surrounding tissie material is shown with a perforated red line. c), d) B-modes with the PWV velocities color-coded and overlaid onto the vessel walls (PWV maps) for each propagation direction. The soft-stiff interface detected with adaptive PWI is denoted by the vertical dotted blue line, the location of the marking in the surrounding material is indicated with a perforated yellow line and subsequently the location of the interface detected via the marking is indicated with a perforated red line.

From the results, it was observed that the soft-stiff interface detection error was relatively small (<12% of the imaged segment length). Thus, the proposed methodology was able to correctly resolve the number and the extent of the soft and the stiff phantom segments, an impossible task by relying solely on the B-mode. Small detection errors of the soft-stiff interface can also attributed to the rough method of localizing the soft-stiff interface via the marking of the surrounding tissue material. The estimated adaptive PWVs of the phantom segments were in agreement with the PWV values estimated via static testing. It needs to be noted that slightly increased error in the PWV estimation in each case can be found in the first segment in the direction of the PWV propagation. This confirms that PWV estimation is affected in part by the wave reflection at stiffness interfaces. This observation is in agreement with a study by Latham et al. where the regional PWV measured in the aortic segment preceding the renal branch - a major reflection site - was higher than the expected value and also compared to the PWV measured in the aortic segment immediately following the renal branch, especially in the lower frequencies [196]. Thus, given that wave reflection has been previously reported to impend regional PWV estimation [110], [172] this phantom setup could be potentially very useful in further investigation of the effects of wave reflection on PWV estimation in a controlled environment.

Figure 3.13 shows the PWV maps for 3 mice at baseline and after 10, 20 and 30 weeks of high-fat diet. Single-segment segmentation was observed in the case of the baseline PWV maps, indicating smooth pulse wave propagation. Additionally, uniform PWV values were found across the baseline mouse aortas. Already after 10 weeks of high-fat diet, there were either

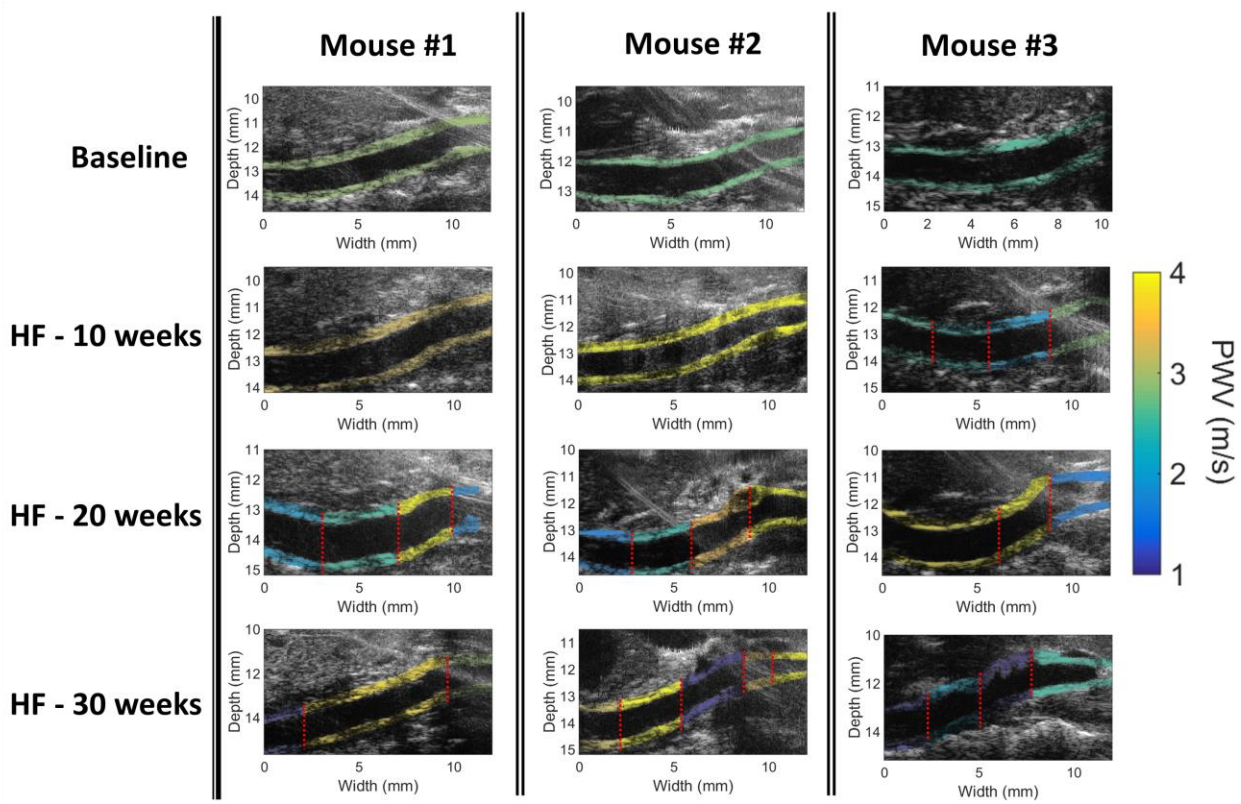

Figure 3.13: PWV maps of three mice at baseline and after 10, 20 and 30 weeks of high-fat diet (HF) the detected interfaces between adaptive PWI segments are indicated with dotted red lines

increased PWV values indicating arterial stiffening or increased number of detected segments alluding to increased inhomogeneity. As the duration of the high-fat diet increased to 20 weeks, the amplitude uniformity and linearity of the pulse wave propagation were further impacted. Additionally, arterial stiffening was observed in several segments with increased PWV. Finally, after 30 weeks, vessel fragmentation and segments with increased stiffness persisted, however, several lower stiffness segments were also found.

Figure 3.14 shows quantitative results for the entire mouse population. Repeated measures ANOVA was performed with the Tukey correction for multiple comparisons. Mean adaptive

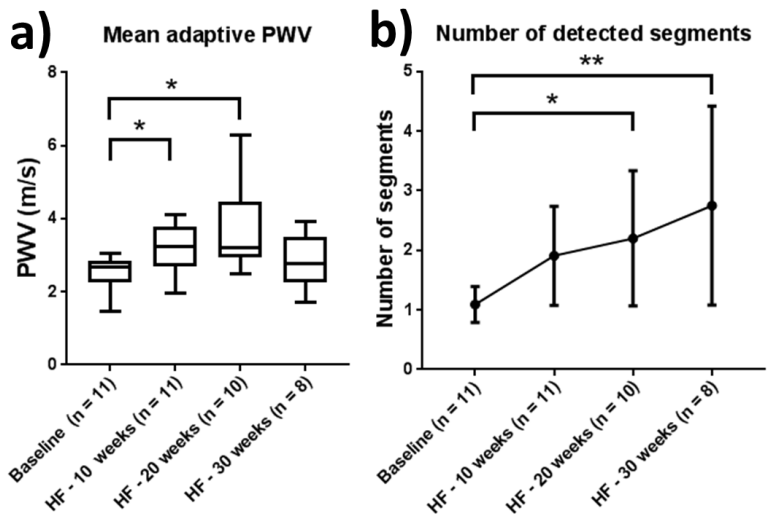

Figure 3.14: Atherosclerotic mouse aortas study statistical results. a) Mean adaptive PWV of atherosclerotic mouse aortas at baseline, after 10, 20 and 30 weeks of high-fat diet (HF). b) Mean number of segments detected with adaptive PWI indicating the level of inhomogeneity of the artery at baseline, after 10, 20 and 30 weeks of high-fat diet (HF).

PWV in baseline aortas (before initiation of the high-fat diet) was found to be $2.55 \pm 0.47 m/s$ ($n = 11$). Significant increases ($p \leq 0.05$) in mean adaptive PWV were found after 10 and 20 weeks of high fat diet ($3.17 \pm 0.67 m/s; n = 11$ and $3.76 \pm 1.20 m/s; n = 10$ respectively). This increase already at 10 weeks of high-fat diet is an interesting finding since it is the period when the first foam cell lesions start to appear in the mouse aorta [173]. This could have implications for the utility of adaptive PWV in the detection of early stage atherosclerotic disease and also is in agreement with the results of the Rotterdam study where even mild aortic atherosclerosis correlated with elevated levels of aortic PWV [54]. Subsequently, mean adaptive PWV dropped after 30 weeks of high-fat diet ($2.82 \pm 0.74 m/s, n = 8$) with increased arterial remodeling being the most probable cause. A similar decrease in arterial

stiffness in an animal model of prolonged atherosclerosis development has also been reported in a study by Farrar et al. [180] as well as in the previously reported pPWI results [172].

The baseline average number of detected segments was 1.1 ± 0.3 segments ($n = 11$) confirming the homogeneous pulse wave propagation in healthy mouse aortas. An increase in the number of detected segments was found after 10 weeks of high-fat diet (1.9 ± 0.8 segments, $n = 11$) indicating the initial appearance of arterial stiffness inhomogeneity. The mouse aortas were found to become less homogeneous after 20 and 30 weeks with significant increases in the number of detected segments compared to the baseline case (2.2 ± 1.1 segments, $p \leq 0.05$ and 2.75 ± 1.7 segments, $p \leq 0.01$ respectively). Consequently, in the case of the mouse aortas after 30 weeks of high fat diet even though arterial stiffness seems to be recovering, this appears to be at the expense of arterial homogeneity. These findings showed that adaptive PWI was able to capture the progression of the level of arterial inhomogeneity from initial sub-endothelial foam cell deposits to more complex and prevalent lesions compromising both elastin fiber organization and the smooth-muscle-cell-rich media layer [173], [197].

In the case of the aneurysmal mouse study, the aim was to investigate whether the aneurysm boundaries (proximal and distal aneurysmal necks), where the dilation of the vessel diameter starts and ends can be detected by adaptive PWI as stiffness interfaces. This would validate the utility of adaptive PWI *in vivo* given that variations in arterial diameter along the investigated vessel correspond to stiffness inhomogeneities and thus sources of reflection [6]. Moreover,

previous studies have reported stiffness variations between aneurysmal and nonaneurysmal aortic tissue [198], [199]. The aneurysm boundaries were detected using the vessel segmentation. More specifically, the vessel diameter was estimated at each lateral position thus creating a diameter waveform. In this waveform, the location of the maximum diameter was determined and the locations of maximum second derivative of the diameter on each side were considered to be the ground truth regarding the aneurysm boundaries, since it's where the dilation of the arterial diameter begins.

Figure 3.15 shows the inhomogeneity interfaces detected by the adaptive PWI methodology and the boundaries of the aneurysms overlaid both onto the B-mode and onto the spatial variation diameter waveform. It was observed that stiffness interfaces were detected in close proximity of the aneurysm boundaries, corroborating the change in mechanical properties occurring in the aneurysmal neck regions. On average the lateral distance between the proximal (closest to heart) aneurysmal boundary and the closest adaptive PWI interface (e_{prox}) was$0.72 \pm 0.41\, mm$, $(n = 8)$ while in the case of the distal (furthest from the heart) aneurysmal boundary (e_{dist}) it was $0.63 \pm 0.46\, mm$, $(n = 8)$. On average these errors corresponded to 13.7% of the imaged aneurysm length. Thus, adaptive PWI delineated the extent of aneurysms, a utility that may prove to be especially useful for surgeons planning aortic reconstruction. This way it can complement aortography by providing an objective and more accurate alternative to conventional ultrasonography that often yields operator-dependent and imprecise estimates of the extent of the AAA [127].

Furthermore, the mean adaptive PWV of the segments contained within the aneurysmal sac was estimated to be$2.39 \pm 1.41 m/s$. Finally, the imaged aneurysmal aortas were divided into 3.6 ± 0.5 segments indicating a relatively high degree of inhomogeneity of the afflicted vessel, a finding that is in agreement with experimental studies showing that AAA produce significant distension wave reflections, especially close to the proximal boundary of the aneurysm [200].

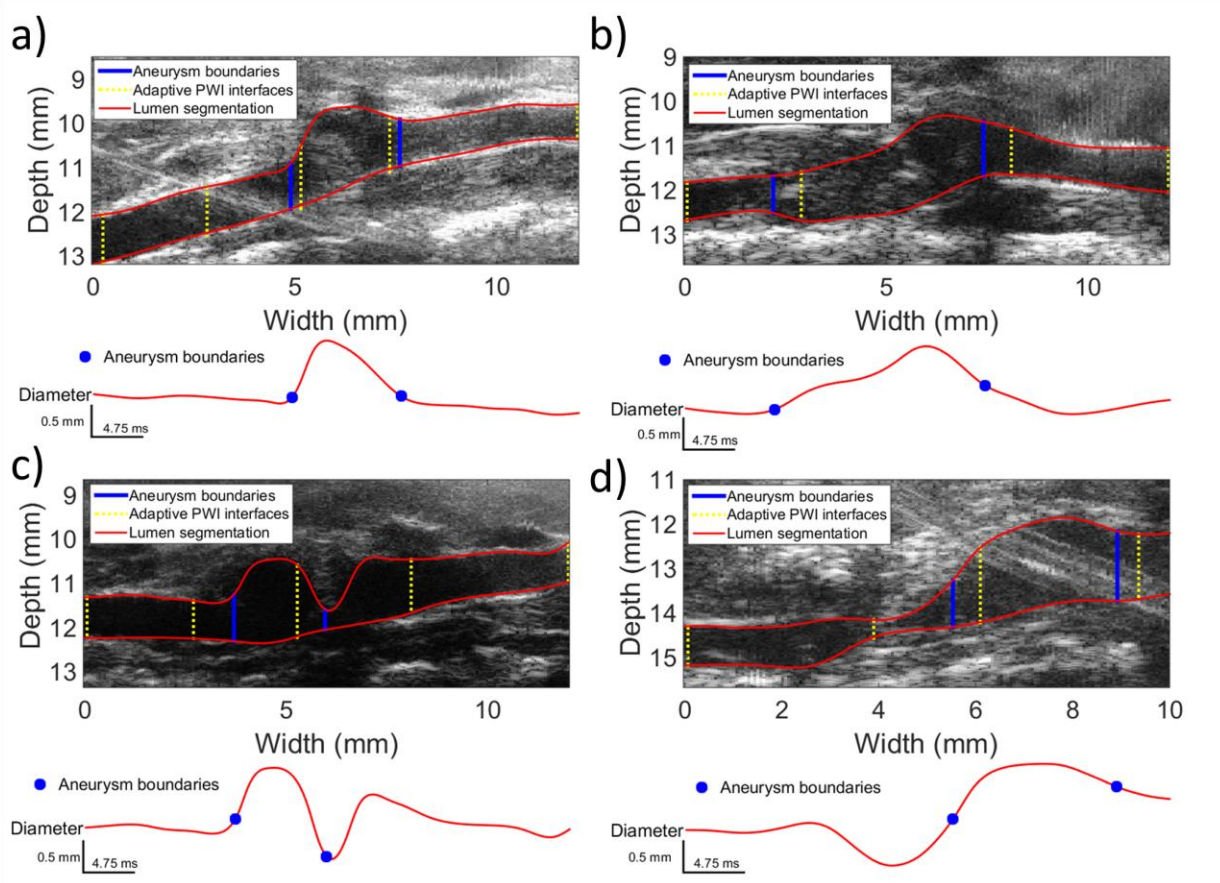

Figure 3.15: Stiffness inhomogeneity interfaces detected by adaptive PWI in mouse aneurysmal aortas overlaid onto the B-mode (vertical yellow perforated lines). The wall-lumen interface is delineated with a continuous red line for both the anterior and the posterior arterial wall. The vertical blue lines indicate the aneurysm boundaries, as detected by the second derivative of the diameter waveform criterion. The diameter waveform is shown for reference for each lateral position beneath each B-mode as a continuous red line.

3.2.3. Limitations and conclusions

While the proposed technique is promising, one of its limitations is that even though it attempts to isolate the most homogeneous arterial segments, it still suffers from PWV estimation errors due to pulse wave reflections. However, this technique can be used in conjunction with the recently introduced pulse wave inverse problem method (PWIP) to account for the reflection waves [170]. More specifically, adaptive PWI can be used as a pre-processing step to determine the segments in which PWIP will be applied and to detect potential reflection sites, an actually serious problem in itself given the previously reported impact on PWV estimation and elusiveness of the reflection sites in the arterial system [112].

Consequently, adaptive PWI was able to detect stiffness interfaces, inconspicuous to the B-mode, in a silicone phantom with soft and stiff segments. Furthermore, it was able to effectively monitor the progression of atherosclerotic mouse aortas from the earliest to the latest stages of the disease. Finally, a preliminary validation of the technique was performed in vivo by relatively accurately detecting the proximal and distal boundaries of AAAs, which are known to be sites of arterial inhomogeneity, in mouse aortas *in vivo*.

Chapter 4. Validation and Optimization of the PWI Parameters Using Coherent Compounding for Use in Humans In Vivo

4.1. Plane wave imaging and coherent compounding

In the previous chapter, a stroboscopic ECG technique was used in order to achieve frame rates in the kHz rate and thus enable local pulse wave tracking. This technique, while successfully applied in the case of mice, would not be as successful in a clinical setting. Given that it requires long acquisition times and that the images can be compromised by breathing, physiological motion of the patient and susceptibility to errors in the case of patients with irregular heart cycles, this technique is not deemed ideal for use in the clinic. Previous PWI studies used the paradigm of conventional ultrasound imaging, where a focused beam was swept across the imaging plane and backscattered signals were sequentially acquired, were able to achieve frame rates in the kHz range only after greatly reducing the number of scan lines and thus significantly compromising spatial resolution [175]. A previous PWI study in human carotid arteries utilized only 16 beams in order to achieve a frame rate of 1 kHz [188], while in another study 16-32 beams were used with a curvilinear array in human aorta scans [168]. Additionally, in a recent simulation study it has been shown that the performance of regional PWV estimation benefits from increasing the number of scan lines used [201]. Consequently, this traditional tradeoff between spatial resolution and frame rate needs to be overcome.

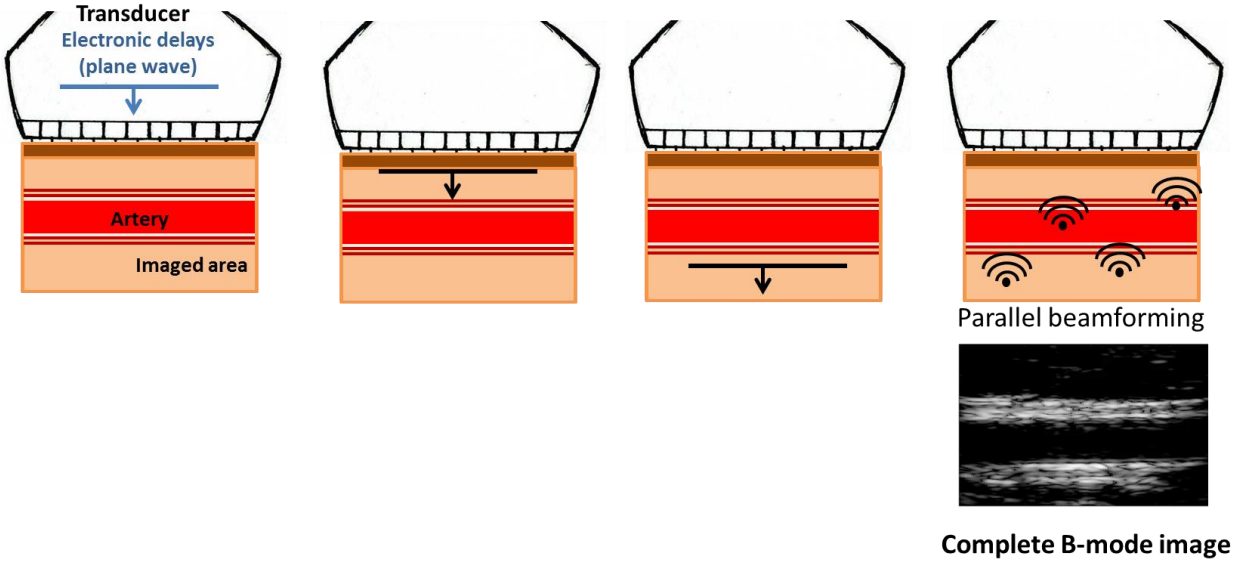

Figure 4.1: Plane wave ultrasound scanning of a common carotid artery. The transducer elements are fired simultaneously and a single plane wave insonifies the whole field of view. Parallel beamforming of the received echoes yields the complete B-mode image.

Plane wave imaging, a relatively recently introduced ultrasound imaging modality [202], [203], [204], has been shown to be capable of acquiring full line density images at ultrafast frame rates (i.e. more than 1 kHz). Its paradigm consists of simultaneously firing all of the piezoelectric elements of the transducer to transmit a single plane wave that insonifies the full imaging plane [204]. Subsequently, parallel processing of the echoes on receive enables the generation of multiple B-mode lines from a single insonification of the imaged medium. Using this modality, theoretically, the frame rate is only limited by the speed of sound and the attenuation of the sound waves in tissues and can thus reach levels above 10 kHz for specific depths. However, it should be noted that there are practical restrictions imposed to the frame rate by the hardware data transfer rate and memory specifications. A schematic illustrating plane wave imaging is shown in Figure 4.1.

The main drawback of plane wave imaging is the decreased image quality (low resolution and contrast) due to the lack of a transmit focus. Furthermore, displacement estimation has been shown to be impacted, with the displacements becoming noisier and leading to underestimation of the actual tissue displacements. This issue has been resolved, however, with the development of coherent compounding [204]. Steered plane waves are being transmitted into the medium at various angles followed by the acquisition and coherent summation of the backscattered echoes. This way, tissue is insonified from different angles and the coherent summation of these acquisitions retrospectively synthesizes a dynamic transmit focus at each depth [203], [204].

Beamforming of the echoes on receive involves determining the echoes that originate from the same scatterer at each element and subsequently coherently add them, thus reinforcing the echoes from each scatterer [205]. In order to achieve this, the raw channel data received from each element of the transducer array are appropriately delayed and then added. Figure 4.2 shows the travelling routes for a plane wave travelling perpendicularly to the transducer's face and for a tilted plane wave. In the first case, the time from the element $(x_{el}, 0)$ to a point in the field of view (x, z) is:

$$t_{forward} = \frac{z}{c} \quad \textbf{(8)}$$

While in the case of a tilted plane wave at an angle α with the face of the transducer the time for the plane wave emission to travel from the element the point in the field of view can be estimated using some trigonometry:

$$t_{forward} = \frac{zcos\alpha + (x - x_{el})sin\alpha}{c} \quad (9)$$

The return time to that element in either case is:

$$t_{backward} = \frac{\sqrt{(x - x_{el})^2 + z^2}}{c} \quad (10)$$

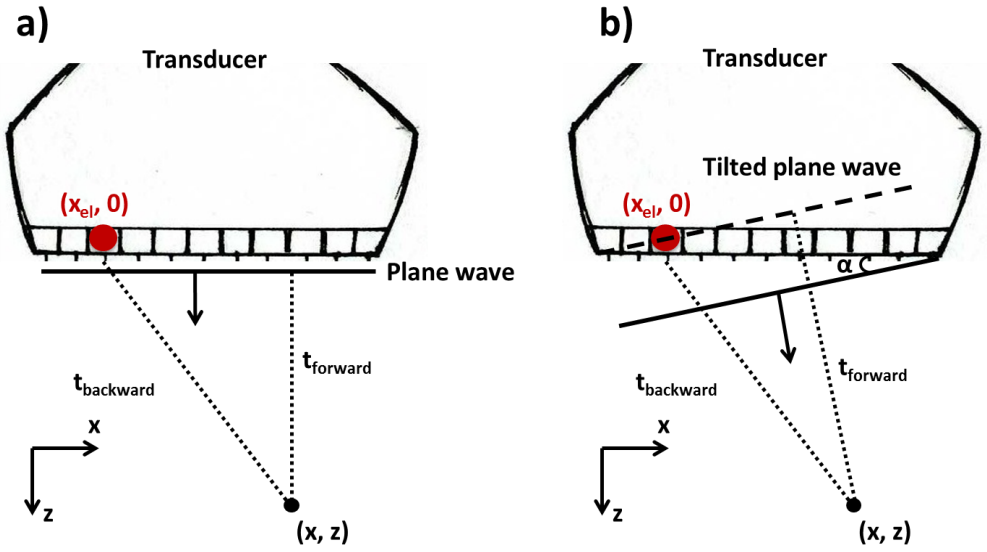

Figure 4.2: Illustration of the travelling routes of the plane wave from the element (x_{el},0) to the point (x,z) (corresponding to a travelling time $t_{forward}$) and of the echoes back to the element (corresponding t a travelling time $t_{backward}$) in the cases of a) a plane wave travelling perpendicularly to the face of the transducer and b) a tilted plane wave. The tilted plane wave in b) with the perforated line corresponds to the time point that (x_{el}, 0) starts transmitting.

Thus making the round-trip delay:

$$t_{tot} = t_{tot}(x, z, x_{el}) = t_{forward} + t_{backward}$$

(11)

Consequently, according to the estimated delays the channel data ($CD(x, t)$) of each element included in the active aperture are delayed and then summed in order to produce RF-frames [204]:

$$RF(x, z) = \int_{x_{el} \in active\ aperture} CD(x_{el}, t_{tot}(x, z, x_{el}))\, dx_{el}$$

(12)

Finally, the RF-data from each tilted transmission are coherently added forming a higher quality image.

This technique leads to higher image signal-to-noise ratio (SNR), decreased sidelobe levels and overall better image quality and has been shown to augment various elastographic ([146], [204], [206]) as well as blood flow estimation techniques ([207], [208]). Consequently, given the advantages of coherent compounding an implementation of PWI using plane wave imaging would prove to be advantageous in a clinical setting.

However, increasing the number of transmitted plane waves comes at the cost of frame rate, thus introducing a new tradeoff between image quality and frame rate, which is regulated by

the number of transmitted plane waves. This tradeoff while not as severe as the one in the case of conventional ultrasound imaging needs to be further investigated in order to achieve optimal pulse wave tracking performance.

4.2. Pulse wave imaging using coherent compounding in a phantom and in vivo

This study involved implementing PWI using coherent compounding and subsequently validating it in silicone phantom vessels and optimizing the imaging parameters for use in vivo using a variety of metrics, including a modified stochastic metric introduced in a previous study by our group [147]. The results of this study have been presented at the 2015 IEEE International Ultrasonics Symposium and at the 14th International Tissue Elasticity Conference (2015) and have been published in [193].

4.2.1. Materials and methods

4.2.1.1. Phantom study design

Silicone gel was used to construct a phantom with a soft and a stiff segment along the longitudinal axis according to [170]. A very soft silicone background was constructed in order to mimic the surrounding tissue around arterial vessels. The phantom was first filled with water to

maintain a circular profile and avoid floating while the background material was filled to approximately 15mm above the top surface of the vessel phantom. The finalized phantom setup is shown in Figure 4.3 a).

Subsequently, two rubber tubes were attached to the outlets of the phantom and its free ends were fixed approximately 7-8 cm above the top surface of it. Static testing was performed similarly to the mechanical testing performed in [170]. More specifically, the system was progressively filled with water and the water level in the tubes was measured at specific time points. The water level measurements provided intraluminal pressure estimates while simultaneously acquired ultrasonic images with a clinical scanner using a 10-MHz linear array (SonixTouch, Ultrasonix Medical Corp., Burnaby, BC, Canada) provided diameter measurements which were then used to estimate intraluminal area. Consequently, specific points of the pressure area relationship of the phantom vessel were recovered and used to provide a compliance estimate. The Bramwell-Hill equation was then employed to produce an expected PWV value. An illustration of the static testing procedure is shown in Figure 4.3 b).

Following static testing, the phantom was connected via rubber tubes to a peristaltic pump, which generated negative pulse waves by pressing and then releasing the rubber tubes at rate of approximately 2 Hz. The scanning setup for each section (soft, stiff) is shown in Figure 4.3 c).

4.2.1.2. In vivo study design

Custom plane wave acquisitions were performed on the right common carotid arteries of six healthy volunteers (age range 22-32 y.o.). Care was taken so that the common carotid was

imaged at least 1cm away from the bifurcation, in order to avoid mixing of the forward and the reflected pulse wave. Some of the acquisitions were repeated after 1-3 days in order to investigate the repeatability of the acquired PWV values. All images were acquired while the subjects were in a sitting position and care was taken in order to perform the repeated measurements at a similar time of the day to avoid PWV variations due to the circadian rhythm of the subjects.

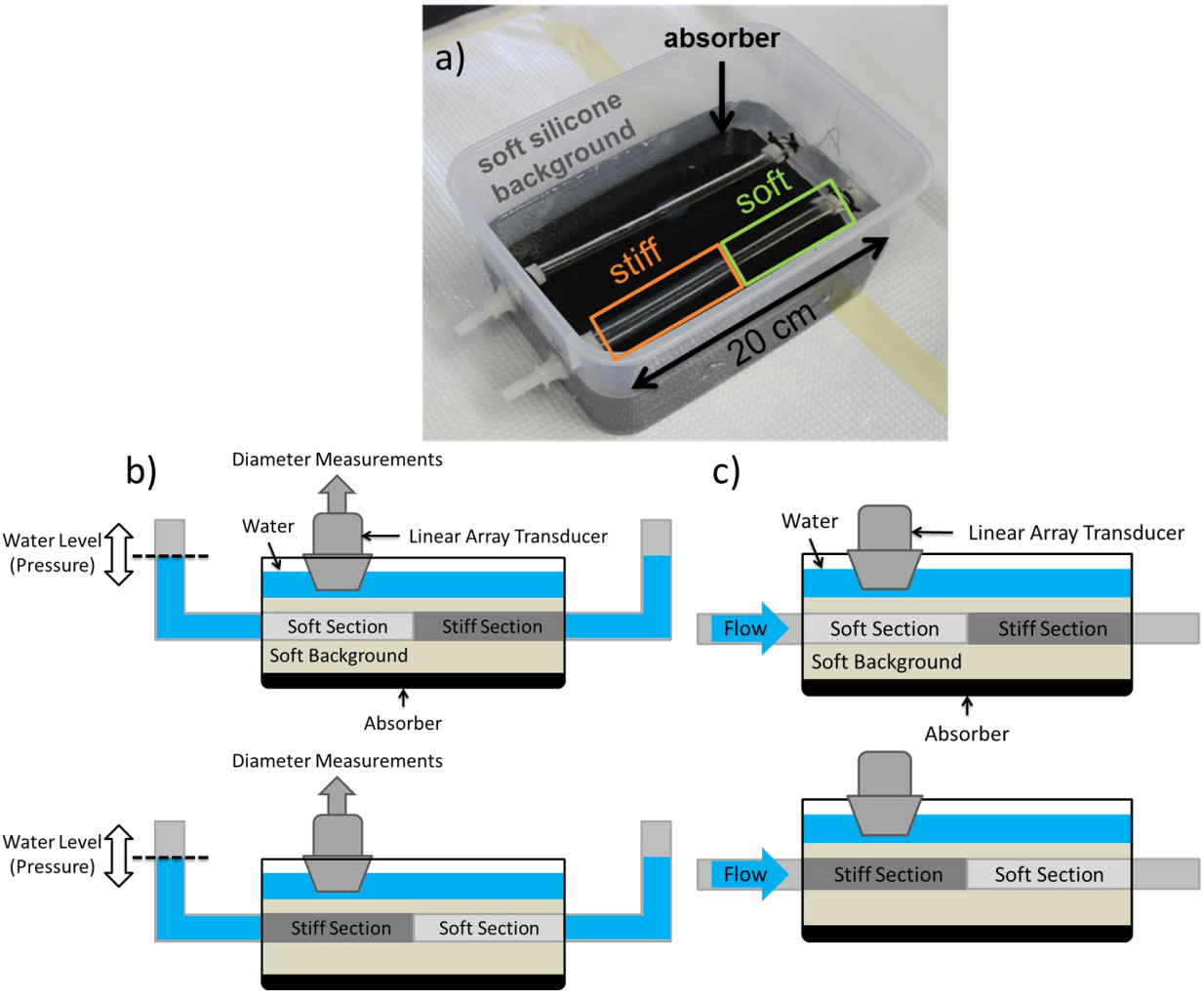

Figure 4.3: (a) Image of the phantom setup used in the present study, (b) schematic of the static testing setup and (c) schematic of the imaging location at each phantom section (top: soft section,

4.2.1.3. Data acquisition

In order to perform the acquisitions and assess the performance of compounded PWI, a programmable ultrasound research scanner (Verasonics Vantage 256, Kirkland, WA, USA) was used. All acquisitions were made using a standard 128-element, 5 MHz linear array transducer (L7-4, ATL Ultrasound, Bothell, WA).

The phantom setup was scanned using a standard 5-plane wave sequence at a frame rate of 926 Hz. The plane wave steering angles were evenly spaced between -4^o to 4^o. In order to investigate whether coherent compounding produced an improvement over single plane wave imaging, the results of using 1, 3 and all 5 of the plane waves were compared.

In the case of the *in vivo* study, three custom acquisition sequences were implemented in order to independently optimize the three compounding parameters (frame rate, plane wave transmission angles, number of compounded plane waves). In all of the cases, the pulse repetition frequency (PRF) was set equal to 8333 Hz. This PRF value was sufficient to accommodate both the time needed for the sound waves to make the required round trip and also the transfer rate between the acquisition system and the host workstation. A schematic illustrating the custom acquisition sequences to test the effects of varying each parameter is shown in Figure 4.4:

1) **Frame rate:** An acquisition sequence transmitting plane waves at the PRF was initially implemented in order to assess the effects of frame rate on the performance of PWI.

The frame rate was decimated at post-processing in order to simulate the frame rate drop caused by adding more steered plane waves. Specifically, by considering all of the frames, a frame rate equal to the PRF was achieved while the frame rate decreased to 2778 Hz, 1667 Hz, 1190 Hz and 926 Hz.

2) **Plane Wave Transmission Angle:** The effects of changing the plane wave transmission angles were investigated using a sequence that transmits nine plane waves at the PRF. The transmission angle strategy consisted of considering the nine plane waves as three sequential triplets transmitted at angles $[-a,a,0]$ with a different angle a for each of the three triplets. Alternate polarity sequencing was utilized in order to avoid lateral shifts of the moving target observed otherwise [194]. Subsequently, the acquired RF-signals from each triplet were compounded resulting in three 3-plane wave compounding image sequences at a frame rate of 926 Hz with different transmission angles of the tilted plane waves. Thus, performance assessment of three different transmission angle values was made possible. This sequence was employed twice in order to compare the following transmission angles: 0^o, 1^o, 3^o and 3^o, 5^o, 10^o. It should be noted that in the case of 0^o compounding practically corresponds to RF image averaging of 3 plane waves. Additionally, the triplet with 3^o was used in both acquisitions in order to serve as a baseline and to facilitate comparison between results from different acquisitions.

3) **Number of Compounded Plane Waves:** A 9-plane wave compounding sequence was implemented. Alternate polarity $[-4^o, 4^o, -3^o, 3^o, -2^o, 2^o, -1^o, 1^o, 0^o]$ was utilized

again in order to avoid lateral shifts of the moving targets. Subsequently, the following subsets of the plane wave acquisitions were used to create compounded images: $[0^o]$, $[-1^o, 1^o, 0^o]$, $[-2^o, 2^o, -1^o, 1^o, 0^o]$, $[-3^o, 3^o, -2^o, 2^o, -1^o, 1^o, 0^o]$ and $[-4^o, 4^o, -3^o, 3^o, -2^o, 2^o, -1^o, 1^o, 0^o]$ and thus utilizing 1, 3, 5, 7 and 9 plane wave acquisitions respectively.

Each of the aforementioned acquisitions lasted for 1.2 seconds generating approximately 2.5 GB of data.

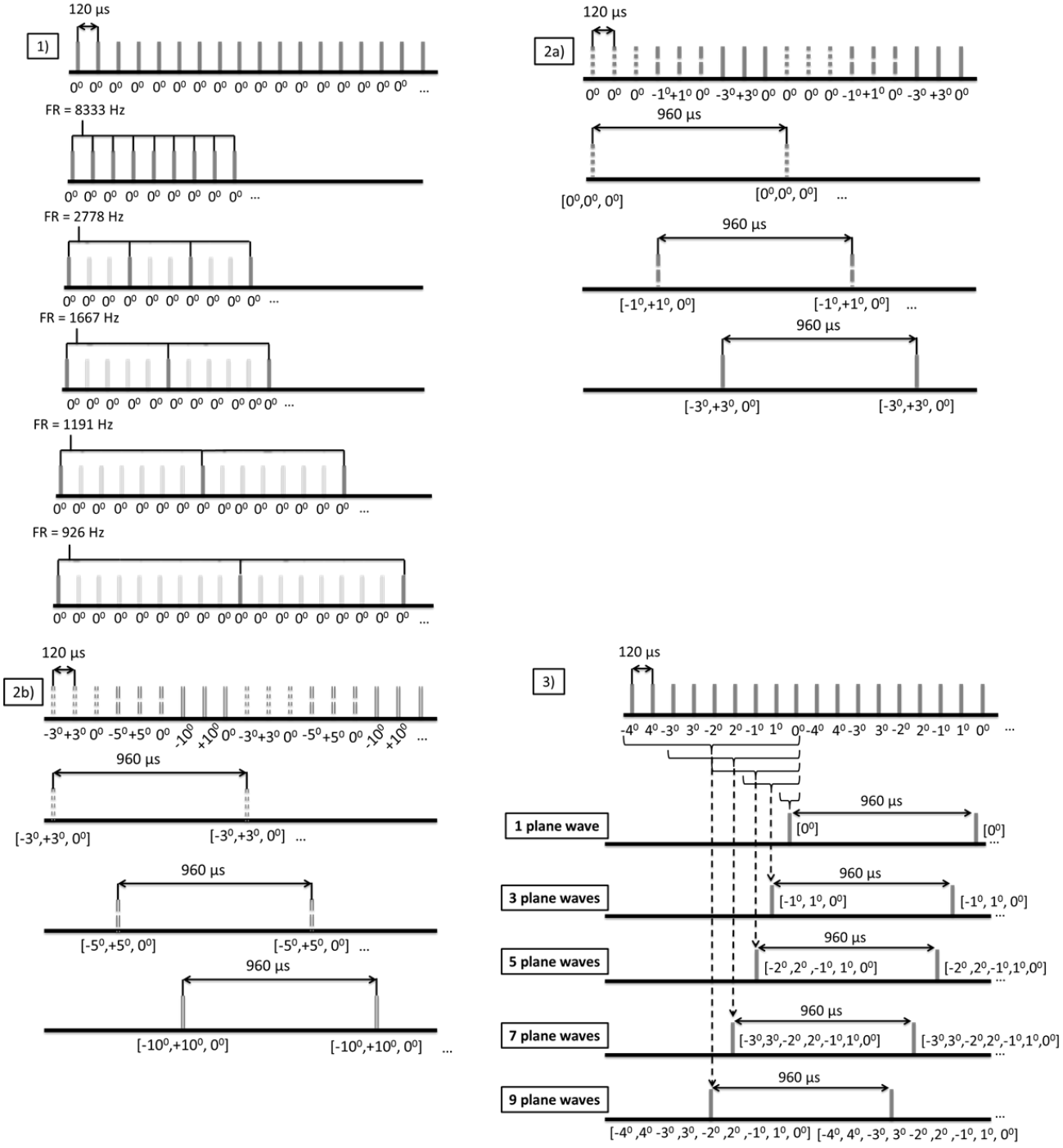

Figure 4.4: Custom acquisition sequences for independent assessment of each imaging parameter. (1) Acquisition sequence for frame rate optimization. (2)(a) and (b) Acquisition sequences for the optimization of the angle of the steered plane waves 2(a) is used to investigate angles 0°, 1° and 3° and 2(b) is used to investigate angles 3° (repeated for comparison baseline purposes), 5° and 10°, 3) acquisition sequence for the optimization of the number of plane waves used in coherent compounding.

4.2.1.4. Data post-processing

In order to process the big bulk of data generated by data acquisition, a GPU-accelerated post-processing framework was implemented. More specifically, the main two bottlenecks in computation time were targeted, namely the beamforming of the RF-data and the motion estimation algorithm.

RF-data were beamformed using a GPU-accelerated version of the delay-and-sum algorithm described previously in the chapter and also shown in [204]. This implementation was coded using the CUDA computing platform (CUDA 6.5, NVIDIA Corporation, Santa Clara, California, U.S.) in order to take advantage of the faster execution time of compiled C code. Working in parallel on the GPU for each pixel of the resulting image, the contributions of each element corresponding to the same scatterrer were determined and then coherently summed. The total round-trip delays for each point to each element were estimated according to equations (8) - (11). The resulting executable file ran on a Tesla C2075 GPU and on average it produced 1000 beamformed RF-frames with 2160 samples and 128 lines within approximately 30 seconds. Subsequently, the produced RF-frames for each tilted acquisition were coherently summed to produce compounded RF-frames.

Similarly, in the case of the motion estimation step of the PWI methodology, a GPU accelerated sub-sample displacement estimation algorithm was implemented. This algorithm essentially parallelized the 1-D normalized cross-correlation (NCC) sum-table method described in [188]. A detailed description of the implemented algorithm is given in Appendix A. The estimated

displacements were multiplied by the frame rate to obtain the normalized by the frame rate PWI axial wall velocities (v_{PWI}). The algorithm was implemented using MATLAB and on average it produced 1000 axial wall velocity frames in 35 seconds.

After the generation of the compounded RF sequence, the estimation of the v_{PWI}, a single line was manually traced through the anterior carotid wall and the v_{PWI} waveforms at each point of the arterial wall trace were sequentially stacked generating a 2D spatio-temporal plot that depicts the v_{PWI} variation over distance and time of the pulse-wave propagation. Distance along the anterior arterial wall trace was calculated by estimating the length of the delineated carotid wall between each point and the leftmost point of the arterial wall trace.

On the 2D spatio-temporal maps, the 50% upstroke point of the v_{PWI} versus time was selected as the tracking feature to estimate the PWV. Linear regression of the relationship between the 50% upstroke arrival time and the previously calculated distance along the anterior wall yielded the slope as the regional PWV value for the whole imaged segment and the corresponding coefficient of determination r^2 as an approximate measure of the pulse wave propagation uniformity. Subsequently, the localized pPWV measurements were estimated with the methodology shown in Chapter III. The 50% upstroke points were divided in 50% overlapping kernels of 20, 30, 40 and 50 points. Linear regressions were performed for each sub-region, thereby providing a localized PWV value along with the corresponding coefficient of determination r^2, indicative of the quality of the linear fit. The size of the kernels was varied to investigate the effects of frame rate and compounding on various levels of PWV localization. A

graphical depiction of the coherent compounding PWI methodology used on a normal common carotid artery is shown in Figure 4.5.

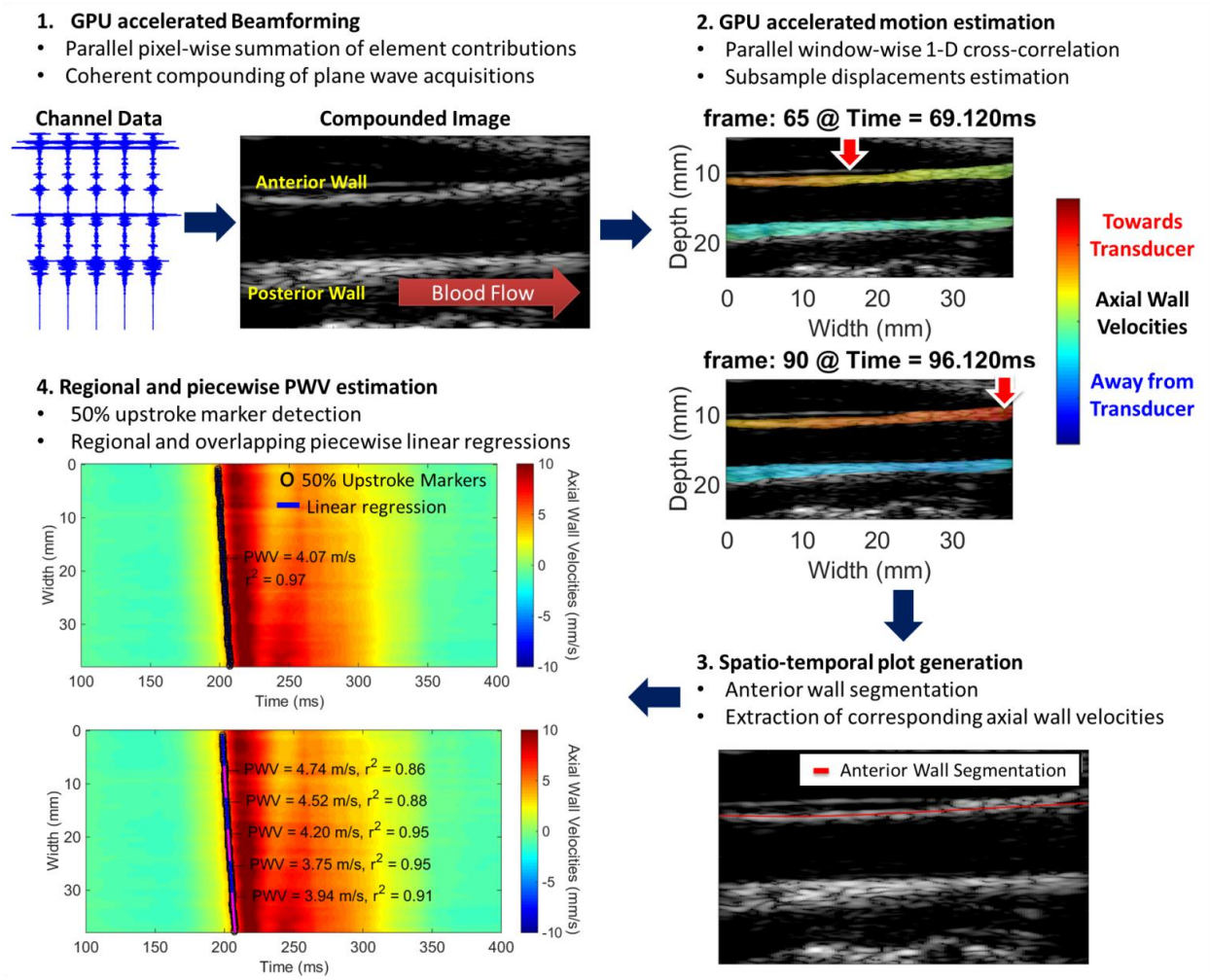

Figure 4.5: Schematic of the compounding PWI post-processing methodology. In 2. vertical red arrows with the white contour indicate the approximate location where the v_{PWI} obtain values close to their 50% upstroke point, thus indicating the pulse wave propagation.

4.2.1.5. Performance metrics

In order to assess the accuracy of the PWI measurements and evaluate the effect of each parameter on the quality of its results, various metrics were used:

- **Regional and piecewise PWV values:** Comparison to static testing derived values in the case of the phantom setup and evaluation of repeatability and agreement between regional and mean piecewise PWVs in the case of the healthy volunteers.

- **Coefficient of determination (r^2):** Comparison of r^2 values for different parameter configurations provides a quality metric contingent upon both varying image SNR as well as frame rate [175].

- **PWI Axial Wall Velocities SNR ($SNR_{v_{PWI}}$):** Similarly to [147], a stochastic metric of precision was used to compare the performance of the PWI axial wall velocity (v_{PWI}) estimation for various imaging configurations. Firstly, the anterior wall of the vessels was manually segmented and subsequently the frames corresponding to a period of 100 ms around the time-point of occurrence of the pulse wave propagation were isolated. $SNR_{v_{PWI}}$ was estimated for each point of the anterior wall within small 2D windows (1mm x 1.2mm). The $SNR_{v_{PWI}}$and v_{PWI} data were used to generate a 2D histogram that corresponds to the probability density function of $SNR_{v_{PWI}}$ for each of the observed v_{PWI} magnitudes. Finally, in order to facilitate comparison the expected value of $SNR_{v_{PWI}}$ was estimated for each v_{PWI} value as follows:

$$E\left(SNR_{v_{PWI}}\middle|v_{PWI}\right) = \int_0^{+\infty} SNR_{v_{PWI}} f\left(SNR_{v_{PWI}}\middle|v_{PWI}\right) dSNR_{v_{PWI}} \quad \textbf{(13)}$$

thus generating easily comparable curves between different imaging sequences. Finally, the mean $SNR_{v_{PWI}}$ was estimated by averaging the estimated $SNR_{v_{PWI}}$ for all the points of the anterior wall.

- **Temporal Resolution Misses (TRM):** This metric was used to evaluate the frame rate's capability to adequately sample the propagation of the pulse wave. More specifically, TRM were estimated as a percentage of the consecutive 50% upstroke markers that occur at the same time point over the total number of 50% upstroke markers. Thus:

$$TRM = \frac{Consecutive\ 50\%\ markers\ at\ the\ same\ time - point}{Total\ 50\%\ upstroke\ markers} \cdot 100$$

Consequently, higher values of this metric correspond to an insufficient frame rate to capture the pulse wave propagation.

4.2.2. Results and discussion

In the case of the phantoms, propagation of the negative pulse wave was observed in both the soft and stiff sections of the phantom. The results of the statistical analysis performed for all of the metrics can be seen in Figure 4.6. The recovered static testing PWV values for the soft and the stiff phantom sections were $PWV_{soft} = 2.49m/s$ and $PWV_{stiff} = 3.41m/s$. The PWI-

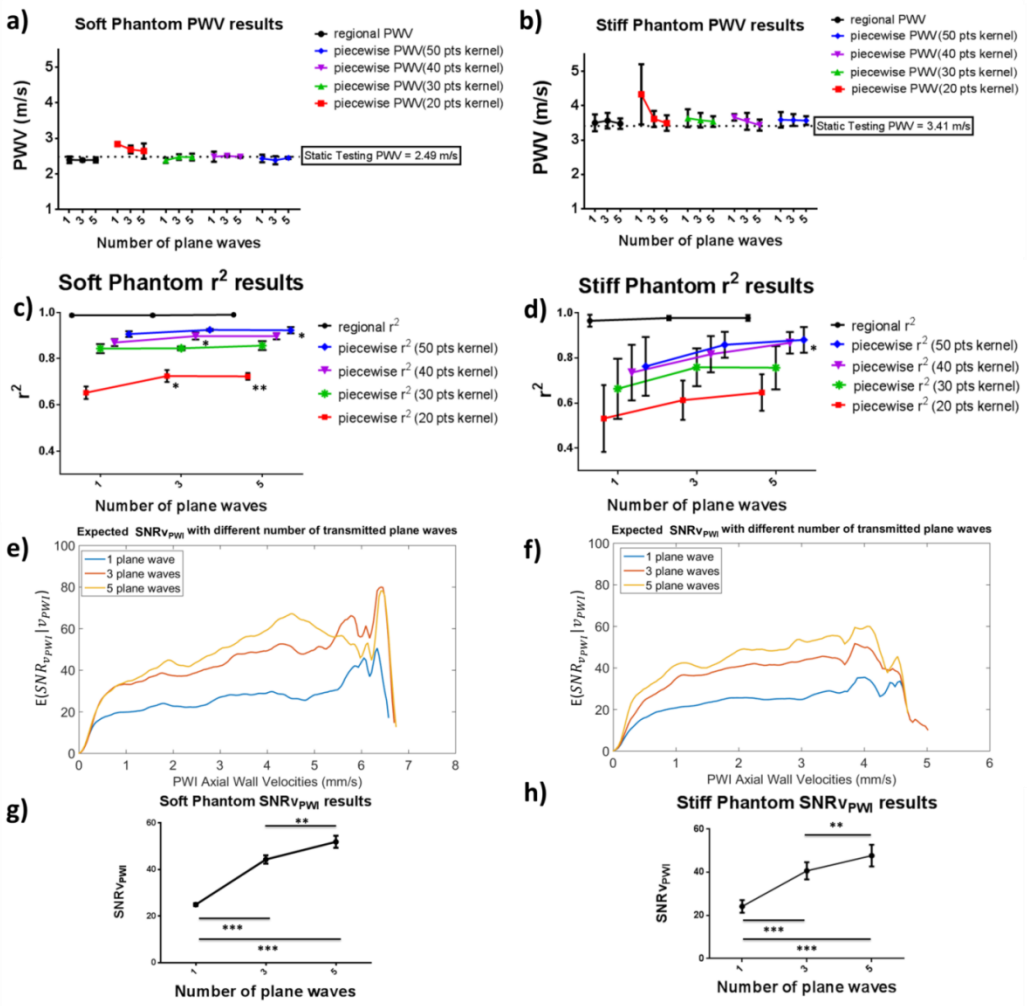

Figure 4.6: Statistical analysis of the phantom PWI validation study. (a) and (b) Regional and piecewise PWVs for different numbers of transmitted plane waves in the cases of the soft and stiff phantom sections respectively. (c) and (d) Regional and piecewise r^2 values for different numbers of transmitted plane waves in the cases of the soft and the stiff phantom sections respectively. The asterisks indicate significant difference compared to the single plane wave case. (e) and (f) Expected SNR_{vPWI} curves for different numbers of transmitted plane waves. In the cases of the soft and the stiff phantom sections respectively (g) and (h) show mean SNR_{vPWI} for different number of transmitted plane waves in the cases of the soft and stiff phantom sections respectively. Asterisks indicate significant difference and the horizontal lines indicate the groups between which the corresponding level of significance was found (*: $p \leqslant 0.05$, **: $p \leqslant 0.01$, ***: $p \leqslant 0.001$).

measured regional and mean piecewise PWVs were validated against the aforementioned static PWVs. Furthermore, agreement was found between the mean piecewise PWVs and the regional PWV, an expected result given the homogeneity of each phantom section.

Increasing the number of plane waves showed an improvement in the performance of PWI, namely there were increases in both the r^2 coefficients and the$SNR_{v_{PWI}}$. However, in the case of the r^2 coefficients a lot of the increases were not significant due to either increased variability of the observed r^2 values or already ideal values. It has to be noted that the smallest piecewise segments (20 points) were found to be the most susceptible to noise, given the low number of markers involved in the linear fit, thus leading to some errors in the PWV estimation. The performance of pPWI with the smallest segments benefitted the greatest from increasing the number of compounded plane waves.

Another interesting finding in the case of the phantom study was that the r^2 coefficients were lower compared to the soft phantom case. This can be attributed in part to the lower v_{PWI} magnitudes in the case of the stiff phantom, which in turn led to the 50% downstroke markers being detected at lower v_{PWI} magnitudes compared to the soft phantom. Thus increased jitter affected the accurate detection of the 50% downstroke points [147].

In the case of the in vivo reproducibility study, good intra-subject reproducibility of the estimated PWVs was found for two cardiac cycles measured 1-3 days apart as seen in Figure 4.7. In all of the cases, the difference between the means of the PWVs estimated during each acquisition did not exceed $1m/s$. Similar findings have been reported in other noninvasive PWV studies using systems mentioned in Chapter I such as the Sphygmocor and the Complior [209], [210] PWV values in the first acquisition were found to be on average $3.97 \pm 1.21\ m/s$ and in

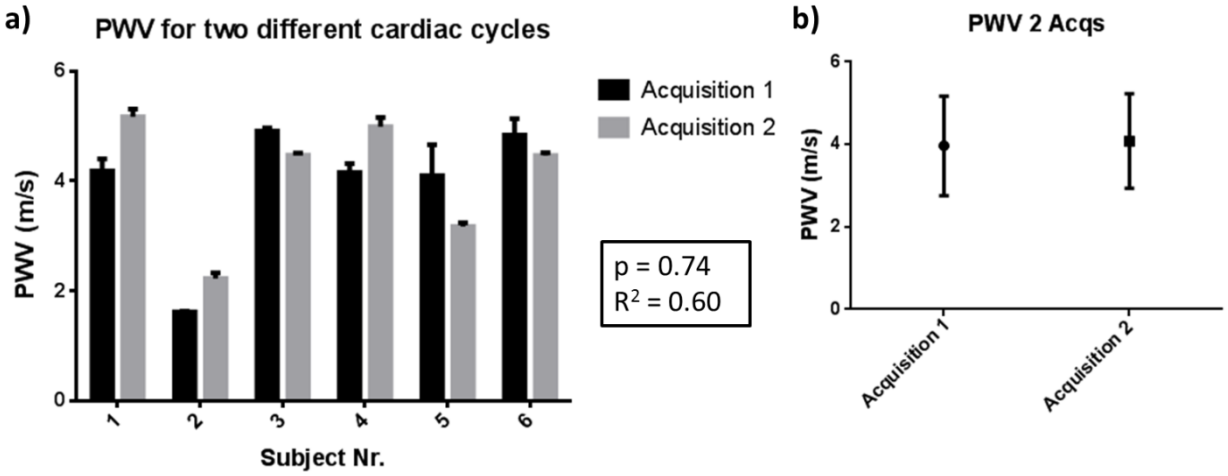

Figure 4.7: (a) PWVs of six (n = 6) healthy subjects measured over two different cardiac cycle acquisitions over the course of 1–3 d. (b) Mean PWVs of all subjects during the first and the second acquisition. The corresponding p-value from using paired t-test and the coefficient of determination R^2 are shown in the middle.

the second acquisition $4.08 \pm 1.15\ m/s$. Furthermore the estimated PWVs were found to be in good agreement with the ones present in literature (3-9 m/s [211]–[213]) as well as with the ones measured in a previous PWI study in human carotids in vivo using conventional ultrasound imaging [188].

In the case of the in vivo optimization study, firstly performance was assessed at different frame rates using single plane wave imaging. As observed in Figure 4.8 while the quality of the spatio-temporal plots remained similar at different frame rates, the layout of the 50% upstroke markers changes significantly. More specifically, for the highest frame rate (8333 Hz) there are no consecutive 50% upstroke markers occurring at the same time. However, this comes at the expense of higher noise, which while not greatly affecting the regional linear fit, has an effect on the smaller kernels. In the case of the lowest frame rate, multiple consecutive 50% upstroke markers lie on the same temporal line causing high TRM percentages and generating a

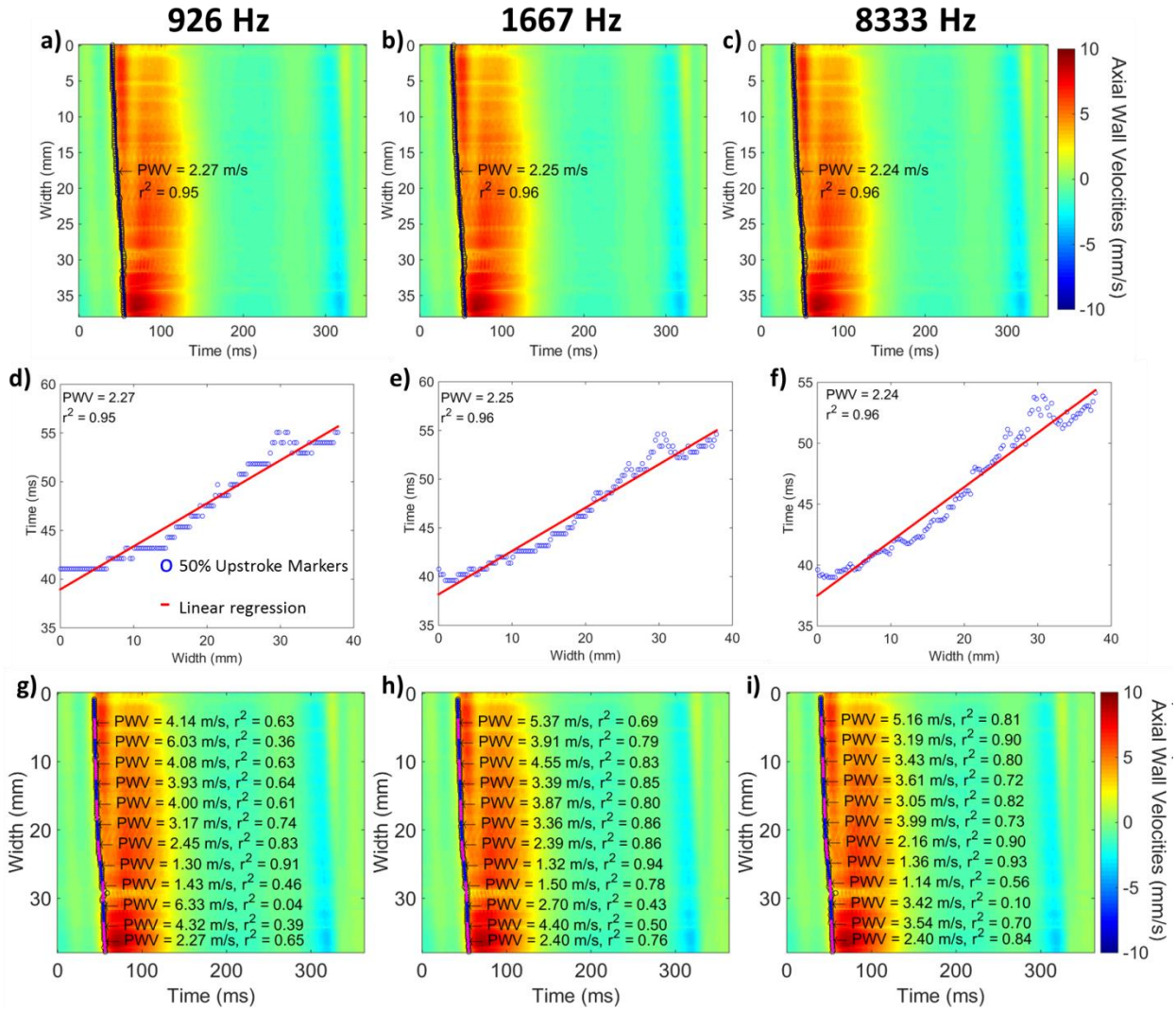

Figure 4.8: (a)–(c) Spatio-temporal plots and regional PWVs of a healthy subject corresponding to frame rates of 926 Hz, 1667 Hz and 8333 Hz respectively. (d)–(f) 50% upstroke markers and regional linear fit determining the regional PWV corresponding to frame rates of 926 Hz, 1667 Hz and 8333 Hz respectively. (g)–(i) Spatio-temporal plots and 20 point kernel piecewise PWVs corresponding to frame rates of 926 Hz, 1667 Hz and 8333 Hz respectively

staggered waveform and indicating that the frame rate is insufficient to capture the local pulse wave propagation. This has a negative effect on the piecewise r^2 values. Thus, the most beneficial frame rates were found to be in the range of 1667 – 2778 Hz. As shown in the appendix of [193] this finding was found to agree with the results produced by Huang et al. in [201] after accounting for the difference in spacing between the RF-data lines.

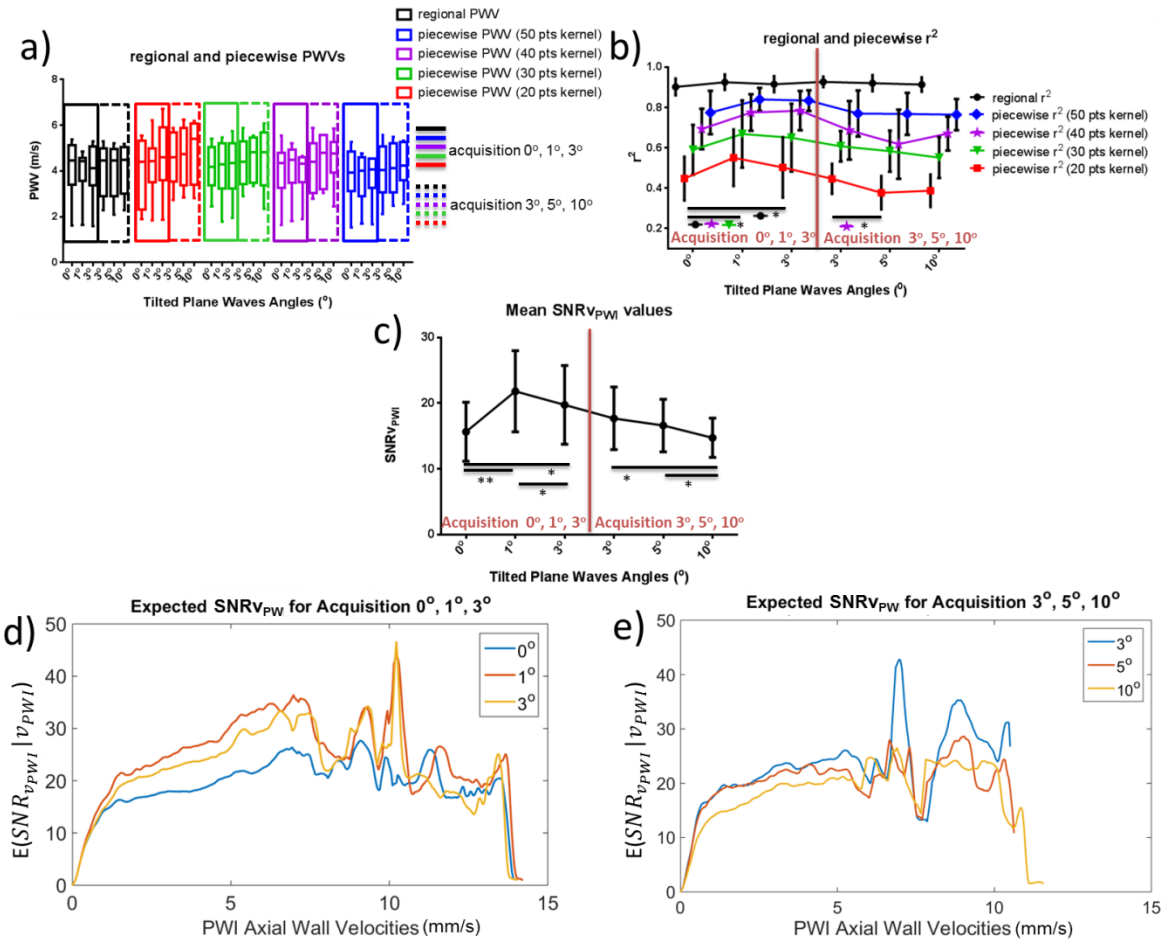

Figure 4.9: Statistical analysis of the in vivo plane wave transmission angle variation results. (a) Regional and piecewise PWVs for different transmission angles (b) regional and piecewise r^2 values for different transmission angles (c) mean SNR_{vPWI} for different transmission angles (d) and (e) expected SNR_{vPWI} curves for different transmission angles (acquisitions 0°, 1°, 3° and 3°, 5°, 10° respectively). Asterisks indicate significant difference and the horizontal lines indicate the groups between which the corresponding level of significance was found (*: $p \leqslant 0.05$, **: $p \leqslant 0.01$, ***: $p \leqslant 0.001$).

In the next section of the study, the performance of PWI was investigated for compounding plane waves transmitted at different angles. The statistical analysis of the estimated metrics in the case of varying transmission angles is shown in Figure 4.9. It was found that 1^o was the angle of the tilted plane waves that produced the best results in terms of both regional and piecewise r^2 values as well as $SNR_{v_{PWI}}$ values with significant increases in the mean $SNR_{v_{PWI}}$

compared to both 0^o and 3^o ($p \leq 0.01$ and $p \leq 0.05$ respectively). Similarly, in [146] it was found that increments of 1^o provided higher image SNR and CNR compared to the case of 3^o angle increments. Transmission angles beyond 3^odidn't produce any significant changes of the r^2, although the mean $SNR_{v_{PWI}}$ values decreased as the angle increased. A possible explanation for this is that as the angle increases, grating lobes start to appear in the field of view, thus impacting the quality of the RF-data.

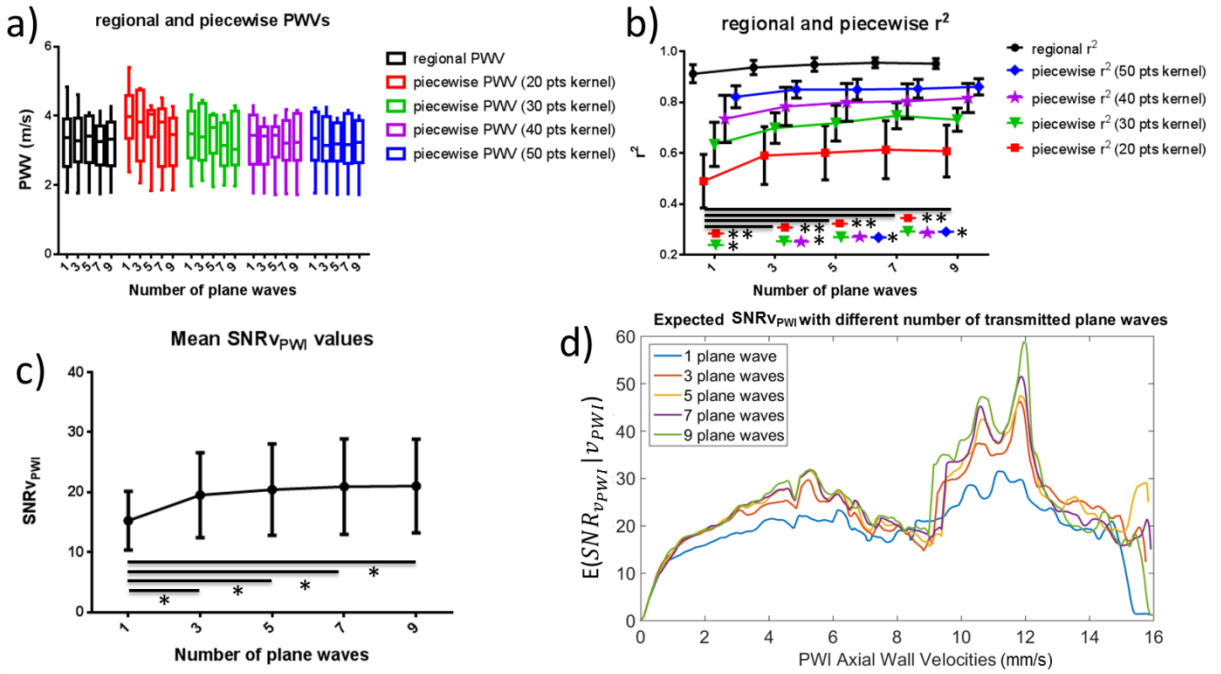

Figure 4.10: Statistical analysis of the in vivo number of transmitted plane waves variation results. (a) Regional and piecewise PWVs for different numbers of transmitted plane waves. (b) Regional and piecewise r^2 values for different numbers of transmitted plane waves. (c) Mean SNR_{vPWI} for different numbers of transmitted plane waves. (d) Expected SNR_{vPWI} curves for different numbers of transmitted plane waves. Asterisks indicate significant difference and the horizontal lines indicate the groups between which the corresponding level of significance was found (*: $p \leqslant 0.05$, **: $p \leqslant 0.01$, ***: $p \leqslant 0.001$).

Finally, the effects of increasing the number of plane waves were investigated. As seen from the statistical results in Figure 4.10, while the $SNR_{v_{PWI}}$ increase from 1 to 3 plane waves was significant ($p < 0.05$) every subsequent increase only produced slight $SNR_{v_{PWI}}$increases, thus indicating saturation. Similar observations were made in the case of the r^2 linear fit quality indicators. This saturation when using more than 3 plane waves was also observed in part in the phantom study and can be attributed to the motion that the imaged vessels undergo between angled plane wave acquisitions, thus resulting to reduced coherence and motion artifacts [214]. Consequently, $SNR_{v_{PWI}}$ gains are limited as the number of transmitted plane waves increases [194].

4.3. Conclusion

In this study a GPU-accelerated framework was developed in order to process the volume of data produced by high-frame rate coherent compounding acquisitions. A phantom study was performed to validate the results of compounded PWI. Reproducibility of the PWVs from compounding sequences was also verified *in vivo* among healthy volunteers. The most beneficial frame rates for tracking the pulse wave in vivo were found to be in the range of 1667 to 2778 Hz. Furthermore, 1^o was found to be the optimal plane wave transmission angle between tilted plane waves. Finally, most significant improvements in the performance of PWI were found with the transition from single plane wave imaging to 3-plane wave compounding acquisitions. Further increase in the number of plane waves produced smaller gains. Consequently, given the limitations in frame rate and the gains in tracking the pulse wave from

increasing the number of transmitted plane waves, acquisitions with 3 plane waves at 2778 Hz and 5 plane waves at 1667 Hz are considered to be optimal for imaging the pulse wave propagation and thus would be the most reliable for regular use in a clinical setting.

Chapter 5. Pulse Wave Velocity (PWV) and Compliance Estimation and Mapping Using Pulse Wave Imaging (PWI) in Healthy, Stenotic and Post-endarterectomy Carotid Arteries In Vivo

After optimization of the plane wave acquisition sequences presented in the previous chapter, the next step was to use them in conjunction with the local PWV estimation methods developed in Chapter III. Using the resulting modality, PWV and compliance mapping was performed in normal and pathological human carotid arteries *in vivo*. Compliance values were obtained with the Bramwell-Hill equation (4). Given that the aforementioned equation alleviates some of the assumptions involved in the Moens-Korteweg equation such as the thin-walled tube assumption and the perfectly circular cross-section of the vessel, it was deemed preferable to employ this equation to estimate the investigated vessel's compliance and generate compliance maps [1]. Another factor that advocated for this was the fact that arterial compliance has been previously investigated in longitudinal clinical studies [215] and although the values provided in those studies corresponded to an average value for the compliance of the whole investigated carotid, they can be used as a form of validation of the range of the PWI computed compliance values.

As mentioned in the introduction, atherosclerosis is known to alter the arterial wall elasticity. More specifically, it has been reported to promote arterial stiffening while also inducing reduced spatial homogeneity of arterial mechanical behavior [6], [54], [121]. However, lower stiffness has been reported in the case of vulnerable plaque components such as the large

necrotic core. Thus, investigating the local elasticity with PWI could prove beneficial for patient care and adverse outcome prevention.

Current clinical criteria for high-risk patients were described in the introduction. Highly stenotic patients often undergo carotid endarterectomy (CEA), an operation that has shown benefits in the case of symptomatic patients with a high degree of stenosis (>70%) [46], [47]. However, it has been reported that in 12-20% of the operated carotids, either residual stenosis (incomplete CEA) or recurrent stenosis appears already 3 months after the operation [216]. Additionally, it has been reported that within 5 years post-operation, even though mostly non-disabling, strokes do occur in approximately 10% of the patients. Hypothesizing that these outcomes are linked to the mechanical properties of the post-operated carotids, investigating the local wall stiffness using PWI may prove to provide some insight into the causes behind post-operation morbidity and complications as well as improve the assessment of CEA.

Consequently, in this study validation of the PWI compliance estimates and maps will be performed in silicone phantoms under dynamic conditions (i.e. while the phantom is connected to the peristaltic pump). Proof of feasibility and validation of compliance mapping will be shown in healthy subjects. The technique will be then tested in the carotid arteries of atherosclerotic patients and in the case of patients undergoing CEA; its results will be compared with histological findings. Finally, stiffness and spatial homogeneity of post-CEA subjects will be investigated and compared with diseased subjects. Findings of this study have been presented

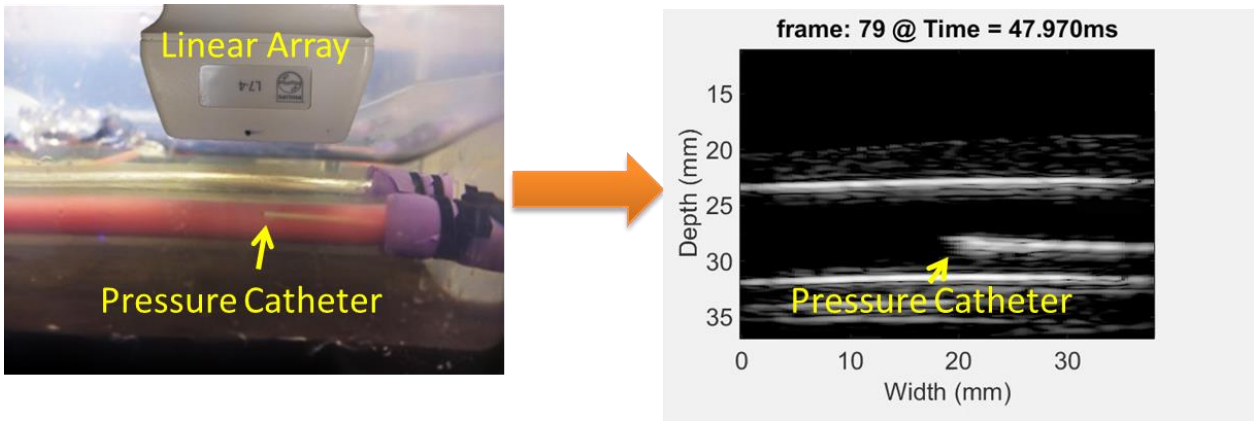

Figure 5.1: Co-localization of the pressure catheter and the linear array trasducer within the lumen of the phantom.

at the 15th International Tissue Elasticity Conference, 2016 and at the 2017 International Ultrasonics Symposium [217].

5.1. Materials and methods

5.1.1. Phantom study

Silicone gel was used to construct a phantom with a soft and a stiff segment along the longitudinal axis, embedded within a soft silicone surrounding material as previously described in Chapter IV. This phantom was then used to perform dynamic testing and thus validate plane wave compounding PWI under dynamic conditions.

The phantom was connected to a peristaltic pump generating pulse waves at a frequency of approximately 2Hz. The setup was scanned using a 5 MHz linear array (L7-4, ATL Ultrasound, Bothell, WA, USA) connected to a research scanner (Verasonics Inc., Redmond, WA, USA). A coherent compounding sequence developed in Chapter IV was used, with 5 plane waves at 1667 Hz to image the pulse wave propagation. Synchronized intraluminal pressure

measurements were made by inserting a pressure catheter inside the phantom's lumen. The catheter was controlled by a pressure control unit (PCU-2000, Milllar, Houston, TX, USA) and the pressure waveforms were obtained by a data acquisition card at a high sampling rate of 10 kHz (CompuScope 14200, Gage Applied Technologies, Lachine, QC, Canada). The catheter pressure acquisition was triggered by the ultrasound acquisition in order to obtain simultaneous measurements. Care was taken to place the catheter tip within the ultrasound field of view (Figure 5.1) and thus acquire co-localized PWI and pressure measurements. Consequently, by simultaneously acquiring ultrasonic and pressure data at the same location, the pressure-area relationship of the vessel was successfully recovered and used to compute a compliance value (C_{dyn}) that was subsequently used to validate the PWI compliance values (C_{PWI}).

5.1.2. *In vivo* study

For the *in vivo study*, the common carotids of nine healthy volunteers (22-35 y.o., mean 27.3 y.o., n = 9) were scanned. Their right common carotids were scanned three times with the subject and transducer resetting after each scan. Furthermore, the diseased carotid arteries of ten atherosclerotic patients were scanned (61-86 y.o., mean 73.7 y.o., n = 10). In five of those cases, a plaque sample was recovered after CEA. Finally, the operated carotids of seven post-operation atherosclerotic patients, approximately 1 month after operation (64-77y.o., mean 71.85 y.o., n = 7).

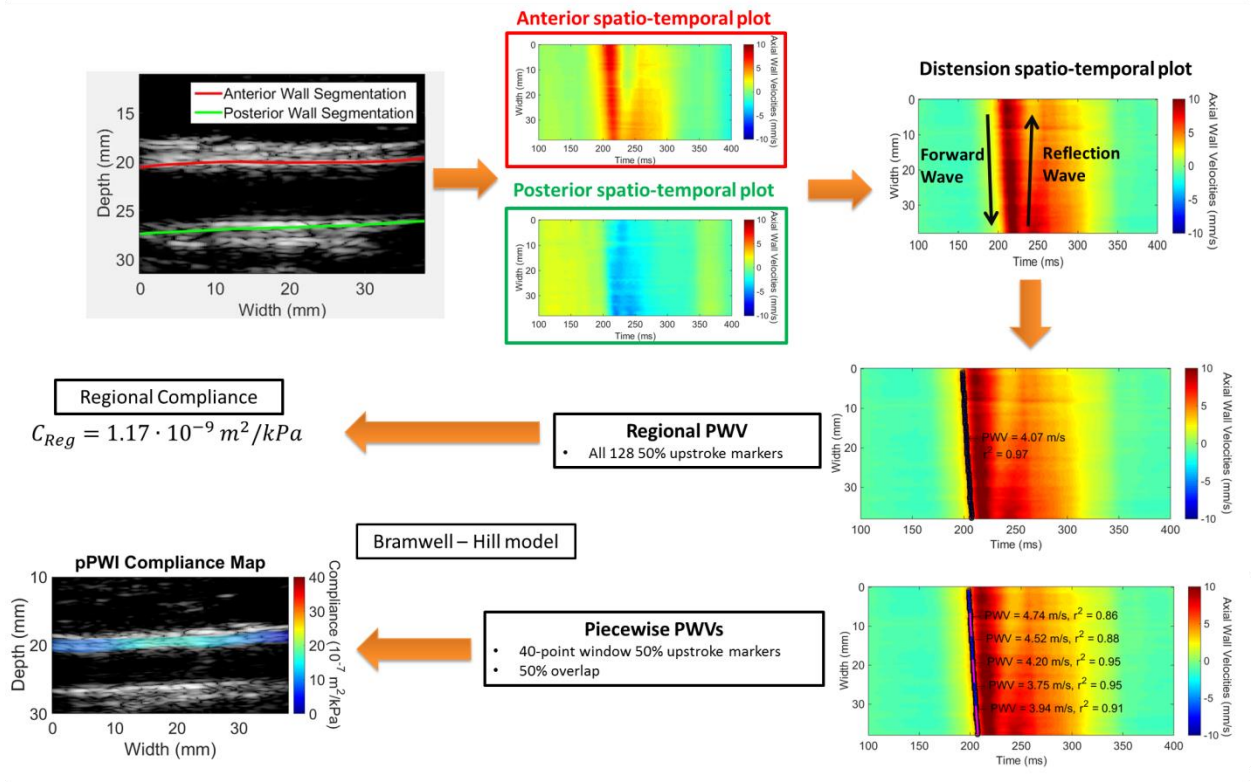

Figure 5.2: Piecewise PWV and compliance estimation and mapping methodology

Imaging was performed using the Verasonics research scanner. In addition to the previously used 5 MHz linear transducer, an 18.5 MHz L22-14vLF transducer (Verasonics Inc, Bothell, WA, USA) was used (67% bandwidth, 0.10 mm pitch, elevation focus at 20 mm) to perform high-frequency scanning of the diseased arteries and thus obtain a higher resolution image of the plaques. This allowed for significantly higher axial resolution (~0.1mm) compared to ultrasonic probes that are generally used for carotid scanning in most large clinical studies investigating the diseased carotid intima media thickness (IMT) [151], [218]. Thus, it is expected to provide the atherosclerotic plaque morphology, which has been reported to be linked to the risk of plaque rupture [219], [220], in greater detail. Furthermore, higher-resolution PWV and compliance maps can be obtained and compared to regular resolution PWI results, thus proving the repeatability of the technique with a different transducer.

Plane wave compounding sequences of either 5 or 3 plane waves were employed at 1667 or 2773 Hz, respectively.

5.1.3. PWI post-processing

The PWI post-processing employed in this study was the one developed in Chapter IV. More specifically, the acquired channel data were beamformed and subsequently the axial wall velocities (v_{PWI}) were estimated in a GPU-enhanced framework. Spatio-temporal maps depicting the v_{PWI} variation over time at each lateral position were then generated for each of the anterior and posterior wall segmentations. Finally, to eliminate any rigid motion and thus make PWV estimation more robust, the two spatio-temporal maps were subtracted and a distension spatio-temporal map was generated.

Subsequently, the 50% upstroke points were estimated for the distension v_{PWI} waveforms at each lateral position. Linear regression was performed on the spatio-temporal variation of the 50% upstroke points at each lateral position along the imaged segment to obtain the slope as the regional PWV and the coefficient of determination r^2 as an index of propagation uniformity. In order to acquire piecewise PWV measurements, the 50% upstroke points were divided in 50% overlapping kernels of 40 points. Linear regressions were performed for each piece (sub-region), thereby providing a piecewise PWV value along with the corresponding coefficient of determination (r^2).

The anterior and posterior wall segmentations were then used to estimate the diameter of the vessel at each lateral position. It should be noted that the diameter estimates were corrected by the slope of the arterial centerline at each lateral position. Mean diameter for all of the lateral positions and regional PWV were used as inputs to the Bramwell-Hill equation (4) and the regional compliance of the imaged vessel was estimated (C_{PWI}). Finally, the piecewise compliances were estimated by using as inputs the piecewise PWV and the mean diameter of each sub-region of the vessel. Piecewise PWVs and compliance values were then color-coded and overlaid onto the B-mode, thus generating piecewise PWV and Compliance maps of the imaged vessel. An overview of this methodology is shown in Figure 5.2.

5.2. Results and discussion

Diameter and intraluminal pressure in the soft and the stiff segments of the phantom were plotted in the same graph as shown in Figure 5.3. It can be seen that they are synchronous and that also they have a similar shape, an expected result given that diameter is linearly linked to local pressure waveform [6], [169], [221]. This also corroborates previous studies *in vivo* where it has been shown *in vivo* that tonometric pressure waveforms can be obtained by linearly scaling diameter waveforms derived from echo-tracking [221], [222]. Figure 5.4a) shows the pressure-area relationship of each phantom plotted on the same plot. Both relationships were found to be linear and to show no hysteresis indicating that the viscous behavior of the phantom was minimal [223]. It can be seen that the slope of the stiff phantom segment is lower indicating a lower compliance and thus confirming the higher stiffness of that vessel segment.

Figure 5.4b) shows that the PWI-derived regional and piecewise compliances are in agreement with the dynamic testing compliances. Low standard deviation of the piecewise measurements along the vessel indicated high homogeneity, a finding that was expected given that the same concentration of silicone was used to construct each section and that vessel radius and wall thickness were the same along the vessel.

In the case of the healthy human subjects compliance maps indicated homogeneity of arterial

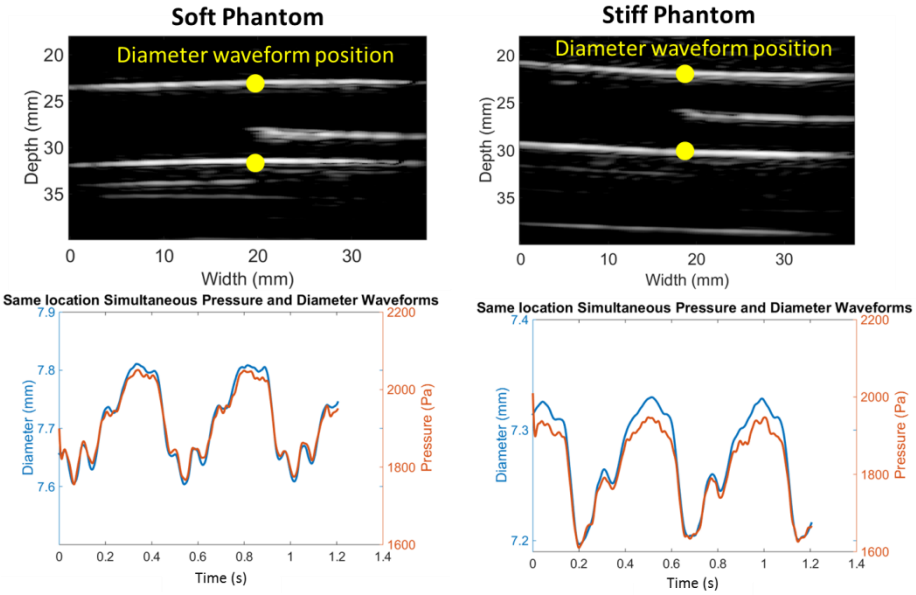

Figure 5.3: Simultaneous tracking of diameter waveform (blue) and intraluminal pressure (orange) measured synchronously at approximately the same location for the soft phantom segment (left) and the stiff phantom segment (right). The catheter tip is shown in both B-mode images within the lumen of the phantom for reference.

wall (Figure 5.5). It should be noted however that a small increase in compliance was found close to the bifurcation. While this spatial distribution of compliance along the healthy common carotid requires independent measurements to be confirmed, in another study by Reneman et al. [41], the arterial wall close to the carotid bulb was found to be more distensible compared to the common carotid in healthy young subjects. This result is in agreement with the higher

compliance found closer to the bifurcation. Additionally, as also seen in Figure 5.5, the compliance values found in healthy subjects were confirmed against arterial compliance values estimated with other methods at single points in the carotid artery.

In the case of the atherosclerotic patients, increased variability of the PWVs and the

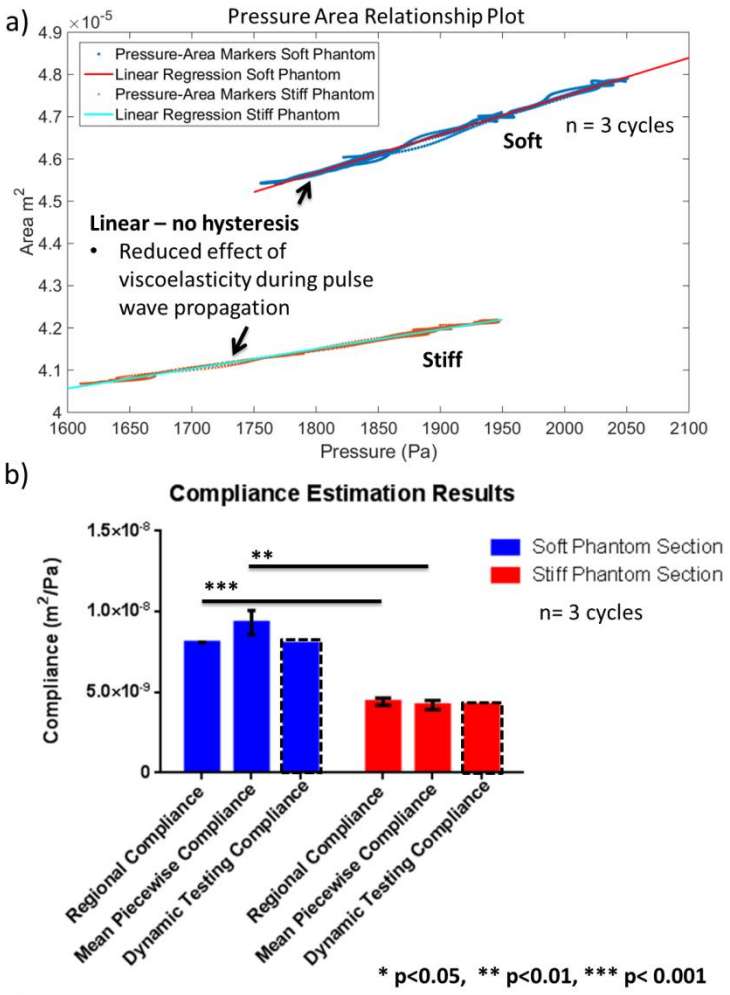

Figure 5.4: a) Pressure area relationship for each phantom section and corresponding linear regression yielding compliance. It can be seen that there is no hysteresis (i.e. pressure wave and distension wave occurring simultaneously with no lag) and that soft section yields higher compliance (dA/dP) compared to the stiff section. b) Statistical results from three peristaltic pump cycles. PWI-derived regional and mean piecewise compliance are compared with dynamic testing compliance.

compliances was found, thus indicating fragmentation of the arterial wall along with increased inhomogeneity. Figure 5.6 shows the case of a CEA patient, where PWI findings are compared to the histological findings of the sample recovered from approximately the same location of the diseased carotid. Increased v_{PWI} are seen at the section of the wall directly preceding the plaque. In agreement with this finding, increased compliance values were found at that

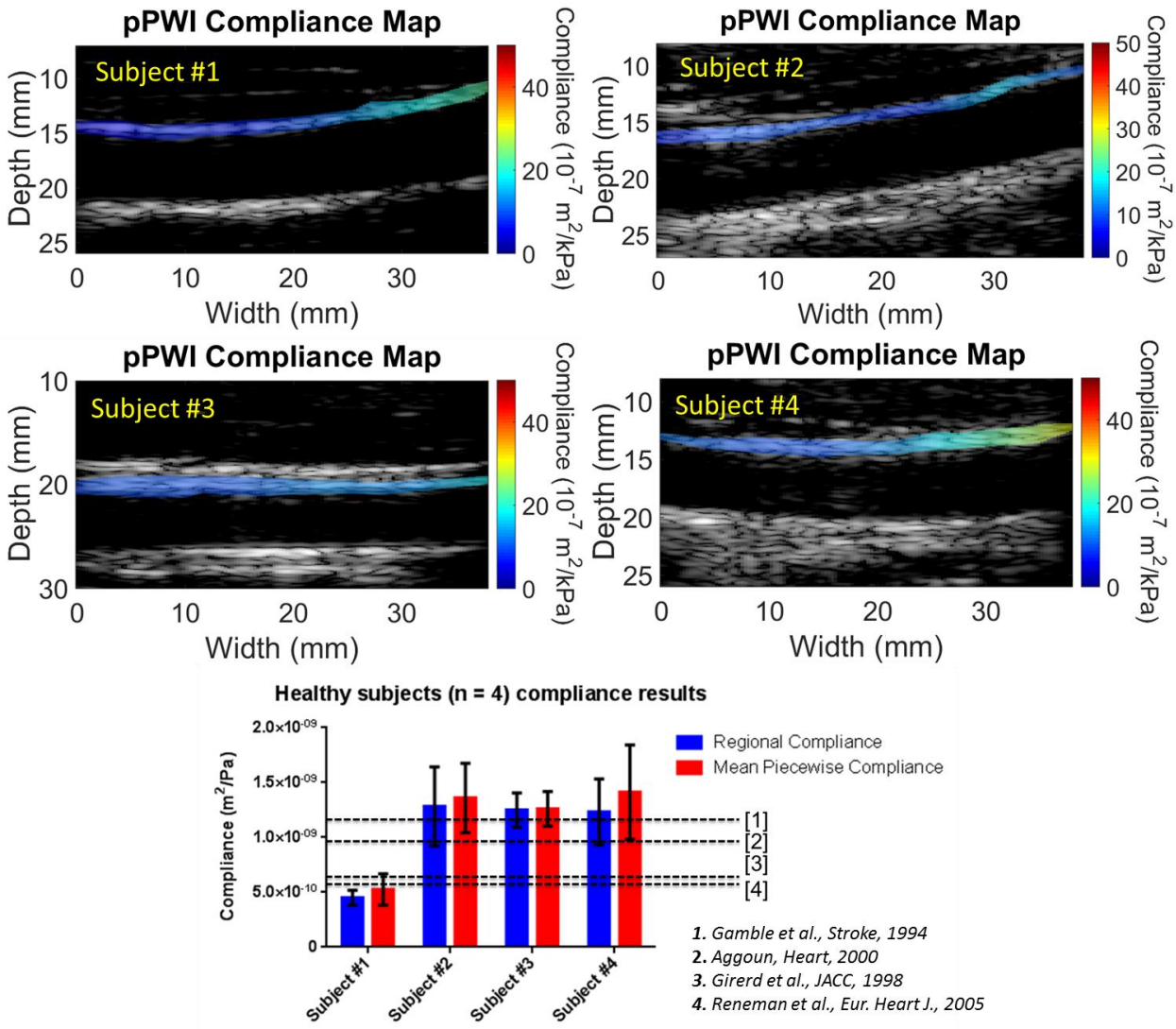

Figure 5.5: Compliance maps in four healthy subjects and the corresponding statistics of regional and mean piecewise compliances for these subjects. In the bar plot dashed lines indicate mean carotid compliances estimated in other clinical studies. Regional and mean piecewise compliances in the four healthy subjects were averaged over 3 cardiac cycles.

segment as seen from the compliance map in Figure 5.6b. Additionally, elastographic studies have shown large deformations at the tissues surrounding calcified plaques [224]. It has been hypothesized that this is due to stress repartition from the stiff plaque and high energy transfer to the surrounding tissue. This finding could potentially provide information on plaque rupture as plaque shoulder is a common site of rupture (site of rupture for approximately 60% of cases [225], [226])

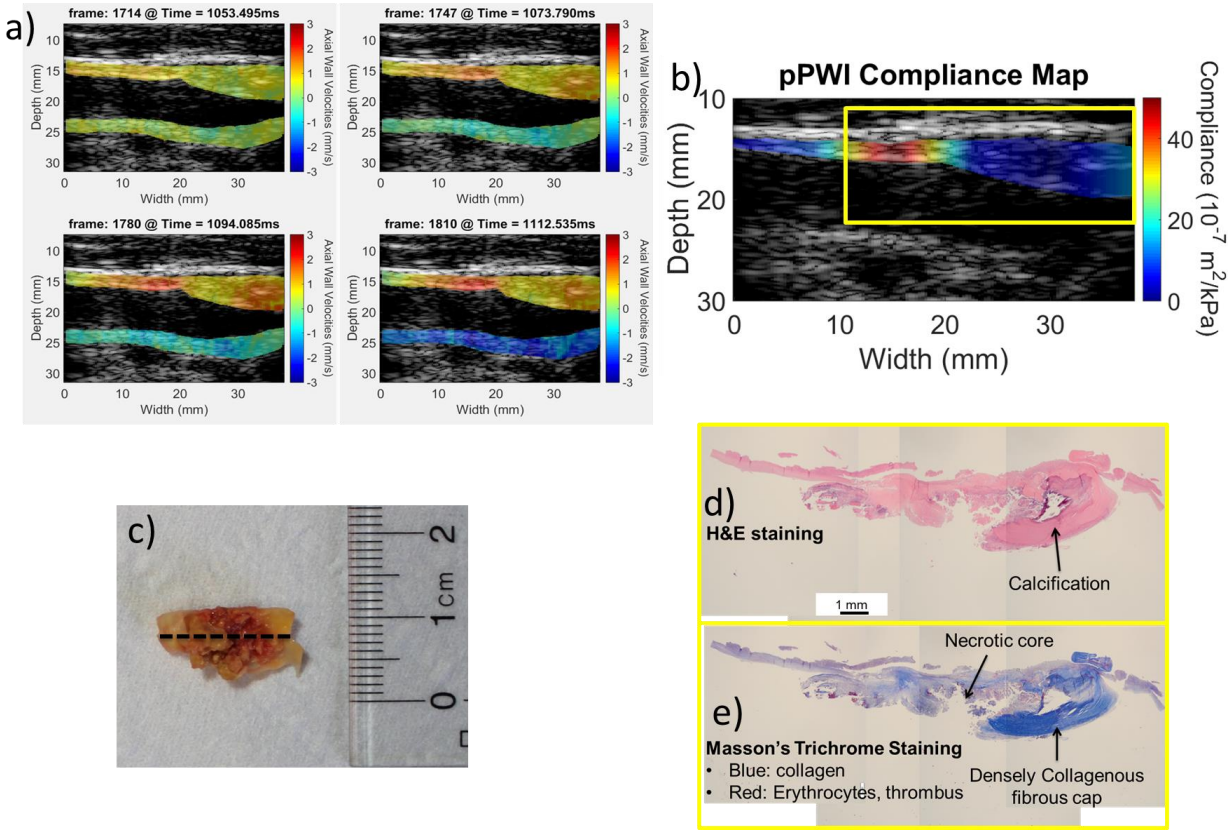

Figure 5.6: a) v_{PWI} images that indicate the propagation of the pulse wave (red indicates motion towards the transducer, top and blue indicates motion away from the transducer, bottom). b) pPWI compliance map. The yellow rectangle indicates the approximate location from where the plaque sample was taken from. c) The recovered plaque sample. Dashed line indicates the section along which the histological slice was taken. d) H&E staining of the plaque sample and e) Masson's Trichrome Staining of the plaque

Gross pathology of the recovered specimen confirmed that increased calcification was present at the plaque site with several focally hard spots. Histology with H&E staining confirmed this and also Masson's Trichrome staining revealed a densely collagenous fibrous cap that also contributes to the increased stiffness of the plaque. Consequently, the histological findings were in good agreement with the PWI compliance map partially validating the PWI results. This finding could potentially provide information on plaque rupture as plaque shoulder is a common site of rupture (site of rupture for approximately 60% of cases [225], [226])

Another example of a CEA patient is shown in Figure 5.7. This patient was scanned with the high-frequency probe (18.5 MHz) in order to acquire a higher resolution view of the plaque. The plaque was found to be more compliant compared to the surrounding wall. This was confirmed in part by the acquired specimen shown in Figure 5.7c with the increased presence of lipids and erythrocytes indicating plaque inflammation. Additionally, Masson's trichrome stain (Figure 5.7e) indicated the decreased presence of collagen, a component of plaque stabilization and increased stiffness within the plaque.

Subsequently, PWI was performed in two atherosclerotic subjects with both regular (5MHz) and high-frequency (18.5 MHz) scanning. The results were compared in Figure 5.8 and Figure 5.9.

In Figure 5.8 the field of view of the higher resolution B-mode image is shown overlaid onto the regular resolution B-mode. The plaque in both images appears to be echogenic but also causes some shadowing at some locations on the posterior wall. This indicates the presence of a small

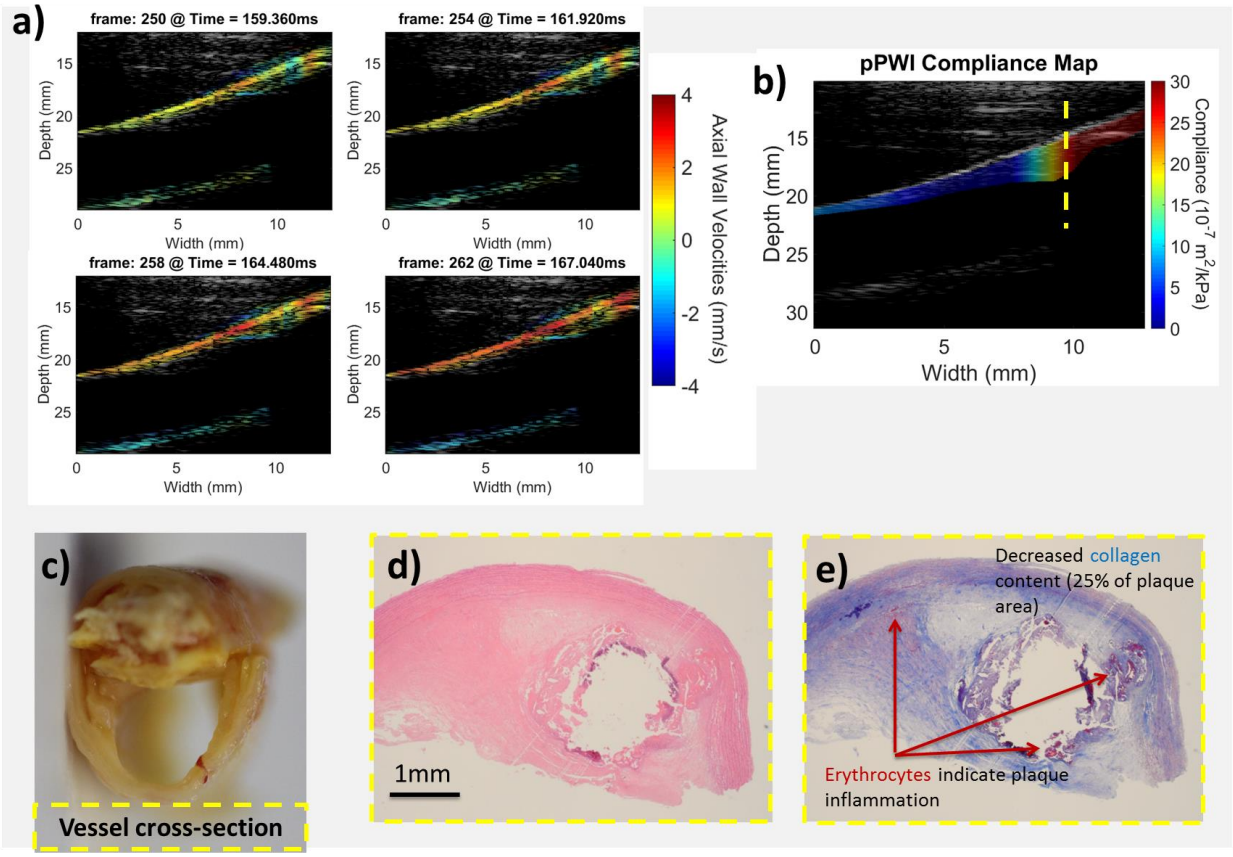

Figure 5.7: a) PWI axial wall velocity images that indicate the propagation of the pulse wave (red indicates motion towards the transducer, top and blue indicates motion away from the transducer, bottom). b) pPWI compliance map. The yellow perforated line indicates the approximate location from where the plaque cross-section sample was taken from. c) The recovered plaque sample. Dashed line indicates the section along which the histological slice was taken. d) H&E staining of the plaque sample and e) Masson's Trichrome Staining of the plaque

degree of calcification in the plaque [227]. Agreement was found between the corresponding distension spatio-temporal plots as seen in Figure 5.8b. The morphologies of both the main wave and the dicrotic notch are similar, while in both cases there is approximately total reflection of the pulse wave at the far end of the plaque as indicated by the perforated black lines. Similarly, good agreement was found in the spatial distribution and magnitude of the

piecewise PWV and compliance values. Low compliance values at the plaque site constituted a finding that indicated the presence of calcifications, as corroborated by the acoustic shadowing.

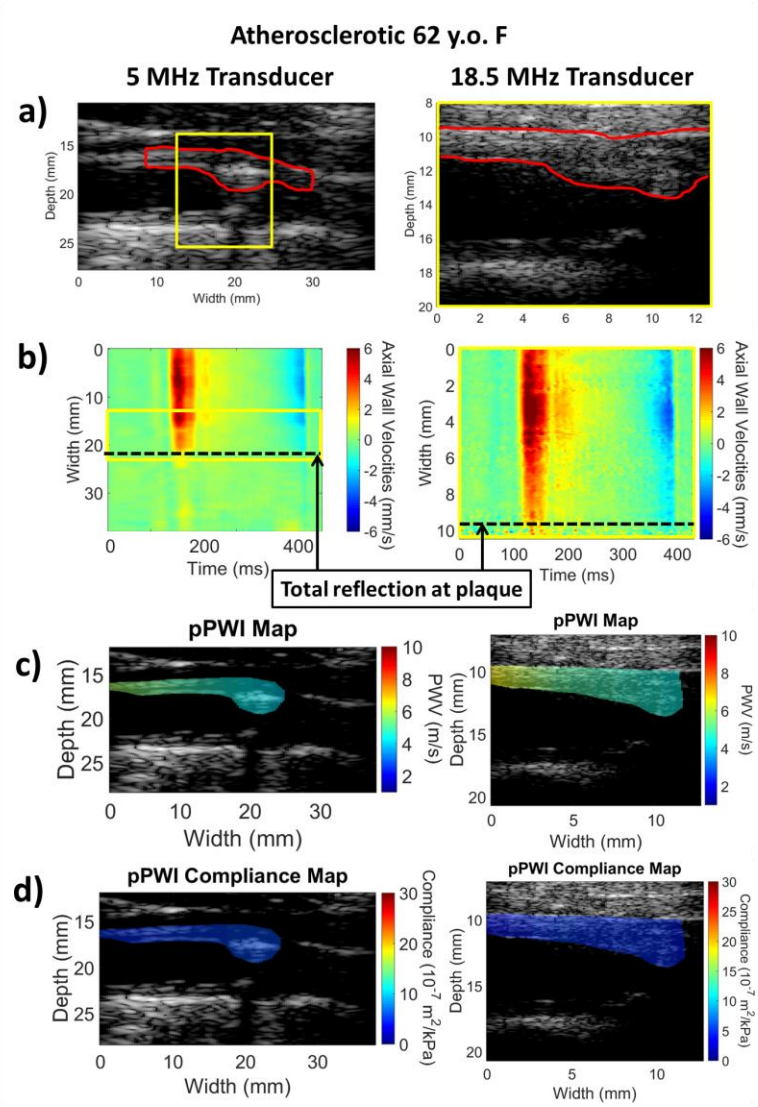

Figure 5.8: Comparison of results using the standard frequency (L7-4, 5 MHz) and the high-frequency (L22-14vLF, 18.5 MHz) probe. a) B-mode comparison. The plaque region is outlined in both cases (red line) and the field of view of the high-frequency probe is indicated onto the B-mode of the regular frequency probe (yellow rectangle). The heart is on the left side of the image while the brain is on the right side. b) spatio-temporal plots for both regular and high-frequency scans. Total reflection can be observed at the right side of the plaque in both scans (perforated black line). c), c) piecewise PWV and compliance maps of the imaged artery with both scans. Similar results can be observed in both cases.

Figure 5.9 shows another example of comparison between the results of regular and high-frequency PWI. Both scans were performed on a 78 y.o. female patient immediately after her admission into the hospital for stroke, alluding to the presence of vulnerable plaque. As seen from Figure 5.9a the high-frequency transducer images the plaque on the anterior wall with increased resolution. The cap of the plaque is better delineated while the necrotic core appears to be echolucent, an indication that the plaque has a lipid-rich core [228]. Figure 5.9b and c show v_{PWI} frames at regular and high frequency, respectively. Similar patterns can be observed with the plaque showing relatively high v_{PWI}, indicating low stiffness. The anterior wall right after the plaque showed decreased v_{PWI} in both cases a finding that is associated with partial reflection of the pulse wave at the plaque site. Finally, Figure 5.9d shows the piecewise PWV maps created with both probes. In both cases the atherosclerotic plaque shows relatively low piecewise PWV while the arterial region immediately after the plaque shows an increase in PWV, in agreement with the reduced v_{PWI}. A benefit of the high-frequency probe can be observed in this case as it provides a higher resolution PWV map providing more localized piecewise PWV values and thus better contrast between the plaque and the arterial segment immediately after the plaque.

Figure 5.10 shows the results for the case of a symptomatic atherosclerotic patient (77 y.o., F) before (left) and after (right) a CEA procedure. Scan alignment was ensured by scanning over the surgeon's incision marking before the operation and scanning right over the patient's stitches after the operation. Figure 5.10a shows v_{PWI} frames at peak systole. In the case of the diseased artery, complex motion patterns can be observed with variation of both the

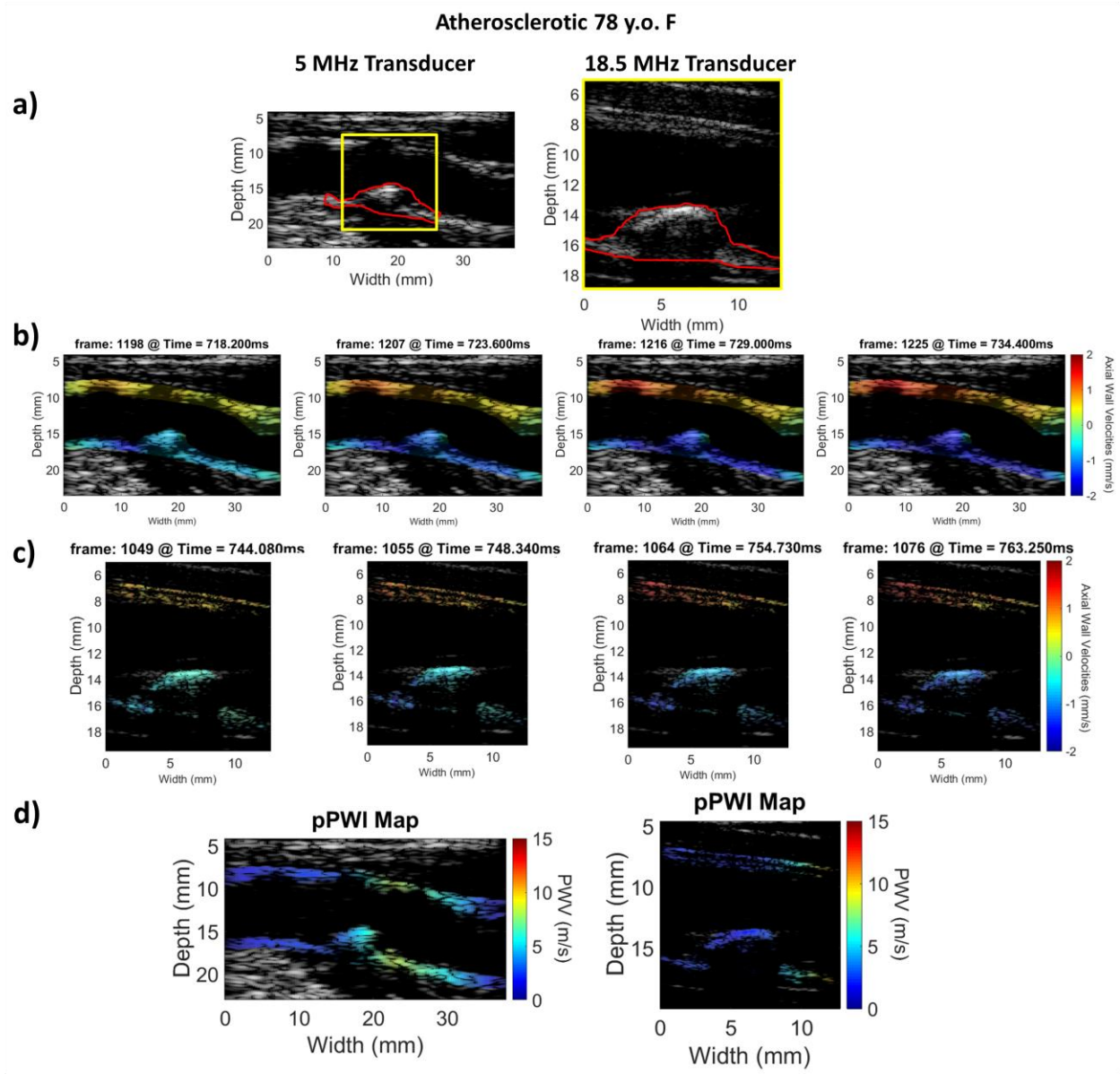

Figure 5.9: Comparison of results using the standard frequency (L7-4, 5 MHz) and the high-frequency (L22-14vLF, 18.5 MHz) probe. a) B-mode comparison. The plaque region is outlined in both cases (red line) and the field of view of the high-frequency probe is indicated onto the B-mode of the regular frequency probe (yellow rectangle). The heart is on the left side of the image while the brain is on the right side. b), c) PWI axial wall velocities overlaid onto the B-mode indicating the pulse wave propagation in the 5 MHz and 18.5 MHz probe cases, respectively d) piecewise PWV maps of the imaged artery with both scans. Similar results can be observed in both cases.

magnitude and the direction of the v_{PWI}. On the contrary, in the case of the operated carotid, uniformity of the v_{PWI}along the arterial wall has been mostly restored. Similar observations can

be made in the case of the spatio-temporal plot with the v_{PWI} acquiring similar peak values along the artery (Figure 5.10b). Additionally, the r^2 quality indicator denotes increased nonlinearity in the propagation of the pulse wave prior to the operation, while linear propagation is mostly restored afterwards. Finally, in both the piecewise PWV and compliance maps, the plaque shows decreased stiffness, a characteristic that is linked to vulnerable plaques. This can be partly supported by the recovered plaque specimen. Gross pathology showed increased plaque ulceration (redness), while histological examination with H&E and Mason's trichrome stains (Figure 5.10f and g, respectively) showed a large complex plaque with a necrotic core and reduced presence of collagen, signs of a vulnerable plaque. This was further supported by the presence of symptoms in the patient and confirmed by the operative notes reporting the presence of thrombus, as also seen in histology (Figure 5.10g). As seen from the PWV and compliance maps, CEA was found to be beneficial, restoring homogeneity of the piecewise PWV and compliance values along the artery, thus restoring the spatial stiffness homogeneity.

It should be noted that both Figure 5.7 and Figure 5.10 indicate that higher compliance may be associated with plaques whose gross pathology and histology exhibit characteristics of a vulnerable plaque (increased complexity, inflammation, reduced collagen, necrotic core). Thus, they show the potential of PWV and compliance mapping as a risk assessment tool for atherosclerotic patients.

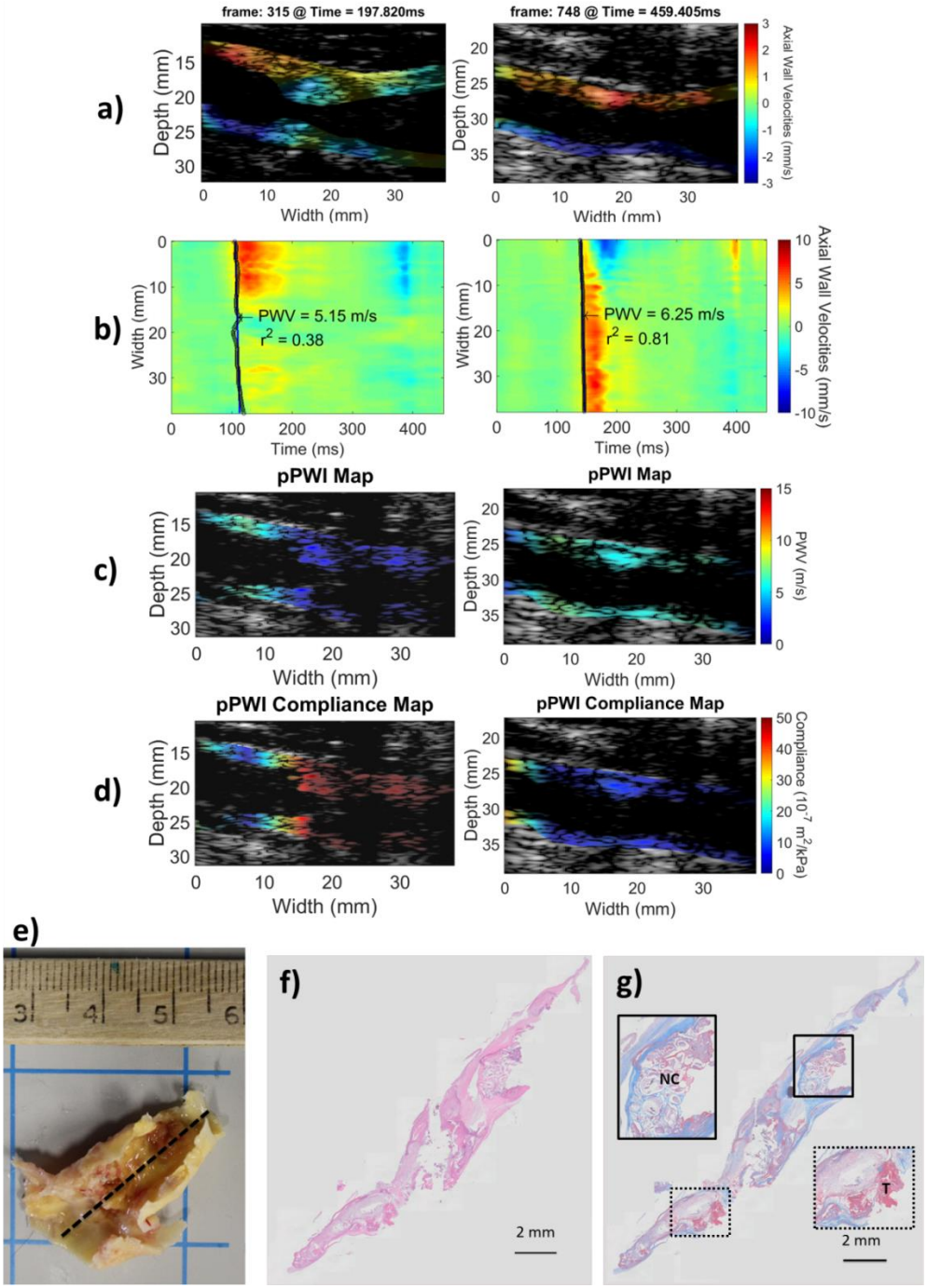

Figure 5.10: Comparison of results for an atherosclerotic patient before (left) and after (right) a CEA procedure. a) PWI axial wall velocity frames at peak systole. b) Comparison of spatio-temporal maps. c), d) piecewise PWV and compliance maps, respectively. e) The recovered plaque specimen. f) H&E staining of a longitudinal slice along the plaque. g) Masson's trichrome staining of a longitudinal slice along the plaque, necrotic core (NC, solid line) and thrombus (T, perforated line) are indicated and shown at a higher magnification.

Overall, the PWV was found to significantly increase (p≤0.05) for the atherosclerotic cases ($8.23 \pm 3.71\ m/s$, n = 10) compared to the healthy subjects ($4.49 \pm 1.00\ m/s$, n = 9). This is in agreement with large clinical studies investigating the effect of atherosclerosis on global PWV [54], [229]. A small drop in PWV was found in post-CEA patients ($7.24 \pm 2.67\ m/s$, n = 7) indicating that endarterectomy may have a beneficial effect by bringing the PWV of the repaired artery closer to normal physiological limits. Furthermore, two spatial homogeneity metrics were investigated, namely, the coefficient of variation of the distension v_{PWI} ($CV_{v_{PWI}}$) along the lateral positions of the imaged artery and the r^2 coefficient of the pulse wave propagation linearity. As expected, the $CV_{v_{PWI}}$ was found to be significantly higher in atherosclerotic subjects compared to the healthy subjects ($p \leq 0.0001$). While the $CV_{v_{PWI}}$ was found to decrease in the case of post-operation patients, it still remained significantly, higher compared to the normal subjects. This could be attributed to residual stenosis remaining after the operation and also to the age difference between the healthy subjects and the patients. However, it should be further investigated as it may provide a marker of how well post-CEA carotids recover their stiffness homogeneity after the procedure. Additionally, given that distension of the arterial wall is linked to the intraluminal pressure, this marker could be used to assess changes in intraluminal pressure at different sites of the artery.

Similar observations can be made in the case of the r^2 indicator. r^2 was found to be significantly higher in the case of healthy subjects (0.92 ± 0.05, n = 9) compared to both the atherosclerotic patients (0.54 ± 0.18, n = 10, $p \leq 0.0001$) and the post-operation patients (0.72 ± 0.17, n = 7, $p \leq 0.05$). An interesting finding is that the increase of r^2 in the post-operation patients compared

to the atherosclerotic ones was found to be on the verge of significance ($p \approx 0.05$), indicating that linearity of pulse wave propagation is partly restored. This was also indicated in Figure 5.10 in the same patient. Thus, longitudinal tracking of the same patients before and after the CEA procedure will provide more insight to its restorative effect to the pulse wave propagation linearity. The aforementioned statistical results are summarized in Figure 5.11.

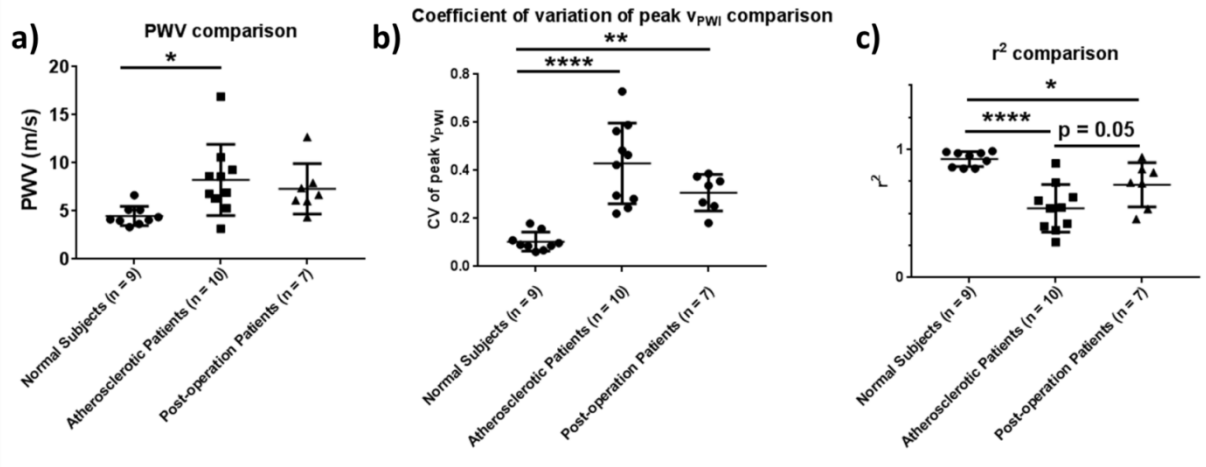

Figure 5.11: Statistical results for the normal subjects, atherosclerotic and post-operation patients. a) Comparison of the estimated PWV. b) Comparison of the coefficient of variation of the peak distension axial wall velocities (v_{PWI}) along the imaged vessel. c) Comparison of the pulse wave propagation linearity indicator (r^2). (* p≤0.05, ** p≤0.01, **** p≤0.0001).

5.3. Conclusions and future work

In this study, PWV and compliance mapping using PWI were introduced and validated in silicone phantoms under dynamic conditions. The developed methodology was then used in the clinic in atherosclerotic and post-operation patients. In the case of atherosclerotic subjects, high-frequency micro-scanning at high frame rates was also introduced for the scanning of atherosclerosis *in vivo*. Its results were in agreement with regular PWI results, while increasing spatial resolution. Furthermore, in atherosclerotic patients undergoing CEA compliance and

PWV mapping were validated against the recovered plaque specimens indicating PWI's utility as a risk assessment tool. Finally, PWI was able to differentiate between normal and diseased subjects, while comparison of stiffness and spatial homogeneity of the mechanical properties between atherosclerotic and post-CEA patients showed improvements in the case of the post-CEA patients. Thus, PWI could be potentially used to further investigate the patient-specific benefits of CEA carotid repair.

Ongoing work includes increasing both the patient population and the number of acquired plaque specimens. Thus, linking the local PWI findings with histology will provide increased support for the utility of PWI. Another ongoing long-term study towards the same aim is associating stiffness and spatial homogeneity measurements with patient outcomes and mortality. Longitudinal studies involving patients before and after CEA will evaluate and establish the restorative effects of the procedure for the diseased vessel's mechanical properties as well serve as a diagnostic tool for significant residual stenosis. Finally, one limitation of this study that needs to be addressed is the scanning of age-matched controls. This way, the effects of age on arterial PWV and compliance will be fully decoupled from those of atherosclerosis [92].

Chapter 6. **Feasibility and Validation of 4-D Pulse Wave Imaging in Phantoms and In Vivo**

As presented in this thesis, PWI technique images the pulse wave propagation in two dimensional, long-axis views of the arteries. However, using 2-D images to characterize a 3-D phenomenon has some limitations. More specifically, it is assumed that the propagation of the pulse wave is parallel to the imaging plane, an assumption that may lead to erroneous tracking of the pulse wave and ultimately PWV estimation, especially given the high level of tortuosity and branching of the arteries. Furthermore, given two-dimensional, longitudinal views of the arteries, isotropy of both the arterial wall displacements and the pulse wave propagation around the axis of the vessel is assumed. While this assumption could be acceptable in the case of homogeneous disease-free arterial walls, in atherosclerotic or aneurysmal walls, this may not be the case. Moreover, with a 2-D image of the artery, a significant and/or critical segment of the pathological tissue might remain outside of the imaging plane, thus impairing diagnosis

Developing a three-dimensional imaging platform for PWI would alleviate the aforementioned limitations, with comprehensive views of the arterial walls and objective estimation of the full PWV vector, unaffected by inter- or intra-observer variability. Given the previously mentioned value of PWV in clinical research as an independent predictor of all-cause cardiovascular mortality and atherosclerotic burden its accurate and objective estimation may provide a useful

metric in the clinic. Certain challenges of conventional three-dimensional ultrasound imaging, such as increased computational cost and decreased frame-rates [230] have been recently addressed. More specifically, the parallel implementation of processing algorithms using graphical processing units (GPUs) as well as the use of efficient 3-D viewing software has rendered the manipulation of large 3-D datasets easier.

Furthermore, recently introduced 3-D high frame rate imaging using plane and diverging waves emitted by 2-D transducer arrays has led to the acquisition of full 3-D volumes at kHz frame rates [231]. This imaging method is an extension of the 2-D plane wave imaging, where all of the elements of a 2-D array transducer are simultaneously fired in order to insonify the full volume of interest (VOI). An illustration of 3-D plane wave imaging of a resolution phantom can be seen in Figure 6.1.

3-D plane and diverging wave imaging has previously been utilized in imaging of the heart [232], in shear-wave imaging [233], in 3-D and 4-D Doppler imaging of blood vessels [232], [234] and more recently in 3-D quasi-static elastography [235] and in 3-D myocardial elastography in vivo [236].

Previous attempts to obtain elastographic information of arteries in 3-D include three dimensional phase contrast MRI with flow sensitivity, enabling volumetric coverage and PWV estimation in the aorta even in the case of complex aortic shapes [114], [237]. Furthermore, 3-D strain images of atherosclerotic carotid artery models were produced by estimating the strains

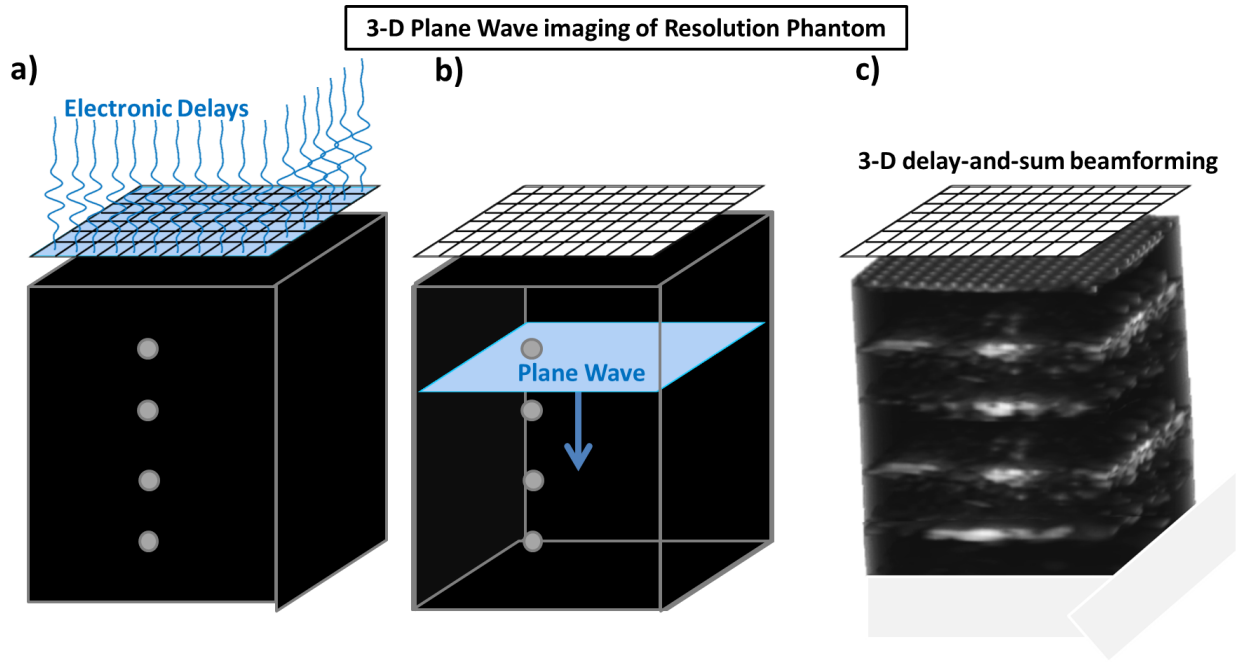

Figure 6.1: Illustration of the 3-D plane wave imaging paradigm. a) Electronic pulses are simultaneously applied to the piezoelectric elements. b) a plane wave is then emitted that insonifies the whole Volume of Interest (VOI). c) By beamforming the returning echoes, a 3-D B-mode is reconstructed. Grey dots correspond to the wires within the resolution phantom.

from multiple 2-D ultrasonic coherent compounded images and then employing post acquisition alignment to produce a single 3-D volume [238], [239]. A similar approach was utilized in a simulation study where sparse array imaging was used to produce 3-D strain volumes of a healthy carotid artery [240]. In another study, the complete 3-D strain tensor was acquired by continuous pullback of an intravascular ultrasound catheter inside excised porcine carotid arteries while acquiring images at 30 frames per second [241]. While the aforementioned ultrasonic methods have showed promising results, post-acquisition registration of arterial image slices was employed. Thus, the objective of this study is to introduce a novel method of estimating the PWV along the path of the pulse wave propagation, validate it and demonstrate its advantages in silicone phantoms utilizing both static and

dynamic testing and test its initial feasibility in healthy human carotid arteries *in vivo*. It should also be noted that this study was first presented at the 2016 International Ultrasonics Symposium (Tours, France) and subsequently published in the IUS 2016 special issue of the IEEE Transactions in Ultrasonics, Ferroelectrics and Frequency Control [242].

6.1. Materials and methods

6.1.1. 3-D volume acquisition

All 3-D imaging in this study was performed using a 16×16 2-D array (Sonic Concepts, Bothell, WA, USA) with a center frequency of $2.5\ MHz$ and a bandwidth of 50%. The spacing of the transducer elements was $0.85\ mm$. A fully programmable ultrasound system with a sufficient number of channels to accommodate all of the array's elements in both emission and receive was used to control the probe (Vantage 256, Verasonics, Kirkland, USA). Plane waves were emitted with the 256 elements firing simultaneously. More specifically, a single plane wave acquisition sequence was designed and implemented with plane waves emitted at a transmission angle of 0^o (transmission direction being perpendicular to the face of the transducer) at a pulse repetition frequency of $2000\ Hz$. The imaging field of view corresponded to the 2-D aperture dimensions, i.e. $13.6\ \times\ 13.6\ mm^2$. A detailed investigation of the lateral resolution of the 2-D array used in the present study obtained with a single plane wave imaging acquisition sequence has been previously performed in a study by Papadacci et al. [235] with the 6 dB width of the point spread function (PSF) in both the x and y dimensions increasing from 1.5 to $3.5\ mm$ as the depth increased from 10 to $60\ mm$. Subsequently, the received

echoes were sampled at 10 MHz and stored in memory. Each acquisition lasted approximately $1s$ at a volume rate of $2000\ vol/s$.

6.1.2. Silicone phantom design

The silicone phantom with the soft and the stiff segments along the longitudinal axis introduced previously in this thesis was used to validate the 4-D PWI PWV measurements. Static testing PWV values were used to validate the 4-D PWI ones.

Subsequently, the phantom was connected via rubber tubes to a peristaltic pump, which generated pulse waves at a rate of approximately $2\ Hz$. Blood-mimicking fluid was used as the circulating fluid. Care was taken when connecting the phantom to the peristaltic pump so that

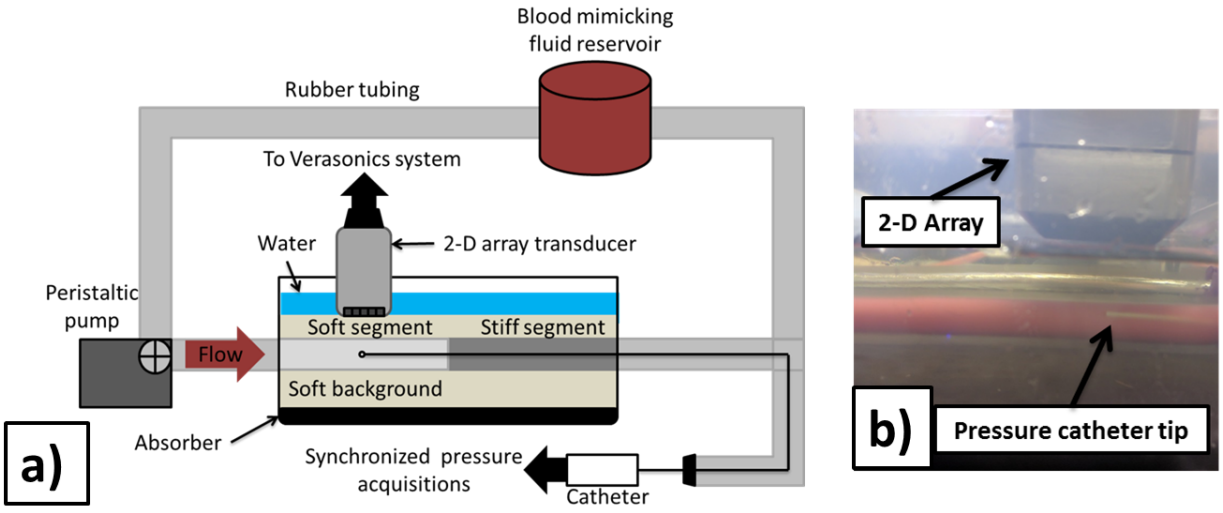

Figure 6.2: a) Schematic of the experimental setup used in the phantom study with the pressure catheter inserted into the phantom's lumen and the catheter tip placed beneath the 2-D array at the scanned location. Schematic depicts imaging of the soft phantom part. Imaging of the stiff part was performed by flipping the phantom so that the stiff part would be away from the fixed end of the phantom along the flow direction. b) Close-up of the 2-D array over the silicone phantom with the pressure catheter tip being within the volume of interest.

the imaged segment (soft, stiff) would be as far as possible from the fixed end of the phantom along the flow direction so as to ensure sufficient travel time for the forward wave before mixing with the reflection wave generated at the fixed end of the phantom.

The phantom was also dynamically tested under the aforementioned conditions and the validation was based on deriving the cross-sectional compliance. More specifically, a pressure catheter was introduced into the lumen. A digitizer (CompuScope 14200, Gage Applied Technologies, Lachine, QC, Canada) was used to synchronize the intraluminal pressure measurements with the 3-D ultrasound acquisitions. Care was taken to get the catheter tip within the imaged volume. Consequently, given the synchronized intraluminal pressure and vessel luminal area measurements obtained at the same location, the pressure-area ($P - A$) relationship of the vessel was recovered at high-frequency sampling and thus dynamic compliance estimates were obtained ($C_{Dyn} = \frac{dA}{dP}$). These were compared to PWI compliance estimates produced via the Bramwell-Hill equation (C_{PWI}). A schematic of the experimental setup with the 2-D probe and the catheter inserted into the phantom is shown in Figure 6.2a). A magnified image of the catheter tip beneath the 2-D array at the imaging location is shown in Figure 6.2b).

In order to demonstrate the 3-D capability of the technique, as well as its advantage compared to conventional PWI, a second phantom was constructed with a plaque embedded on the antero-lateral wall. A homogeneous cylindrical phantom was created according to the previously described protocol used for the construction of the soft phantom segment. The plaque was subsequently added by injecting an extra quantity of the “stiff” material mix onto

the vessel wall with a syringe. After about an hour of curing time, the generated plaque adhered to the surrounding vessel wall. Next, the phantom was mounted so that the plaque would appear at an antero-lateral location of the phantom wall.. The phantom segment containing the plaque was scanned with the 2-D array as well as with a standard linear array (L7-4, ATL Ultrasound, Bothell, WA, USA) with 128 elements, a central frequency of $5\ MHz$, 60% bandwidth and $294\ \mu m$ of element spacing connected to the Verasonics research system. A coherent compounding PWI acquisition was implemented with the linear array using plane wave imaging. The acquisition sequence consisted of emitting 3 at a frame rate of 2778 Hz. The received channel data were beamformed with the previously descibed GPU-accelerated delay-and-sum technique and the pulse wave tracking was carried out with the conventional PWI post-processing methodology. Two conventional PWI acquisitions were made with the plaque being inside and outside of the field of view.

6.1.3. *In vivo* feasibility study design

The right common carotid of six healthy subjects ($n = 6$) was imaged with the 2-D array previously described. The subjects were 24 to 35 years old, with an average age 29.2 y.o. The experiments were conducted with the subject in a sitting position, freely breathing. First, the location of the carotid bifurcation was determined with 2-D ultrasound real-time B-mode imaging. The L7-4 linear probe connected to the Verasonics research system was used for the imaging. Subsequently, the 3-D acquisition was performed about $2\ cm$ below the bifurcation. The sample size of six subjects was deemed sufficient to capture a wide range of physiological PWV values. In order to validate the results, the previously described conventional PWI

acquisition sequence was also used to scan the common carotids of three of the healthy subjects at approximately the same location. Subsequently, the resulting PWVs were compared to the ones obtained by 4-D PWI

6.1.4. 4-D PWI methodology

A parallel 3-D delay-and-sum-based algorithm was implemented and used to beamform the acquired channel data. The beamforming algorithm was implemented on the CUDA computing platform (CUDA 6.5, NVIDIA Corporation, Santa Clara, CA, USA). Subsequently, the sub-sample PWI axial wall velocities (v_{PWI}) were estimated by the GPU-accelerated 1-D normalized cross-correlation algorithm described previously in the current thesis. Calculations were performed on a Tesla C2075 GPU (NVIDIA, Santa Clara, CA, USA).

In order to produce PWI image sequences depicting the pulse wave propagation, the walls of the vessels were isolated in multiple cross section slices and subsequently interpolated to produce a mask. The v_{PWI} corresponding to the mask's borders were used to move the mask accordingly with the vessel's motion over time. The isolated v_{PWI} were then color-coded and overlaid onto the corresponding segmented B-modes. 3-D rendering was performed with the Amira software (Visualization Sciences Group, Burlington, MA, USA). A schematic outlining the steps of the post-processing methodology is provided in Figure 6.3.

Points on the anterior wall were manually selected at multiple cross-section slices of the vessel and subsequently interpolated in order to generate a 32×32 point grid. The v_{PWI} at each

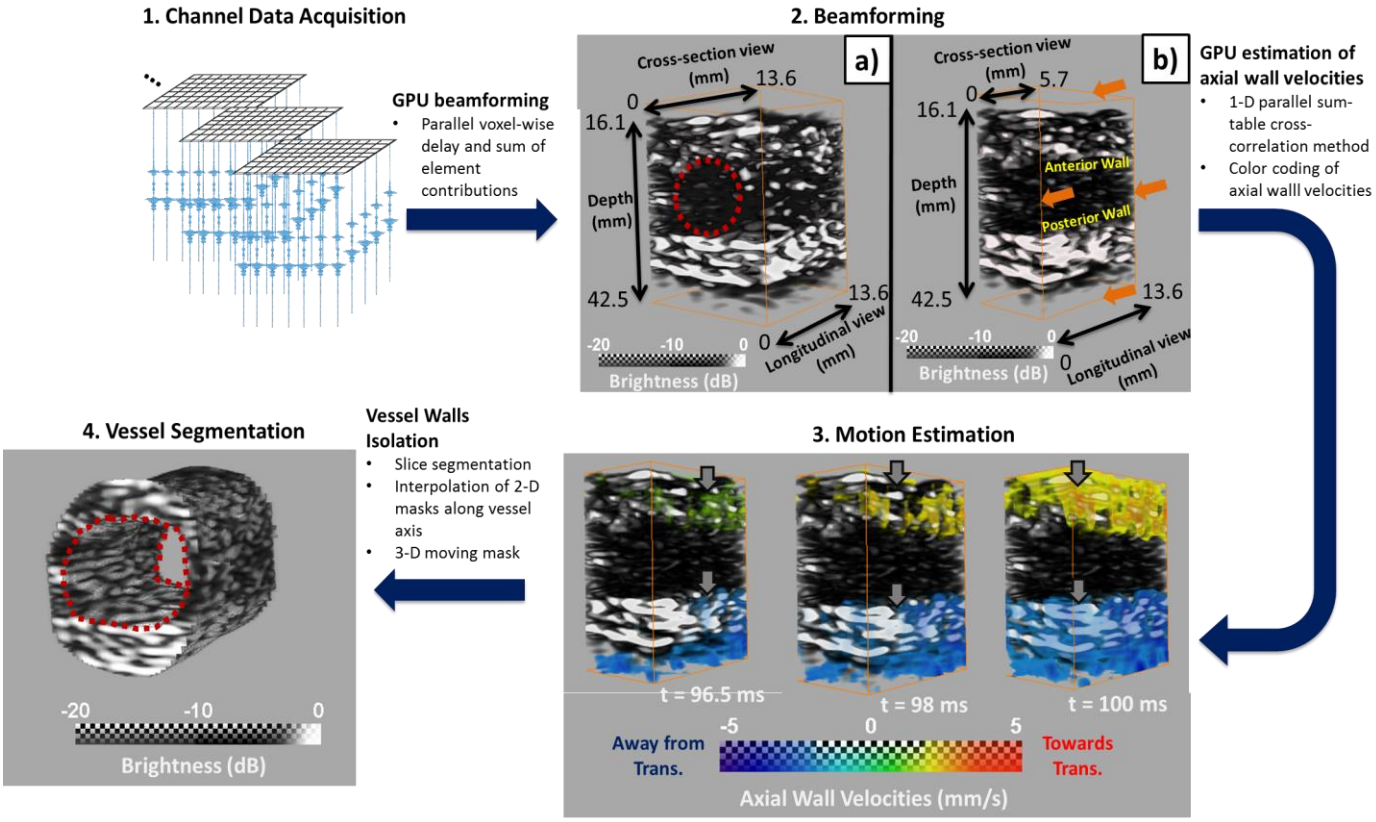

Figure 6.3: Illustration of the 4-D PWI post-processing methodology in the case of a silicone phantom. 1. Collection of channel data. 2. Beamforming of the channel data to generate sequences of 3-D RF volumes. 2a) Depicts a sample beamformed 3-D volume and 2b) shows a sub-volume by slicing close to the center of the imaged vessel. Red circle indicates the approximate position of the vessel 3. Sequence of 4-D PWI axial wall velocity (v_{PWI}) volumes indicating the pulse wave propagation. Red indicates motion towards the transducer (top) and blue indicates motion away from it (bottom). Grey arrows indicate the progression of the pulse wave propagation. 4. Segmented vessel.

point of the grid were extracted and plotted as a function of time, thus generating a 3-D spatio-temporal map depicting the directional propagation of the pulse wave. To ensure that the selected grid points correspond to wall locations and more specifically to regions showing adequate signal to noise ratio (SNR), where the quality of the axial wall velocities is expected to be satisfactory, they were selected in regions of the top and bottom walls that exhibited

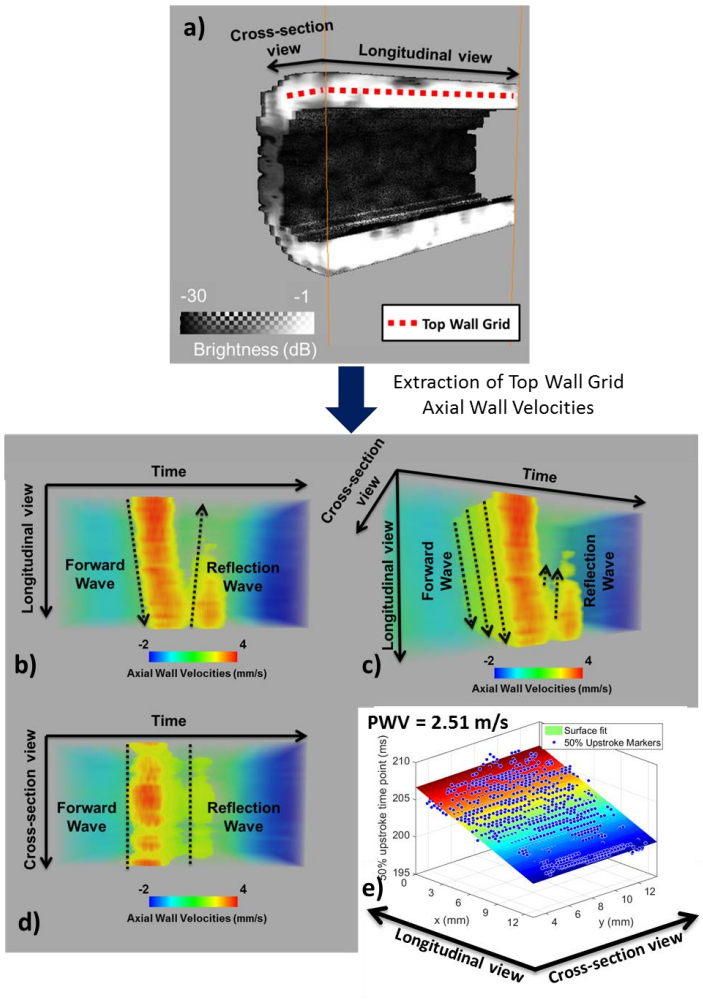

Figure 6.4: Estimation of PWV in 3-D. a) illustration of the top wall grid overlaid onto the anterior wall cross-sectional and longitudinal section views b), c), d) different views of the 3-D spatio-temporal map e) Estimated 50% upstroke markers and corresponding plane fit. The estimated PWV value is shown in the left top corner.
the upper left corner.

sufficient echogenicity. More specifically, the points of the each wall grid were selected in regions of the B-mode volumes that exhibited a brightness of at least -6 dB (approximately 0.5 of the highest brightness amplitude). Thus, noisy velocities and motion artifacts were mostly avoided. The lateral walls were also avoided when selecting the points for the anterior and posterior wall grids due to the decreased values and SNR of the v_{PWI}. Thus, these grids

corresponded to broad sections of the anterior and posterior walls where the axial wall velocities were expected to be of higher quality. In cases where there was significant rigid motion, the spatio-temporal maps created for each of the anterior and the posterior walls were subtracted in order to eliminate any potential rigid motion interference and keep only the distension wave.

Subsequently, to maintain consistency with the 2-D case, the 50% upstroke points were used as the pulse wave tracking feature. The inverse of the gradient of the regression plane fitted between the 50% upstroke arrival time and the point location yielded the PWV along the direction of the pulse wave propagation. A schematic of the methodology of 4-D PWI is shown in Figure 6.4

6.2. Results and discussion

6.2.1. Silicone phantom study

Figure 6.5 shows the propagation of the pulse wave along the soft and the stiff segments of the phantom. As it can be seen the magnitude of the v_{PWI} is higher and the duration of the pulse wave propagation is longer in the case of the soft segment compared to the stiff segment. Similar observations have been made in [172] in vivo, between normal and stiffer atherosclerotic aortas in mice. More specifically, atherosclerotic aortas, known to be stiffer compared to healthy ones were shown to have both higher PWVs and lower v_{PWI} , thus being in agreement with the findings of the current study.

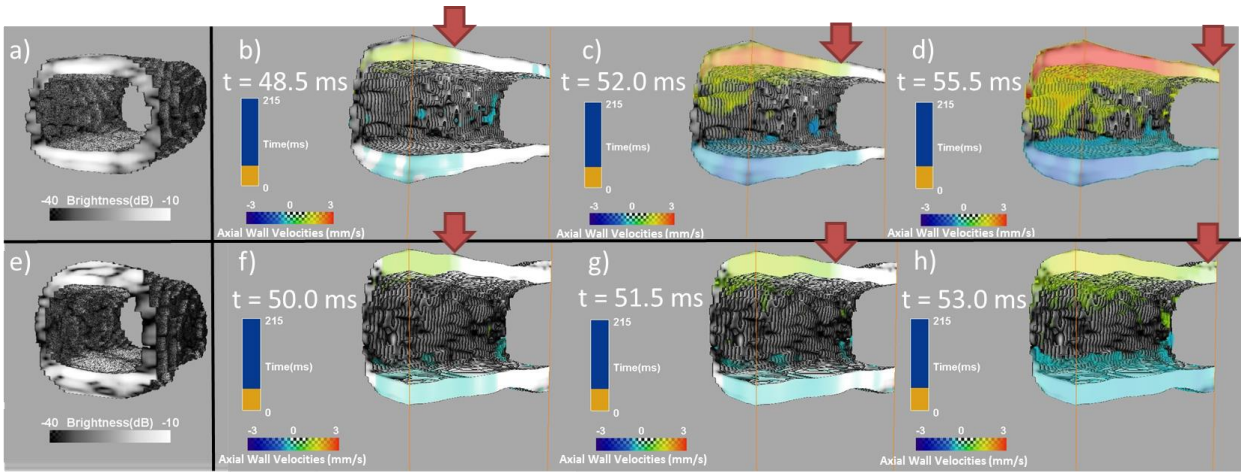

Figure 6.5: a) Segmented B-mode of the soft part of the phantom, b), c), d) PWI pulse wave propagation image sequence for the soft part, e) Segmented B-mode of the stiff part of the phantom, f), g), h) PWI pulse wave propagation image sequence for the stiff part. The solid red arrows denote the pulse wavefront.

PWVs estimated with the static testing were found to be in agreement with the 4-D PWI derived PWV over three different cycles (n = 3) in each phantom segment, as shown in TABLE 6.1. A B-mode slice of the phantom with the catheter in view inside the lumen is depicted in Figure 6.6. The same figure shows the simultaneously acquired and co-localized pressure and diameter waveforms as well as the pressure-area plot of the phantom yielding C_{dyn}. The resulting pressure-area relationship was found to be linear, showing no hysteresis between pressure and area measurements. This indicated the reduced influence of the phantom's wall viscosity. The mean compliance estimated via the Bramwell-Hill equation and the 4-D derived PWV was found to be $C_{PWI} = 71.33 \pm 1.63 \cdot 10^{-7} m^2 \cdot kPa^{-1}$ (n=3 cycles), while the corresponding mean compliance estimated by dynamic testing over three [209], [210]cycles was $C_{dyn} = 73.10 \pm 2.39 \cdot 10^{-7} m^2 \cdot kPa^{-1}$ (n=3 cycles). Thus, with the dynamic testing the results of 4-D PWI were validated with the phantom connected to the peristaltic pump (i.e. under dynamic conditions).

Figure 6.7 shows the PWI pulse propagation image sequences in the cases of the conventional PWI acquisitions with the plaque outside and within the field of view. Furthermore, the 4-D PWI pulse wave propagation image sequences are shown with the wall clipped outside of the plaque region to visualize propagation within the phantom wall and also clipped at the plaque region to visualize intra-plaque pulse wave propagation.

This experiment showcased some advantages of 4-D PWI compared to the conventional

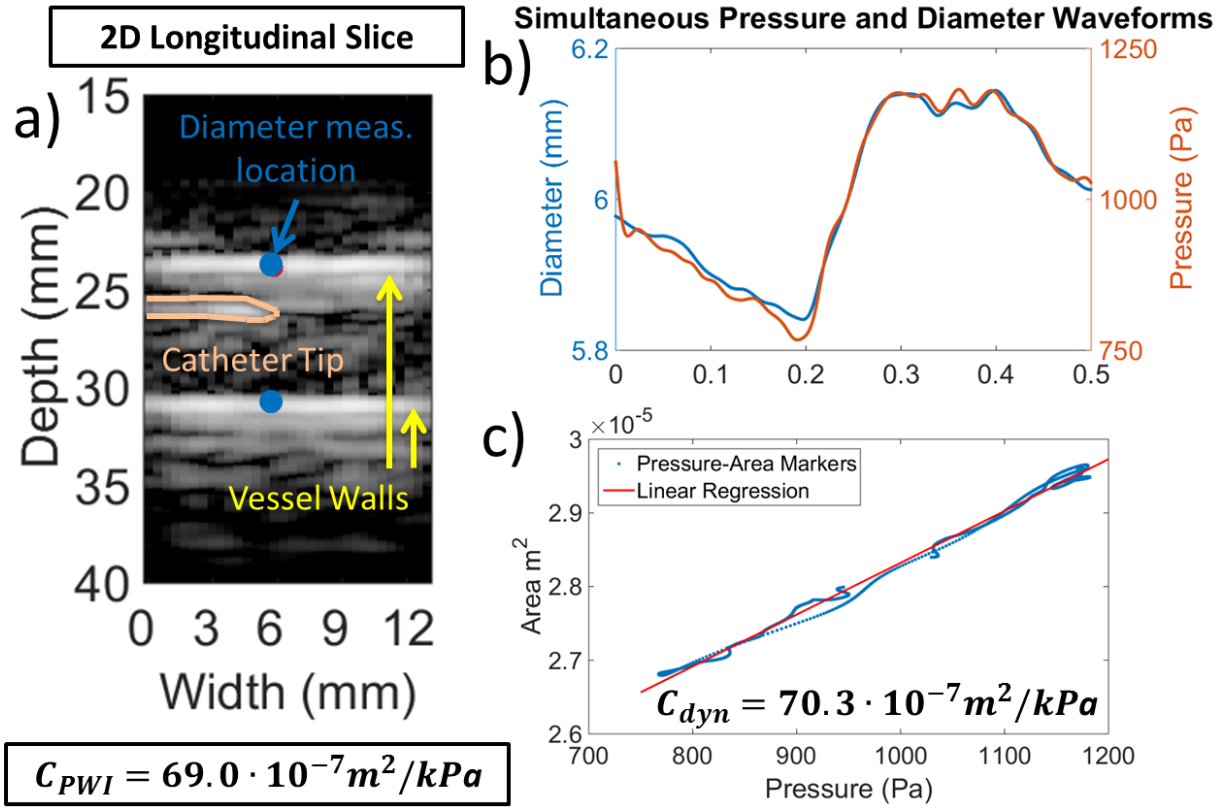

Figure 6.6: a) Longitudinal section of the phantom at the center of the volume. The catheter tip can be seen within the phantom lumen. Diameter was measured between the points indicated with blue color. b) Pressure and diameter waveforms measured simultaneously at the same location. c) Resulting pressure - area relationship and the corresponding linear fit yielding the dynamic testing compliance C_{Dyn}. PWI compliance (C_{PWI}) is also provided.

	Soft Segment	Stiff Segment
$PWV_{PWI}(m/s)$	2.41 ± 0.07	$3.42 + \_0.23$
r^2	$0.76 + \_0.04$	0.72 ± 0.08
$PWV_{static}(m/s)$	2.49	3.41

TABLE 6.1: PWV Results (n=3 cycles)

The plaque phantom experiment showcased some advantages of 4-D PWI compared to the conventional technique. More specifically, it showed that while pulse wave propagation was detected using the conventional PWI method with the plaque region both within and outside of the field of view, plaque detection was harder and could have potentially been missed from the PWI analysis. On the contrary, 4-D PWI was able to delineate the full extent of both the phantom's wall and the plaque attached to it, thus providing comprehensive, angle-independent views of the vessel. This advantage is intrinsically linked to the use of 3-D ultrasound in the diagnosis of atherosclerosis. Using conventional 2-D imaging, even with a high quality B-mode, plaque severity may be overestimated, underestimated or even completely undetected depending on the orientation of the 2-D imaging plane [128]. This may induce errors in both the correct diagnosis and the accurate estimation of the plaque and vessel morphological characteristics (i.e. plaque thickness, cross-sectional luminal area). This has been corroborated by a large scale study where 3-D ultrasound was able to detect more plaques than conventional imaging in an older population [243]. Thus, the objective examination and increased sensitivity provided by 3-D ultrasound may prove to be crucial for PWI, since it aims

at investigating the progression and the mechanical properties of plaques from the earliest stages to the higher risk morphologies.

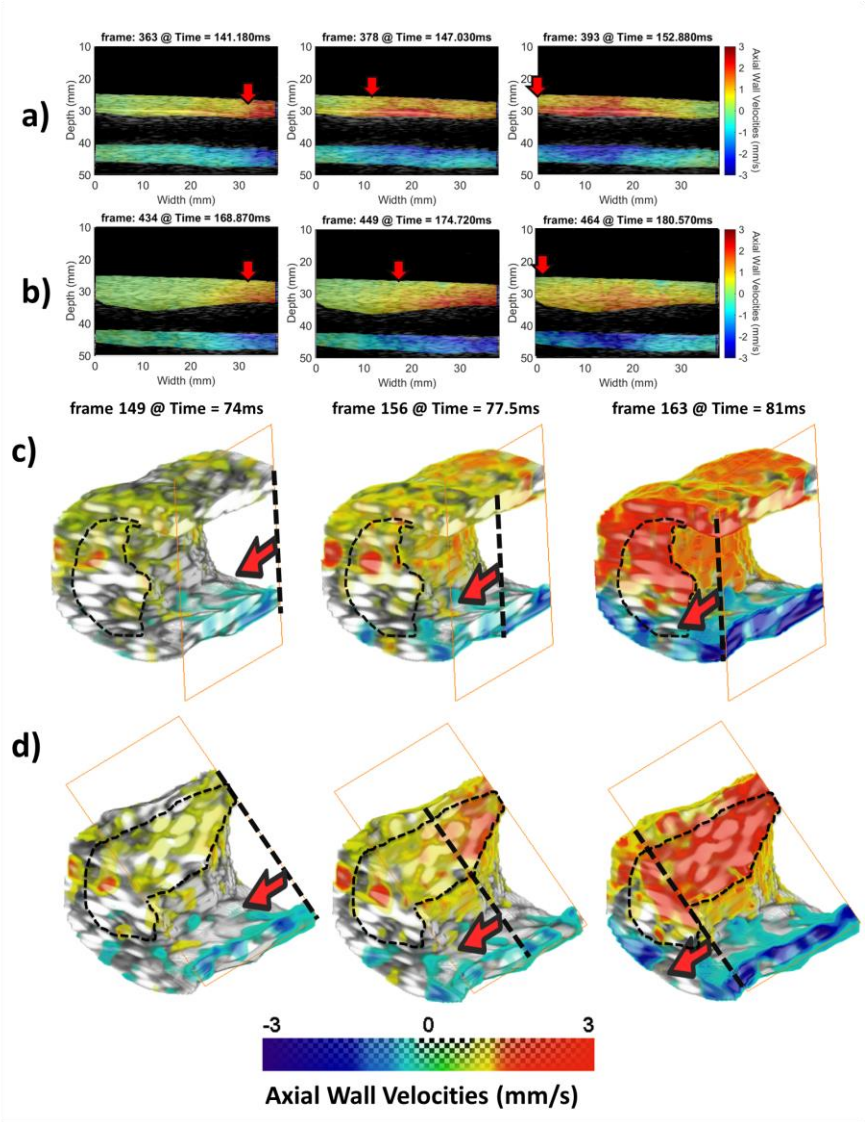

Figure 6.7: a) Conventional PWI pulse propagation image sequence with the plaque outside of the field of view. b) Conventional PWI pulse propagation image sequence with the plaque within the field of view. c) 4-D PWI pulse propagation image sequence. The phantom wall has been clipped outside of the plaque region to better illustrate pulse wave propagation. d) 4-D PWI pulse propagation image sequence. The phantom wall has been clipped at the plaque region to visualize intra-plaque pulse propagation. The solid red arrows and the transverse perforated lines denote the pulse wavefront and propagation is from right to left side. The extent of the plaque has been delineated with thin black perforated lines

Additionally, the Bramwell-Hill equation and the Pulse Wave Inverse Problem (PWIP), in addition to the accurate estimation of the PWV, require the correct estimation of the cross-sectional luminal area. 4-D PWI is advantageous in this case, since it is able to provide comprehensive views of the investigated vessels, whereas conventional PWI assumes circumferential homogeneity and symmetry of the vessel, an assumption that often does not hold in the case of atherosclerotic vessels.

Furthermore, as shown in Figure 6.7, another advantage of 4-D PWI is that it provides the v_{PWI} throughout the entire imaged vessels circumference and length simultaneously. On the contrary, conventional PWI only provides the v_{PWI} at a single slice, dramatically decreasing the amount of available information for further analysis.

6.2.2. *In vivo* feasibility study

In the case of the *in vivo study* proposed 4-D PWI processing method was applied to six sets of data from healthy subjects. Snapshots of the propagation of the pulse wave can be seen in Figure 6.9. The spatio-temporal maps of the propagation of the distension pulse wave were obtained from the 2-D and 3-D acquisitions for three of the subjects (A,B and C) and compared for each one of them, as shown in Figure 6.8. Good qualitative agreement between conventional and 3-D spatio-temporal maps was obtained. Quantitatively, the PWVs estimated with the 4-D PWI technique were close to the PWVs estimated with conventional PWI. On average, the difference was $0.52\ m/s$, which is less than $1.1\ m/s$ the maximum reported difference in PWVs measured during different cardiac cycles of the same subject by both commercial systems [209], [210] and PWI studies [188], [193].

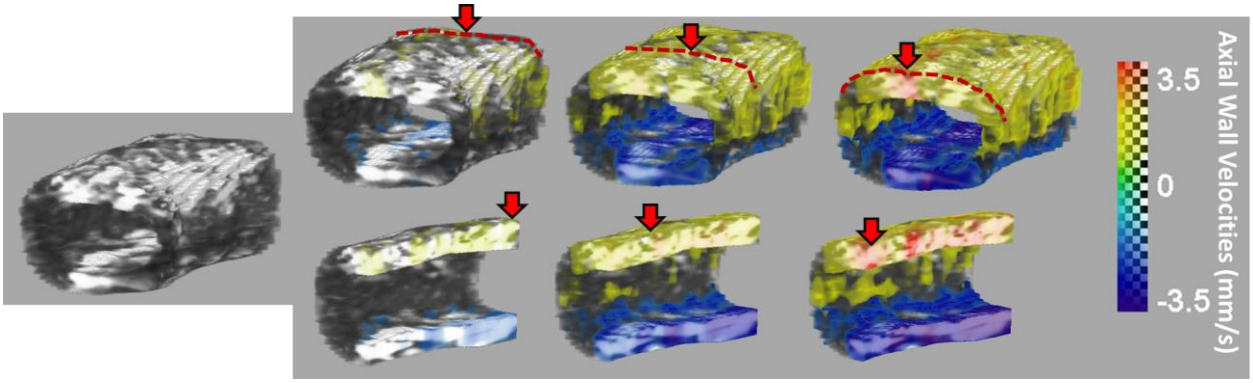

Figure 6.9: Segmented vessel and PWI pulse wave propagation image sequences showing the 3-D propagation of the pulse wave in a portion of the common carotid of a healthy subject. The same vessel is shown in the bottom row with the arterial wall clipped to show intra-wall pulse propagation. Red dotted lines and red solid arrows indicate the progression of the pulse wave.

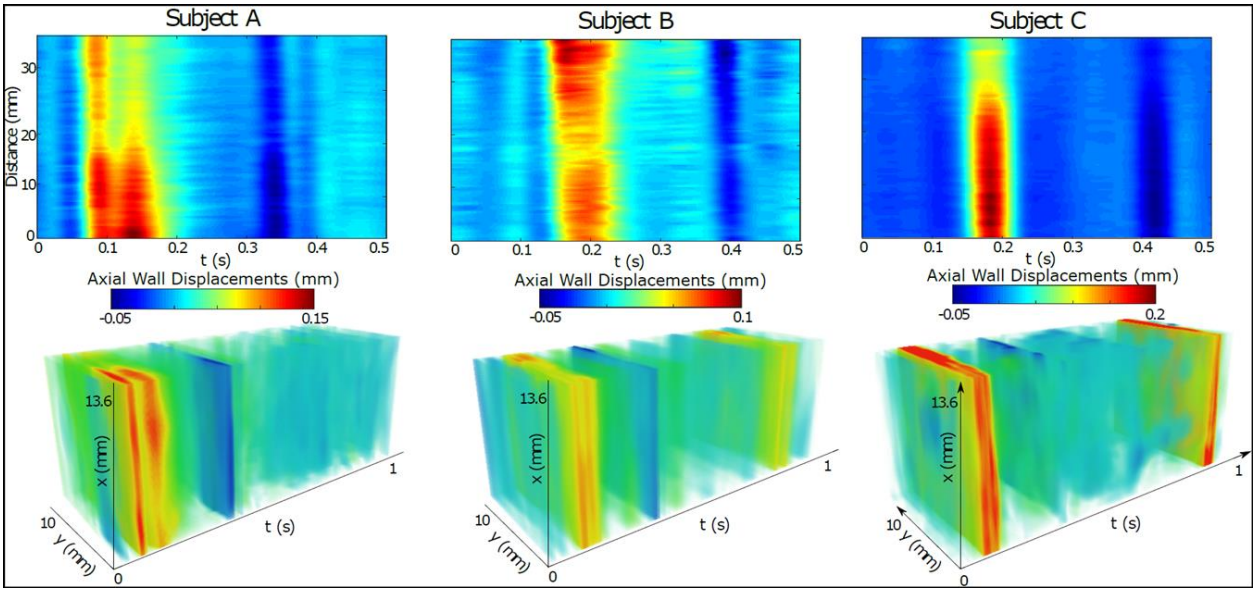

Figure 6.8: Comparison of the spatio-temporal maps obtained from conventional 2-D measurements (top row) and with the proposed 3-D approach (bottom row) for three different subjects.

6.2.3. Limitations and future directions

The main drawbacks of the 4-D PWI method compared to conventional PWI are pertinent to the 2-D array used. More specifically, lower image quality and overall SNR can be observed in

both the B-mode volumes and the estimated v_{PWI} , as also discussed in [235], mainly due to the lower number of elements along each direction (16×16 elements), lower frequency (2.5 MHz) and lower frequency bandwidth (50%) compared to the linear array used in conventional PWI (128 elements, 5 MHz, 60% bandwidth). These limitations are expected to be alleviated with the acquisition of a new probe with a higher central frequency and more piezo-electric elements.

Another limitation of the current technique is that lateral v_{PWI} were not estimated and thus pulse wave propagation was based solely on the axial v_{PWI} . As expected, lateral walls exhibited reduced axial motion and were mostly avoided for the tracking of the pulse wave propagation. However, it should be noted that the same limitation would apply to conventional PWI, since also in conventional PWI only the axial v_{PWI} are tracked. Nevertheless, axial v_{PWI} were found to be sufficient to enable 4-D PWI's main functionality and main advantage compared to conventional PWI, the correct tracking of the pulse wave in 3-D along the propagation direction.

Ongoing work aims at the estimation of lateral v_{PWI} which will ultimately lead to the acquisition of the full vector of the v_{PWI} and not just their axial component, thus alleviating any perceived angle dependence of the method and also providing increased insight to arterial wall motion. This will be of great importance especially in the case of focal vascular disease exhibiting anisotropic 3-D motion and complex mechanical behavior.

6.3. Conclusions

4-D PWI was successfully implemented with plane waves at high volume rates. PWVs were estimated along the direction of the pulse wave propagation and were validated in the case of a silicone phantom against PWV values derived from static testing. Compliance values derived with dynamic testing were also found to be similar to the PWI-derived compliance. Pulse wave propagation was comprehensively visualized in a plaque phantom using 4-D PWI and its advantage was demonstrated against conventional PWI. Finally, the in vivo feasibility was demonstrated by imaging the pulse wave propagation along the carotid artery wall of six healthy subjects.

Chapter 7. **Integration of PWI with Color and Vector Doppler**

As mentioned in the introduction of this thesis, the pulse wave generated by the left ventricle at the start of every cardiac cycle manifests itself as a pressure, flow velocity, and wall displacement wave. PWI has traditionally only looked at the latter type of wave. In this chapter, PWI is expanded upon and integrated with modalities that will allow the investigation of the blood flow wave travelling along the arterial tree simultaneously with the wall distension wave and thus provide tools investigate the relationship between them.

This is an important development for the progress in the study of arterial wall biomechanics, especially given that arterial wall motion and blood flow are coupled and influence each other. A significant number of fluid-solid interaction (FSI) models have been published, attempting to model the blood flow within large elastic arteries under the influence of a moving elastic arterial wall [244], [245], [246], [247]. Simultaneous and co-localized imaging of blood flow and arterial wall velocities is expected to aid in providing validation of FSI models as well as increase the amount of available information that can be used to increase the level of sophistication of the derived models of the biomechanical behavior of the investigated arteries [248], [245].

Additionally, as explained in the introduction, blood flow patterns precipitate changes in the mechanical properties of the arterial wall and often lead to arterial dilation or stenosis [249], [39], [250]. Therefore, a technique that provides simultaneous and co-localized information on both the arterial wall mechanics and the blood flow patterns could potentially improve arterial

disease screening and early diagnosis, also contributing to the development of novel arterial disease prevention strategies [249].

Furthermore, Doppler techniques have been previously used to determine the velocity profiles of the blood flow and subsequently estimate the wall shear stress according to the Womersley model [251], [252], [253]. Given that high wall shear stress is indicated as a major plaque destabilization factor [42], simultaneous imaging of the diseased arterial wall motion and the blood flow velocities can provide insight into both the mechanical properties of the plaque and the wall shear stress acting upon it and thus lead to more accurate estimates of plaque's risk of rupture.

As mentioned in the introduction, color Doppler techniques have been traditionally used to diagnose atherosclerotic disease in the extracranial arteries. More specifically, the utility of color Doppler has been repeatedly demonstrated by correlating blood flow velocities with the degree of stenosis in patients [134]–[136]. These techniques have relatively recently been implemented with high frame rate plane wave imaging and tested with coherent compounding [3], [4]. This development offers significant advantages, as the traditional tradeoff between frame-rate, region of interest and precision of the velocity estimates is broken, thus producing full field-of-view color Doppler images at high frame rates [5]. More recently, cross-beam vector flow Doppler techniques, eliminating the traditional Doppler angle dependence limitation, have been developed with plane wave imaging [254]–[256]. Most of these

techniques utilize triangulation to acquire the lateral and axial components of the 2-D vector of the blood flow velocities.

Initial attempts to acquire information on both the arterial wall dynamics as well as on the blood flow involved single element ultrasound transducers [41], [253]. With the development of plane wave imaging and parallel receive beamforming, techniques integrating wall displacement estimators and blood velocity Doppler techniques were developed and initially used in simulations or applied to phantom setups [257], [258], [259] and have shown the feasibility of simultaneous imaging of wall dynamics and blood flow velocities in simulations, phantoms and *in vivo*. However, they suffer either from poor spatial resolution or insufficient temporal resolution for the tracking of the pulse wave as tissue Doppler is being used to derive the arterial wall displacements. On the other hand, a similar study by our group utilized cross-correlation to estimate both the wall and the blood flow velocities in healthy and diseased mouse aortas [248]. It should be noted, however, that while cross-correlation has been validated as a blood tracking technique, it is not a standard modality in most clinical systems.

In this chapter, the methodology of integrating PWI with a plane wave compounding color Doppler technique and subsequently, a vector Doppler modality will be shown. The feasibility of the resulting complex modalities will be tested in healthy subjects *in vivo and metrics*.

7.1. Materials and methods

7.1.1. Data acquisition

For the purpose of this study a 3-plane wave spatial compounding acquisition imaging sequence was designed similarly to [193] and implemented on a Verasonics Vantage 256 research platform (Verasonics, Bothell, WA, USA). In this case, the PRF was increased to 10 kHz in order to minimize flow velocities aliasing. For the compound color Doppler sequence, the plane wave transmission angles were similarly to [260]: $-3^o, 3^o$ and 0^o. However, in the case of the vector Doppler sequence, the transmission angles were wider at $-10^o, 10^o$ and 0, thus facilitating the vector velocity triangulation scheme, slightly impacting, however, the SNR of the axial wall velocities (v_{PWI}) [193].

The common carotids of four (n=4) healthy volunteers were scanned with the compound color Doppler acquisition scheme and the common carotids of six (n=6) along with one carotid bifurcation was scanned with the vector Doppler acquisition scheme.

7.1.2. Post-processing methodology

7.1.2.1. Beamforming and wall motion estimation

The received channel data for each transmission angle were beamformed with a GPU-accelerated beamforming algorithm and coherently summed, producing compounded RF frames. Subsequently, the estimation of the axial wall velocities (v_{PWI}) was performed using a parallel implementation of the 1-D cross-correlation sum-table method [193].

The anterior and posterior walls were segmented with the semi-automatic algorithm introduced in [172] and the v_{PWI} waveforms at each point of each segmentation were

obtained. The v_{PWI} waveforms of the posterior wall were then subtracted from the v_{PWI} waveforms of the anterior wall, thus producing distension v_{PWI} free from the imaged vessel's rigid motion. Thus, a distension v_{PWI} waveform was acquired for each lateral position of the imaged vessel.

Additionally, the wall segmentations were tracked in time using the estimated v_{PWI} and the positions of the anterior and the posterior wall segmentations were subtracted in each frame yielding an arterial diameter waveform at each lateral position of the vessel.

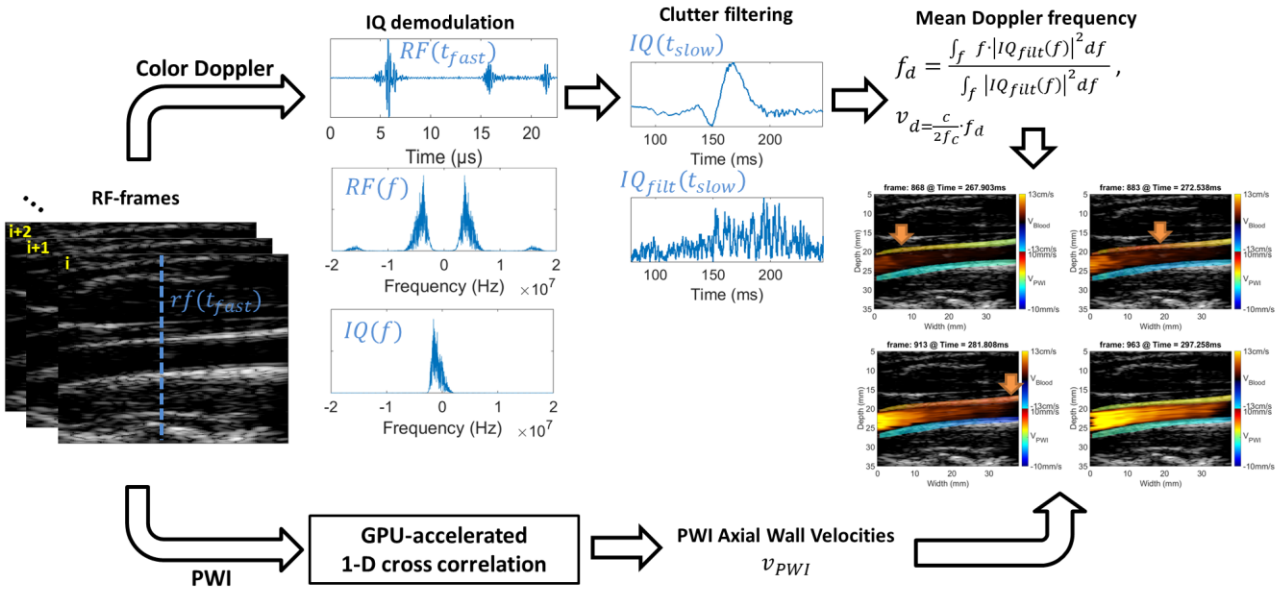

Figure 7.1: Schematic providing an overview of the methodology for generating PWI-Color Doppler frames. t_{fast} and t_{slow} correspond to the rf-data sampling time points (depends on the sampling frequency) and the rf-frame acquisition time points (depends on the frame rate). IQ and IQ_{filt} are the signals obtained after demodulation of the rf-signals and clutter filtering of the resulting IQ signals, respectively. Orange arrows in the PWI-Color Doppler frames denote the progress of pulse wave propagation at the arterial wall.

7.1.2.2. Compound color doppler

The beamformed compounded RF-data were in-phase and quadrature (IQ)-demodulated producing IQ-data which were subsequently clutter filtered in order to eliminate any influence of the wall motion on the estimation of the blood flow velocities. This was done using a spatio-temporal clutter filter based on singular value decomposition of the ultrasound data, previously introduced in [261].

The IQ frame sequences were then divided into ensembles of 40 frames (i.e. ~12 ms) with 90% overlap so that the resulting color Doppler frame sequence would have a frame rate of 833 Hz. Standard color Doppler images were acquired by estimating the mean frequency of the power Doppler spectrum for each pixel for each ensemble:

$$f_d(\boldsymbol{r}) = \frac{\int_f f\left|IQ_{filt}(\boldsymbol{r},t)e^{-j2\pi ft}dt\right|^2 df}{\int_f \left|IQ_{filt}(\boldsymbol{r},t)e^{-j2\pi ft}dt\right|^2 df},$$

where $f_D(\boldsymbol{r})$ is the Doppler frequency at each position $\boldsymbol{r}$ in the clutter filtered IQ frame at time$t$: $IQ_{filt}(\boldsymbol{r},t)$. Subsequently, the Doppler velocities (v_d) along the ultrasound beam were estimated from the Doppler equation:

$$v_d = \frac{c}{2F_c} \cdot f_d$$

For visualization purposes the v_d and the v_{PWI}were respectively color-coded using the Doppler and the jet colormaps and overlaid onto the B-mode with appropriate moving masks corresponding to the arterial lumen where the flow velocities exceed a preset threshold and to the arterial walls, respectively. Given the different frame rates between the color Doppler frame sequence and the B-mode and v_{PWI} sequences, care was taken so that the color Doppler frames were assigned to the B-mode frames closest in time. Thus, sequences of v_{PWI} and blood flow velocities v_d images were created. A schematic of the methodology for the production of the PWI - Color Doppler frames is shown in Figure 7.1.

Subsequently, the v_d waveforms within the lumen that exceeded the preset threshold were averaged at each lateral position thus producing a single average blood velocity waveform v_d per lateral position. The foot and the peak of each average $v_d$waveform were then estimated and compared with the corresponding foot and peak timings of the v_{PWI} and the diameter waveforms at the same lateral position. The foot was estimated using the Complior tangent method [262] while the peak was selected as the first prominent peak of the velocity waveform after the foot of the wave.

7.1.2.3. Vector doppler

For the vector Doppler processing, the acquisitions made at each transmission angle (-10^o, 10^o and 0^o) were separately processed. Standard color Doppler images indicating the blood flow velocities along the beam direction (v_d) were generated by applying the previously described color Doppler methodology for the RF-data from each transmission angle. Subsequently, by

decomposing the true blood flow velocity vector (v) into a vector along the axial direction (v_z) and one along the lateral direction (v_x) and using the revised form of the Doppler equation [263], [264] we have the following system of equations:

$$v_z(\cos(\theta_t) + 1) + v_x \sin(\theta_t) = \frac{c}{f_c} f_d^{\theta_t} = v_d^{\theta_t}$$

Where θ_t is the transmission angle of the plane wave and thus $\theta_{t_{1,2,3}}$ = -10°, 10° and 0°, f_c is the center frequency of the ultrasound, c is the speed of sound and $f_D^{\theta_t}$ and $v_d^{\theta_t}$ indicate the estimated Doppler frequency shifts and blood velocities, respectively, for the tilted plane wave transmission at an angle θ_t. Thus, a system with three equations and two unknowns was created for each point on the Doppler images and was solved in parallel for all the image points using a GPU-enhanced least-squares solver:

$$\begin{bmatrix} v_x \\ v_z \end{bmatrix} = A^{+} \begin{bmatrix} v_d^{\theta_{t1}} \\ v_d^{\theta_{t2}} \\ v_d^{\theta_{t3}} \end{bmatrix}$$

Where A^{+} is the pseudoinverse matrix of A, the matrix containing the steering angles:

$$A = \begin{bmatrix} \sin(\theta_{t1}) & \cos(\theta_{t1}) + 1 \\ \sin(\theta_{t2}) & \cos(\theta_{t2}) + 1 \\ \sin(\theta_{t3}) & \cos(\theta_{t3}) + 1 \end{bmatrix}$$

The GPU accelerated algorithm was implemented using MATLAB 2014b (Mathworks Inc, Natick, MA, USA).

Subsequently, the magnitude of the derived velocity vectors was color-coded and overlaid onto the B-mode. To visualize the direction of the velocity vectors a vector field was overlaid on top of the color-coded magnitude of the velocities. The v_{PWI} were also overlaid onto the B-mode. Thus, the resulting images provided insight on both the directional blood flow velocities and the wall motion.

7.2. Results and discussion

7.2.1. PWI and color doppler

PWI and color Doppler frames for the common carotids of two healthy volunteers are shown in Figure 7.2a) and b). Propagation of the pulse wave can be observed in the arterial walls along with the simultaneous flow dynamics. Figure 7.2c) shows the spectral Doppler acquired by applying short-time Fourier transform to the signals within the gate indicated in Figure 7.2b). It has a similar appearance to conventional pulsed-wave (PW) Doppler waveforms. Figure 7.2d) shows the distension v_{PWI}, the average v_d and the corresponding diameter waveforms collected at the same lateral position. It can be observed that the foot of each waveform occurs approximately at the same time, while the peak v_{PWI} precedes peak v_d, which in turn precedes peak diameter. It should be noted that the overall measured v_d are lower compared to conventional color Doppler values and to peak systolic velocity (PSV) values derived for both healthy and diseased subjects [265]. This is because the plane wave transmission angles are small ($\theta_t \leq 3^o$) and thus the angle between the ultrasonic beam and the flow velocities is close to 90^o. Consequently, the component of the blood velocities along the ultrasound beam is relatively small. Using larger transmission angles could be a possible solution to this issue;

however, it would also result to decreased quality of the compounded RF-data and the estimated v_{PWI} while also affecting the SNR of the generated color Doppler images given also the appearance of grating lobes at larger angles, which may result to Doppler artifacts [266], [267], [193]. The effects of the transmission angle on the blood flow and the axial wall velocities needs to be further investigated, in order to optimize this novel imaging modality.

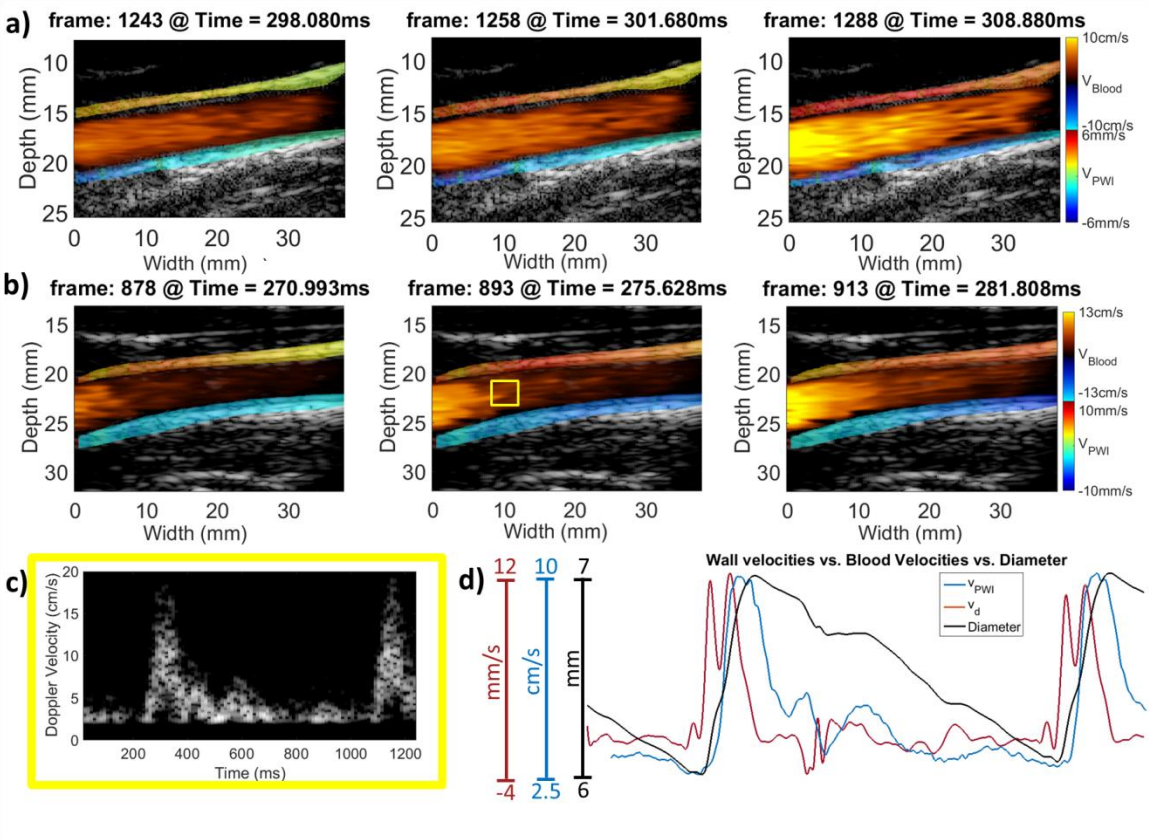

Figure 7.2: a), b) Sequences of Color Doppler and PWI images for the common carotids of two healthy volunteers. Axial wall velocities (v_{PWI}) are color-coded with the jet colormap (bottom colorbar) and blood flow velocities (v_d) are color-coded with the color Doppler colormap (top colorbar). c) Spectral Doppler waveform generated from the signals within the yellow range-gate in b). d) Average v_d, distension v_{PWI} and diameter waveforms recorded synchronously at the same image lateral position. The scales for each waveform are color-coded with the waveform's corresponding color.

The aforementioned observations were corroborated by collecting the foot and the peak of the v_{PWI}, v_d and diameter waveforms at each lateral position of the imaged vessels from the four healthy volunteers. Figure 7.3a) and b) show different angles of 3-D plots of the v_{PWI} and the v_d waveforms at each lateral position of a healthy volunteer overlaid onto each other along with the corresponding foot and peak features.

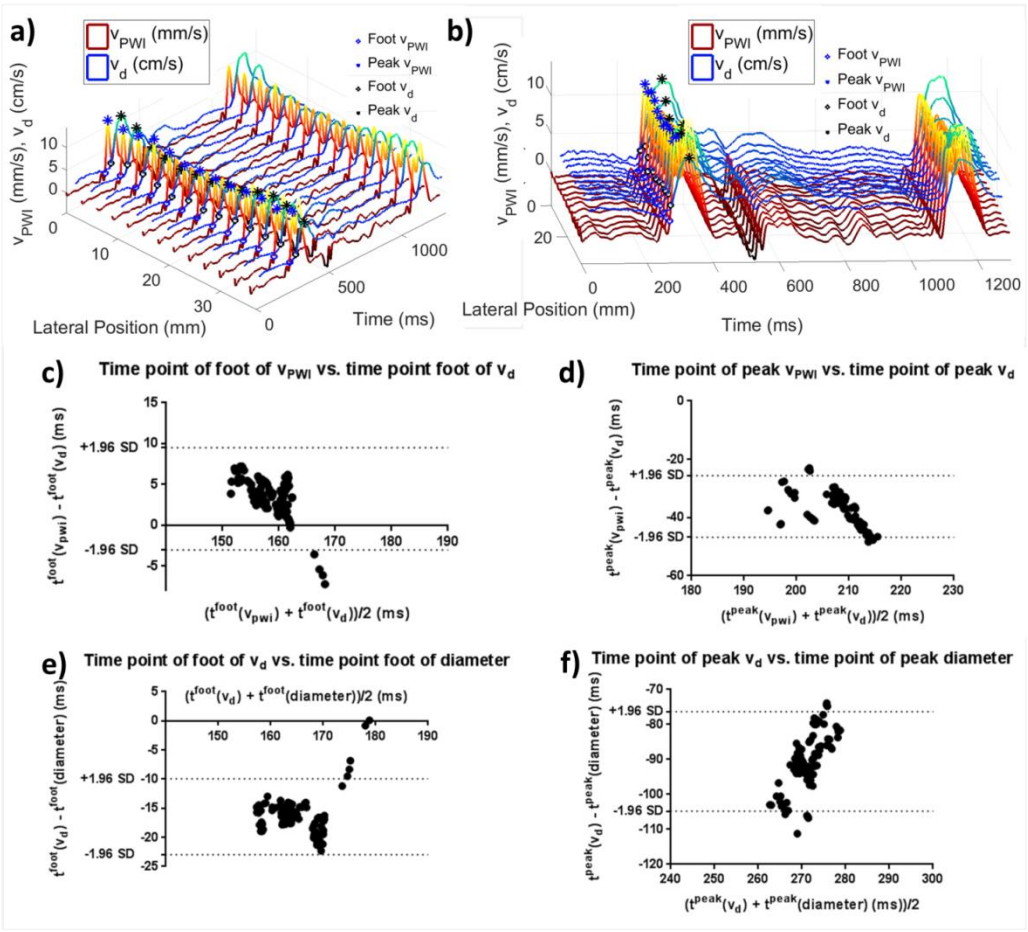

Figure 7.3: a), c) 3-D plots showing different angles of the axial wall velocity (v_{PWI}, red colormap) and the blood flow velocity (v_d, blue colormap) waveforms with the foot and peak features overlaid onto them. c) Bland-Altman plot showing the average vs. difference of time of foot of the v_{PWI} and the v_d waveforms at each lateral position of the carotids of the four healthy volunteers. d) Bland-Altman plot showing the average vs. difference of time of peak of the v_{PWI} and the v_d waveforms at each lateral position of the carotids of the four healthy volunteers. e) Bland-Altman plot showing the average vs. difference of time of foot of the v_d and the diameter waveforms at each lateral position of the carotids of the four healthy volunteers. f) Bland-Altman plot showing the average vs. difference of time of peak of the v_d and the diameter waveforms at each lateral position of the carotids of the four healthy volunteers.

Figure 7.3c) shows a Bland-Altman plot with the average foot time point of the v_{PWI} and the v_d waveforms at each lateral position on the x axis and the difference between these time points on the y axis. The foot of the v_{PWI} and the v_d waveforms at each image line was found to arrive almost simultaneously with a negligible bias (bias: 3.24 ms and 95% CI -3.03 to 9.503 ms, n=4) with the v_d foot arriving slightly earlier. This result is in agreement with [248] where the upstroke onsets of the wall and blood velocities in healthy mouse aortas were found to be synchronous. Although not explicitly stated, a similar result can be observed in [268] where the upstroke of the wall and blood velocity waveforms appears to arrive simultaneously.

Figure 7.3e) similarly shows the average timings of the foot versus the corresponding difference between the v_d and the diameter waveforms at each line. A relatively small bias can be seen with the foot of the blood velocities preceding than the diameter foot (bias: -16.45 ms and 95% CI -22.97 to -9.934 ms, n=4). In elastic arteries, diameter is linearly linked to local pressure waveform [6], [117], [221]. Thus, the aforementioned small bias is expected, given that pressure increase has been found to come at approximately the same time as increase in flow [6], [269].

Additionally, Figure 7.3d) and f) provide similar Bland-Altman plots for the timings of the foot of the v_{PWI} and the v_d waveforms (bias: -36.21 ms and 95% CI -46.78 to -25.64 ms, n=4) and the v_d and the diameter waveforms, respectively (bias: -90.54 ms and 95% CI -104.8 to -76.31 ms, n=4). The pronounced gap between the peak v_d and peak diameter has been previously reported with the peak v_d preceding the peak diameter [6], [268], [269]. This phase delay has

been attributed to the fact that in flow velocities are linked to the gradient of pressure waveform along the artery, which is in turn can be approximated by the diameter waveform [221]. Additionally, a small delay in the arrival of the peak v_{PWI} compared to the arrival of peak v_d has also been observed in a previous PWI cross-correlation based study [248].

7.2.2. PWI and vector doppler

Figure 7.4 shows the v_{PWI} and the vector flow velocity (v) frame sequences for two healthy volunteers (a) and (b). It can be seen that in both cases the propagation of the pulse wave can be tracked via the v_{PWi} and that the v follow the direction of the imaged vessel.

Additionally, using the estimated v vectors, streamlines were plotted onto the B-mode in order to provide improved visualization of the directional flow in the common carotid. The arterial centerline has also been plotted (perforated yellow line) as a reference of the vessel's axis. The resulting frames can be observed in Figure 7.5. At peak distension v_{PWI} the streamlines align with the centerline of the artery, providing an initial validation of the direction of the estimated

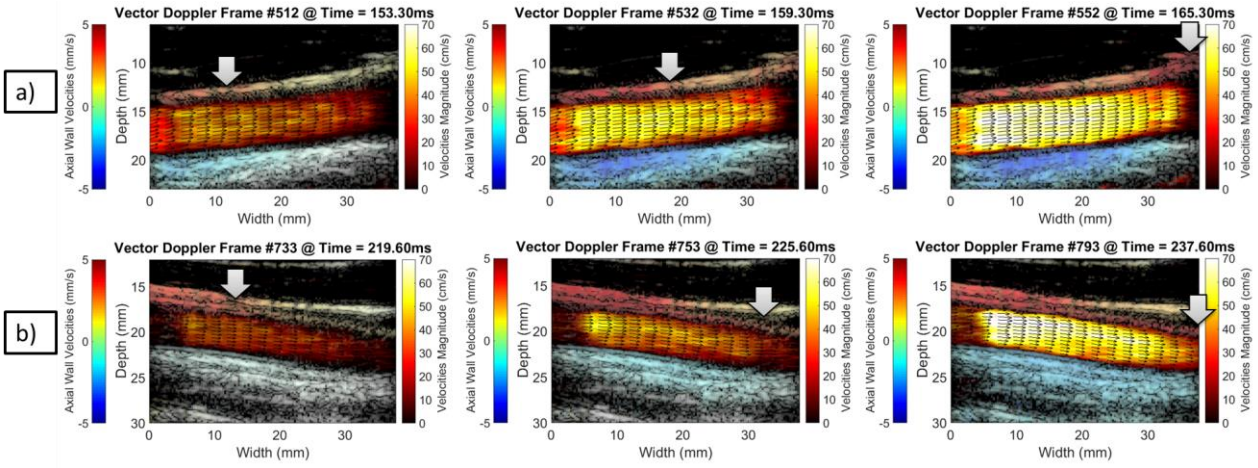

Figure 7.4: Sequences of frames illustrating the v_{PWI} and the 2-D vector flow velocities in two healthy subjects (a) and (b). Propagation of the arterial pulse wave is indicated with the gray arrows.

v. Subsequently, in order to provide quantitative validation, the slope of the centerline was obtained at each lateral position and compared to the average angle of the vectors v at peak distension of the vessel at each lateral position for the six healthy volunteers (n=6). Excellent agreement was found with a mean difference of $1^o \pm 0.6^o$ (n = 6) indicating that the vector velocities closely followed the shape of the artery at peak systole.

The mean peak magnitude of the vector velocities v were found to be reproducible with a mean of 60.0 ± 16.5 cm/s (n=6). This is in agreement with the peak systolic velocity values measured in previous studies implementing vector Doppler imaging of the common carotid artery, providing angle-independent estimates of the blood flow velocities [270]–[272].

Additionally the mean peak v_{PWI} was found to be equal to 4.68 ± 1.58 mm/s and the mean PWI derived PWV 4.87 ± 0.39m/s in six healthy subjects (n=6). Both were found to be within physiological limits [193], [213].

Finally, this technique was applied to the carotid bifurcation of a healthy subject as shown in Figure 7.6. The vector velocities follow the shape of the artery and also reveal some interesting flow patterns such as the flow hitting the flow divider in the bifurcation during systole causing some turbulence and complex flow to appear (2nd and 3rd images in Figure 7.6a and 2nd image in Figure 7.6b) [273]. Furthermore, a vortex can be seen in the carotid sinus after the peak systole revealing turbulence at the deceleration phase as also seen in other vector Doppler and biomechanics studies [274], [275].

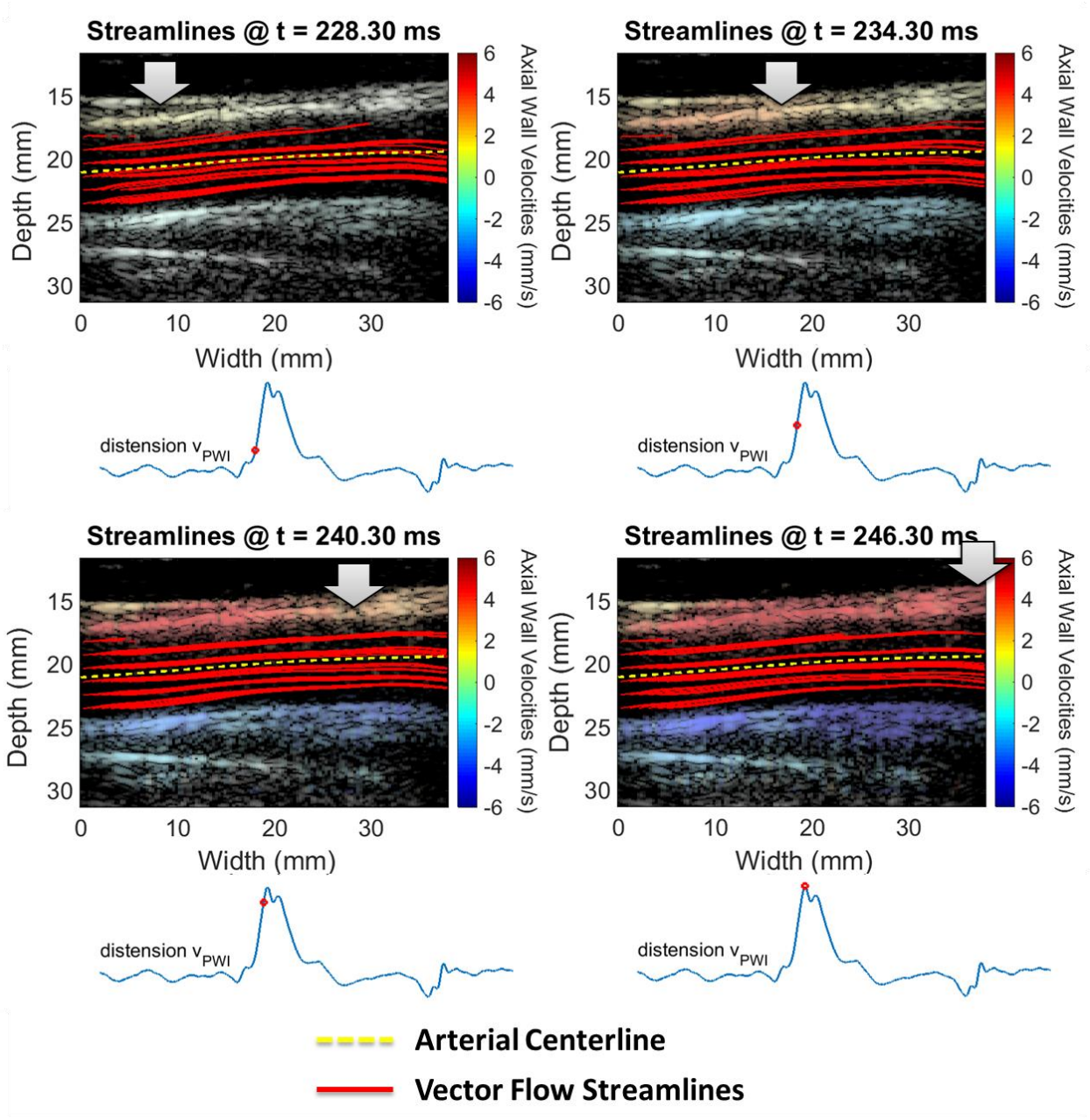

Figure 7.5: Sequence of frames with the v_{PWI} and the blood flow streamlines (red lines) overlaid onto the B-mode. The perforated line corresponds to the arterial centerline as estimated by averaging the anterior and posterior wall segmentations. Solid gray arrows indicate the progress of the pulse wave propagation. Below each image the distension v_{PWI} of at the center of the imaged vessel is shown as a time reference for each frame.

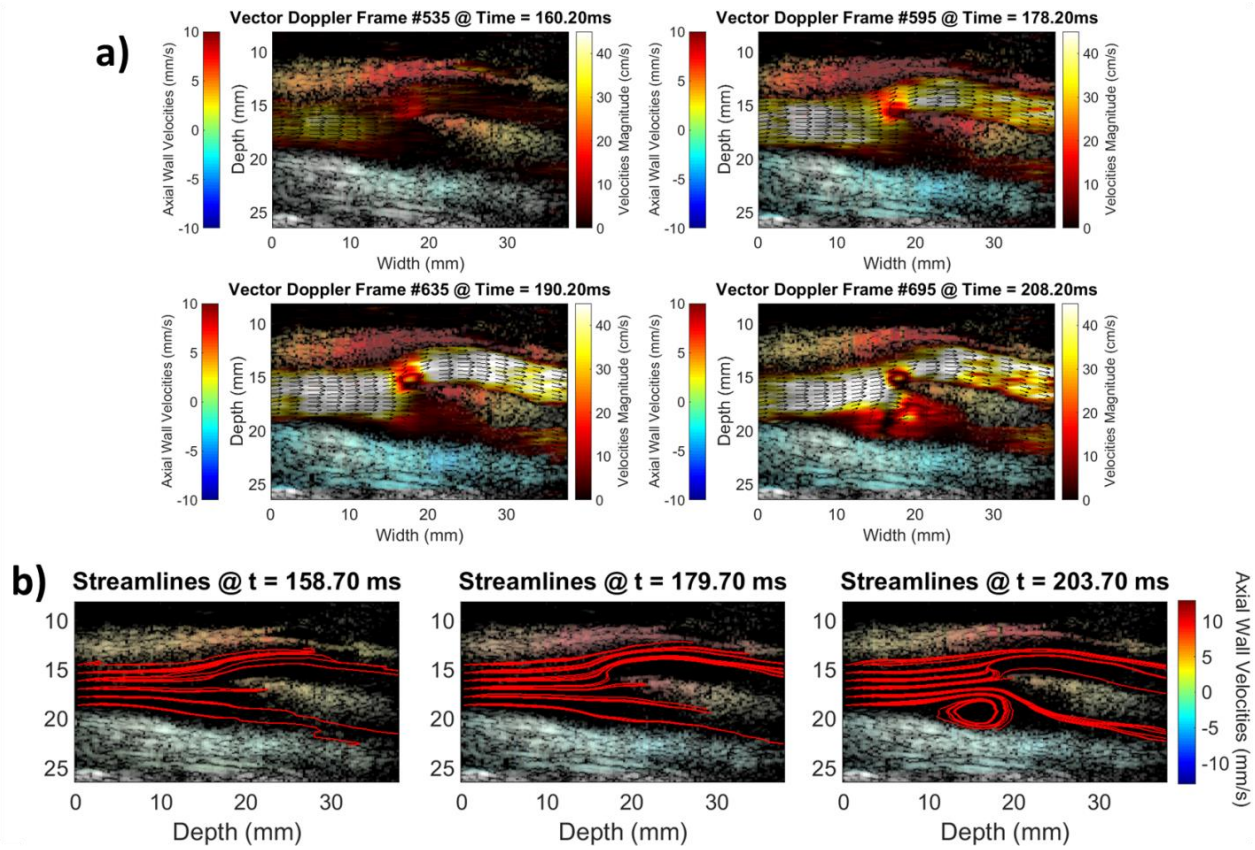

Figure 7.6: a) Sequences of frames illustrating the v_{PWI} and the 2-D vector flow velocities in the carotid bifurcation of a healthy subject. b) Sequence of frames with the v_{PWI} and the blood flow streamlines (red lines) overlaid onto the B-mode.

7.3. Conclusion and future work

In the current study, full field-of-view, high frame-rate, simultaneous and co-localized imaging of the arterial wall dynamics and color flow as well as 2-D vector flow was implemented. The feasibility of both techniques was tested in healthy subjects *in vivo.* The relationship between the timings of the flow and wall velocities was investigated at all imaged vessel wall locations and compared with existing single-location literature. Vector flow velocities were found to be aligned with the vessel's centerline during peak systole in the common carotid and interesting flow patterns were revealed in the case of the carotid bifurcation that can be linked in the

future to the corresponding v_{PWI}. This novel technique is expected to provide a plethora of data that can be used to better understand the carotid artery biomechanics as well as important additional information to determine onset and progression disease.

Ongoing work includes optimizing the acquisition parameters and sequencing in order to enable the scanning of atherosclerotic patients where the higher velocity flows require higher PRF as well as increased image SNR. Finally, an estimate of wall shear stress can be obtained by the estimated flow velocities [253] and strains can be obtained by the v_{PWI} thus enabling the study of the arterial stress-strain relationship at high spatial and temporal resolution.

Chapter 8. **Summary and Ongoing Work**

8.1. Summary and key findings

In this dissertation, Pulse Wave Imaging (PWI) was augmented and further developed into a 2-D and 3-D technique for the detection and monitoring of focal vascular disease at high temporal and spatial resolution. The improved modality was also integrated with blood flow imaging modalities aiming to render PWI a comprehensive methodology for the study of arterial biomechanics *in vivo*.

First, the spatial resolution was increased with the introduction of piecewise PWI, a modality that enabled extremely localized measurements arterial stiffness in diseased arteries. This novel technique was used to measure PWV within small sub-regions of the imaged vessel in murine aneurysmal aortas and in murine atherosclerotic aortas and carotids *in vivo*. It provided detailed PWV and stiffness maps that captured the progressive arterial stiffening caused by atherosclerosis. Additionally, the spatial variation of piecewise PWV and the corresponding decrease of the PWV's quality indicator (r^2) corroborated the arterial spatial inhomogeneity induced by both atherosclerosis and aortic aneurysms *in vivo* [172].

Additionally, a sophisticated adaptive algorithm was incorporated into piecewise PWI, enabling it to optimally partition the imaged artery into relatively homogeneous segments automatically isolating arterial inhomogeneities. Thus, the potential of adaptive PWI as a methodology

pertinent to the rapidly evolving field of computer-aided diagnosis was shown. Adaptive PWI was validated in silicone phantoms consisting of segments of varying stiffness and then tested in murine aortas *in vivo*. Increased fragmentation and higher PWVs were detected in atherosclerotic mouse aortas compared to healthy ones. Additionally, adaptive PWI was able to identify abdominal aortic aneurysm boundaries *in vivo*, validating its stiffness interface detection capabilities [276].

Furthermore, both spatial and temporal resolutions were significantly increased with the plane wave compounding implementation of PWI, allowing the acquisition of full field of view frames at over 2000 kHz. A GPU-accelerated PWI post-processing framework was developed for the processing of the big bulk of data generated by this technique. The resulting modality was validated in silicone phantoms under both static (without pulsatile flow through the phantom) and dynamic (with the phantom connected to the peristaltic pump) conditions. Furthermore, reproducibility was tested and the parameters of coherent compounding were optimized in the carotids of healthy volunteers indicating. As a result, sequences with 3-5 plane waves at approximately 1.5 kHz – 3 kHz were found to yield the best performance at capturing the transient arterial wall dynamics [193].

The optimized sequences were used in clinical cases to assess their performance in investigating the mechanical properties of atherosclerotic and post-endarterectomy carotid arteries. In the case of atherosclerotic patients undergoing carotid endarterectomy, the local

PWV and compliance imaging results were compared with the recovered atherosclerotic plaque specimens. Furthermore, PWI was used in assessing how carotid endarterectomy affects the operated carotids mechanical properties. PWVs in post-endarterectomy patients were found to be closer to the physiological range and also the homogeneity of the artery was found to be partly restored. Finally, investigation of the mechanical properties of plaques was conducted for the first time with a high-frequency transducer (18.5 MHz). Thus, high temporal and spatial resolution spatio-temporal plots and PWV maps were generated and compared to the ones generated by regular scanning [217].

A very important development presented in the current work, was the 3-D plane wave implementation of PWI (4-D PWI). This allowed the acquisition of comprehensive views of the imaged vessels at high frame rates (2 kHz). Thus, the amount of spatial information acquired from PWI acquisitions greatly increased, while also addressing several conventional PWI limitations. 4-D PWI enabled the vector of PWV, alleviating the assumption that the pulse wave propagates along the plane of imaging, present in conventional PWI. Additionally, it provided imaging of the full circumference of the investigated vessels, thus also addressing the circumferential inhomogeneity present, especially in diseased arteries. In particular, this was showcased in a plaque phantom, where the plaque was comprehensively imaged with 4-D PWI, whereas the phantom was scanned with the plaque both in and out of the imaging plane with conventional PWI. The feasibility of 4-D PWI was shown in the carotid arteries of healthy volunteers and the PWVs were compared to conventional PWI-derived PWV values [242].

Finally, PWI was integrated with flow imaging modalities such as Color and Vector Doppler. The aim was, firstly, to improve the performance of PWI in the case of atherosclerotic carotid artery disease diagnosis but also develop a modality that can be used to comprehensively study the arterial dynamics, providing crucial data for biomechanical studies. Thus, full field-of-view, high frame-rate, simultaneous and co-localized imaging of the arterial wall dynamics and color flow as well as 2-D vector flow was implemented. The feasibility of both techniques was tested in healthy subjects *in vivo*. The relationship between the timings of the flow and wall velocities was investigated at all imaged vessel wall locations and compared with existing single-location literature. Vector flow velocities were found to be aligned with the vessel's centerline during peak systole in the common carotid and interesting flow patterns were revealed in the case of the carotid bifurcation.

8.2. Ongoing work

8.2.1. Validation of PWI compliance mapping *in vivo*

In order to obtain validation of the compliance maps in vivo and also to further investigate the pressure-area relationship in vivo, the dynamic testing method described in this section will be applied to canine carotids. More specifically, the carotid arteries of the canines will be catheterized using a pressure catheter synchronized to the ultrasound acquisition system. The catheter will be moved until it appears in the ultrasound field of view. Subsequently, the synchronized ultrasound-catheter system will make acquisitions at a grid of locations on the ultrasonic image by progressively retracting the catheter after each acquisition. Consequently, the pressure-area relationships will be recovered at various points of the arterial vessel and

dynamic compliance maps will be generated that can be compared to PWI derived compliance maps from the canine carotid. An initial effort is shown in Figure 8.1.

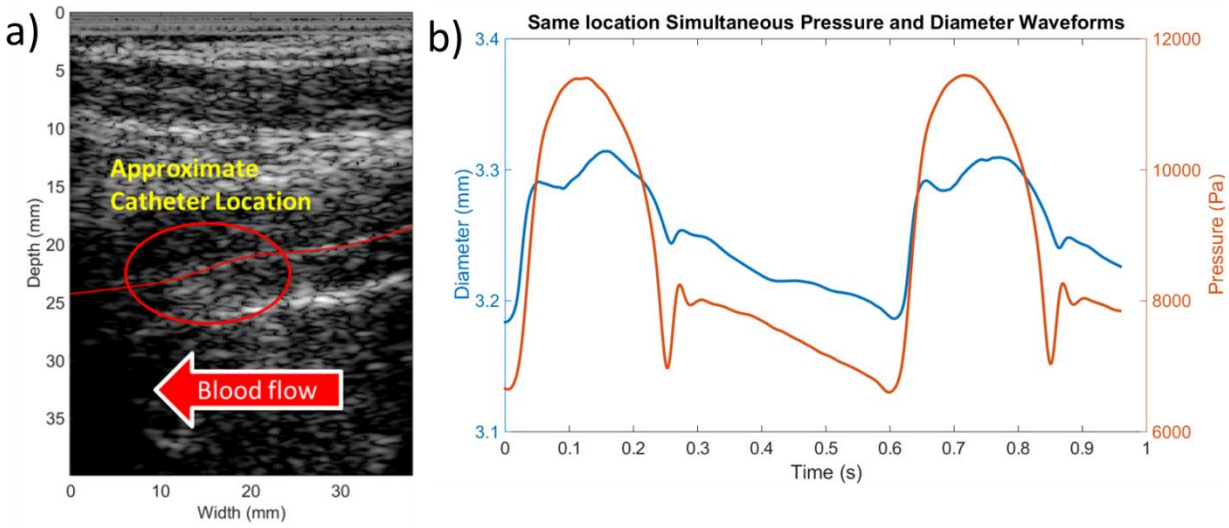

Figure 8.1: a) B-mode of a right common carotid of a canine with the catheter in the ultrasonic field of view. (The red line delineates the approximate location of the anterior arterial wall) b) Synchronized pressure and diameter Waveforms recovered from the pressure catheter and from the ultrasound data respectively at approximately the same location

8.2.2. Development of 4-D PWI for clinical use

Given the advantages that 4-D PWI presents over conventional PWI, its use in the monitoring of atherosclerotic and aneurysmal subjects will be of paramount importance. However, towards that end it needs to be further developed and augmented with modalities that will aid it to reach its full potential as a vascular diagnostic tool.

Firstly, given that 3-D plane wave imaging yields poor image quality due to the lack of focus, 3-D coherent compounding [231] would aid in producing 3-D volumes of higher quality. Furthermore, it would be advantageous in the case of PWI since tilted plane waves would aid in visualizing the lateral walls of arterial vessels. This would be beneficial in the case that plaques or other arterial wall inhomogeneities exist on the lateral walls, a site that traditional 2-D ultrasound cannot reach. Furthermore, complete comparison with the acquired endarterectomy specimens can be achieved as the full circumference of the diseased vessel is imaged at once. As a result not only longitudinal but also circumferential stiffness homogeneity will be investigated, providing insight into arterial stiffness anisotropy of atherosclerotic and aneurysmal vessels

Additionally, currently in the case of 4-D PWI only the axial component of the PWI axial wall velocities is estimated. This, even though PWI only needs the timing of the occurrence of the 50% upstroke and not the exact magnitude of the PWI axial wall velocities, induces slight angle dependence to the method. In order to overcome this limitation and also gain insight to the complex arterial wall motion, especially in the case of pathological tissue, a method to estimate the radial displacements of the vessel will be implemented by extending the GPU-accelerated cross-correlation method introduced in this work in 3-D. An initial extension of the 1-D GPU-accelerated cross-correlation algorithm has been implemented into 2-D and used to successfully track axial and lateral wall motion of arterial cross sections. Thus, the accurate tracking of lumen area is enabled. Additionally, a recent simulation study [238], where atherosclerotic carotid arteries were simulated in 3-D, has shown that estimating displacements in 3-D greatly benefitted strain estimation

Finally, integrating Doppler techniques with 4-D PWI will provide an arterial imaging modality that will provide comprehensive information on the arterial wall and flow dynamics in 3-D, enabling increased accuracy in the diagnosis and monitoring of arterial disease using ultrasound. Some initial results of integrating 4-D PWI and 3-D Color Doppler applied to a healthy common carotid *in vivo* can be seen in Figure 8.2.

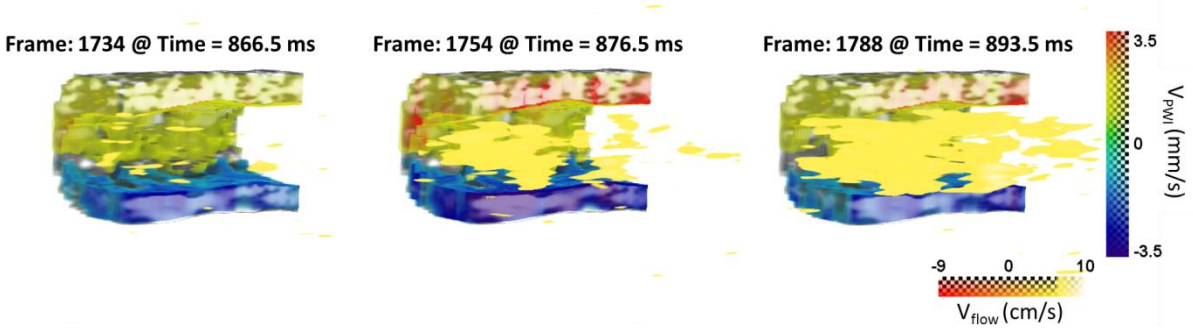

Figure 8.2: Simultaneous 4-D PWI and Color Doppler volumes depicting pulse wave propagation in both the arterial wall and the blood flow of a healthy subject. The artery has been clipped in half, in order to better illustrate the v_{PWI} and the v_{flow}.

8.2.3. Development of a wave reflection-filtering methodology

As previously stated throughout the present dissertation, wave reflections have been detrimental factors for the accurate tracking of the pulse wave propagation. Consequently, developing a methodology for locally eliminating the influence of pulse wave reflections would be quintessential for accurate stiffness mapping. Current methodologies for eliminating wave reflections include methods that are mostly based on solutions of inverse problems [170] and directional filtering [277]. Ongoing work by our group includes appropriate filtering of the spatio-temporal plots in order to keep only the higher frequency components of the pulse wave (thus the ones with the shorter wavelength) and thus minimize the merging of the forward and

the reflected waves facilitated by the long wavelength of the pulse wave [6]. Additionally, adaptive low-pass filtering may also aid in reducing the effects of reflections. Early attempts of reflection-filtering examples are shown in the spatio-temporal plots of Figure 8.3.

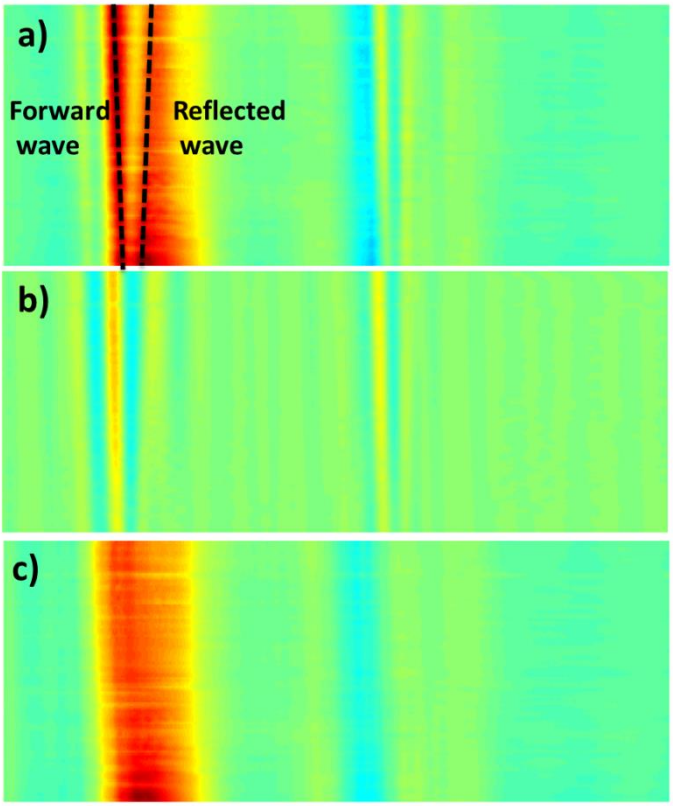

Figure 8.3: Illustration of early attempts of reflection-filtering techniques. a) Spatio-temporal plot indicating the forward and the reflected pulse wave from the bifurcation of a common carotid artery. b) High-pass filtering of the pulse wave, it can be seen that only pulse wave components with a similar wavelength to the dicrotic notch remain on the image. c) Residual pulse wave, the reflected wave seems to have been eliminated, however further investigation is needed.

8.2.4. Expansion of PWI clinical research

In order to establish PWI as a clinical tool for vascular diseases, expanded clinical research studies are needed. As mentioned in Chapter V, more atherosclerotic subjects are needed to

investigate PWI's utility as a risk assessment tool. Mechanical testing of the endarterectomy-acquired plaque samples will further test the accuracy of PWI stiffness mapping.

Additionally, longitudinal studies of subjects at high risk of developing atherosclerotic plaques (hyperlipidemic, diabetic subjects) can be used to assess adaptive PWI's early arterial stiffness inhomogeneity detection capabilities. Similar studies would also be of interest in the case of post-endarterectomy subjects, assessing the performance of the developed techniques at detecting residual or recurrent stenosis.

Further improvements of PWI in order to ensure its smooth transition to the clinic include improving the acquired B-mode images and real-time implementation. Given that clinicians rely on high-quality B-mode images to assess arterial disease, this improvement would facilitate the clinical use of PWI. Improved beamforming algorithms, and nonlinear filtering are some of the methods that have been previously implemented towards that end [205], [278], [279]. Additionally, real-time PWI would provide immediate results to the clinicians without long processing times, a typical characteristic of ultrasound imaging. With the GPU-enhanced framework implemented in the current study near-real-time times are achieved in data processing. However, manual input needs to be fully eliminated in order to achieve a fully automated, real-time modality. More specifically, our group has been working on the fully automatic detection and tracking of the arterial walls in real-time. Towards this end, dynamic contour or more sophisticated machine learning-based algorithms can be used to fully automate PWI [280], [281].

Consequently, with the aforementioned improvements and the inclusion of 3-D imaging, PWI is expected to provide comprehensive information on the mechanical properties of pathological arteries, providing clinicians with a powerful tool for the early detection of vascular abnormalities undetectable on the B-mode or Doppler, allowing for monitoring of fully developed vascular pathology and assessment of the recovery of post-operated vessels.

Bibliography

[1] Y.C. Fung, “Biomechanics - Circulation,” *Springer*, 1997. .

[2] F. N. van de Vosse and N. Stergiopulos, “Pulse Wave Propagation in the Arterial Tree,” *Annu. Rev. Fluid Mech.*, vol. 43, no. 1, pp. 467–499, Jan. 2011.

[3] W. S. Moore, *Vascular surgery : a comprehensive review*. Saunders, 1991.

[4] R. M. Alexander, *Animal mechanics*. London: Sidgwick & Jackson, 1968.

[5] R. E. Shadwick, “Mechanical design in arteries,” *J. Exp. Biol.*, vol. 202, no. 23, 1999.

[6] W. Nichols, M. F. O’Rourke, and C. Vlachopoulos, “McDonald’s blood flow in arteries, sixth edition: theoretical, experimental and clinical principles,” *CRC pr*, 2011. .

[7] N. Westerhof, J.-W. Lankhaar, and B. E. Westerhof, “The arterial Windkessel,” *Med. Biol. Eng. Comput.*, vol. 47, no. 2, pp. 131–141, Feb. 2009.

[8] N. Westerhof, G. Elzinga, and P. Sipkema, “An artificial arterial system for pumping hearts.,” *J. Appl. Physiol.*, vol. 31, no. 5, pp. 776–81, Nov. 1971.

[9] J. D. Humphrey, “VASCULAR MECHANICS, MECHANOBIOLOGY, AND REMODELING.,” *J. Mech. Med. Biol.*, vol. 9, no. 2, pp. 243–257, 2009.

[10] Y.-C. Fung, “Mechanical Properties and Active Remodeling of Blood Vessels,” in *Biomechanics*, New York, NY: Springer New York, 1993, pp. 321–391.

[11] J. E. Wagenseil and R. P. Mecham, “Elastin in large artery stiffness and hypertension,” *J. Cardiovasc. Transl. Res.*, vol. 5, no. 3, pp. 264–273, 2012.

[12] D. Mozaffarian, E. J. Benjamin, A. S. Go, D. K. Arnett, M. J. Blaha, M. Cushman, S. R. Das, S. de Ferranti, J.-P. Després, H. J. Fullerton, V. J. Howard, M. D. Huffman, C. R. Isasi, M. C.

Jiménez, S. E. Judd, B. M. Kissela, J. H. Lichtman, L. D. Lisabeth, S. Liu, R. H. Mackey, D. J. Magid, D. K. McGuire, E. R. Mohler, C. S. Moy, P. Muntner, M. E. Mussolino, K. Nasir, R. W. Neumar, G. Nichol, L. Palaniappan, D. K. Pandey, M. J. Reeves, C. J. Rodriguez, W. Rosamond, P. D. Sorlie, J. Stein, A. Towfighi, T. N. Turan, S. S. Virani, D. Woo, R. W. Yeh, and M. B. Turner, "Heart Disease and Stroke Statistics—2016 Update," *Circulation*, vol. 133, no. 4, 2016.

[13] E. J. Benjamin, M. J. Blaha, S. E. Chiuve, M. Cushman, S. R. Das, R. Deo, S. D. de Ferranti, J. Floyd, M. Fornage, C. Gillespie, C. R. Isasi, M. C. Jiménez, L. C. Jordan, S. E. Judd, D. Lackland, J. H. Lichtman, L. Lisabeth, S. Liu, C. T. Longenecker, R. H. Mackey, K. Matsushita, D. Mozaffarian, M. E. Mussolino, K. Nasir, R. W. Neumar, L. Palaniappan, D. K. Pandey, R. R. Thiagarajan, M. J. Reeves, M. Ritchey, C. J. Rodriguez, G. A. Roth, W. D. Rosamond, C. Sasson, A. Towfighi, C. W. Tsao, M. B. Turner, S. S. Virani, J. H. Voeks, J. Z. Willey, J. T. Wilkins, J. H. Wu, H. M. Alger, S. S. Wong, and P. Muntner, "Heart Disease and Stroke Statistics—2017 Update: A Report From the American Heart Association," *Circulation*, vol. 135, no. 1, pp. e1–e458, 2017.

[14] European Heart Network, "European Cardiovascular Disease Statistics 2017 edition," Brussels, 2017.

[15] N. Townsend, L. Wilson, P. Bhatnagar, K. Wickramasinghe, M. Rayner, and M. Nichols, "Cardiovascular disease in Europe: epidemiological update 2016," *Eur. Heart J.*, vol. 37, no. 42, pp. 3232–3245, Nov. 2016.

[16] L. Liu, D. Wang, K. S. L. Wong, and Y. Wang, "Stroke and stroke care in China: huge burden, significant workload, and a national priority.," *Stroke*, vol. 42, no. 12, pp. 3651–4,

Dec. 2011.

[17] N. Handa, M. Matsumoto, H. Maeda, H. Hougaku, and T. Kamada, “Ischemic stroke events and carotid atherosclerosis. Results of the Osaka Follow-up Study for Ultrasonographic Assessment of Carotid Atherosclerosis (the OSACA Study).,” *Stroke*, vol. 26, no. 10, pp. 1781–6, Oct. 1995.

[18] A. J. Grau, C. Weimar, F. Buggle, A. Heinrich, M. Goertler, S. Neumaier, J. Glahn, T. Brandt, W. Hacke, and H. C. Diener, “Risk factors, outcome, and treatment in subtypes of ischemic stroke: the German stroke data bank.,” *Stroke*, vol. 32, no. 11, pp. 2559–66, Nov. 2001.

[19] J. Golledge, R. M. Greenhalgh, and A. H. Davies, “The symptomatic carotid plaque.,” *Stroke*, vol. 31, no. 3, pp. 774–81, Mar. 2000.

[20] A. Karras, J.-P. Haymann, E. Bozec, M. Metzger, C. Jacquot, G. Maruani, P. Houillier, M. Froissart, B. Stengel, P. Guardiola, S. Laurent, P. Boutouyrie, M. Briet, and Nephro Test Study Group, “Large Artery Stiffening and Remodeling Are Independently Associated With All-Cause Mortality and Cardiovascular Events in Chronic Kidney Disease,” *Hypertension*, vol. 60, no. 6, pp. 1451–1457, Dec. 2012.

[21] V. R. Bellinazzi, J. a. Cipolli, M. V. Pimenta, P. V. Guimarães, J. a. Pio-Magalhães, O. R. Coelho-Filho, T. Biering-Sørensen, J. R. Matos-Souza, A. C. Sposito, and W. Nadruz, “Carotid flow velocity/diameter ratio is a predictor of cardiovascular events in hypertensive patients,” *J. Hypertens.*, vol. 33, no. 10, pp. 2054–2060, 2015.

[22] M. Naghavi, P. Libby, E. Falk, S. W. Casscells, S. Litovsky, J. Rumberger, J. J. Badimon, C. Stefanadis, P. Moreno, G. Pasterkamp, Z. Fayad, P. H. Stone, S. Waxman, P. Raggi, M.

Madjid, A. Zarrabi, A. Burke, C. Yuan, P. J. Fitzgerald, D. S. Siscovick, C. L. de Korte, M. Aikawa, K. E. Juhani Airaksinen, G. Assmann, C. R. Becker, J. H. Chesebro, A. Farb, Z. S. Galis, C. Jackson, I.-K. Jang, W. Koenig, R. A. Lodder, K. March, J. Demirovic, M. Navab, S. G. Priori, M. D. Rekhter, R. Bahr, S. M. Grundy, R. Mehran, A. Colombo, E. Boerwinkle, C. Ballantyne, W. Insull, R. S. Schwartz, R. Vogel, P. W. Serruys, G. K. Hansson, D. P. Faxon, S. Kaul, H. Drexler, P. Greenland, J. E. Muller, R. Virmani, P. M. Ridker, D. P. Zipes, P. K. Shah, and J. T. Willerson, "From Vulnerable Plaque to Vulnerable Patient: A Call for New Definitions and Risk Assessment Strategies: Part I," *Circulation*, vol. 108, no. 14, pp. 1664–1672, Oct. 2003.

[23] R. L. Maurice, J. Fromageau, É. Brusseau, G. Finet, G. Rioufol, and G. Cloutier, "On the Potential of the Lagrangian Estimator for Endovascular Ultrasound Elastography: In Vivo Human Coronary Artery Study," *Ultrasound Med. Biol.*, vol. 33, no. 8, pp. 1199–1205, 2007.

[24] Y. Nakashima, H. Fujii, S. Sumiyoshi, T. N. Wight, and K. Sueishi, "Early Human Atherosclerosis: Accumulation of Lipid and Proteoglycans in Intimal Thickenings Followed by Macrophage Infiltration," *Arterioscler. Thromb. Vasc. Biol.*, vol. 27, no. 5, pp. 1159–1165, Mar. 2007.

[25] I. Tabas, K. J. Williams, and J. Borén, "Subendothelial lipoprotein retention as the initiating process in atherosclerosis: update and therapeutic implications.," *Circulation*, vol. 116, no. 16, pp. 1832–44, Oct. 2007.

[26] K. J. Williams and I. Tabas, "The response-to-retention hypothesis of atherogenesis reinforced.," *Curr. Opin. Lipidol.*, vol. 9, no. 5, pp. 471–4, Oct. 1998.

[27] K. J. Williams and I. Tabas, “The response-to-retention hypothesis of early atherogenesis.,” *Arterioscler. Thromb. Vasc. Biol.*, vol. 15, no. 5, pp. 551–61, May 1995.

[28] L. R. Tannock, “ProteoglycaneLDL interactions: A novel therapeutic target?,” *Atherosclerosis*, vol. 233, pp. 232–233, 2014.

[29] P. Libby, P. M. Ridker, and G. K. Hansson, “Progress and challenges in translating the biology of atherosclerosis,” *Nature*, vol. 473, no. 7347, pp. 317–325, May 2011.

[30] P. Libby, P. M. Ridker, and G. K. Hansson, “Progress and challenges in translating the biology of atherosclerosis,” *Nature*, vol. 473, no. 7347, pp. 317–325, May 2011.

[31] T. Seimon and I. Tabas, “Mechanisms and consequences of macrophage apoptosis in atherosclerosis.,” *J. Lipid Res.*, vol. 50 Suppl, no. Suppl, pp. S382-7, Apr. 2009.

[32] C. Stefanadis, C.-K. Antoniou, D. Tsiachris, and P. Pietri, “Coronary Atherosclerotic Vulnerable Plaque: Current Perspectives.,” *J. Am. Heart Assoc.*, vol. 6, no. 3, p. e005543, Mar. 2017.

[33] T. M. Doherty, K. Asotra, L. A. Fitzpatrick, J.-H. Qiao, D. J. Wilkin, R. C. Detrano, C. R. Dunstan, P. K. Shah, and T. B. Rajavashisth, “Calcification in atherosclerosis: bone biology and chronic inflammation at the arterial crossroads.,” *Proc. Natl. Acad. Sci. U. S. A.*, vol. 100, no. 20, pp. 11201–6, Sep. 2003.

[34] M. Abedin, Y. Tintut, and L. L. Demer, “Vascular calcification: mechanisms and clinical ramifications.,” *Arterioscler. Thromb. Vasc. Biol.*, vol. 24, no. 7, pp. 1161–70, Jul. 2004.

[35] N. M. Rajamannan, T. B. Nealis, M. Subramaniam, S. Pandya, S. R. Stock, C. I. Ignatiev, T. J. Sebo, T. K. Rosengart, W. D. Edwards, P. M. McCarthy, R. O. Bonow, and T. C. Spelsberg, “Calcified rheumatic valve neoangiogenesis is associated with vascular

endothelial growth factor expression and osteoblast-like bone formation.," *Circulation*, vol. 111, no. 24, pp. 3296–301, Jun. 2005.

[36] N. Nighoghossian, L. Derex, and P. Douek, "The vulnerable carotid artery plaque: current imaging methods and new perspectives.," *Stroke*, vol. 36, no. 12, pp. 2764–72, Dec. 2005.

[37] J. N. E. Redgrave, J. K. Lovett, P. J. Gallagher, and P. M. Rothwell, "Histological Assessment of 526 Symptomatic Carotid Plaques in Relation to the Nature and Timing of Ischemic Symptoms," *Circulation*, vol. 113, no. 19, 2006.

[38] R. Virmani, A. P. Burke, A. Farb, and F. D. Kolodgie, "Pathology of the Vulnerable Plaque," *J. Am. Coll. Cardiol.*, vol. 47, no. 8, pp. C13–C18, Apr. 2006.

[39] C. K. Zarins, D. P. Giddens, B. K. Bharadvaj, V. S. Sottiurai, R. F. Mabon, and S. Glagov, "Carotid bifurcation atherosclerosis. Quantitative correlation of plaque localization with flow velocity profiles and wall shear stress," *Circ. Res.*, vol. 53, no. 4, pp. 502–514, Oct. 1983.

[40] J. Ohayon, G. Finet, S. Le Floc'h, G. Cloutier, A. M. Gharib, J. Heroux, and R. I. Pettigrew, "Biomechanics of Atherosclerotic Coronary Plaque: Site, Stability and In Vivo Elasticity Modeling.," *Ann. Biomed. Eng.*, Sep. 2013.

[41] R. S. Reneman, T. van Merode, P. Hick, and A. P. Hoeks, "Flow velocity patterns in and distensibility of the carotid artery bulb in subjects of various ages.," *Circulation*, vol. 71, no. 3, pp. 500–9, Mar. 1985.

[42] C. Slager, J. Wentzel, F. Gijsen, A. Thury, A. van der Wal, J. Schaar, and P. Serruys, "The role of shear stress in the destabilization of vulnerable plaques and related therapeutic implications," *Nat. Clin. Pract. Cardiovasc. Med.*, vol. 2, no. 9, pp. 456–464, Sep. 2005.

[43] H. C. Groen, F. J. H. Gijsen, A. van der Lugt, M. S. Ferguson, T. S. Hatsukami, A. F. W. van der Steen, C. Yuan, and J. J. Wentzel, “Plaque rupture in the carotid artery is localized at the high shear stress region: a case report.,” *Stroke*, vol. 38, no. 8, pp. 2379–81, Aug. 2007.

[44] G. A. Holzapfel, G. Sommer, and P. Regitnig, “Anisotropic mechanical properties of tissue components in human atherosclerotic plaques.,” *J. Biomech. Eng.*, vol. 126, no. 5, pp. 657–65, Oct. 2004.

[45] J. C. Grotta, “Carotid stenosis,” *N Engl J Med*, vol. 369, no. 12, pp. 1143–50, 2013.

[46] N. A. S. C. E. T. Collaborators*, “Beneficial Effect of Carotid Endarterectomy in Symptomatic Patients with High-Grade Carotid Stenosis,” *N. Engl. J. Med.*, vol. 325, no. 7, pp. 445–453, Aug. 1991.

[47] A. Halliday, A. Mansfield, J. Marro, C. Peto, R. Peto, J. Potter, D. Thomas, and MRC Asymptomatic Carotid Surgery Trial (ACST) Collaborative Group, “Prevention of disabling and fatal strokes by successful carotid endarterectomy in patients without recent neurological symptoms: randomised controlled trial.,” *Lancet (London, England)*, vol. 363, no. 9420, pp. 1491–502, May 2004.

[48] H. J. M. Barnett, D. W. Taylor, M. Eliasziw, A. J. Fox, G. G. Ferguson, R. B. Haynes, R. N. Rankin, G. P. Clagett, V. C. Hachinski, D. L. Sackett, K. E. Thorpe, H. E. Meldrum, and J. D. Spence, “Benefit of Carotid Endarterectomy in Patients with Symptomatic Moderate or Severe Stenosis,” *N. Engl. J. Med.*, vol. 339, no. 20, pp. 1415–1425, Nov. 1998.

[49] “Randomised trial of endarterectomy for recently symptomatic carotid stenosis: final results of the MRC European Carotid Surgery Trial (ECST),” *Lancet (London, England)*, vol.

351, no. 9113, pp. 1379–87, May 1998.

[50] T. Saam, T. S. Hatsukami, N. Takaya, B. Chu, H. Underhill, W. S. Kerwin, J. Cai, M. S. Ferguson, and C. Yuan, “The vulnerable, or high-risk, atherosclerotic plaque: noninvasive MR imaging for characterization and assessment.,” *Radiology*, vol. 244, no. 1, pp. 64–77, Jul. 2007.

[51] J. M. Mann and M. J. Davies, “Vulnerable Plaque,” *Circulation*, vol. 94, no. 5, 1996.

[52] A. Taylor, L. J. Shaw, Z. Fayad, D. O’Leary, B. G. Brown, S. Nissen, D. Rader, and P. Raggi, “Tracking atherosclerosis regression: a clinical tool in preventive cardiology.,” *Atherosclerosis*, vol. 180, no. 1, pp. 1–10, May 2005.

[53] S. Glagov, E. Weisenberg, C. K. Zarins, R. Stankunavicius, and G. J. Kolettis, “Compensatory enlargement of human atherosclerotic coronary arteries.,” *N. Engl. J. Med.*, vol. 316, no. 22, pp. 1371–5, May 1987.

[54] N. M. Van Popele, D. E. Grobbee, M. L. Bots, R. Asmar, J. Topouchian, R. S. Reneman, A. P. Hoeks, D. A. Van Der Kuip, A. Hofman, and J. C. Witteman, “Association between arterial stiffness and atherosclerosis: The Rotterdam study,” *Stroke*, vol. 32, no. 2, pp. 454–460, Feb. 2001.

[55] P. Tracqui, A. Broisat, J. Toczek, N. Mesnier, J. Ohayon, and L. Riou, “Mapping elasticity moduli of atherosclerotic plaque in situ via atomic force microscopy.,” *J. Struct. Biol.*, vol. 174, no. 1, pp. 115–23, Apr. 2011.

[56] T. J. Czernuszewicz, J. W. Homeister, M. C. Caughey, M. A. Farber, J. J. Fulton, P. F. Ford, W. A. Marston, R. Vallabhaneni, T. C. Nichols, and C. M. Gallippi, “Non-invasive in Vivo Characterization of Human Carotid Plaques with Acoustic Radiation Force Impulse

Ultrasound: Comparison with Histology after Endarterectomy," *Ultrasound Med. Biol.*, vol. 41, no. 3, pp. 685–697, 2015.

[57] M. Takano, K. Mizuno, K. Okamatsu, S. Yokoyama, T. Ohba, and S. Sakai, "Mechanical and structural characteristics of vulnerable plaques: analysis by coronary angioscopy and intravascular ultrasound," *J. Am. Coll. Cardiol.*, vol. 38, no. 1, pp. 99–104, Jul. 2001.

[58] S. Le Floc'h, J. Ohayon, P. Tracqui, G. Finet, A. M. Gharib, R. L. Maurice, G. Cloutier, and R. I. Pettigrew, "Vulnerable Atherosclerotic Plaque Elasticity Reconstruction Based on a Segmentation-Driven Optimization Procedure Using Strain Measurements: Theoretical Framework," *IEEE Trans. Med. Imaging*, vol. 28, no. 7, pp. 1126–1137, Jul. 2009.

[59] K. R. Nandalur, A. D. Hardie, P. Raghavan, M. J. Schipper, E. Baskurt, and C. M. Kramer, "Composition of the Stable Carotid Plaque: Insights From a Multidetector Computed Tomography Study of Plaque Volume," *Stroke*, vol. 38, no. 3, pp. 935–940, Mar. 2007.

[60] A. J. Taylor, A. P. Burke, P. G. O'Malley, A. Farb, G. T. Malcom, J. Smialek, and R. Virmani, "A comparison of the Framingham risk index, coronary artery calcification, and culprit plaque morphology in sudden cardiac death.," *Circulation*, vol. 101, no. 11, pp. 1243–8, Mar. 2000.

[61] H. M. Loree, B. J. Tobias, L. J. Gibson, R. D. Kamm, D. M. Small, and R. T. Lee, "Mechanical properties of model atherosclerotic lesion lipid pools.," *Arterioscler. Thromb. a J. Vasc. Biol.*, vol. 14, no. 2, pp. 230–4, Feb. 1994.

[62] J. R. Doherty, D. M. Dumont, G. E. Trahey, and M. L. Palmeri, "Acoustic radiation force impulse imaging of vulnerable plaques: A finite element method parametric analysis," *J. Biomech.*, vol. 46, no. 1, pp. 83–90, Jan. 2013.

[63] C. L. de Korte, S. Fekkes, A. J. Nederveen, R. Manniesing, and H. R. H. G. Hansen, “Review: Mechanical Characterization of Carotid Arteries and Atherosclerotic Plaques,” *IEEE Trans. Ultrason. Ferroelectr. Freq. Control*, vol. 63, no. 10, pp. 1613–1623, Oct. 2016.

[64] A. T. Hirsch, Z. J. Haskal, N. R. Hertzer, C. W. Bakal, M. A. Creager, J. L. Halperin, L. F. Hiratzka, W. R. C. Murphy, J. W. Olin, J. B. Puschett, K. A. Rosenfield, D. Sacks, J. C. Stanley, L. M. Taylor, C. J. White, J. White, and R. A. White, “ACC/AHA 2005 Practice Guidelines for the Management of Patients With Peripheral Arterial Disease (Lower Extremity, Renal, Mesenteric, and Abdominal Aortic),” *Circulation*, vol. 113, no. 11, 2006.

[65] M. Wassef, “Views in Research on Abdominal Aortic Aneurysms,” *Ann. N. Y. Acad. Sci.*, vol. 1085, no. 1, pp. xv–xvii, Nov. 2006.

[66] D. L. Hoyert and J. Xu, “Deaths: Preliminary Data for 2011 Table of contents,” *Natl. Vital Stat. Reports*, vol. 61, no. 6, 2011.

[67] J. D. Humphrey and G. A. Holzapfel, “Mechanics, mechanobiology, and modeling of human abdominal aorta and aneurysms,” *J. Biomech.*, vol. 45, no. 5, pp. 805–814, Mar. 2012.

[68] C. M. Crawford, K. Hurtgen-Grace, E. Talarico, and J. Marley, “Abdominal aortic aneurysm: an illustrated narrative review,” *J. Manipulative Physiol. Ther.*, vol. 26, no. 3, pp. 184–195, 2003.

[69] J. D. Humphrey and G. A. Holzapfel, “Mechanics, mechanobiology, and modeling of human abdominal aorta and aneurysms,” *J. Biomech.*, vol. 45, no. 5, pp. 805–814, 2012.

[70] J. D. (Jay D. Humphrey, *Cardiovascular solid mechanics : cells, tissues, and organs*. Springer, 2002.

[71] Y. Nakashima, Y. Shiokawa, and K. Sueishi, “Alterations of elastic architecture in human aortic dissecting aneurysm.,” *Lab. Invest.*, vol. 62, no. 6, pp. 751–60, Jun. 1990.

[72] T. J. M. Schlatmann and A. E. Becker, “Histologic changes in the normal aging aorta: Implications for dissecting aortic aneurysm,” *Am. J. Cardiol.*, vol. 39, no. 1, pp. 13–20, Jan. 1977.

[73] D. A. Vorp, “Biomechanics of abdominal aortic aneurysm,” *J. Biomech.*, vol. 40, no. 9, pp. 1887–1902, Jan. 2007.

[74] M. J. Thubrikar, M. Labrosse, F. Robic, “Mechanical properties of abdominal aortic aneurysm wall,” *J. Med. Eng. Technol.*, vol. 25, no. 4, pp. 133–142, Jan. 2001.

[75] I. S. Hatzaras, J. E. Bible, G. J. Koullias, M. Tranquilli, M. Singh, and J. A. Elefteriades, “Role of Exertion or Emotion as Inciting Events for Acute Aortic Dissection,” *Am. J. Cardiol.*, vol. 100, no. 9, pp. 1470–1472, Nov. 2007.

[76] M. J. Thubrikar, F. Robicsek, M. Labrosse, V. Chervenkoff, and B. L. Fowler, “Effect of thrombus on abdominal aortic aneurysm wall dilation and stress.,” *J. Cardiovasc. Surg. (Torino).*, vol. 44, no. 1, pp. 67–77, Feb. 2003.

[77] N. Sakalihasan, R. Limet, and O. D. Defawe, “Abdominal aortic aneurysm.,” *Lancet (London, England)*, vol. 365, no. 9470, pp. 1577–89, 1995.

[78] F. A. Lederle, G. R. Johnson, S. E. Wilson, D. J. Ballard, W. D. Jordan, J. Blebea, F. N. Littooy, J. A. Freischlag, D. Bandyk, J. H. Rapp, A. A. Salam, and Veterans Affairs Cooperative Study #417 Investigators, “Rupture rate of large abdominal aortic aneurysms in patients refusing or unfit for elective repair.,” *JAMA*, vol. 287, no. 22, pp. 2968–72, Jun. 2002.

[79] D. C. Brewster, J. L. Cronenwett, J. W. Hallett, K. W. Johnston, W. C. Krupski, J. S. Matsumura, and Joint Council of the American Association for Vascular Surgery and Society for Vascular Surgery, "Guidelines for the treatment of abdominal aortic aneurysms. Report of a subcommittee of the Joint Council of the American Association for Vascular Surgery and Society for Vascular Surgery.," *J. Vasc. Surg.*, vol. 37, no. 5, pp. 1106–17, May 2003.

[80] D. C. Brewster, J. L. Cronenwett, J. W. Hallett, K. W. Johnston, W. C. Krupski, and J. S. Matsumura, "Guidelines for the treatment of abdominal aortic aneurysms: Report of a subcommittee of the Joint Council of the American Association for Vascular Surgery and Society for Vascular Surgery," *J. Vasc. Surg.*, vol. 37, no. 5, pp. 1106–1117, May 2003.

[81] I. Van Herzeele and F. Vermassen, "Selection, technique, and follow-up: keys to success in EVAR," *The Lancet*, vol. 388, no. 10058. Elsevier, pp. 2326–2328, 12-Nov-2016.

[82] R. Patel, M. J. Sweeting, J. T. Powell, and R. M. Greenhalgh, "Endovascular versus open repair of abdominal aortic aneurysm in 15-years' follow-up of the UK endovascular aneurysm repair trial 1 (EVAR trial 1): a randomised controlled trial," *Lancet*, vol. 388, no. 10058, pp. 2366–2374, Nov. 2016.

[83] E. Salloum, A. Bertrand-Grenier, S. Lerouge, C. Kauffman, H. Héon, E. Therasse, I. Salazkin, M.-H. Roy Cardinal, G. Cloutier, and G. Soulez, "Endovascular Repair of Abdominal Aortic Aneurysm: Follow-up with Noninvasive Vascular Elastography in a Canine Model," *Radiology*, vol. 279, no. 2, pp. 410–419, May 2016.

[84] M. F. Fillinger, S. P. Marra, M. L. Raghavan, and F. E. Kennedy, "Prediction of rupture risk in abdominal aortic aneurysm during observation: Wall stress versus diameter," *J. Vasc.*

Surg., vol. 37, no. 4, pp. 724–732, Apr. 2003.

[85] D. A. Vorp, M. L. Raghavan, S. C. Muluk, M. S. Makaroun, D. L. Steed, R. Shapiro, and M. W. Webster, "Wall strength and stiffness of aneurysmal and nonaneurysmal abdominal aorta," *Ann. N. Y. Acad. Sci.*, vol. 800, no. 1 The Abdominal, pp. 274–276, Nov. 1996.

[86] S. I. Rabben, N. Stergiopulos, L. R. Hellevik, O. A. Smiseth, S. Slørdahl, S. Urheim, and B. Angelsen, "An ultrasound-based method for determining pulse wave velocity in superficial arteries," *J. Biomech.*, vol. 37, no. 10, pp. 1615–1622, Oct. 2004.

[87] M. P. Spencer and A. B. Denison, "The Aortic Flow Pulse as Related to Differential Pressure," *Circ. Res.*, vol. 4, no. 4, pp. 476–484, Jul. 1956.

[88] S. Laurent, J. Cockcroft, L. Van Bortel, P. Boutouyrie, C. Giannattasio, D. Hayoz, B. Pannier, C. Vlachopoulos, I. Wilkinson, and H. Struijker-Boudier, "Expert consensus document on arterial stiffness: methodological issues and clinical applications.," *Eur. Heart J.*, vol. 27, no. 21, pp. 2588–605, Nov. 2006.

[89] S. Laurent, P. Boutouyrie, R. Asmar, I. Gautier, B. Laloux, L. Guize, P. Ducimetiere, and A. Benetos, "Aortic stiffness is an independent predictor of all-cause and cardiovascular mortality in hypertensive patients.," *Hypertension*, vol. 37, no. 5, pp. 1236–1241, 2001.

[90] "2002-safar-independent-cardiovascular-risk.pdf." .

[91] G. Mancia, R. Fagard, K. Narkiewicz, J. Redán, A. Zanchetti, M. Böhm, T. Christiaens, R. Cifkova, G. De Backer, A. Dominiczak, M. Galderisi, D. E. Grobbee, T. Jaarsma, P. Kirchof, S. E. Kjeldsen, S. Laurent, A. J. Manolis, P. M. Nilsson, L. M. Ruilope, R. E. Schmieder, P. A. Sirnes, P. Sleight, M. Viigimaa, B. Waeber, and F. Zannad, "2013 Practice guidelines for the management of arterial hypertension of the European Society of Hypertension (ESH)

and the European Society of Cardiology (ESC)," *J. Hypertens.*, vol. 31, no. 10, pp. 1925–1938, Oct. 2013.

[92] T. R. V. for A. S. Reference Values for Arterial Stiffness' Collaboration, "Determinants of pulse wave velocity in healthy people and in the presence of cardiovascular risk factors: 'establishing normal and reference values'.," *Eur. Heart J.*, vol. 31, no. 19, pp. 2338–50, Oct. 2010.

[93] P. Tozzi, A. Corno, and D. Hayoz, "Definition of arterial compliance," *Am. J. Physiol. - Hear. Circ. Physiol.*, vol. 278, no. 4, 2000.

[94] A. Mahmud and J. Feely, "Favourable effects on arterial wave reflection and pulse pressure amplification of adding angiotensin II receptor blockade in resistant hypertension," *J. Hum. Hypertens.*, vol. 14, no. 9, pp. 541–546, Sep. 2000.

[95] W. K. Laskey and W. G. Kussmaul, "Arterial wave reflection in heart failure.," *Circulation*, vol. 75, no. 4, pp. 711–22, Apr. 1987.

[96] W. W. Nichols, S. J. Denardo, I. B. Wilkinson, C. M. McEniery, J. Cockcroft, and M. F. O'Rourke, "Effects of arterial stiffness, pulse wave velocity, and wave reflections on the central aortic pressure waveform.," *J. Clin. Hypertens. (Greenwich).*, vol. 10, no. 4, pp. 295–303, Apr. 2008.

[97] P. Albaladejo, X. Copie, P. Boutouyrie, B. Laloux, A. D. Declere, H. Smulyan, and A. Benetos, "Heart Rate, Arterial Stiffness, and Wave Reflections in Paced Patients," *Hypertension*, vol. 38, no. 4, pp. 949–952, 2001.

[98] Y. Ben-Shlomo, M. Spears, C. Boustred, M. May, S. G. Anderson, E. J. Benjamin, P. Boutouyrie, J. Cameron, C.-H. Chen, J. K. Cruickshank, S.-J. Hwang, E. G. Lakatta, S.

Laurent, J. Maldonado, G. F. Mitchell, S. S. Najjar, A. B. Newman, M. Ohishi, B. Pannier, T. Pereira, R. S. Vasan, T. Shokawa, K. Sutton-Tyrell, F. Verbeke, K.-L. Wang, D. J. Webb, T. Willum Hansen, S. Zoungas, C. M. McEniery, J. R. Cockcroft, and I. B. Wilkinson, "Aortic pulse wave velocity improves cardiovascular event prediction: an individual participant meta-analysis of prospective observational data from 17,635 subjects.," *J. Am. Coll. Cardiol.*, vol. 63, no. 7, pp. 636–46, Feb. 2014.

[99] P. Boutouyrie, A. I. Tropeano, R. Asmar, I. Gautier, A. Benetos, P. Lacolley, and S. Laurent, "Aortic Stiffness Is an Independent Predictor of Primary Coronary Events in Hypertensive Patients," *Hypertension*, vol. 39, no. 1, 2002.

[100] S. Laurent, S. Katsahian, C. Fassot, A.-I. Tropeano, I. Gautier, B. Laloux, and P. Boutouyrie, "Aortic Stiffness Is an Independent Predictor of Fatal Stroke in Essential Hypertension," *Stroke*, vol. 34, no. 5, 2003.

[101] S. C. Millasseau, A. D. Stewart, S. J. Patel, S. R. Redwood, and P. J. Chowienczyk, "Evaluation of Carotid-Femoral Pulse Wave Velocity," *Hypertension*, vol. 45, no. 2, 2005.

[102] T. Pereira, C. Correia, and J. Cardoso, "Novel Methods for Pulse Wave Velocity Measurement.," *J. Med. Biol. Eng.*, vol. 35, no. 5, pp. 555–565, 2015.

[103] T. Weber, S. Wassertheurer, B. Hametner, S. Parragh, and B. Eber, "Noninvasive methods to assess pulse wave velocity: comparison with the invasive gold standard and relationship with organ damage.," *J. Hypertens.*, vol. 33, no. 5, pp. 1023–31, May 2015.

[104] T. Willum-Hansen, J. Staessen, C. Torp-Pedersen, S. Rasmussen, L. Thijs, H. Ibsen, and J. Jeppesen, "Prognostic value of aortic pulse wave velocity as index of arterial stiffness in the general population.," *Circulation*, vol. 113, no. 5, pp. 664–70, Feb. 2006.

[105] G. F. Mitchell, S.-J. Hwang, R. S. Vasan, M. G. Larson, M. J. Pencina, N. M. Hamburg, J. A. Vita, D. Levy, and E. J. Benjamin, “Arterial stiffness and cardiovascular events: the Framingham Heart Study.,” *Circulation*, vol. 121, no. 4, pp. 505–11, Feb. 2010.

[106] F. U. S. Mattace-Raso, “Arterial Stiffness and Risk of Coronary Heart Disease and Stroke: The Rotterdam Study,” *Circulation*, vol. 113, no. 5, pp. 657–663, Feb. 2006.

[107] A. Adji, M. F. O’Rourke, and M. Namasivayam, “Arterial stiffness, its assessment, prognostic value, and implications for treatment.,” *Am. J. Hypertens.*, vol. 24, no. 1, pp. 5–17, Jan. 2011.

[108] M. Karamanoglu, “Errors in Estimating Propagation Distances in Pulse Wave Velocity,” *Hypertension*, vol. 41, no. 6, 2003.

[109] J. Xu, “Do we need a better approach for measuring pulse-wave velocity?,” *Ultrasound Med. Biol.*, vol. 29, no. 9, p. 1373, Sep. 2003.

[110] E. Hermeling, K. D. Reesink, R. S. Reneman, and A. P. Hoeks, “Confluence of incident and reflected waves interferes with systolic foot detection of the carotid artery distension waveform,” *J. Hypertens.*, vol. 26, no. 12, pp. 2374–2380, Dec. 2008.

[111] P. Segers, J. Kips, B. Trachet, A. Swillens, S. Vermeersch, D. Mahieu, E. Rietzschel, M. De Buyzere, and L. Van Bortel, “Limitations and pitfalls of non-invasive measurement of arterial pressure wave reflections and pulse wave velocity,” *Artery Res.*, vol. 3, no. 2, pp. 79–88, 2009.

[112] B. E. Westerhof, J. P. van den Wijngaard, J. P. Murgo, and N. Westerhof, “Location of a reflection site is elusive: consequences for the calculation of aortic pulse wave velocity.,” *Hypertens. (Dallas, Tex. 1979)*, vol. 52, no. 3, pp. 478–83, Sep. 2008.

[113] V. Herold, M. Parczyk, P. Mörchel, C. H. Ziener, G. Klug, W. R. Bauer, E. Rommel, and P. M. Jakob, “In vivo measurement of local aortic pulse-wave velocity in mice with mr microscopy at 17.6 tesla.,” *Magn. Reson. Med.*, vol. 61, no. 6, pp. 1293–9, Jun. 2009.

[114] M. Markl, W. Wallis, S. Brendecke, J. Simon, A. Frydrychowicz, and A. Harloff, “Estimation of global aortic pulse wave velocity by flow-sensitive 4D MRI,” *Magn. Reson. Med.*, vol. 63, no. 6, pp. 1575–1582, Apr. 2010.

[115] H.-Y. Yu, H.-H. Peng, J.-L. Wang, C.-Y. Wen, and W.-Y. I. Tseng, “Quantification of the pulse wave velocity of the descending aorta using axial velocity profiles from phase-contrast magnetic resonance imaging,” *Magn. Reson. Med.*, vol. 56, no. 4, pp. 876–883, Oct. 2006.

[116] B. D. Bolster, E. Atalar, C. J. Hardy, and E. R. McVeigh, “Accuracy of arterial pulse-wave velocity measurement using MR.,” *J. Magn. Reson. Imaging*, vol. 8, no. 4, pp. 878–88.

[117] A. Eriksson, E. Greiff, T. Loupas, M. Persson, and P. Pesque, “Arterial pulse wave velocity with tissue doppler imaging,” *Ultrasound Med. Biol.*, vol. 28, no. 5, pp. 571–580, May 2002.

[118] C. J. Hartley, G. E. Taffet, L. H. Michael, T. T. Pham, and M. L. Entman, “Noninvasive determination of pulse-wave velocity in mice.,” *Am. J. Physiol.*, vol. 273, no. 1 Pt 2, pp. H494–H500, 1997.

[119] P. G. de Jong, T. Arts, A. P. Hoeks, and R. S. Reneman, “Determination of tissue motion velocity by correlation interpolation of pulsed ultrasonic echo signals.,” *Ultrason. Imaging*, vol. 12, no. 2, pp. 84–98, Apr. 1990.

[120] P. J. Brands, J. M. Willigers, L. A. Ledoux, R. S. Reneman, and A. P. Hoeks, “A noninvasive

method to estimate pulse wave velocity in arteries locally by means of ultrasound.," *Ultrasound Med. Biol.*, vol. 24, no. 9, pp. 1325–35, Nov. 1998.

[121] J. . Meinders, P. . Brands, J. . Willigers, L. Kornet, and A. P. . Hoeks, "Assessment of the spatial homogeneity of artery dimension parameters with high frame rate 2-D B-mode," *Ultrasound Med. Biol.*, vol. 27, no. 6, pp. 785–794, 2001.

[122] D. Christensen, *Ultrasonic bioinstrumentation*. Wiley, 1988.

[123] R. S. C. Cobbold, "Foundations of Biomedical Ultrasound," *Oxford Univ. Press*, pp. 45–51, 2007.

[124] N. Handa, M. Matsumoto, H. Maeda, H. Hougaku, S. Ogawa, R. Fukunaga, S. Yoneda, K. Kimura, and T. Kamada, "Ultrasonic evaluation of early carotid atherosclerosis.," *Stroke*, vol. 21, no. 11, pp. 1567–72, Nov. 1990.

[125] R. Kagawa, K. Moritake, T. Shima, and Y. Okada, "Carotid surgery versus medical therapy in asymptomatic carotid stenosis. The CASANOVA Study Group.," *Stroke*, vol. 22, no. 10, pp. 1229–35, Oct. 1991.

[126] P. R. Hoskins and D. A. Kenwright, "Recent developments in vascular ultrasound technology.," *Ultrasound*, vol. 23, no. 3, pp. 158–65, Aug. 2015.

[127] J. F. Desforges and C. B. Ernst, "Abdominal Aortic Aneurysm," *N. Engl. J. Med.*, vol. 328, no. 16, pp. 1167–1172, Apr. 1993.

[128] W. J. Zwiebel, C. W. Austin, J. F. Sackett, and C. M. Strother, "Correlation of high-resolution, B-mode and continuous-wave Doppler sonography with arteriography in the diagnosis of carotid stenosis.," *Radiology*, vol. 149, no. 2, pp. 523–32, Nov. 1983.

[129] J. A. Jensen, *Estimation of Blood Velocities Using Ultrasound: A Signal Processing*

Approach. Cambridge: Cambridge University Press, 1996.

[130] P. Hoskins, K. Martin, and A. Thrush, *Diagnostic Ultrasound: Physics and Equipment*. Cambridge University Press, 2010.

[131] D. Evans, J. Jensen, and M. Nielsen, "Ultrasonic colour Doppler imaging.," no. May, 2011.

[132] C. Kasai, K. Namekawa, A. Koyano, and R. Omoto, "Real-Time Two-Dimensional Blood Flow Imaging Using an Autocorrelation Technique," *IEEE Trans. SONICS Ultrason.*, no. 3, 1985.

[133] T. Loupas, J. T. Powers, and R. W. Gill, "Axial velocity estimator for ultrasound blood flow imaging, based on a full evaluation of the Doppler equation by means of a two-dimensional autocorrelation approach," *IEEE Trans. Ultrason. Ferroelectr. Freq. Control*, vol. 42, no. 4, pp. 672–688, 1995.

[134] A. V. Alexandrov, D. S. Brodie, A. McLean, P. Hamilton, J. Murphy, and P. N. Burns, "Correlation of Peak Systolic Velocity and Angiographic Measurement of Carotid Stenosis Revisited," *Stroke*, vol. 28, no. 2, 1997.

[135] T. Wada, K. Kodaira, K. Fujishiro, and T. Okamura, "Correlation of common carotid flow volume measured by ultrasonic quantitative flowmeter with pathological findings.," *Stroke.*, vol. 22, no. 3, pp. 319–23, Mar. 1991.

[136] J. R. Grajo and R. G. Barr, "Duplex Doppler Sonography of the Carotid Artery," *Ultrasound Q.*, vol. 23, no. 3, pp. 199–202, Sep. 2007.

[137] E. G. Grant, C. B. Benson, G. L. Moneta, A. V. Alexandrov, J. D. Baker, E. I. Bluth, B. A. Carroll, M. Eliasziw, J. Gocke, B. S. Hertzberg, S. Katanick, L. Needleman, J. Pellerito, J. F. Polak, K. S. Rholl, D. L. Wooster, and R. E. Zierler, "Carotid Artery Stenosis: Gray-Scale and

Doppler US Diagnosis—Society of Radiologists in Ultrasound Consensus Conference," *Radiology*, vol. 229, no. 2, pp. 340–346, Nov. 2003.

[138] G. M. Hathout, J. R. Fink, S. M. El-Saden, and E. G. Grant, "Sonographic NASCET index: a new doppler parameter for assessment of internal carotid artery stenosis.," *AJNR. Am. J. Neuroradiol.*, vol. 26, no. 1, pp. 68–75, Jan. 2005.

[139] J.-L. Gennisson, T. Deffieux, M. Fink, and M. Tanter, "Ultrasound elastography: Principles and techniques," *Diagn. Interv. Imaging*, vol. 94, no. 5, pp. 487–495, 2013.

[140] J. Ophir, S. K. Alam, B. Garra, F. Kallel, E. Konofagou, T. Krouskop, and T. Varghese, "Elastography: Ultrasonic estimation and imaging of the elastic properties of tissues," *Proc. Inst. Mech. Eng. Part H J. Eng. Med.*, vol. 213, no. 3, pp. 203–233, Mar. 1999.

[141] C. L. De Korte, E. I. Cespedes, a. F. W. Van Der Steen, G. Pasterkamp, and N. Bom, "Intravascular ultrasound elastography: Assessment and imaging of elastic properties of diseased arteries and vulnerable plaque," *Eur. J. Ultrasound*, vol. 7, no. 3, pp. 219–224, 1998.

[142] C. L. de Korte, G. Pasterkamp, A. F. van der Steen, H. A. Woutman, and N. Bom, "Characterization of plaque components with intravascular ultrasound elastography in human femoral and coronary arteries in vitro.," *Circulation*, vol. 102, no. 6, pp. 617–23, Aug. 2000.

[143] H. Kanai, H. Hasegawa, M. Ichiki, F. Tezuka, and Y. Koiwa, "Elasticity imaging of atheroma with transcutaneous ultrasound: Preliminary study," *Circulation*, vol. 107, no. 24, pp. 3018–3021, 2003.

[144] R. L. Maurice, J. Ohayon, Y. Frétigny, M. Bertrand, G. Soulez, and G. Cloutier,

"Noninvasive Vascular Elastography: Theoretical Framework," *IEEE Trans. Med. Imaging*, vol. 23, no. 2, pp. 164–180, 2004.

[145] H. H. G. Hansen, R. G. P. Lopata, T. Idzenga, and C. L. de Korte, "An Angular Compounding Technique Using Displacement Projection for Noninvasive Ultrasound Strain Imaging of Vessel Cross-Sections," *Ultrasound Med. Biol.*, vol. 36, no. 11, pp. 1947–1956, Nov. 2010.

[146] J. Poree, D. Garcia, B. Chayer, J. Ohayon, and G. Cloutier, "Noninvasive vascular elastography with plane strain incompressibility assumption using ultrafast coherent compound plane pave imaging.," *IEEE Trans. Med. Imaging*, vol. 34, no. 12, pp. 2618–31, Dec. 2015.

[147] E. A. Bunting, J. Provost, and E. E. Konofagou, "Stochastic precision analysis of 2D cardiac strain estimation in vivo.," *Phys. Med. Biol.*, vol. 59, no. 22, pp. 6841–58, Nov. 2014.

[148] K. Nightingale, M. S. Soo, R. Nightingale, and G. Trahey, "Acoustic radiation force impulse imaging: in vivo demonstration of clinical feasibility.," *Ultrasound Med. Biol.*, vol. 28, no. 2, pp. 227–35, Feb. 2002.

[149] D. Dumont, R. H. Behler, T. C. Nichols, E. P. Merricks, and C. M. Gallippi, "ARFI imaging for noninvasive material characterization of atherosclerosis.," *Ultrasound Med. Biol.*, vol. 32, no. 11, pp. 1703–11, Nov. 2006.

[150] T. J. Czernuszewicz, J. W. Homeister, M. C. Caughey, M. A. Farber, J. J. Fulton, P. F. Ford, W. A. Marston, R. Vallabhaneni, T. C. Nichols, and C. M. Gallippi, "Non-invasive in vivo characterization of human carotid plaques with acoustic radiation force impulse ultrasound: comparison with histology after endarterectomy.," *Ultrasound Med. Biol.*, vol. 41, no. 3, pp. 685–97, Mar. 2015.

[151] R. H. Behler, T. C. Nichols, H. Zhu, E. P. Merricks, and C. M. Gallippi, “ARFI Imaging for Noninvasive Material Characterization of Atherosclerosis Part II: Toward In Vivo Characterization,” *Ultrasound Med. Biol.*, vol. 35, no. 2, pp. 278–295, 2009.

[152] J. Bercoff, M. Tanter, and M. Fink, “Supersonic Shear Imaging: A New Technique for Soft Tissue Elasticity Mapping,” *ieee Trans. Ultrason. Ferroelectr. Freq. Control*, vol. 51, no. 4, 2004.

[153] M. Couade, M. Pernot, C. Prada, E. Messas, J. Emmerich, P. Bruneval, A. Criton, M. Fink, and M. Tanter, “Quantitative Assessment of Arterial Wall Biomechanical Properties Using Shear Wave Imaging,” *Ultrasound Med. Biol.*, vol. 36, no. 10, pp. 1662–1676, Oct. 2010.

[154] E. Widman, E. Maksuti, D. Larsson, M. W. Urban, A. Bjällmark, and M. Larsson, “Shear wave elastography plaque characterization with mechanical testing validation: a phantom study,” *Phys. Med. Biol.*, vol. 60, no. 8, pp. 3151–3174, Apr. 2015.

[155] E. Maksuti, E. Widman, D. Larsson, M. W. Urban, M. Larsson, and A. Bjällmark, “Arterial Stiffness Estimation by Shear Wave Elastography: Validation in Phantoms with Mechanical Testing,” *Ultrasound Med. Biol.*, vol. 42, no. 1, pp. 308–321, Jan. 2016.

[156] K. V Ramnarine, J. W. Garrard, B. Kanber, S. Nduwayo, T. C. Hartshorne, and T. G. Robinson, “Shear wave elastography imaging of carotid plaques: feasible, reproducible and of clinical potential,” *Cardiovasc. Ultrasound*, vol. 12, no. 1, p. 49, Dec. 2014.

[157] D. A. Shcherbakova, A. Caenen, A. Swillens, P. Segers, S. Chatelin, C. Papadacci, and M. Pernot, “Experimental study on the effect of the cylindrical vessel geometry on arterial shear wave elastography,” in *2015 IEEE International Ultrasonics Symposium (IUS)*, 2015, pp. 1–4.

[158] J. M. Meinders, L. Kornet, P. J. Brands, and A. P. G. Hoeks, “Assessment of Local Pulse Wave Velocity in Arteries Using 2D Distension Waveforms,” *Ultrason. Imaging*, vol. 23, no. 4, pp. 199–215, Oct. 2001.

[159] K. Fujikura, J. Luo, V. Gamarnik, M. Pernot, R. Fukumoto, M. D. Tilson, and E. E. Konofagou, “A novel noninvasive technique for pulse-wave imaging and characterization of clinically-significant vascular mechanical properties in vivo.,” *Ultrason. Imaging*, vol. 29, no. 3, pp. 137–54, Jul. 2007.

[160] I. Cespedes, Y. Huang, J. Ophir, S. Spratt, I. Céspedes, Y. Huang, J. Ophir, and S. Spratt, “Methods for estimation of subsample time delays of digitized echo signals.,” *Ultrason. Imaging*, vol. 17, no. 1995, pp. 142–171, 1995.

[161] P. de Jong, T. Arts, A. Hoeks, and R. Reneman, “Determination of tissue motion velocity by correlation interpolation of pulsed ultrasonic echo signals,” *Ultrason. Imaging*, vol. 12, no. 2, pp. 84–98, Apr. 1990.

[162] J. Luo and E. Konofagou, “A fast normalized cross-correlation calculation method for motion estimation.,” *IEEE Trans. Ultrason. Ferroelectr. Freq. Control*, vol. 57, no. 6, pp. 1347–57, Jun. 2010.

[163] J. Luo, K. Fujikura, L. S. Tyrie, M. D. Tilson, and E. E. Konofagou, “Pulse wave imaging of normal and aneurysmal abdominal aortas in vivo.,” *IEEE Trans. Med. Imaging*, vol. 28, no. 4, pp. 477–86, Apr. 2009.

[164] S. D. Nandlall, M. P. Goldklang, A. Kalashian, N. A. Dangra, J. M. D’Armiento, and E. E. Konofagou, “Monitoring and Staging Abdominal Aortic Aneurysm Disease With Pulse Wave Imaging,” *Ultrasound Med. Biol.*, vol. 40, no. 10, pp. 2404–2414, Oct. 2014.

[165] S. D. Nandlall and E. E. Konofagou, “Assessing the Stability of Aortic Aneurysms with Pulse Wave Imaging,” *Radiology*, vol. 281, no. 3, pp. 772–781, Dec. 2016.

[166] S. D. Nandlall, M. P. Goldklang, A. Kalashian, N. A. Dangra, J. M. D’Armiento, and E. E. Konofagou, “Monitoring and Staging Abdominal Aortic Aneurysm Disease With Pulse Wave Imaging,” *Ultrasound Med. Biol.*, vol. 40, no. 10, pp. 2404–2414, Oct. 2014.

[167] J. Vappou, J. Luo, and E. E. Konofagou, “Pulse wave imaging for noninvasive and quantitative measurement of arterial stiffness in vivo.,” *Am. J. Hypertens.*, vol. 23, no. 4, pp. 393–8, Apr. 2010.

[168] R. X. Li, J. Luo, S. K. Balaram, F. a Chaudhry, D. Shahmirzadi, and E. E. Konofagou, “Pulse wave imaging in normal, hypertensive and aneurysmal human aortas in vivo: a feasibility study.,” *Phys. Med. Biol.*, vol. 58, no. 13, pp. 4549–62, 2013.

[169] A. Eriksson, E. Greiff, T. Loupas, M. Persson, and P. Pesque, “Arterial pulse wave velocity with tissue Doppler imaging.,” *Ultrasound Med. Biol.*, vol. 28, no. 5, pp. 571–80, May 2002.

[170] M. Mcgarry, R. Li, I. Apostolakis, P. Nauleau, and E. E. Konofagou, “An inverse approach to determining spatially varying arterial compliance using ultrasound imaging,” *Phys. Med. Biol.*, vol. 61, no. 15, pp. 5486–5507, Aug. 2016.

[171] M. McGarry, P. Nauleau, I. Apostolakis, and E. Konofagou, “In vivo repeatability of the pulse wave inverse problem in human carotid arteries,” *J. Biomech.*, vol. 64, pp. 136–144, 2017.

[172] I. Z. Apostolakis, S. D. Nandlall, and E. E. Konofagou, “Piecewise pulse wave imaging (ppwi) for detection and monitoring of focal vascular disease in murine aortas and

carotids in vivo.," *IEEE Trans. Med. Imaging*, vol. 35, no. 1, pp. 13–28, Jan. 2016.

[173] Y. Nakashima, a. S. Plump, E. W. Raines, J. L. Breslow, and R. Ross, "ApoE-deficient mice develop lesions of all phases of atherosclerosis throughout the arterial tree," *Arterioscler. Thromb. Vasc. Biol.*, vol. 14, no. 1, pp. 133–140, Jan. 1994.

[174] M. Pernot, K. Fujikura, S. D. Fung-Kee-Fung, and E. E. Konofagou, "ECG-gated, mechanical and electromechanical wave imaging of cardiovascular tissues in vivo.," *Ultrasound Med. Biol.*, vol. 33, no. 7, pp. 1075–85, Jul. 2007.

[175] R. X. Li, W. Qaqish, and E. E. Konofagou, "Performance assessment of pulse wave imaging using conventional ultrasound in canine aortas ex vivo and normal human arteries in vivo.," *Artery Res.*, vol. 11, pp. 19–28, Sep. 2015.

[176] V. Herold, J. Wellen, C. H. Ziener, T. Weber, K.-H. Hiller, P. Nordbeck, E. Rommel, A. Haase, W. R. Bauer, P. M. Jakob, and S. K. Sarkar, "In vivo comparison of atherosclerotic plaque progression with vessel wall strain and blood flow velocity in apoE(-/-) mice with MR microscopy at 17.6 T.," *MAGMA*, vol. 22, no. 3, pp. 159–66, Jun. 2009.

[177] Y. Wang, M. Halks-miller, R. Vergona, M. E. Sullivan, R. Fitch, C. Mallari, B. Martin-mcnulty, V. Cunha, A. Freay, G. M. Rubanyi, K. Kauser, R. O. N. Vergona, B. M. C. Nulty, and V. D. A. Cunha, "Increased aortic stiffness assessed by pulse wave velocity in apolipoprotein E-deficient mice Increased aortic stiffness assessed by pulse wave velocity in apolipoprotein E-deficient mice," 2012.

[178] A. Agianniotis and N. Stergiopulos, "Wall properties of the apolipoprotein E-deficient mouse aorta.," *Atherosclerosis*, vol. 223, no. 2, pp. 314–20, Aug. 2012.

[179] D. J. Farrar, M. G. Bond, J. K. Sawyer, and H. D. Green, "Pulse wave velocity and

morphological changes associated with early atherosclerosis progression in the aortas of cynomolgus monkeys.," *Cardiovasc. Res.*, vol. 18, no. 2, pp. 107–18, Feb. 1984.

[180] D. J. Farrar, M. G. Bond, W. a Riley, and J. K. Sawyer, "Anatomic correlates of aortic pulse wave velocity and carotid artery elasticity during atherosclerosis progression and regression in monkeys.," *Circulation*, vol. 83, no. 5, pp. 1754–1763, 1991.

[181] M. Cecelja and P. Chowienczyk, "Role of arterial stiffness in cardiovascular disease.," *JRSM Cardiovasc. Dis.*, vol. 1, no. 4, Jul. 2012.

[182] W. R. Mower, W. J. Quiñones, and S. S. Gambhir, "Effect of intraluminal thrombus on abdominal aortic aneurysm wall stress," *J. Vasc. Surg.*, vol. 26, no. 4, pp. 602–608, 1997.

[183] A. Daugherty, M. W. Manning, and L. A. Cassis, "Angiotensin II promotes atherosclerotic lesions and aneurysms in apolipoprotein E–deficient mice," *J. Clin. Invest.*, vol. 105, no. 11, pp. 1605–1612, Jun. 2000.

[184] D. M. Tham, B. Martin-McNulty, Y.-X. Wang, V. Da Cunha, D. W. Wilson, C. N. Athanassious, A. F. Powers, M. E. Sullivan, and J. C. Rutledge, "Angiotensin II injures the arterial wall causing increased aortic stiffening in apolipoprotein E-deficient mice.," *Am. J. Physiol. Regul. Integr. Comp. Physiol.*, vol. 283, no. 6, pp. R1442–R1449, 2002.

[185] C. J. Hartley, G. E. Taffet, L. H. Michael, T. T. Pham, and M. L. Entman, "Noninvasive determination of pulse-wave velocity in mice.," *Am. J. Physiol.*, vol. 273, no. 1 Pt 2, pp. H494-500, Jul. 1997.

[186] L. C. Santelices, S. J. Calano, J. C. Erhart, R. L. Prantil, J. L. Haney, D. a Vorp, and J. M. Ahearn, "Experimental system for ex vivo measurement of murine aortic stiffness.," *Physiol. Meas.*, vol. 28, no. 8, pp. N39–N49, 2007.

[187] X. Guo and G. S. Kassab, “Variation of mechanical properties along the length of the aorta in C57bl/6 mice.,” *Am. J. Physiol. Heart Circ. Physiol.*, vol. 285, no. 6, pp. H2614–H2622, 2003.

[188] J. Luo, R. X. Li, and E. E. Konofagou, “Pulse wave imaging of the human carotid artery: an in vivo feasibility study.,” *IEEE Trans. Ultrason. Ferroelectr. Freq. Control*, vol. 59, no. 1, pp. 174–81, Jan. 2012.

[189] L. Gan, J. Grönros, U. Hägg, J. Wikström, C. Theodoropoulos, P. Friberg, and R. Fritsche-Danielson, “Non-invasive real-time imaging of atherosclerosis in mice using ultrasound biomicroscopy.,” *Atherosclerosis*, vol. 190, no. 2, pp. 313–20, Feb. 2007.

[190] M. Ni, M. Zhang, S. F. Ding, W. Q. Chen, and Y. Zhang, “Micro-ultrasound imaging assessment of carotid plaque characteristics in apolipoprotein-E knockout mice.,” *Atherosclerosis*, vol. 197, no. 1, pp. 64–71, Mar. 2008.

[191] R. S. Reneman, T. van Merode, P. J. Brands, and A. P. Hoeks, “Inhomogeneities in arterial wall properties under normal and pathological conditions.,” *J. Hypertens.*, vol. 10, no. 6, pp. S35–S39, 1992.

[192] C. Huang, Q. He, M. Huang, L. Huang, X. Zhao, C. Yuan, and J. Luo, “Non-Invasive Identification of Vulnerable Atherosclerotic Plaques Using Texture Analysis in Ultrasound Carotid Elastography: An In Vivo Feasibility Study Validated by Magnetic Resonance Imaging,” *Ultrasound Med. Biol.*, vol. 43, no. 4, pp. 817–830, Apr. 2017.

[193] I. Z. Apostolakis, M. D. J. McGarry, E. A. Bunting, and E. E. Konofagou, “Pulse wave imaging using coherent compounding in a phantom and in vivo,” *Phys. Med. Biol.*, vol. 62, no. 5, pp. 1700–1730, Mar. 2017.

[194] B. Denarie, T. A. Tangen, I. K. Ekroll, N. Rolim, H. Torp, T. Bjastad, and L. Lovstakken, "Coherent plane wave compounding for very high frame rate ultrasonography of rapidly moving targets," *IEEE Trans. Med. Imaging*, vol. 32, no. 7, pp. 1265–1276, 2013.

[195] R. Bellman, "On a Routing Problem," *Quarterly of Applied Mathematics*, vol. 16. Brown University, pp. 87–90, 1958.

[196] R. D. Latham, N. Westerhof, P. Sipkema, B. J. Rubal, P. Reuderink, and J. P. Murgo, "Regional wave travel and reflections along the human aorta: a study with six simultaneous micromanometric pressures.," *Circulation*, vol. 72, no. 6, pp. 1257–69, Dec. 1985.

[197] R. L. Reddick, S. H. Zhang, and N. Maeda, "Atherosclerosis in mice lacking apo E. Evaluation of lesional development and progression.," *Arterioscler. Thromb.*, vol. 14, no. 1, pp. 141–147, 1994.

[198] C. M. He and M. R. Roach, "The composition and mechanical properties of abdominal aortic aneurysms," *J. Vasc. Surg.*, vol. 20, no. 1, pp. 6–13, Jul. 1994.

[199] M. J. Thubrikar, F. Labrosse, and M. Robic, "Mechanical properties of abdominal aortic aneurysm wall," *J. Med. Eng. Technol.*, vol. 25, no. 4, pp. 133–142, Jan. 2001.

[200] A. Swillens, L. Lanoye, J. De Backer, N. Stergiopulos, P. R. Verdonck, F. Vermassen, and P. Segers, "Effect of an Abdominal Aortic Aneurysm on Wave Reflection in the Aorta," *IEEE Trans. Biomed. Eng.*, vol. 55, no. 5, pp. 1602–1611, May 2008.

[201] C. Huang, T.-L. Ren, and J. Luo, "Effects of parameters on the accuracy and precision of ultrasound-based local pulse wave velocity measurement: a simulation study.," *IEEE Trans. Ultrason. Ferroelectr. Freq. Control*, vol. 61, no. 12, pp. 2001–18, Dec. 2014.

[202] M. Tanter, J. Bercoff, L. Sandrin, and M. Fink, “Ultrafast compound imaging for 2-D motion vector estimation: Application to transient elastography,” *IEEE Trans. Ultrason. Ferroelectr. Freq. Control*, vol. 49, no. 10, pp. 1363–1374, 2002.

[203] M. Tanter and M. Fink, “Ultrafast imaging in biomedical ultrasound,” *IEEE Trans. Ultrason. Ferroelectr. Freq. Control*, vol. 61, no. 1, pp. 102–119, 2014.

[204] G. Montaldo, M. Tanter, J. Bercoff, N. Benech, and M. Fink, “Coherent plane-wave compounding for very high frame rate ultrasonography and transient elastography,” *IEEE Trans. Ultrason. Ferroelectr. Freq. Control*, vol. 56, no. 3, pp. 489–506, 2009.

[205] G. Matrone, A. S. Savoia, G. Caliano, and G. Magenes, “The Delay Multiply and Sum Beamforming Algorithm in Ultrasound B-Mode Medical Imaging,” *IEEE Trans. Med. Imaging*, vol. 34, no. 4, pp. 940–949, Apr. 2015.

[206] C. Papadacci, M. Pernot, M. Couade, M. Fink, and M. Tanter, “High-contrast ultrafast imaging of the heart,” *IEEE Trans. Ultrason. Ferroelectr. Freq. Control*, vol. 61, no. 2, pp. 288–301, 2014.

[207] B.-F. Osmanski, M. Pernot, G. Montaldo, A. Bel, E. Messas, and M. Tanter, “Ultrafast doppler imaging of blood flow dynamics in the myocardium,” *IEEE Trans. Med. Imaging*, vol. 31, no. 8, pp. 1661–1668, 2012.

[208] I. K. Ekroll, M. M. Voormolen, O. K.-V. Standal, J. M. Rau, and L. Lovstakken, “Coherent compounding in doppler imaging.,” *IEEE Trans. Ultrason. Ferroelectr. Freq. Control*, vol. 62, no. 9, pp. 1634–43, Sep. 2015.

[209] I. B. Wilkinson, S. A. Fuchs, I. M. Jansen, J. C. Spratt, G. D. Murray, J. R. Cockcroft, and D. J. Webb, “Reproducibility of pulse wave velocity and augmentation index measured by

pulse wave analysis.," *J. Hypertens.*, vol. 16, no. 12 Pt 2, pp. 2079–84, Dec. 1998.

[210] C. J. Huck, U. G. Bronas, E. B. Williamson, C. C. Draheim, D. A. Duprez, and D. R. Dengel, "Noninvasive measurements of arterial stiffness: repeatability and interrelationships with endothelial function and arterial morphology measures.," *Vasc. Health Risk Manag.*, vol. 3, no. 3, pp. 343–9, 2007.

[211] M. Couade, M. Pernot, E. Messas, J. Emmerich, a. Hagège, M. Fink, and M. Tanter, "Ultrafast imaging of the arterial pulse wave," *Irbm*, vol. 32, no. 2, pp. 106–108, Apr. 2011.

[212] H. Hasegawa and H. Kanai, "High-frame-rate echocardiography using diverging transmit beams and parallel receive beamforming," *J. Med. Ultrason.*, vol. 38, no. 3, pp. 129–140, May 2011.

[213] P. Kruizinga, F. Mastik, S. C. H. van den Oord, A. F. L. Schinkel, J. G. Bosch, N. de Jong, G. van Soest, and A. F. W. van der Steen, "High-definition imaging of carotid artery wall dynamics.," *Ultrasound Med. Biol.*, vol. 40, no. 10, pp. 1–12, 2014.

[214] J. Wang and J. Lu, "Motion artifacts of extended high frame rate imaging.," *IEEE Trans. Ultrason. Ferroelectr. Freq. Control*, vol. 54, no. 7, pp. 1303–1315, 2007.

[215] R. S. Reneman, J. M. Meinders, and A. P. G. Hoeks, "Non-invasive ultrasound in arterial wall dynamics in humans: what have we learned and what remains to be solved," *Eur. Heart J.*, vol. 26, no. 10, 2005.

[216] W. S. Moore, R. F. Kempczinski, J. J. Nelson, and J. F. Toole, "Recurrent carotid stenosis : results of the asymptomatic carotid atherosclerosis study.," *Stroke*, vol. 29, no. 10, pp. 2018–25, Oct. 1998.

[217] I. Z. Apostolakis, P. Nauleau, P. Kemper, E. S. Connolly, and E. Konofagou, “Pulse wave velocity (PWV) and compliance estimation and mapping using pulse wave imaging (PWI) in healthy, stenotic and post-endarterectomy carotid arteries in vivo,” in *2017 IEEE International Ultrasonics Symposium (IUS)*, 2017, pp. 1–1.

[218] T. K. Lim, E. Lim, G. Dwivedi, J. Kooner, and R. Senior, “Normal Value of Carotid Intima-Media Thickness–A Surrogate Marker of Atherosclersosis: Quantitative Assessment by B-Mode Carotid Ultrasound,” *J. Am. Soc. Echocardiogr.*, vol. 21, no. 2, pp. 112–116, Feb. 2008.

[219] C. I. Christodoulou, C. S. Pattichis, M. Pantziaris, and A. Nicolaides, “Texture-based classification of atherosclerotic carotid plaques,” *IEEE Trans. Med. Imaging*, vol. 22, no. 7, pp. 902–912, Jul. 2003.

[220] O. Honda, S. Sugiyama, K. Kugiyama, H. Fukushima, S. Nakamura, S. Koide, S. Kojima, N. Hirai, H. Kawano, H. Soejima, T. Sakamoto, M. Yoshimura, and H. Ogawa, “Echolucent carotid plaques predict future coronary events in patients with coronary artery disease,” *J. Am. Coll. Cardiol.*, vol. 43, no. 7, pp. 1177–1184, Apr. 2004.

[221] L. M. Van Bortel, E. J. Balkestein, J. J. van der Heijden-Spek, F. H. Vanmolkot, J. A. Staessen, J. A. Kragten, J. W. Vredeveld, M. E. Safar, H. A. Struijker Boudier, and A. P. Hoeks, “Non-invasive assessment of local arterial pulse pressure: comparison of applanation tonometry and echo-tracking.,” *J. Hypertens.*, vol. 19, no. 6, pp. 1037–44, Jun. 2001.

[222] J. Kips, F. Vanmolkot, D. Mahieu, S. Vermeersch, I. Fabry, J. de Hoon, L. Van Bortel, and P. Segers, “The use of diameter distension waveforms as an alternative for tonometric

pressure to assess carotid blood pressure," *Physiol. Meas.*, vol. 31, no. 4, pp. 543–553, Apr. 2010.

[223] M. E. Safar, M. F. O'Rourke, and E. D. Frohlich, *Blood Pressure and Arterial Wall Mechanics in Cardiovascular Diseases*, First. London: Springer London, 2014.

[224] C. Schmitt, G. Soulez, R. L. Maurice, M.-F. Giroux, and G. Cloutier, "Noninvasive Vascular Elastography: Toward A Complementary Characterization Tool of Atherosclerosis in Carotid Arteries," *Ultrasound Med. Biol.*, vol. 33, no. 12, pp. 1841–1858, Dec. 2007.

[225] L. Cardoso and S. Weinbaum, "Changing views of the biomechanics of vulnerable plaque rupture: a review.," *Ann. Biomed. Eng.*, vol. 42, no. 2, pp. 415–31, Feb. 2014.

[226] A. Maseri and V. Fuster, "Is there a vulnerable plaque?," *Circulation*, vol. 107, no. 16, pp. 2068–71, Apr. 2003.

[227] K. J. Hunt, J. S. Pankow, S. Offenbacher, S. B. Kritchevsky, B. B. Duncan, E. Shahar, A. R. Sharrett, and G. Heiss, "B-mode ultrasound-detected carotid artery lesions with and without acoustic shadowing and their association with markers of inflammation and endothelial activation: the atherosclerosis risk in communities study," *Atherosclerosis*, vol. 162, no. 1, pp. 145–155, May 2002.

[228] E. B. Mathiesen, K. H. Bønaa, and O. Joakimsen, "Echolucent plaques are associated with high risk of ischemic cerebrovascular events in carotid stenosis: the tromsø study.," *Circulation*, vol. 103, no. 17, pp. 2171–5, May 2001.

[229] T. Tomonori, S. Keiko, H. Shinkichi, N. Yoji, and T. Akira, "Carotid atherosclerosis and arterial peripheral pulse wave velocity in cerebral thrombosis," *J. Clin. Neurosci.*, vol. 13, no. 1, pp. 45–49, Jan. 2006.

[230] A. Fenster, D. B. Downey, and H. N. Cardinal, “Three-dimensional ultrasound imaging,” *Phys. Med. Biol.*, vol. 46, no. 5, pp. R67–R99, May 2001.

[231] J. Provost, C. Papadacci, J. E. Arango, M. Imbault, M. Fink, J.-L. Gennisson, M. Tanter, and M. Pernot, “3D ultrafast ultrasound imaging in vivo.,” *Phys. Med. Biol.*, vol. 59, no. 19, pp. L1–L13, Oct. 2014.

[232] J. Provost, C. Papadacci, C. Demene, J.-L. Gennisson, M. Tanter, and M. Pernot, “3-D ultrafast doppler imaging applied to the noninvasive mapping of blood vessels in Vivo,” *IEEE Trans. Ultrason. Ferroelectr. Freq. Control*, vol. 62, no. 8, pp. 1467–1472, Aug. 2015.

[233] J.-L. Gennisson, J. Provost, T. Deffieux, C. Papadacci, M. Imbault, M. Pernot, and M. Tanter, “4-D ultrafast shear-wave imaging.,” *IEEE Trans. Ultrason. Ferroelectr. Freq. Control*, vol. 62, no. 6, pp. 1059–65, Jun. 2015.

[234] M. Correia, J. Provost, M. Tanter, and M. Pernot, “4D ultrafast ultrasound flow imaging: in vivo quantification of arterial volumetric flow rate in a single heartbeat,” *Phys. Med. Biol.*, vol. 61, no. 23, pp. L48–L61, Dec. 2016.

[235] C. Papadacci, E. A. Bunting, and E. E. Konofagou, “3D Quasi-Static Ultrasound Elastography With Plane Wave In Vivo,” *IEEE Trans. Med. Imaging*, vol. 36, no. 2, pp. 357–365, Feb. 2017.

[236] C. Papadacci, E. A. Bunting, E. Y. Wan, P. Nauleau, and E. E. Konofagou, “3D myocardial elastography in vivo,” *IEEE Trans. Med. Imaging*, pp. 1–1, Nov. 2016.

[237] M. Markl, W. Wallis, C. Strecker, B. P. Gladstone, W. Vach, and A. Harloff, “Analysis of pulse wave velocity in the thoracic aorta by flow-sensitive four-dimensional MRI: reproducibility and correlation with characteristics in patients with aortic

atherosclerosis.," *J. Magn. Reson. Imaging*, vol. 35, no. 5, pp. 1162–8, May 2012.

[238] S. Fekkes, A. E. S. Swillens, H. H. G. Hansen, A. E. C. M. Saris, M. M. Nillesen, F. Iannaccone, P. Segers, and C. L. de Korte, "2D versus 3D cross-correlation-based radial and circumferential strain estimation using multiplane 2D ultrafast ultrasound in a 3D atherosclerotic carotid artery model," *IEEE Trans. Ultrason. Ferroelectr. Freq. Control*, vol. 63, no. 10, pp. 1543–1553, 2016.

[239] S. Fekkes, A. E. S. Swillens, H. H. G. Hansen, A. E. C. M. Saris, M. M. Nillesen, F. Iannaccone, P. Segers, and C. L. de Korte, "Semi-3D strain imaging of an atherosclerotic carotid artery by multi-cross-sectional radial strain estimations using simulated multi-angle plane wave ultrasound," in *2014 IEEE International Ultrasonics Symposium*, 2014, pp. 519–522.

[240] S. Korukonda and M. M. Doyley, "3D ultrafast elastography imaging of the carotid artery using sparse arrays," in *2011 IEEE International Ultrasonics Symposium*, 2011, pp. 721–724.

[241] Y. Liang, H. Zhu, M. H. Friedman, D. A. N. P. W. F. R. R. J. K. B. J. and B. V Arbab-Zadeh A, W. H. Y. H. J. E. M. K. S. R. and K. S. H. Bank A J, F. J. F. G. D. P. and V. D. Brusseau E, O. J. P. H. and M. N. Cespedes I, M. R. H. and R. D. Chandrashekara R, M. F. and V. D. S. A. F. W. Danilouchkine M G, C. S. G. M. F. D. M. M. V. D. S. A. F. W. S. P. W. and B. N. de Korte C L, C. E. I. vanderSteen A. F. W. and L. C. T. de Korte C L, S. M. J. M. F. S. C. S. J. A. V. E. P. G. S. P. W. and V. D. S. A. F. W. de Korte C L, de K. C. L. and V. D. S. A. F. W, D. P. B, F. E, H. J. D, de K. C. L. V. D. H. M. S. W. C. P. and V. D. S. A. F. W. Janssen C R M, G. A. J. F. E. H. K. R. D. and S. F. J. Lee R T, B. R. A. M. F. S. J. A. G. A. and V. D. S. A. F. W. Leung K Y E, L.

J. and D. T. S, Z. H. and F. M. H. Liang Y, Z. H. G. T. and F. M. H. Liang Y, L. P, K. R. D. S. R. G. and L. R. T. Loree H M, M. R. L. and B. R, B. E. F. G. and C. G. Maurice R L, F. J. B. L. F. G. R. G. and C. G. Maurice R L, F. J. C. M. H. R. D. M. de M. E. R. J. and C. G. Maurice R L, O. J. F. G. and C. G. Maurice R L, K. H. K. Y. I. M. and T. F. Mita H, B. D. and F. A. Nadkarni S K, C. I. P. H. Y. Y. and L. X. Ophir J, B. A. L. G. J. M. N. R. F. A. Y. R. W. C. and L. M. B. Potkin B N, R. L. K. and F. F. S, V. D. S. A. F. W. Saijo Y, de K. C. L. M. F. B. R. R. E. de F. P. S. C. J. V. D. S. A. F. W. and S. P. W. Schaar J A, de K. C. L. M. F. van D. L. C. A. K. R. S. P. W. and V. D. S. A. F. W. Schaar J A, M. F. R. E. den U. C. A. G. F. J. W. J. J. S. P. W. and V. D. S. A. F. W. Schaar J A, C. J. R. E. R. E. S. Y. E. M. J. and O. M. Shapo B M, C. J. R. S. A. R. E. M. J. C. N. A. and O. M. Shapo B M, S. R. and C. J, W. L. S. and N. M. L. Talhami H E, H. D. O. C. M. I. and V. S. L. K. Tozzi P, O. J. and C. I. Varghese T, V. R. P. and D. S. A, de F. P. J. de V. E. A. L. W. G. B. N. N. A. R. J. R. and S. P. W. von Birgelen C, and L. Y. M. L. J. B. C. Y. Y. and Z. X. D. Wan M X, “Measurement of the 3D arterial wall strain tensor using intravascular B-mode ultrasound images: a feasibility study,” *Phys. Med. Biol.*, vol. 55, no. 21, pp. 6377–6394, Nov. 2010.

[242] I. Z. Apostolakis, P. Nauleau, C. Papadacci, M. D. McGarry, and E. E. Konofagou, “Feasibility and Validation of 4-D Pulse Wave Imaging in Phantoms and In Vivo,” *IEEE Trans. Ultrason. Ferroelectr. Freq. Control*, vol. 64, no. 9, pp. 1305–1317, Sep. 2017.

[243] H. Sillesen, P. Muntendam, A. Adourian, R. Entrekin, M. Garcia, E. Falk, and V. Fuster, “Carotid Plaque Burden as a Measure of Subclinical Atherosclerosis,” *JACC Cardiovasc. Imaging*, vol. 5, no. 7, 2012.

[244] A. Swillens, J. Degroote, J. Vierendeels, L. Lovstakken, and P. Segers, “A simulation

environment for validating ultrasonic blood flow and vessel wall imaging based on fluid-structure interaction simulations: Ultrasonic assessment of arterial distension and wall shear rate," *Med. Phys.*, vol. 37, no. 8, pp. 4318–4330, Jul. 2010.

[245] P. Crosetto, P. Reymond, S. Deparis, D. Kontaxakis, N. Stergiopulos, and A. Quarteroni, "Fluid–structure interaction simulation of aortic blood flow," *Comput. Fluids*, vol. 43, no. 1, pp. 46–57, Apr. 2011.

[246] K. Perktold and G. Rappitsch, "Computer simulation of local blood flow and vessel mechanics in a compliant carotid artery bifurcation model.," *J. Biomech.*, vol. 28, no. 7, pp. 845–56, Jul. 1995.

[247] Y. Bazilevs, J. R. Gohean, T. J. R. Hughes, R. D. Moser, and Y. Zhang, "Patient-specific isogeometric fluid–structure interaction analysis of thoracic aortic blood flow due to implantation of the Jarvik 2000 left ventricular assist device," *Comput. Methods Appl. Mech. Eng.*, vol. 198, no. 45–46, pp. 3534–3550, Sep. 2009.

[248] J. Luo and E. E. Konofagou, "Imaging of wall motion coupled with blood flow velocity in the heart and vessels in vivo: a feasibility study.," *Ultrasound Med. Biol.*, vol. 37, no. 6, pp. 980–95, Jun. 2011.

[249] G. Pasterkamp, D. P. . de Kleijn, and C. Borst, "Arterial remodeling in atherosclerosis, restenosis and after alteration of blood flow: potential mechanisms and clinical implications," *Cardiovasc. Res.*, vol. 45, no. 4, pp. 843–852, Mar. 2000.

[250] D. N. Ku, D. P. Giddens, C. K. Zarins, and S. Glagov, "Pulsatile flow and atherosclerosis in the human carotid bifurcation. Positive correlation between plaque location and low oscillating shear stress," *Arterioscler. Thromb. Vasc. Biol.*, vol. 5, no. 3, pp. 293–302, May

1985.

[251] J. R. Womersley, “Method for the calculation of velocity, rate of flow and viscous drag in arteries when the pressure gradient is known,” *J. Physiol.*, vol. 127, no. 3, pp. 553–563, Mar. 1955.

[252] P. C. Struijk, P. a. Stewart, K. L. Fernando, V. J. Mathews, T. Loupas, E. a P. Steegers, and J. W. Wladimiroff, “Wall shear stress and related hemodynamic parameters in the fetal descending aorta derived from color Doppler velocity profiles,” *Ultrasound Med. Biol.*, vol. 31, no. 11, pp. 1441–1450, 2005.

[253] P. Tortoli, T. Morganti, G. Bambi, C. Palombo, and K. V. Ramnarine, “Noninvasive simultaneous assessment of wall shear rate and wall distension in carotid arteries,” *Ultrasound Med. Biol.*, vol. 32, no. 11, pp. 1661–1670, Nov. 2006.

[254] S. Fadnes, I. K. Ekroll, S. A. Nyrnes, H. Torp, and L. Lovstakken, “Robust angle-independent blood velocity estimation based on dual-angle plane wave imaging,” *IEEE Trans. Ultrason. Ferroelectr. Freq. Control*, vol. 62, no. 10, pp. 1757–1767, Oct. 2015.

[255] I. K. Ekroll, H. Torp, L. Lovstakken, A. Swillensz, and P. Segersz, “Simultaneous quantification of flow and tissue velocities based on multi-angle plane wave imaging with an extended velocity range,” in *2011 IEEE International Ultrasonics Symposium*, 2011, pp. 438–441.

[256] B. Y. S. Yiu and A. C. H. Yu, “Least-Squares Multi-Angle Doppler Estimators for Plane Wave Vector Flow Imaging,” *IEEE Trans. Ultrason. Ferroelectr. Freq. Control*, vol. PP, no. 99, pp. 1–1, 2016.

[257] H. Hasegawa and H. Kanai, “Simultaneous imaging of artery-wall strain and blood flow by

high frame rate acquisition of RF signals," *IEEE Trans. Ultrason. Ferroelectr. Freq. Control*, vol. 55, no. 12, pp. 2626–2639, Dec. 2008.

[258] I. K. Ekroll, A. Swillens, P. Segers, T. Dahl, H. Torp, and L. Lovstakken, "Simultaneous quantification of flow and tissue velocities based on multi-angle plane wave imaging," *IEEE Trans. Ultrason. Ferroelectr. Freq. Control*, vol. 60, no. 4, pp. 727–738, Apr. 2013.

[259] A. J. Y. Chee, C. K. Ho, B. Y. S. Yiu, and A. C. H. Yu, "Walled Carotid Bifurcation Phantoms for Imaging Investigations of Vessel Wall Motion and Blood Flow Dynamics," *IEEE Trans. Ultrason. Ferroelectr. Freq. Control*, vol. 63, no. 11, pp. 1852–1864, Nov. 2016.

[260] J. Bercoff, G. Montaldo, T. Loupas, D. Savery, F. Mézière, M. Fink, and M. Tanter, "Ultrafast compound doppler imaging: Providing full blood flow characterization," *IEEE Trans. Ultrason. Ferroelectr. Freq. Control*, vol. 58, no. 1, pp. 134–147, 2011.

[261] C. Demene, T. Deffieux, M. Pernot, B.-F. Osmanski, V. Biran, J.-L. Gennisson, L.-A. Sieu, A. Bergel, S. Franqui, J.-M. Correas, I. Cohen, O. Baud, and M. Tanter, "Spatiotemporal Clutter Filtering of Ultrafast Ultrasound Data Highly Increases Doppler and fUltrasound Sensitivity," *IEEE Trans. Med. Imaging*, vol. 34, no. 11, pp. 2271–2285, Nov. 2015.

[262] P. Salvi, E. Magnani, F. Valbusa, D. Agnoletti, C. Alecu, L. Joly, and A. Benetos, "Comparative study of methodologies for pulse wave velocity estimation," *J. Hum. Hypertens.*, vol. 22, no. 10, pp. 669–677, Oct. 2008.

[263] I. K. H. Tsang, B. Y. S. Yiu, and A. C. H. Yu, "A least-squares vector flow estimator for synthetic aperture imaging," in *2009 IEEE International Ultrasonics Symposium*, 2009, pp. 1387–1390.

[264] B. Dunmire, K. W. Beach, K.-H. Labs, M. Plett, and D. E. Strandness, "Cross-beam vector

Doppler ultrasound for angle-independent velocity measurements," *Ultrasound Med. Biol.*, vol. 26, no. 8, pp. 1213–1235, Oct. 2000.

[265] V. S. Lee, B. S. Hertzberg, M. J. Workman, T. P. Smith, M. A. Kliewer, D. M. DeLong, and B. A. Carroll, "Variability of Doppler US Measurements along the Common Carotid Artery: Effects on Estimates of Internal Carotid Arterial Stenosis in Patients with Angiographically Proved Disease," *Radiology*, vol. 214, no. 2, pp. 387–392, Feb. 2000.

[266] M. A. Pozniak, J. A. Zagzebski, and K. A. Scanlan, "Spectral and color Doppler artifacts.," *Radiographics*, vol. 12, no. 1, pp. 35–44, Jan. 1992.

[267] A. E. C. M. Saris, H. H. G. Hansen, S. Fekkes, M. M. Nillesen, M. C. M. Rutten, and C. L. de Korte, "Does large beam-steered angle velocity compounding using plane wave transmission improve blood vector velocity estimation in a 3D carotid artery flow field?," in *2014 IEEE International Ultrasonics Symposium*, 2014, pp. 1726–1729.

[268] C. J. Hartley, A. K. Reddy, S. Madala, M. L. Entman, L. H. Michael, and G. E. Taffet, "Noninvasive ultrasonic measurement of arterial wall motion in mice.," *Am J Physiol Hear. Circ Physiol*, vol. 287, pp. H1426–H1432, 2004.

[269] S. Perlini, P. L. Soldà, M. Piepoli, A. Calciati, M. Paro, G. Marchetti, F. Meno, G. Finardi, and L. Bernardi, "Time course of pressure and flow in ascending aorta during ejection," *Int. J. Cardiol.*, vol. 30, no. 2, pp. 169–179, Feb. 1991.

[270] P. Tortoli, M. Lenge, D. Righi, G. Ciuti, H. Liebgott, and S. Ricci, "Comparison of Carotid Artery Blood Velocity Measurements by Vector and Standard Doppler Approaches," *Ultrasound Med. Biol.*, vol. 41, no. 5, pp. 1354–1362, May 2015.

[271] J. A. Jensen, S. I. Nikolov, A. C. H. Yu, and D. Garcia, "Ultrasound Vector Flow Imaging—

Part II: Parallel Systems," *IEEE Trans. Ultrason. Ferroelectr. Freq. Control*, vol. 63, no. 11, pp. 1722–1732, Nov. 2016.

[272] A. Swillens, P. Segers, H. Torp, and L. Lovstakken, "Two-dimensional blood velocity estimation with ultrasound: speckle tracking versus crossed-beam vector doppler based on flow simulations in a carotid bifurcation model," *IEEE Trans. Ultrason. Ferroelectr. Freq. Control*, vol. 57, no. 2, pp. 327–339, Feb. 2010.

[273] A. Goddi, C. Bortolotto, I. Fiorina, M. V. Raciti, M. Fanizza, E. Turpini, G. Boffelli, and F. Calliada, "High-frame rate vector flow imaging of the carotid bifurcation.," *Insights Imaging*, vol. 8, no. 3, pp. 319–328, Jun. 2017.

[274] J. Udesen, M. B. Nielsen, K. R. Nielsen, and J. A. Jensen, "Examples of In Vivo Blood Vector Velocity Estimation," *Ultrasound Med. Biol.*, vol. 33, no. 4, pp. 541–548, Apr. 2007.

[275] D. N. Ku and D. P. Giddens, "Pulsatile flow in a model carotid bifurcation.," *Arteriosclerosis*, vol. 3, no. 1, pp. 31–9, Jan. 1983.

[276] I. Z. Apostolakis, P. Nauleau, S. D. Nandlall, and E. E. Konofagou, "Adaptive Pulse Wave Imaging: automatited spatial inhomogeneity detection in phantoms and in vivo," *IEEE Trans. Med. imaging (under Rev.*, 2018.

[277] T. Deffieux, J.-L. Gennisson, J. Bercoff, and M. Tanter, "On the effects of reflected waves in transient shear wave elastography," *IEEE Trans. Ultrason. Ferroelectr. Freq. Control*, vol. 58, no. 10, pp. 2032–2035, Oct. 2011.

[278] M. A. Lediju, G. E. Trahey, B. C. Byram, and J. J. Dahl, "Short-lag spatial coherence of backscattered echoes: imaging characteristics," *IEEE Trans. Ultrason. Ferroelectr. Freq.*

Control, vol. 58, no. 7, pp. 1377–1388, Jul. 2011.

[279] J. Kang, J. Y. Lee, and Y. Yoo, "A New Feature-Enhanced Speckle Reduction Method Based on Multiscale Analysis for Ultrasound B-Mode Imaging," *IEEE Trans. Biomed. Eng.*, vol. 63, no. 6, pp. 1178–1191, Jun. 2016.

[280] C. J. Bouma, W. J. Niessen, K. J. Zuiderveld, E. J. Gussenhoven, and M. A. Viergever, "Automated lumen definition from 30 MHz intravascular ultrasound images," *Med. Image Anal.*, vol. 1, no. 4, pp. 363–377, Sep. 1997.

[281] F. Destrempes, J. Meunier, M.-F. Giroux, G. Soulez, and G. Cloutier, "Segmentation in Ultrasonic *B* -Mode Images of Healthy Carotid Arteries Using Mixtures of Nakagami Distributions and Stochastic Optimization," *IEEE Trans. Med. Imaging*, vol. 28, no. 2, pp. 215–229, Feb. 2009.

[282] P. Libby, "ATHEROSCLEROSIS: THE NEW VIEW," *Scientific American*, vol. 286. Scientific American, a division of Nature America, Inc., pp. 46–55, 2002.

Appendix

Let f(m,l,n) and g(m,l,n) represent the values of the reference and comparison RF-signal at m-th sample, l-th line and n-th frame, respectively. The NCC between the reference and the comparison windows is defined as:

$$R_{NCC}(u,l,n,\tau) = \frac{\sum_{m=u}^{u+W-1} f(m,l,n)g(m+\tau,l,n)}{\sqrt{\sum_{m=u}^{u+W-1} f^2(m,l,n) \cdot \sum_{n=u}^{u+W-1} g^2(m+\tau,l,n)}} \qquad (A.1)$$

Where u is the origin of the reference window, W is the window size and τ is the shift between the comparison and reference windows, which in this study is confined between -1 and 1 in order to yield sub-sample displacements.

The first step of the proposed algorithm consists of estimating in parallel the sum-tables for each line (l) in each frame (n) of the image sequence. The sum-table for the comparison windows is given by the following formula:

$$s_g^2(m,l,n) = \begin{cases} g^2(m,l,n) + s_g^2(m-1,l,n), & 1 \le m \le M \\ 0, & m = 0 \end{cases} \qquad (A.2)$$

where M is the number of samples for each line. Similarly for the reference windows:

$$s_f^2(m,l,n) = \begin{cases} f^2(m,l,n) + s_f^2(m-1,l,n), & 1 \le m \le M \\ 0, & m = 0 \end{cases} \qquad (A.3)$$

And finally the sum-table for the nominator of equation (A.1) can be constructed for τ = -1, 0 and 1:

$$s_{f.g}(m,l,n,\tau) = \begin{cases} f(m,l,n) \cdot g(m+\tau,l,n) + s_{f,g}(m-1,l,n,\tau), & 1 \le m \le M \\ 0, & m = 0 \end{cases} \qquad (A.4)$$

Subsequently, the R_{NCC} function is estimated in parallel for all the lines in all the frames in the image sequence for τ = -1, 0 and 1. Thus:

$$R_{NCC}(u,l,n,\tau)$$

$$= \frac{s_{f,g}(u+W-1,l,n,\tau) - \ s_{f,g}(u-1,l,n,\tau)}{\sqrt{(s_f^2(u+W-1,l,n) - s_f^2(u-1,l,n)) \cdot (s_g^2(u+W-1,l,n) - s_g^2(u-1,l,n))}} \quad (A.5)$$

The resulting 4-D matrix containing R_{NCC} has a size of (number of windows)x(number of lines)x(number of frames)x3. Given that R_{NCC} only contained integer lags interpolation is necessary to improve the estimation accuracy. A cosine function was selected to fit to the three points (τ = -1,0, 1) [161] and thus, in order to estimate the axial wall displacements (d_{PWI}) in parallel for all the windows in all the lines of all the frames the following calculations were made:

$$\omega(u,l,n) = \operatorname{acos}\left(\frac{R_{NCC}(u,l,n,-1) + R_{NCC}(u,l,n,1)}{2 \cdot R_{NCC}(u,l,n,0)}\right)$$

$$\varphi(u,l,n) = \operatorname{atan}\left(\frac{R_{NCC}(u,l,n,-1) + R_{NCC}(u,l,n,1)}{2 \cdot R_{NCC}(u,l,n,0) \cdot \sin(\omega(u,l,n))}\right)$$

$$d_{PWI}(u,l,n) = \ -\frac{\varphi(u,l,n)}{\omega(u,l,n)}$$

Where $d(u,l,n)$ are the sub-sample axial wall displacements at each window position u, line l and frame n.